CORA Cork Open Research Archive
Cartlann Taighde Oscailte Chorcaí

Title	Data-driven analysis of reliability, accessibility and survivability in marine renewable energy projects
Authors	Barker, Aaron
Publication date	2019
Original Citation	Barker, A. 2019. Data-driven analysis of reliability, accessibility and survivability in marine renewable energy projects. PhD Thesis, University College Cork.
Type of publication	Doctoral thesis
Rights	© 2019, Aaron Barker. - http://creativecommons.org/licenses/by-nc-nd/3.0/
Download date	2026-10-30 22:30:59
Item downloaded from	https://hdl.handle.net/10468/8197



UCC
University College Cork, Ireland
Coláiste na hOllscoile Corcaigh

Department of Civil & Environmental Engineering

"Data-Driven Analysis of Reliability, Accessibility and Survivability in Marine Renewable Energy Projects"

Aaron Barker, B.E.



UCC

University College Cork, Ireland
Coláiste na hOllscoile Corcaigh

A thesis submitted for the degree of Doctor of Philosophy

In Faculty of Engineering

National University of Ireland, Cork

Volume 1 of 1

Supervisor: Dr. Jimmy Murphy,

Hydraulics & Maritime Research Centre,

Dept. Civil & Environmental Engineering,

University College Cork,

Ireland.

2019

Declaration

This is to certify that the work I am submitting is my own and has not been submitted for another degree, either at University College Cork or elsewhere. All external references and sources are clearly acknowledged and identified within the contents. I have read and understood the regulations of University College Cork concerning plagiarism.

ABSTRACT

Increased activity in the Marine Renewable Energy industry has driven the need for an improved understanding of the wave climate and wave energy resource, which are fundamental to the development of any marine energy project.

This thesis assesses the characterisation of the wave energy resource available at the Killard Point site in Co. Clare, as part of a joint industry project on the Electricity Supply Board (ESB)'s's WestWave project, Ireland's first proposed commercial wave energy installation.

This assessment is done with an eye on the newly formed International Electrotechnical Commission standards for metocean resource assessment, with a focus on producing a standardised analysis method which informs the extractable wave energy resource.

Many existing practices are questioned, and their merits assessed. This thesis adds novel tools and advanced data analysis methods, which are implemented to develop new methodologies for enhancing our understanding of our wave resource, and which subsequently enable improved assessment of the impacts of reliability, accessibility and survivability of Marine Renewable Energy projects.

The impact of spectral shape on device energy production is examined using both a theoretical and practical application, to show the disconnect between currently accepted practices and the level of certainty which will be required to drive commercial success.

A new methodology for the assessment of extreme wave conditions is developed, while a large contribution of this thesis is in developing and applying machine learning techniques to enhance the accuracy and dependability of wave parameter relationships and the prediction of device energy production by improving the estimation of absent wave data. This approach has been shown to result in a reduction in power production error at Killard Point from 30% to just 3.5%. This novel Machine Learning method is integral in enabling the level of characterisation that will be necessary for the commercial success of Marine Renewable Energy projects.

The major contribution of this thesis is the development of an enhanced understanding of the available wave resource at the Killard Point site; producing a numerical hindcast nearshore wave model which attempts to bring the project to the level required by IEC standards, while

addressing technical issues which affect the standardisation, accuracy, usability and predictability of the data gathered.

This work does not focus on the Marine Renewable Energy technology in use, nor will it explore in great detail the economic vagaries of MRE projects. Instead, it focusses on developing methods which will provide a large missing piece of the puzzle in MRE development, accurate and dependable metocean analysis.

The results presented here have wider applicability, and indeed much of this research has taken place, or has been verified at, other sites along the west-coast of Ireland.

ACKNOWLEDGEMENTS

I firmly believe that it is not possible to undertake great research alone, and I would not have been able to complete this PhD thesis were it not for the support of so many people. I would like to sincerely thank the people that made this PhD thesis possible. My supervisors, Dr. Jimmy Murphy, for encouraging and enabling this research at all stages, and for his guidance over the past number of years; and Prof. Tony Lewis, whose vision has been at the core of founding the institutions that made this possible.

I have been fortunate to be part of a growing and flourishing research area, and surrounded by a wonderful team; first at the Hydraulics and Maritime Research Centre, then at the headquarters of the Marine and Renewable Energy Ireland centre at the Beaufort building. I have had many wonderful times with my colleagues here, and will cherish the memories that we have created. I am deeply grateful for the assistance, guidance and support of all those fellow researchers in the Marine Renewable Energy industry, whose dedication and innovation continues to inspire me. I look forward to working together in the future.

Thank you to my friends and family, many of whom have become more engrossed in wave energy in reading my thesis and listening to me than any sane person had right to. I am forever grateful to Rachel for giving up her time to proof read this thesis, and for keeping me focused on the positive through difficult times.

Thank you too, to Andrew who was constantly available to explore new ideas, discuss new methods, and provide a proximate sounding board for my quibbles and programming problems.

I would like to thank my parents, who instilled the value of education and learning in me, and who were ever-willing to support any academic adventure.

Finally, I would like to acknowledge the joint financial support of Science Foundation Ireland (SFI) and the Electricity Supply Board (ESB) Group which funded this PhD. Acknowledgement is owed to ESB for recognising the value of research where others are focused solely on commercial outcomes.

Contents

1 Introduction 1

1.1 Wave Energy Context 1

1.1.1 Early Wave Energy 1

1.1.2 The development of Wave Energy 1

1.1.3 Wave Energy in the modern world 2

1.1.4 Potential for wave energy in Ireland 3

1.2 Technology Development and Economic Status of Projects 5

1.2.1 Progress of Wave Energy hindered by development approach 5

1.3 Research Outline 9

1.4 Publications 13

2 Literature Review 15

2.1 Wave Data Sources 15

2.1.1 Measured Data 15

2.1.2 Model Data 28

2.2 Wave Data Analysis 44

2.2.1 Time-series analysis 45

2.2.2 Spectral Analysis 47

2.2.3 Error Analysis of Wave Data 52

2.3 Metocean Analysis 53

2.3.1 Overview 53

2.3.2 Scatter plots 54

2.3.3 Extreme prediction 55

2.3.4 Weather Windows 59

2.3.5 Power Production Estimates 59

2.4 Standards for assessment of Marine Renewable Energy Projects 61

2.5 Machine Learning 62
2.5.1 k-fold cross validation 63
2.5.2 Leave One Out Cross Validation (LOOCV) 65
2.5.3 Ordinary Least Squares 65
2.5.4 Other Methods 67
2.5.5 Selection of best subset 67
2.5.6 Shrinkage Methods 67
2.5.7 Ridge regression model 68
2.5.8 Lasso Model 69
2.5.9 Selection of Alpha parameter 70
2.6 Literature Review Summary 72
3 Machine Learning Applied to Wave Parameters 73
3.1 Introduction 73
3.2 Machine Learning 74
3.2.1 Background and Development 75
3.2.2 Machine Learning as a WPR estimator 76
3.2.3 Existing Approaches 77
3.2.4 Approach Taken 77
3.3 Test Case 1 79
3.3.1 Belmullet Introduction 79
3.3.2 Model development for Belmullet 80
3.3.3 Determination of T_e 81
3.3.4 Python scikit-learn Workflow 81
3.3.5 Programmatic method 81
3.3.6 Comparison of models 82
3.3.7 Determination of T_E using Lasso based method 87

3.3.8 Method of Alpha Selection 88
3.3.9 Parameter Selection 90
3.3.10 Learning Curve: Analysis of required training time 93
3.3.11 Seasonal variability 95
3.3.12 Error Assessment for Seasonal LOOCV approach 104
3.3.13 Prediction accuracy 105
3.3.14 Prediction accuracy for energy production 106
3.3.15 Detailed comparison of model error 107
3.4 Test Case 2 108
3.4.1 Killard Point Introduction 108
3.4.2 Model Development 109
3.4.3 Parameter Selection 110
3.4.4 WPR analysis at Killard Point 111
3.4.5 Parameter Selection 113
3.4.6 Learning Curve Analysis 116
3.4.7 Error Analysis 117
3.4.8 Comparison of model error across test value range. 117
3.5 Conclusions 119
4 Extreme Wave Assessment Techniques 124
4.1 Introduction 124
4.2 Method 126
4.2.1 Current Extreme Prediction Methods 126
4.2.2 Proposed Analysis 127
4.2.3 Location & Data Sources 128
4.3 Analysis 130
4.3.2 Analysis of Anomaly Index from H_{max}/H_s 138

4.3.3 Determination of wave steepness at the extremes 141
4.3.4 Calculation of extreme T_z using regression analysis 142
4.3.5 Calculation of extreme Wave Power 144
4.4 Cross-validated ACER approach 146
4.4.1 Purpose 146
4.4.2 Introduction to Average Conditional Exceedance Rate extreme function 147
4.4.3 Method 148
4.5 Conclusions 153
5 Metocean Assessment to IEC standards 157
5.1 Introduction 157
5.2 Background and Development 158
5.2.1 IEC-TS 159
5.2.2 Test Case: WestWave Project, Killard Point 164
5.3 Metocean Modelling 169
5.3.1 Introduction 169
5.3.2 Wave Model Setup 171
5.3.3 Modelling Methodology 181
5.4 Wave Resource Characterisation 197
5.4.1 Magnitude and Variability of Wave Resource at Killard Point 198
5.4.2 Power Production 221
5.4.3 Extreme Analysis 225
5.4.4 Spectral Analysis 235
5.4.5 Wave Period Ratio 239
5.4.6 Weather Windows 240
5.4.7 Forecasting Prediction Accuracy 244
5.5 Modelling & Characterisation Summary 262

5.5.1 Outcomes of Numerical Modelling....262
5.5.2 Outcomes of Characterisation....262
5.5.3 Killard Point Site Specific Details....263
5.6 IEC-TS Methodology Summary....265
5.6.1 Practicalities of Implementing IEC-TS....265
5.6.2 Suggestions for alterations to IEC-TS....267
5.7 Conclusions....269
6 Impact of Spectral Shape on Device Energy Production....271
6.1 Introduction....271
6.2 Background....272
6.2.1 Current Methods....273
6.3 Theoretical Examination....274
6.3.1 Assessing Variation in Spectral Energy....274
6.3.2 Processing Data Records for Spectral Analysis....275
6.3.3 Selection of Sea-States for Assessment....279
6.3.4 Theoretical Device Power Study....287
6.4 Small Scale Tank Testing of OWC Devices....297
6.4.1 Tank Testing Necessity & Requirements....297
6.4.2 Preliminary Actions....299
6.4.3 Experiment Setup....299
6.4.4 Tank Testing....314
6.4.5 Analysis of Tank Test Results....320
6.5 Addressing Spectral Shape Variation....352
6.5.1 Modification of Standard Spectral Shapes....352
6.5.2 Wave Period Ratios (WPRs)....362

6.6 Framework for Implementation of Enhanced Spectral Shape Information in Wave Energy Projects 367
6.6.1 Class 1 – Reconnaissance: 369
6.6.2 Class 2 – Feasibility: 370
6.6.3 Class 3 – Design: 370
6.6.4 Additional requirements and summation. 371
6.7 Conclusions 371
6.7.1 Spectral Shape analysis 371
6.7.2 Ability of Tank to Generate Waves 372
6.7.3 Power Production Estimation 373
6.7.4 Determining Power Production from Sea-states. 374
7 Conclusions 375
7.1 Machine Learning Applied to Wave Parameters 376
7.2 Extreme Wave Assessment Techniques 378
7.3 Metocean Analysis of Killard Point to IEC standards 380
7.4 Impact of Spectral Shape on Device Energy Production 381
7.5 Further Work 383

List of Figures

Figure 1: An ESB cost projection for projects based on indicative wave energy technology (OES IA and IEA Energy Technology Network, 2012) 8
Figure 2: Automatic tide gauge at Port Protection, Alaska, 1915. (NOAA Photo Library, 2018) 16
Figure 3: Datawell Waverider particle following buoy (https://www.rsaqua.co.uk/products/mkiii-waverider-buoy/, 2018 and https://qld.gov.au, 2018) 17
Figure 4: Fugro Wavescan Buoy awaiting deployment (www.aboutoilandgas.org, 2017) 18
Figure 5: Met Éireann map of coastal stations and M-Buoys (Maintained by Marine Institute) (MET Eireann, 2017) 21
Figure 6: Location of AMETS and Galway Bay Test facilities (Blavette, 2013) 22
Figure 7: Proposed layout of test site infrastructure at AMETS 23
Figure 8: Illustration of sub-sea observation equipment at Galway Bay (SmartBay, 2018) 23
Figure 9: WestWave nearshore and offshore Sites, Killard, Co.Clare, Ireland 24
Figure 10: Teledyne ADCP, Tripod bottom mooring device for ADCP, Bottom-mounted ADCP in-use measuring Wave particle velocities (ocean-innovations.net, mooringsystems.com) .. 25
Figure 11: Principles of operation of satellite altimetry (NOAA, NESDIS and STAR, 2017) 26
Figure 12: Example wave model input boundary shown in Mike 21 SW. Red, Green, Blue and Yellow represent separate input data derived from global WW3 model and interpolated along boundary. Land boundary shown in aqua-blue. 30
Figure 13: Sample WaveWatch 3 global model output displaying shaded map of wave height (NOAA, 2008) 32
Figure 14: Overview of the role of numerical models in resource assessment in relation to measurement techniques (EquiMar, 2010a) 34
Figure 15: Zero Crossing Waves. Diagram displays four zero up-crossing waves and their Height (H) and Period (T) (Manly Hydraulics Laboratory, 2017) 46
Figure 16: Non-Dimensionalised histogram of wave height based on a Rayleigh distribution (Bretschneinder, 1964) 47
Figure 17: Superposition of sine waves to make irregular sea (St. Denis and Pierson, 1953) 48

Figure 18: Transformation of time-domain information to Energy Density Spectrum via Fourier Analysis (Journée and Pinkster, 2002) 49
Figure 19: Generation of Wave Energy Spectrum from timeseries 50
Figure 20: Simplified overall Design Process for commercial site selection 54
Figure 21: Example H_s - T_z scatterplot 55
Figure 22: Illustration of the selection of a threshold value (Thompson 2001) 56
Figure 23: Illustration of lognormal probability distribution function 58
Figure 24: Example Power Matrix for Wavebob WEC (Babarit *et al.*, 2012) 60
Figure 25: Families of Machine Learning Estimators, classifiers, and assessment techniques 63
Figure 26: Cross-Validation approach illustrated 64
Figure 27: Leave One Out Cross-Validation (LOOCV) approach illustrated 65
Figure 28: OLS estimation viewed as a projection onto the linear space spanned by the regressors 66
Figure 29: Coordinate Descent path illustration 70
Figure 30: Layout of the Atlantic Marine Energy Test Site (Image courtesy of SEAI) 80
Figure 31: AIC and BIC used to select optimal value of regularization parameter of Lasso Estimator 88
Figure 32: Coordinate descent estimation of alpha parameter for Lasso model 89
Figure 33: LARS selection of optimal alpha parameter 90
Figure 34: Lasso path coefficient analysis for Belmullet dataset 91
Figure 35: Naive Bayes classifier Learning curve for Belmullet data. Number of cross-folds =10 94
Figure 36: Seasonal T_e/T_1 Wave Period Relationship at Belmullet 96
Figure 37: Winter Trained LOOCV learning curve for Belmullet 98
Figure 38: Spring trained LOOCV learning curve for Belmullet 99
Figure 39: Summer trained LOOCV Learning Curve for Belmullet 101
Figure 40: Autumn Trained LOOCV Learning Curve for Belmullet 102
Figure 41: Learning Curve for Belmullet Seasonal Data 103
Figure 42: Comparison of Model Bias Error Across Test Period Values. Histogram Overlaid Representing data availability for each bin of test value 107

Figure 43: Comparison of model Square error across Test Period values. Histogram overlaid representing data availability for each bin of test value. 108
Figure 44: Least Absolute Regression and Shrinkage Plot for Killard Point Test Site 114
Figure 45: Lasso Path Analysis at Killard Point site 115
Figure 46: Learning Curve at Killard Point. Test set ratios from 0.1 to 1.0. 116
Figure 47: Comparison of model Square error across Test Period values. Histogram overlaid representing data availability for each bin of test value. 118
Figure 48: Comparison of model Bias error across Test Period values. Histogram overlaid representing data availability for each bin of test value. 119
Figure 49: Hs/Tz Occurrence Scatter Plot at AMETS Berth B 129
Figure 50: Quantile-Quantile Plot Hs 98th Percentile Values at Belmullet Berth B 133
Figure 51: Quantile-Quantile plot of adjusted dataset of monthly maximum values at Belmullet Berth B. 135
Figure 52: Quantile-Quantile plot of distribution fit for H_{max} Extreme estimation 137
Figure 53: Regression analysis of AI using 98th Percentile H_S/H_{MAX} data 139
Figure 54: Wave steepness (Reciprocal) Regression Analysis against H_s 141
Figure 55: Regression analysis to determine T_z/H_s relationship at AMETS 143
Figure 56: Variation in Acer Extreme H_s prediction across 10 folds consisting of 1 year of data at M3. 150
Figure 57: Average ACER Extreme H_s prediction for 1-5 year return period at M3 using 1 year data. 151
Figure 58: Variance of ACER Extreme H_s prediction across 10 Folds for 1-5 Year Return Period at M3 using 1 year segment of prediction data 152
Figure 59: Variance of Lower Confidence Interval for ACER Extreme H_s prediction for 1-5 Year Return Period at M3 using 1 year segment of prediction data 152
Figure 60: Variance of Upper Confidence Interval for ACER Extreme H_s prediction for 1-5 Year Return Period at M3 using 1 year segment of prediction data 153
Figure 61: Killard Point Development Area 164
Figure 62: Percentage Occurrence Scatter Plot for H_{m0} / T_{02} (mean period) at Killard Point DL1 167
Figure 63: Histogram of H_{m0} distribution for buoy data at deployment location 1. 168
Figure 64: Tz histogram of buoy data at deployment location 1. 168

Figure 65: Wave Height distribution across 30 (peak) directional sectors for Buoy data in 2014 (1st January – 30th April) 169
Figure 66: Process and setup of Mike 21 Numerical model at Killard Point 172
Figure 67: Site assessment Hierarchy for Killard Point and WestWave project 173
Figure 68: INFOMAR survey of County Clare Area at 20m resolution. 175
Figure 69: Killard Point Mesh Creation in MIKE 21 SW 176
Figure 70: Model Calibration Data at M6 Weather Buoy provided by MeteoGroup 178
Figure 71: Model Calibration Data at M4 weather buoy provided by MeteoGroup 179
Figure 72: Model Calibration Data at M3 Weather Buoy provided by MeteoGroup 180
Figure 73: Killard Point Stepped Triangular Mesh (MIKE 21 SW) 182
Figure 74: Model Domain (Buoy Deployment 1-3 Locations used for initial Calibration highlighted - deep red) 183
Figure 75: Model Domain (Nearshore and Offshore Model output points highlighted) 184
Figure 76: Under prediction of H_{m0} condition during storm events using IOWAGA WW3 input 186
Figure 77: H_s Comparison - MIKE21 model hindcast using MeteoGroup data at deployment location 1 187
Figure 78: H_s Calibration at Deployment Location 1 188
Figure 79: H_s Calibration at Deployment Location 2 189
Figure 80: H_s Calibration at Deployment Location 3 189
Figure 81: Mean Wave Direction Calibration at Deployment Location 1 190
Figure 82: Mean Wave Direction Calibration at Deployment Location 2 190
Figure 83: Mean Wave Direction Calibration at Deployment Location 3 191
Figure 84: T_p Calibration at Deployment Location 1 192
Figure 85: T_p Calibration at Deployment Location 2 192
Figure 86: T_p Calibration at Deployment Location 3 193
Figure 87: Hierarchy of conditions assessed for each analysis at Killard Point Site 198
Figure 88: Machine Learning Model Development overview 200
Figure 89: Annual Mean H_s and variability at Killard Point 201
Figure 90: Annual Mean H_s and Variability (Nearshore and Offshore) at killard Point 202
Figure 91: Annual T_{01} variability at Killard Point sites 203
Figure 92: Annual T_p variability at Killard Point sites 204

Figure 93: Annual mean T_e wave period 204
Figure 94: Annual mean omni-directional wave power 205
Figure 95: Monthly H_{m0} Variability at Killard Point Site 207
Figure 96: Monthly T_{01} Variability at Killard Point Site 208
Figure 97: Monthly T_p Variability at Killard Point Site 208
Figure 98: $H_{m0} – T_{02}$ Scatterplot of occurrence percentage for 24 year hindcast 211
Figure 99: H_{m0} - T_e Percentage Occurrence Scatter Plot for 2014 using output of Mike21 modelled data (8760 measurements) 212
Figure 100: Percentage Occurrence Scatter Plot for average December conditions using output of MIke21 data (744 measurements) 212
Figure 101: Histogram of H_{m0} distribution for Nearshore model 24 year hindcast. 213
Figure 102: Histogram of H_{m0} distribution for Offshore model 24 year hindcast. 213
Figure 103: T_{01} histogram of nearshore modelled data. 214
Figure 104: T_{01} Histogram of Offshore modelled data 215
Figure 105: Wave rose of H_{m0} 216
Figure 106: Wave Height distribution across 30 (mean) directional sectors for MeteoGroup boundary input wave data in 2014. 217
Figure 107: Wave Height distribution across 30 (peak) directional sectors for MeteoGroup boundary input wave data in 2014. 217
Figure 108: Significant Wave Height Offshore (Left) and Nearshore (Right) at Killard Point in 2012 218
Figure 109: Mean Wave Period Offshore (Left) and Nearshore (Right) at Killard Point in 2012 218
Figure 110: Significant Wave Height Distribution at Killard Point for Summer and winter: June (Left), November (Right) 219
Figure 111: Absolute change in Offshore to Nearshore H_{m0} across all directions 220
Figure 112: Relative change in Offshore to Nearshore H_{m0} across all directions 221
Figure 113: Monthly variation of wave power at Killard Point 222
Figure 114: Theoretical Monthly Power Production at Killard Point Site for WEC device 224
Figure 115: Theoretical Annual Power Production at Killard Point Site for WEC device 224
Figure 116: Largest storm event recorded during buoy deployments at deployment location 3 - January 2014 225

Figure 117: Hindcast Model conditions Offshore during largest recorded wave at buoy – January 2014 226
Figure 118: Hindcast Model conditions Nearshore during largest recorded wave at buoy - January 2014 226
Figure 119: Largest Nearshore storm event in 24 year hindcast - occurring during February 1991. 227
Figure 120: Largest Offshore storm event in 24 year hindcast - occurring during February 1991 227
Figure 121: Extreme Wave Curve fitting R^2 values for Fisher-Tippett and Weibull curves. Nearshore modelled data, using n_{max}=30. FT-1 curve selected as best fit. 228
Figure 122: Regression Model of Anomaly Index vs H_s. Determined Equation parameters output 231
Figure 123: Anomaly Index vs H_s during November 2011 Killard Point Buoy Deployment 231
Figure 124: Analysis of timeseries data from Waverider buoys at Killard Point to produce Spectral Shape information 236
Figure 125: Individual (grey), Average (blue) and Bretschneider Representation (red) for 4 of the most commonly occurring sea-states at Killard Point 237
Figure 126: R^2 Correlation between default Bretschneider Spectrum and average spectrum for each sea-state at Killard Point during Buoy Deployment 1 238
Figure 127: T_e/T_{01} Wave Period Ratios binned by wave height and period 240
Figure 128: Nearshore and Offshore Persistence analysis at 1.5m H_{m0} Threshold for 12 hour window 242
Figure 129: Nearshore and Offshore Persistence analysis at 1.5m H_{m0} Threshold for 24 hour window 242
Figure 130: Nearshore and Offshore Persistence analysis at 2m H_{m0} Threshold for 12 hour window 243
Figure 131: Nearshore and Offshore Persistence analysis at 2m H_{m0} Threshold for 24 hour window 243
Figure 132: Belmullet Berth A Significant wave height comparison (day 1-6) 248
Figure 133: Belmullet Berth B H_s comparison (day 1 - 6) 250
Figure 134: Killard Point Forecast Accuracy Assessment (Day 1 - 6) 252
Figure 135: Scatter Index Forecast Accuracy Comparison 254

Figure 136: Max Error forecast accuracy comparison 254
Figure 137: Mean Average Error forecast accuracy comparison 254
Figure 138: Mean Error forecast accuracy comparison 255
Figure 139: Mean Square Error forecast accuracy comparison 255
Figure 140: R^2 correlation forecast accuracy comparison 255
Figure 141: RMSE forecast accuracy comparison 256
Figure 142: Maximum Error Forecast Accuracy Comparison (T_z) 256
Figure 143: Mean Average Error Forecast Accuracy Comparison (T_z) 256
Figure 144: Mean Error Forecast Accuracy Comparison (T_z) 257
Figure 145: Mean Square Error Forecast Accuracy Comparison (T_z) 257
Figure 146: R^2 Correlation Forecast Accuracy Comparison (T_z) 257
Figure 147: RMSE Forecast Accuracy Comparison (T_z) 258
Figure 148: Scatter Index Forecast Accuracy Comparison (T_z) 258
Figure 149: Mean Energy Production Buoy Vs. Prediction at Belmullet Berth A 259
Figure 150: Mean Energy Production Buoy Vs. Prediction at Belmullet Berth B 260
Figure 151: Mean Energy Production Buoy Vs. Prediction at Galway Bay 260
Figure 152: Mean Energy Production Buoy Vs. Prediction at Killard Point 261
Figure 153: Method for processing timeseries files to Spectra, binning, and generating equivalent Bretschneider for comparison 276
Figure 154: Average Spectra from time-series records (blue) with Bretschneider (Red) spectra generated from average H_{mo} and Period records overlaid. All spectral records for each time-series file are depicted in grey. 278
Figure 155: Comparison process for recorded vs theoretical spectral shape data 279
Figure 156: Percentage Occurrence Scatter Plot for H_{m0} / T_{02} at Killard Point DL1 280
Figure 157: Histogram of H_{m0} distribution for buoy data at deployment location 1. 281
Figure 158: H_s-T_p Occurrence Matrix at killard point Deployment Location 1-3 (combined) 283
Figure 159: H_s-T_p Power Contribution Matrix at killard point Deployment Location 1-3 (combined) 283
Figure 160: Example of double peaked spectra at Killard Point 284
Figure 161: Selection of time-series record matching average spectral energy distribution in chosen bin 286

Figure 162: Comparison of Heave Spectral Amplitude for Recorded spectrum vs. an assumed Bretschneider spectrum for a sea-state with Parameters: 2.268 m H_s and 6.838 s T_p. 290
Figure 163: Comparison of Spectral Shape and Energy Production for Sea-States with H_S 2.5-3m and T_p 9.5-10.5s.....292
Figure 164: COMPARISON OF SPECTRAL SHAPE AND ENERGY PRODUCTION FOR SEA-STATES WITH H_S 3.5-4M AND T_P 10.5-11.5S.....293
Figure 165: COMPARISON OF SPECTRAL SHAPE AND ENERGY PRODUCTION FOR SEA-STATES WITH H_S 4.5-5M AND T_P 12.5-13.5S.....294
Figure 166:Comparison of Spectral Shape and Energy Production for Sea-States with HS 5.5-6m and Tp 12.5-13.5s 295
Figure 167: Comparison of Spectral Shape and Energy Production for Sea-States with HS 6.5-7M and Tp 12.5-13.5s 296
Figure 168: Deep Water Ocean Basin Overview.....300
Figure 169: Deep Water Ocean Basin Schematic 301
Figure 170: OWC Device Solidworks assembly diagram.....302
Figure 172: Devices, attachment mechanism and instrument bridge 303
Figure 172: OWC water surface piston representation.....305
Figure 173: Resonance Period of device vs. submerged depth.....307
Figure 174: Tank arrangement for wave calibration 309
Figure 175: Wave Probe Arrangement in tank 309
Figure 176: Wave Probe Installation on instrumentation bridge.....310
Figure 177: WAVE PROBE SENSOR VOLTAGE AS A FUNCTION OF WATER SURFACE ELEVATION 311
Figure 178: Tank arrangement for testing.....312
Figure 179: Wave probes and devices installed on Instrumentation bridge.....313
Figure 180: Top view of OWC device showing pressure sensor and attachment configuration 313
Figure 181: Edinburgh Designs Wave Generation Software Overview 315
Figure 182: Njord Wave Synthesis Input interface: Generation of bi-modal time-series with H_s 0.1074m and T_p 1.4497s (at scale) 315
Figure 183: Tank control interface: Showing tank controls and ability to select generated time-series files to be created by wavemaker 316

Figure 184: Rig for Orifice Calibration 317
Figure 185: Flow Velocity in OWC chamber during orifice calibration.....318
Figure 186: Pressure Vs Flow during orifice calibration. Positive and negative best fit shown 319
Figure 187: Sample recorded data from LabVIEW for test 001.....326
Figure 188: Requested time-series vs probe readings for test 042.....326
Figure 189: Data from Test 001 showing probe readings and requested time-series after the time-series have been aligned.....328
Figure 190: Requested and recorded time-series measurements for Test 001 / Bretschneider sea-state 1.....329
Figure 191: Wave Spectral Density distribution comparison for requested and recorded Bretschneider and time-series conditions.....346
Figure 192: Comparison of Input and Recorded Spectra for Bretschneider and Real Spectra – Sea State 1: 2.5-3m Hs, 9.5-10.5s Tp (requested) 347
Figure 193: COMPARISON OF INPUT AND RECORDED SPECTRA FOR BRETSCHNEIDER AND REAL SPECTRA – SEA STATE 5: 3.5-4M HS, 10.5-11.5s TP (REQUESTED).....347
Figure 194: COMPARISON OF INPUT AND RECORDED SPECTRA FOR BRETSCHNEIDER AND REAL SPECTRA – SEA STATE 9: 4.5-5m HS, 12.5-13.5s TP (REQUESTED).....348
Figure 195: COMPARISON OF INPUT AND RECORDED SPECTRA FOR BRETSCHNEIDER AND REAL SPECTRA – SEA STATE 14: 5.5-6M HS, 12.5-13.5s TP (REQUESTED).....348
Figure 196: COMPARISON OF INPUT AND RECORDED SPECTRA FOR BRETSCHNEIDER AND REAL SPECTRA – SEA STATE 17: 6.5-7M HS, 12.5-13.5s TP (REQUESTED).....349
Figure 197: Comparative testing of Bretschneider and recorded time-series records to determine power production variation.....350
Figure 198: Bretschneider Spectrum Equation Notation and Shape affecting parameters highlighted 354
Figure 199: Bretschneider Spectra with Constant values in B parameter from 0.63 to 0.8 (standard value 0.751).....355
Figure 200: Bretschneider Spectra with M values -3.6 to -4 (standard value -4).....356
Figure 201: Bretschneider Spectra with N values -4.6 to -5 (standard value -5) 356
Figure 202: R^2 Correlation between default Bretschneider Spectrum and average spectra for each sea-state. 358

Figure 203: Optimal "B constant" values for Bretschneider Spectrum at Killard Point 359
Figure 204: R^2 correlation between idealised Bretschneider Spectrum and average spectra for each sea-state 360
Figure 205: Occurrence of each sea-state within DL1 time-series records – each time-series record represents a 28minute recording.....361
Figure 206: R Correlation between Idealised JONSWAP Spectrum and average spectra for each sea state 362
Figure 207: T_e/T_{01} WPRs Binned by wave height and period.....364
Figure 208: Killard Point DL1 T_e/T_{02} WPRs binned by wave height and period 365
Figure 209: Killard Point DL1 T_{01}/T_{02} WPRs binned by wave height and period.....366
Figure 210: Recorded and requested data for generation of bi-modal sea-state.....406

Inspiration

Art

"La mobilité et l'inégalité successive des vagues, après s'être élevées comme des montagnes, s'affaissent l'instant après, entraînant dans leurs mouvements tous les corps qui surnagent, quels que soient leur poids et leur volume. La masse énorme d'un vaisseau de ligne, qu'aucune puissance connue ne serait capable de soulever, obéit cependant au moindre mouvement de l'onde"

("The motion and successive inequality of waves, which after having been elevated like mountains fall away in the following instant, take into their motion all bodies which float on them, regardless of their weight or volume. The imposing mass of a vessel, which no other known force is capable of lifting, responds to the slightest wave motions") – Girard, father and son, Paris, 1799

Economics

"Glendenning … said that much of it would be inaccessible for economic exploitation, as the line extended well north of the Hebrides and transmission became difficult, if not impossible. But that was said in 1977. No one would say it today (1992), when the oil industry has shown that inaccessible areas suddenly become reachable when there is energy to be won" David Ross, Energy from Ocean Waves, 1992

Abbreviations

ADCP	Acoustic Doppler Current Profiler
AIC	Akaike Information Criterion
BEM	Boundary Element Method
BIC	Bayes Information Criterion
BRET	Bretschneider WPR (Model)
CDF	Cumulative Distribution Function
CFSR	Climate Forecast System Re-Analysis
CSV	Comma Separated Value (file format)
CWPR	Constant Wave Period Ratio (Model)
DFT	Discrete Fourier Transform
DGPS	Differential Global Positioning System
DHI	Dutch Hydraulics Institute
DIWAR	Digital Waverider Receiver
ECMWF	European Centre for Medium Range Weather Forecasts
ECN	Ecole Centrale de Nantes
ESA	European Space Agency
FFT	Fast Fourier Transform
FMEA	Failure Modes and Effects Analysis
FNMOC	Fleet Numerical and Meteorology and Oceanographic Centre
GPS	Global Positioning System
HF	High Frequency
IAHR	International Association for Hydraulic Research
ICASP	International Conference on Applied Statistics and Probability
IEC	International Electrotechnical Commission
IET	The Institution of Engineering and Technology
INFOMAR	Integrated Mapping For the Sustainable Development of Ireland's Marine Resource
IOWAGA	Integrated Ocean Waves for Geophysical and Other Application
ITTC	International Towing Tank Conference
JONSWAP	Joint North Sea Wave Program
KNN	K-Nearest Neighbours
LADS	Laser Airborne Depth Sounder

LARS	Least Angle Regression and Shrinkage
LASSO	Least Absolute Shrinkage and Selection Operator
LIR NOTF	LIR National Ocean Test Facility
LOOCV	Leave-One-Out Cross-Validation
MAE	Mean Average Error
MaREI	Marine and Renewable Energy Centre
MCP	Measure Correlate Predict
ML	Machine Learning
MLM	Maximum Likelihood Method
MSE	Mean Square Error
NASA	National Aeronautics and Space Administration
NOAA	National Oceanic and Atmospheric Association
NOMAD	Navy Oceanographic Meteorological Automatic Device
ODAS	Ocean Data Acquisition System
OLS	Ordinary Least Squares
OSES	Offshore Energy & Storage Symposium
OWC	Oscillating Water Column
PDF	Probability Distribution Function
PDF	Probability Distribution Function
QC	Quality Control
RAO	Response Amplitude Operator
RAO	Response Amplitude Operator
RAW	Raw Elevation file (Datawell Waverider Directional Buoy)
RCORR	R Correlation Coefficient
REFIT	Renewable Energy Feed In Tariff
RMSE	Root Mean Square Error
RW	Raw Elevation file (Datawell Waverider Non-Directional Buoy)
SEAI	Sustainable Energy Authority of Ireland
SI	Scatter Index
SLOOCV	Seasonal Leave-One-Out Cross-Validation
SP	Wave Spectrum file (Datawell Waverider Non-Directional Buoy)
SPA	Spectral Partitioning Algorithm

SPT	Wave Spectrum file (Datawell Waverider Directional Buoy)
SW	Spectral Wave
SWAN	Simulating Waves Nearshore
THREDDS	Thematic Real-time Environmental Distributed Data Services
WAM	Wave Model
WAMIT	Wave Analysis MIT (Massachusetts Institute of Technology)
WEC	Wave Energy Convertor
WMO	World Meteorological Organisation
WPR	Wave Period Ratio
WV	Wave statistics file (Datawell Non-directional Waverider Buoy)
WVS	Wave statistics file (Datawell Directional Waverider Buoy)
WW3	Wave Watch 3

1 Introduction

1.1 Wave Energy Context

1.1.1 Early Wave Energy

Man has, for a long time, had a fascination with the extraction of energy from the environment. From the earliest days of coal mining to the extraction of oil, the quest for energy has permeated man's history. Recognising the potential for extracting power from water, the ancient Greeks and Romans are credited with the invention of the water wheel sometime between the 3rd and 1st century BC, and they were the first to use it as a power source. The simplicity of this extraction of energy rapidly lead to its use in mining projects and so began its widespread use. The 3rd generation of water wheel, known as the breastshot water wheel, employed a horizontal axle and was found in the majority of excavated Roman Watermills. One such watermill, the Barbegal watermill complex, fed by an artificial aqueduct, came to be known as "the greatest known concentration of mechanical power in the ancient world." (Greene, 2000) Continued developments led to the displacement of water wheels by smaller and more efficient turbines, beginning with the first model developed by Benoit Fourneyron in 1827. Modern hyrdro-electric dams, too, can be viewed as direct descendants of these water wheels. The development of wave energy, however, precedes even the creation of these modern turbines. Towards the end of the 18th century, the love affair with extracting energy from the movement of water manifested itself in the creation of the earliest known wave energy device, developed and patented in 1799 by a Parisian, Girard, and his son. (Clément *et al.*, 2002)

1.1.2 The development of Wave Energy

Later attempts at the creation of a wave energy device came in the 1940s, with heavy development efforts leading to around 1974, spurned by the likes of Yoshio Masuda, and on the European front, Steven Salter - of the famed Salter's duck - and Kjell Budal. The work took place in the US, too, under Michael E. McCormick. Fascinated by the ability of waves to generate power and enticed by the promises of carbon free, abundant energy from natural resources, large government-funded R&D programmes began during the late 1970s, in the UK, Sweden and Norway, and later followed in other countries. (Falnes, 2007). The "first oil shock," in 1973 which sent oil prices soaring from $3 to over $12 resulted in a new fervour to develop alternative

energy sources which were not as susceptible to selfish actions of consortiums and superpowers. The "second oil shock," in 1979 served as a reminder that commodity prices will always be subject to manipulation and fluctuations, and this undoubtedly acts as a continued driving force behind the bid to produce renewable energy technologies today. Throughout the early 1980s, set against the backdrop of a declining oil price and short-sighted leaders, wave energy funding was massively reduced. A number of first generation prototypes did enter testing, including large production units in Norway (Falcão, 2010), but it has not been until recent years that energy policy roadmaps and global agreements in the name of reducing environmental impact and enhancing energy security for the future have re-aligned their goals in favour of the development of alternative renewable energy technologies.

1.1.3 Wave Energy in the modern world

Technical challenges plagued many early wave energy devices, and these technical and economic challenges continue to be a theme within wave energy development up to 2015 (Astariz and Iglesias, 2015), preventing many projects from achieving success. Recent failures include Pelamis (reNEWS, 2015), Ocean Linx (The Australian, 2014), both resulting in liquidation, with many more experiencing high funding or technical inertia in moving from prototype scale to full-scale testing. (Aqumarine Power Ltd., 2014) taking the strategic decision to downsize as a result of the difficulties faced by the company was indicative of the overall state of the industry at that time.

Increasing unease about the remaining supply of oil, coal and natural gas, as well as global warming concerns, however, has acted to accelerate the pace of renewable energy technologies, with Europe's RES 2020 "Reference Document on Renewable Energy Sources Policy & Potential," (EU, 2008) mandating a 16% share of RES on the final consumption of energy in 2020, while in an Irish context, Ireland's own Strategy for Renewable Energy: 2012-2020 document specifically highlights our ocean resources as a key resource to be used in attaining these targets by 2020. As such, there is renewed fervour in theorising of wave energy device designs, despite a growing reluctance to fund what are now being viewed as especially risky projects.

As a result of this reluctance, there exist now only a handful of commercial full-scale developments, which include deployed and grid-connected devices. Notably, Seabased AB who have deployed in Ada, Ghana and Smögen, Sweden. ISWEC (Vissio et al., 2017), an Inertial Sea Wave Energy Converter with a 100kW rating, has been deployed off the coast of Pantelleria and has shown some early promising signs relating to the theorised cost of electricity when used in an array. AW Energy's–device has received Lloyd's register certification based on testing that is underway in Peniche, Portugal, representing a significant step in the legitimisation of the WEC industry. In December 2017, the Marmok 5 device, one of very few grid-connected devices, celebrated its first anniversary at sea (opera, 2017). These projects currently form the pinnacle of devices that have made it to commercial scale. A number of test sites such as EMEC, in Orkney and Wavehub off the coast of Cornwall are full-featured, grid-connected sites that are awaiting their first developers but have had limited uptake as yet. In the United States, Oregon State University's Northwest National Marine Renewable Energy Center (NNMREC) has received $40m from the US Department Of Energy to test one of the first large scale open water wave energy testing facilities. (Tidal Energy Today, 2016)

1.1.4 Potential for wave energy in Ireland

Ireland is endowed with a particularly energetic wave resource. Providing first land-fall for waves travelling the vast expanse of the Atlantic, it is exposed to waves of significant fetch which travel as far as 6,000km from the prevailing south-westerly wind direction, and experiences frequent winter storms which bring further large wave systems from the north and north-east.

The primary source of information on general levels of available wave resource for Ireland comes from the ESB Wave Atlas, which suggests an annual energy resource of up to 460Twh/year, with approximately 11.72Twh/year of this practically accessible. (Sustainable Energy Authority Ireland, ESBI and Marine Institute, 2005). Further research in this area has shown that this may in-fact represent an under-estimation of the wave resource due to the methods used, and the accessible wave energy figure may yet be greater than this (Cahill, 2014). To put this in context, Ireland's final energy consumption of electricity was at 29TWh in 2015. (SEAI, 2016).

Several global wave atlases allow for a determination of the average power levels of the Irish coast (Arinaga and Cheung, 2012) (Gunn and Stock-Williams, 2012), with these showing Ireland to possess amongst the most energetic wave resources in the world. A numerical evaluation of the wave energy resource along the Atlantic European coast (Guedes Soares et al., 2014) showed Ireland to have the most energetic resource of the areas studied by a convincing margin, with power flux of between 50 – 60 kW/m within 25km of the Mayo and Kerry Coasts.

This energy potential has been identified by Irish leadership, with the overarching "Strategy for Renewable Energy" outlined in Ireland's Offshore Renewable Energy Development Plan (Department of Communications and Resources, 2014) including specific consideration for offshore wind and ocean energy sectors in the context of energy policy to 2020. This document, too, reiterates the Government's commitment to realising the long term economic potential of Ireland's wave and tidal resources. The Offshore Renewable Energy Development Plan for Ireland outlines the Irish government's target of 40% of electricity from renewable sources by 2020, and highlights the commitment to the long term economic potential of Ireland's wave and tidal resources. In a broader context, "Ocean Research in Horizon 2020: The Blue Growth Potential," (Policy Department A and ITRE committee, 2014) a study which aims to provide a description of the key blue growth sectors of the European Union economy, assigns a minimum value of €1Bn to ocean renewable energies.

In addition to these messages of support, a number of government backed initiatives have enabled research in the area of Marine Renewable energy. SEAI's Prototype Development Fund assists device developers in financing fundamental research; while the establishment of the Marine and Renewable Energy Ireland centre at the Beaufort building, which houses the LIR National Ocean Test Facility, proves a huge boon for fundamental research of wave energy concepts through the state-of-the-art tank test facilities it provides.

A crucial part of the infrastructure, as devices graduate from small-scale testing, are Ireland's two test sites. The Galway Bay test site is a quarter-scale site which has been in operation since 2006, and now includes power and data connectivity, subsea test

and monitoring platforms, as well as a floating sea station platform – installed in 2015.

The Atlantic Marine Energy Test Site (AMETS), located off Annagh Head, west of Belmullet in County Mayo, is a full-scale grid-connected site which will allow developers to test both the energy production and survivability of their devices. AMETS is being developed by Sustainable Energy Authority of Ireland (SEAI) to facilitate testing of full scale wave energy converters in an open ocean environment and will be connected to the national grid. This site is an integral component of Ireland's Ocean Energy Strategy and is being developed in accordance with the national Offshore Renewable Energy Development Plan (SEAI, 2017).

While the original government target of 500MW of ocean energy installed by 2020 now seems an unlikely, if not impossible, prospect; it remains clear that Ireland is poised to become a leader in Marine Renewable Energy technologies.

1.2 Technology Development and Economic Status of Projects

1.2.1 Progress of Wave Energy hindered by development approach

Wave energy has made continuous, but disjointed progress towards commercialization over the last five years. Though there are large and thriving research and development communities and device developers worldwide who are taking part in fundamental hydrodynamic research, applied research and technology development of wave energy devices (Bahaj, 2011), the large detractor to the economic viability of wave energy thus far has been the lack of clear technological leader. This presents a number of problems, including the current immaturity of the technology which has resulted in high risk premiums on loans on projects using less mature technologies. This is highlighted by a joint report commissioned by the order of the European Commission and prepared by a team including Ernst & Young (Ecofys *et al.*, 2011). The risk of using unproven technologies, or technologies proven at much smaller scale, increases the interest rates charged on loans drastically as a perceived hedge against the risk of complete failure resulting in inability to pay back the loan. The confluence of device technologies would do much to improve certainty in the reliability and costing characteristics of commercial wave energy projects. In addition to funding concerns, the fractured field of play has also resulted in intense secrecy

which is toxic to the development of the industry as a whole. Developers are reluctant to share sensitive information such as the power matrix of their device, and collaboration with universities and research departments is subject to close and often stifling scrutiny.

There are lessons to be learned from the wind energy industry. Few early manufacturers are still in business, but these early pioneers contributed significantly to the development of the industry and convergence of technology. Despite difficulties encountered by their companies, these individuals still have employment in the now-booming wind energy industry. Taking this approach with wave energy would be a recognition by the wave energy industry that it is best for companies to pursue the long-term approach of creating a successful and prosperous industry, rather than stifling growth in a small pond. Though it has been theorized that wave energy will follow a similar learning curve to wind energy, this theory has yet to stand firm on its own (Garrad, 2012). Examining the development of the wind energy industry from the early 80s on - which was then at the approximate stage that Marine Renewables are now - there were many parallels which can now be drawn with the development of wave energy. The research space for wind energy included a large number of available device types, with survivability being a crucial issue. A number of competitive wind turbine manufacturers sank due to hardware failures at inopportune times. The eventual sorting of the market led to a convergence towards the modern horizontal axis turbine, 3-bladed type. This conferred a number of key benefits; but chiefly it allowed more research and effort to be spent on a viable design type and this resulted in solving of the survivability issues that plagued early companies such as WEG and Hoden. However, despite these technical advancements, it is likely that economic incentives in the form of tax-rebates were the ultimate driver of the wind energy successfully crossing this chasm to the realm of commercial success (Hirsh, 1999). The two primary locations of wind turbine development, California and Germany, saw vastly increased installed capacity with the introduction of the Public Utility Regulatory Policies Act (PURPA) and "Stromeinspeisungsgesetz" (StrEG) respectively.

As of December 2017, there is still no support scheme available for renewable energy technologies in Ireland, though a range of technologies (including offshore) are being considered under the new Renewable Electricity Support Scheme under development by the Department of Communications, Climate Action and Environment (Netherlands Enterprise Agency, 2017). Only Spain has a specific feed-in tariff for wave energy, and this provides just €0.0689/kWh, far below what is required to support the development of large projects.

While the development environment may be restrictive, the weight of knowledge that has built up in the research and development of pilot devices, test sites, novel technology concepts, training and teaching institutions has slowly begun to eke out a number of tentative commercial scale projects. These are predominantly small-scale arrays in Europe that are less focused on power output, and instead champion the much-needed learning boost that is brought about by constructing grid-connected arrays. Most devices are at the very early stages of development, TRL 6 or below, representing the first step in deploying fully operational converters for real sea trials at scales of 1:2 - 1:5. Given that survivability is a key test for devices when moving towards full-scale deployment, it is fitting that more focus should be put on this to determine the most promising design type, rather than attempting to chase larger scale development which increases rated power output at the expense of real-world energy production and buildability.

Despite the wealth of domain-specific information being generated, a number of key knowledge gaps still exist. Energy production, which is the main driver of project income, will remain the primary focus of selecting a site. For this, energetic wave climate is a necessity, and this typically brings with it the caveat of limited accessibility. Weather windows for deployment, proximity to shore, availability of vessels, proximity to grid connection, and extreme wave conditions all need to be considered. This presents a greater need for meteocean analysis which accurately characterizes the sea-states in which future renewable projects will be deployed and operate, and while this analysis has been taking place for quite a number of years, the outputs are often non-standard and can vary significantly between projects, companies and analysts. Introduction of recent standards for metocean assessment

have sought to address this – such as the International Electrotechnical Commission TS 626-100 standards – but the methods used are still deficient in assessing a number of areas; such as device performance and the characterisation of extreme conditions. Wave energy projects are currently dominated by high research, CAPEX and OPEX costs, and the many failures have led to a high inertia whereby large commercial partners are afraid to undertake projects. With these costs being relatively fixed, the profitability of a project depends heavily on an understanding of the site conditions and wave characteristics. Thus, resource and site assessments are crucial to any economic analysis of the viability of an ocean energy project.

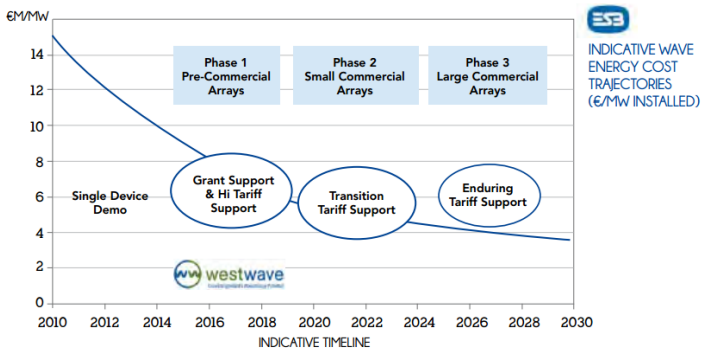


FIGURE 1: AN ESB COST PROJECTION FOR PROJECTS BASED ON INDICATIVE WAVE ENERGY TECHNOLOGY (OES IA and IEA Energy Technology Network, 2012)

A key difficulty identified in attempting to quantify the profitability of a wave energy project is the lack of operational experience in the sector. Estimates of operational costs and device availability are associated with a high degree of uncertainty and are often arbitrary selections where data is simply not available. The experience of industries that carry out similar activities, such as offshore wind and oil and gas exploration, can be drawn on to assess the costs and effectiveness associated with a particular components intended for use in wave farm developments (Teillant et al., 2012). With the deployment of the first commercial machines, Failure Modes and Effects Analysis (FMEA) data with a breakdown of the various components of a system will lead to great strides in our understanding of operational costs for devices in the field (OES IA and IEA Energy Technology Network, 2012).

As wave energy gets closer to commercialisation, costs have begun a rapid upward trajectory. A greater understanding of cost drivers in economic projects has indicated that operating costs will be higher than previously anticipated. This is very common in the development of new technologies and new industry sectors as the optimism of early phases of product development yield to greater understanding of device performance and expected and observed costs (Chwastyk and Kołosowski, 2014).

It is envisaged that the ultimate project cost of wave energy development will follow the trajectory outlined in Figure 1, requiring significant external funding support in its early stages as demonstration-scale sites are developed and expanded to create the first true wave energy farms, and slowly becoming more self-sustaining, with continually decreasing reliance on funding supports.

1.3 Research Outline

The increasing interest in wave farm test site development, device development, and funding presents a greater need for metocean analysis which accurately characterizes the sea-states in which future renewable projects will be deployed and operate. The research in this thesis seeks to develop novel data-driven methodologies which improve the utility of metocean analysis, as well as developing entirely new approaches which extend the accuracy and dependability of these types of analysis. This work does not focus on the MRE technology in use, nor will it explore in great detail the economic vagaries of MRE projects. Instead, it is focussed on developing methods which provide a large missing piece of the puzzle in MRE development, accurate and dependable metocean analysis.

This thesis will first cover the development of a novel set of methodologies which improve the estimation of extreme wave conditions (via programmatic determination of the best fitting distribution and better estimation of the wave periods coincident with extreme wave occurrence), estimation of the relationship between wave parameters (via a Machine Learning approach) , and the estimation of energy production (informed by the newly-developed IEC-TS for metocean analysis, and enhanced via the Machine Learning approach developed); using multiple sites on the West Coast of Ireland as a test-case. This will subsequently be

followed the application of these novel methods to the characterisation of the Killard Point site in Co. Clare, as part of the WestWave project. The overarching goal of the work is to remove some of the largest barriers in the commercialisation of MRE Projects, by tackling the issues which have the largest economic impact. These are the understanding of survival of structures, ability to access and maintain project sites, and the energy production from devices, as well as the standardisation of the approach taken in assessing projects. This work will address these issues with the following research areas:

- Identification of areas of metocean analysis that are currently lacking and would benefit most from a data-driven approach.
- Review of the existing literature and methods for wave data analysis, metocean analysis and standards governing the analysis (Chapter 2).
- Overview of Machine Learning methods and the utility they can bring to the Marine Renewable Energy field (Chapter 2).
- Utilising data available at the Belmullet test-site to examine the relationship between wave height and wave period at extreme conditions, with the aim of improving the understanding of covariate distribution of these parameters, as well as obtaining a value of Abnormality Index/Anomaly Index (AI) for this West-Coast site (Chapter 4).
- Validation of this Machine Learning Model using data available at West Coast sites in Ireland (Belmullet and Killard Point).
- Establishment of a Nearshore domain model for the Killard Point Site in Co. Clare in MIKE21 SW to provide long term hindcast data for energy production prediction and operational decision-making processes (Chapter 5).
- Metocean analysis of the Killard Point site in Co. Clare using the newly formed IEC TS 626-101 standards, and a first-of-kind examination of the efficacy of these new standards in relation to wave modelling and characterisation for Marine Renewable Energy Projects.
- Characterisation of ocean sites using modelled data, and determination of the effect which over-reliance on modelled data can have on the ultimate

production of energy at the site, as well as the impact on operation and maintenance actions.

- Analysis of device power production differences between a standard theoretical spectrum and a real recorded spectrum using OWC devices in deep ocean basin test at MaREI facility (Chapter 6).

Commented [AB1]: Put methods first, then Killard point work, then spectral shape – to better reflect actual flow of thesis.

Through the pursuit of these studies, the best practice methods used in the industry can be re-worked to ensure that they provide a more accurate picture of the real-world outcome of projects. The full body of work is provided in this thesis, which adheres to the following structure:

Chapter 2 outlines the existing literature in the area of Marine Renewable Energy resource assessment. Currently accepted methods of metocean assessment, climate validation and wave modelling are described; and a review of data capture methods, available wave models, and wave energy standards is conducted. Rapidly emerging fields in Computer Science, encompassing data-driven approaches such as Machine Learning which offer great promise in expanding and improving the work done in the renewable energy field, are outlined, and their utility in Marine Renewable Energy analysis explored.

Chapter 3 is motivated by the desire to improve the accuracy of energy production estimates for the Marine Renewables industry. This work addresses the determination of wave parameter relationships using a Machine Learning (ML) based model, with a view to identifying and selecting the optimal method for the conversion of wave parameters (T_e, T_{01}) in coastal Irish Waters. This approach is then validated at two sites on the West Coast of Ireland. It is the aim of this work to highlight the utility of ML in approximating the relationship between wave parameters; using both buoy and modelled data, and mapping the predicted outcomes for a Wave Energy Converter (WEC) based on a variety of ML and Measure Correlate Predict (MCP) approaches. Additionally, the specific task of calibrating modelled data to better fit site conditions, as measured by a wave buoy, is conducted using this model.

Chapter 4 addresses the methods of extreme wave prediction currently in use, with a view to determining improved methods for the prediction of extreme wave conditions (H_s, H_{max} and T_z). This work identifies pitfalls and drawbacks of current extreme prediction methods, with particular attention given to the use of limited in time buoy data from coastal locations where development is likely to take place. In addition, a new methodology for determining extreme wave periods, that is the wave periods occurring coincidentally with the most extreme wave heights, is established and analysed using a limiting-steepness based approach. The average conditional exceedance rate (ACER) method is applied to the prediction of extreme wave heights using a cross-validation method to obtain an insight into its behaviour. This will also examine the influence of variability, and of the data selection method, on prediction variability in a long-term dataset.

Chapter 5 introduces the Killard Point Site in County Clare, identified for development of a 5MW demonstration wave energy project "WestWave" by ESB. This work aims to highlight the implications of fulfilling IEC TS 62600-101: Wave Energy Resource Assessment & Characterization standards in the context of a utility-led wave energy project: WestWave; and will be the first work to implement these standards for a true commercial project. The work performed in Chapter 5 of this thesis attempts to validate the potential of the IEC-TS for wider use, and its ability to offer consistent, replicable and reliable results. It details the measurement campaigns which provide the necessary bathymetry, wave buoy, and other data to drive the modelling and analysis of the project. A full metocean assessment of the site is conducted, with a summary of results provided. The wave climate and resource modelling methodology and validation processes undertaken will be detailed. Issues associated with data acquisition of hindcast boundary conditions, validation of data sources and modelling of the area in MIKE 21 SW software will also be highlighted. Additionally, potential opportunities for further work to improve upon best practice in terms of validity, cost and the practicality of implementing IEC TS 62600-101 will be discussed. This work further serves as a test-case to validate the methodologies developed in Chapter 3 and Chapter 4.

Chapter 6 aims to examine the impact of spectral shape on WEC energy production, with the goal of improving the accuracy of energy production estimates. It is proposed to test the impact of this variation in a real-world environment, using prototype-scale WEC model. This offers the opportunity to verify the power production difference that exists between recorded time-series data and theoretical spectra. This work will explain and quantify the impact that the use of the accurate spectral shape information can have on energy production versus the use of a theoretical spectrum. This will be completed first in a theoretical approach, then by empirical testing of Oscillating Water Column (OWC) devices using real time-series conditions from the Killard Point site, and comparing these to Bretschneider estimates with equivalent summary statistics. Looking towards the commercial application of Marine Renewable Energy devices, this work will demonstrate the value of improved spectral fitting, novel methods of resource binning and characterisation, and display a testing framework that should be used for future device testing to enhance the accuracy of the energy estimates produced.

Chapter 7 contains a final discussion of the results presented here and the conclusions that can be drawn from the work done in the thesis.

1.4 Publications

The research in this thesis has formed a number of publications and papers which are outlined below.

Barker, A., Murphy, J., Pakrashi, V. (2015). *Reliability of Extreme Wave Prediction Methods,* conference paper presented at the 12th international conference on Application of Statistics and Probability in Civil Engineering, ICASP12, Vancouver, Canada, 12th – 15th July 2015

Barker, A., Murphy, J. (2015) *Reliability of numerically modelled wave data for use in the marine renewables industry,* conference paper presented at the 36th IAHR World Congress, The Hague, Netherlands, 28th June - 3rd July 2015

Barker, A., Murphy, J. (2016) *Machine Learning approach for optimal determination of wave parameter relationships,* conference paper presented at the Offshore Energy

& Storage symposium and industry connector Event (OSES) 2016, Valletta, Malta 13th - 15th July 2016

Barker, A., Murphy, J. (2017) *Machine Learning approach for optimal determination of wave parameter relationships,* Journal paper in IET Renewable Energy Journal OSES special edition, 22nd June 2017

Barker, A., Murphy, J. (2017) *Characterisation of Ocean Energy Resource to IEC standards: WestWave Project Experience,* conference paper presented at the European Wave and Tidal Energy Conference (EWTEC), Cork, Ireland, 29th August 2017

2 Literature Review

Understanding and accurately assessing the resource at locations of potential wave energy installation requires measurement, analysis and detailed characterisation. The process of doing so is outlined in this Chapter. The common methods for capturing, modelling, assessing and analysing wave measurements are described in Sections 2.1, 2.2 and 2.3 . Particular attention is paid to modelled wave data, which represents the primary source of information on the wave climate utilised in this thesis. Methods of assessing the output of buoy and modelled data are also considered. A review of published literature which deals with the proposed and accepted standards for defining and characterising wave energy resource has been undertaken, with these results included in Section 2.3 and 2.4. Given that the field of Machine Learning contains a vast array of information which does not overlap with the Offshore Renewable Energy field, and Machine Learning represents an incredibly valuable tool for this application, an overview of the common theory and analysis methods is provided in Section 2.5.

Commented [AB2]: Previously read: " The field of Machine Learning deviates significantly from widely-held information in the Marine Renewable Energy field,

2.1 Wave Data Sources

2.1.1 Measured Data

2.1.1.1 Buoy Data

Wave buoys represent the primary source of accurate measurements of wave conditions, and are an essential tool in characterising the available wave energy resource and in validating the performance of numerical models.

Historically, wave measurements began with visual observations taken by sailors aboard ships. The need to produce wave data that was accurate and replicable, and could capture greater temporal and spatial variation, however, led to the development of scientific sensing equipment. Land-based methods for wave and tide measurement first arrived in the form of fixed wave staffs. Early models were essentially tall wooden rulers that had to be read manually; and were predominantly used for measuring changes in coastal water levels.



FIGURE 2: AUTOMATIC TIDE GAUGE AT PORT PROTECTION, ALASKA, 1915. (NOAA PHOTO LIBRARY, 2018)

Commented [AB3]: Image added

Later models used two parallel wires partially submerged in the water, to measure water depth and its variation. These work by the principal of resistance or capacitance, with alterations in these values effecting a change in voltage, which, when calibrated, allows for the time series of water surface elevation to be determined. These wave staffs were frequently used for providing information about the wave climate tailored to the design of coastal infrastructure and offshore installations such as oil and gas platforms (Tucker and Pitt, 2001).

The first wave buoys were developed in the 1960s as a response to the need for accurate and portable systems that could be deployed at a wide range of sites, collecting data as part of a wider coastal observation network. This development saw a particular expansion of the ability to gather wave measurements in deep-water areas.

2.1.1.1.1 Particle Following Buoys

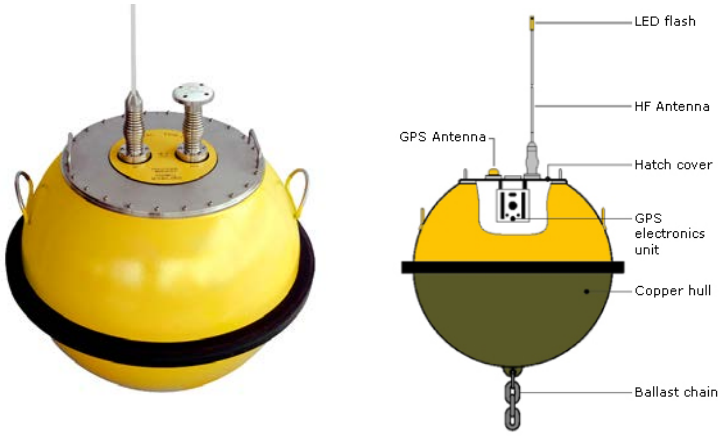


FIGURE 3: DATAWELL WAVERIDER PARTICLE FOLLOWING BUOY (HTTPS://WWW.RSAQUA.CO.UK/PRODUCTS/MKIII-WAVERIDER-BUOY/, 2018 AND HTTPS://QLD.GOV.AU, 2018)

Two types of wave buoys are most commonly found; and these are particle-following buoys and pitch-roll-heave (PRH) buoys. Particle/Surface following buoys are in widespread use as measurement instruments for a variety of ocean engineering studies. These buoys are typically small in size and consist of a spherical hull, with ballast or mooring attachments below, and instrumentation on the upper deck of the buoy –comprising an antenna, GPS unit, and motion sensing instrumentation, which can be either GPS or accelerometer based. Their small size makes these buoys easy to deploy and recover by hand, removing the need for specialist transport, and greatly expanding their utility. The Datawell Directional Waverider buoys ((Datawell, 2012) and pictured - Figure 3) are amongst the most commonly used type, and these have been deployed at both the AMETS and Galway Bay wave energy test sites. The Waverider has a diameter of 0.9 m, and can accurately measure waves with periods in the range 1.6 – 30 s, with the lowest frequency threshold for accurate response of the buoy governed by its natural period.

The principle of operation of particle following buoys is based on the assumption that the buoy is small in comparison to the incident wavelength, and will replicate the profile of passing waves; this being referred to as Lagrangian motion (where the position and velocity of the particle or particles is known), as opposed to Eulerian

motion (where changes in fluid motion are considered at a fluid element that is fixed in space) – which is associated with surface profiles measured by fixed sensors.

The surface elevation of the buoy is measured by either the accelerometer or GPS-based unit housed within a stabilised platform. To obtain the motions of the buoy, the surface elevation accelerations are observed, with this signal double-integrated to determine the heave motion of the buoy. The directional information is similarly determined through analysis of the vertical and horizontal acceleration components.

The accuracy of the directional Waverider, and its non-directional predecessor, has been the subject of validation against other sensors (O'Reilly *et al.*, 1996) and it has been demonstrated that estimates of directional parameters from the Datawell Waverider are a significant improvement on those produced by the NDBC 3 m Discus buoy introduced in the following Section. It is theorised that the large, stable platform of the typical Pitch-Roll-Heave buoy conflicts with the wave following ability of the buoy, and its ability to measure sea-surface slopes.

2.1.1.1.2 Pitch-Roll-Heave Buoys



FIGURE 4: FUGRO WAVESCAN BUOY AWAITING DEPLOYMENT (WWW.ABOUTOILANDGAS.ORG, 2017)

Pitch-roll-heave (PRH) buoys are disc shaped buoys which follow the slope of the water surface, as opposed to tracking orbital motion as is the case with the particle following buoys discussed in Section 2.1.1.1.1. With PRH buoys a sensor captures the pitch and roll inclinations alongside the vertical heave motion. The combination of these measurements allows the directional characteristics of the waves to be determined.

The large size of these buoys, typically beginning at 2.8/3.0m, makes them especially suited to carrying additional metocean sensing equipment, such as anemometers or other measuring devices for wind; barometers and thermometers. These additional measurements can have great utility in the overall characterisation of a site. Additionally, the large size of the buoys makes them quite robust, with even larger models, such as the 6 and 12m discus buoy, being operated by the National Data Buoy Centre (NDBC) in areas where survivability is a concern. The 3m discus buoy is the primary source of offshore directional wave measurements along the U.S. Coastline.

2.1.1.1.3 Treatment of buoy data

The work done in this thesis deals primarily with the data output produced by wave buoys and wave models which give information on ocean conditions around Irish coasts. The output of typical wave model data is in the form of summary spectral parameters such as the significant wave height (H_s) and the peak period (T_p) at hourly or three-hourly intervals, but the output of buoy data is often more complex and fractured; featuring multiple data formats, timeseries and spectral records, records of varying duration and with variation in the included parameters, and missing or invalid data due to equipment failures or adverse conditions.

The Datawell Waverider data, used extensively in this work, has three main outputs/file types. The buoy data is typically recorded as:

- Raw time-series data files of the measured surface elevation at a sampling frequency of 1.28Hz for 30 minutes ('.raw' files).
- Spectral density files which include directional parameters for 64 frequency components from 0.025Hz to 0.58Hz ('.spt' files). These files contain a record

of eight spectra produce by analysis of 200 second intervals of surface elevation time series.

- History of spectral parameter files ('.his' files). These files contain a history of the summary spectral parameters over each 30-minute period.

Further information on the data types and processing of Waverider buoy data can be found in the latest Datawell documentation (Datawell, 2012). The buoy data used in this work has been obtained using the Marine Institute data portal (Marine Institute, 2015), and provided by ESB as part of the WestWave project.

2.1.1.2 Ireland's Buoy Data Network

Commented [AB4]: Created new section to deal specifically with Ireland's buoy data network/test sites.

The Datawell Waverider (Datawell, 2012) is the most commonly found buoy off the coasts of Ireland, with the Marine Institute operating a network of six buoys located around the Irish Coast (Figure 5).



FIGURE 5: MET ÉIREANN MAP OF COASTAL STATIONS AND M-BUOYS (MAINTAINED BY MARINE INSTITUTE) (MET Eireann, 2017)

These, however, only provide summary statistics such as significant wave height (H_s) and the average zero-crossing period (T_z). The time-series data is collected but is not made available. This creates difficulty when attempting to analyse or validate conditions in the seas around Ireland, though the development of test sites in Galway Bay and near Belmullet have increased the capability and utility of Ireland's wave measurement network.

Commented [AB5]: Detail on data available clarified.

2.1.1.3 Ireland's Wave Energy Test Sites

Ireland now features a number of pilot sites for the development of Wave Energy. Two of these, the Atlantic Marine Energy Test Site (AMETS), and the Galway Bay Test Site are purpose-built test sites for the development of Marine Renewable Energy devices, while Killard Point in County Clare is the designated site for the WestWave project.

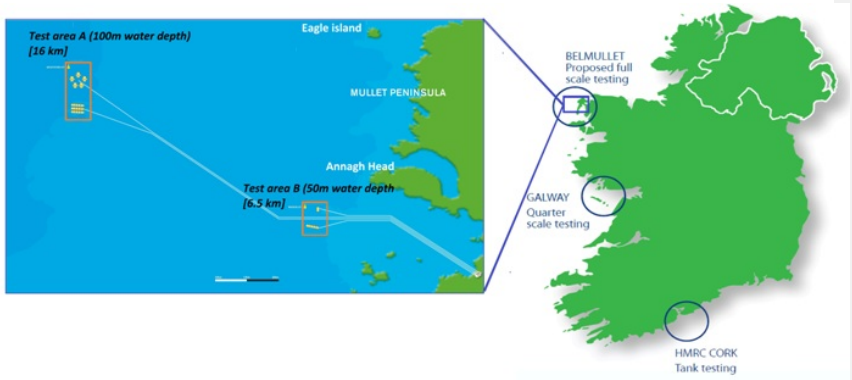


FIGURE 6: LOCATION OF AMETS AND GALWAY BAY TEST FACILITIES (Blavette, 2013)

The Atlantic Marine Energy Test Site (AMETS) (Figure 6), located off Annagh Head, west of Belmullet in County Mayo, is a full-scale grid-connected site which will allow developers to test both the energy production and survivability of their devices. Two test areas are currently under development: "Test Area A" at 100m water depth and located 16km out from Belderra Strand, and "Test Area B" at 50m water depth and located 6km from the stand (Figure 7).

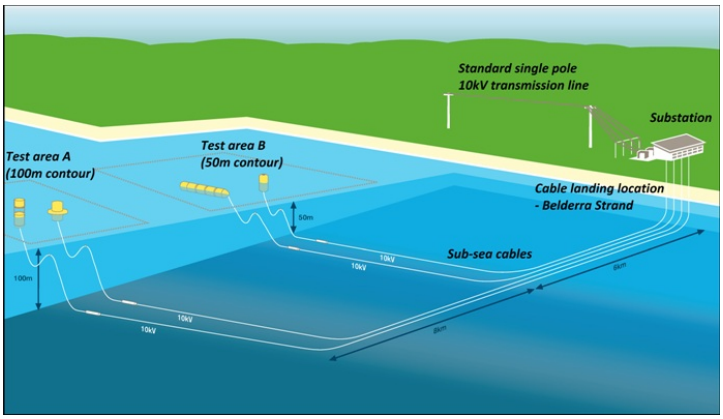


FIGURE 7: PROPOSED LAYOUT OF TEST SITE INFRASTRUCTURE AT AMETS

AMETS is being developed by Sustainable Energy Authority of Ireland (SEAI) to facilitate testing of full scale wave energy converters in an open ocean environment and will be connected to the national grid. This site is an integral component of Ireland's Ocean Energy Strategy and is being developed in accordance with the national Offshore Renewable Energy Development Plan (SEAI, 2017).

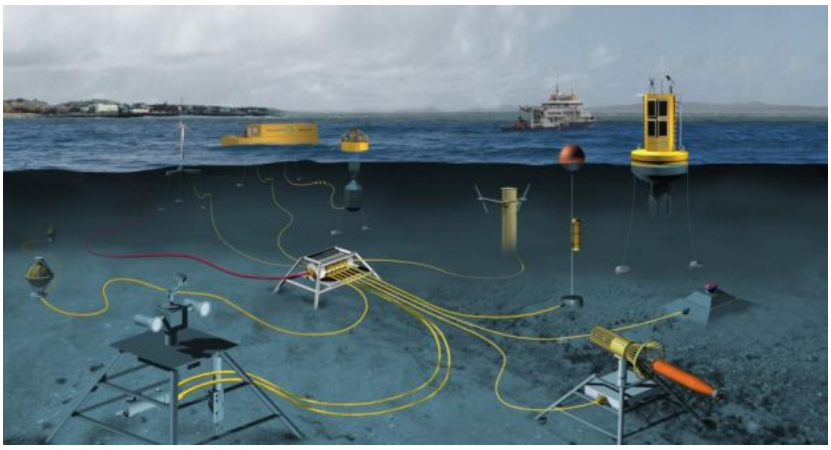


FIGURE 8: ILLUSTRATION OF SUB-SEA OBSERVATION EQUIPMENT AT GALWAY BAY (SMARTBAY, 2018)

The Galway Bay Test Site (Figure 8) is a quarter-scale site which has been in operation since 2006, and now includes power and data connectivity, subsea test and monitoring platforms, as well as a floating sea station platform – installed in 2015.

Waverider buoys have been deployed on an almost continuous basis at the Galway Bay site since 2005. Real-time oceanographic data is available on the Galway Bay data portal dashboard, while timeseries and spectral information is available through the Marine Institute's Data Request service (Marine Institute, 2018).

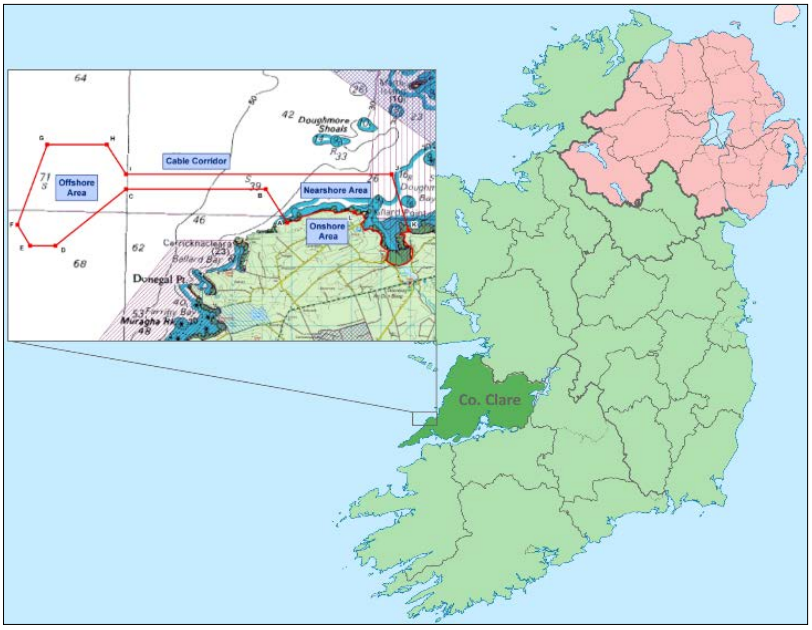


FIGURE 9: WESTWAVE NEARSHORE AND OFFSHORE SITES, KILLARD, CO.CLARE, IRELAND

The WestWave project represents the first designated commercial wave array project in Ireland, with the development of a 5MW Wave Energy Converter (WEC) array off the coast of Killard Point in Co. Clare. The WestWave project represents a critical project in the ocean energy development roadmap for Ireland, aiming to demonstrate technology readiness, develop the required marine capabilities and supply-chain processes, gain public acceptance for wave energy, and to disseminate and prove the opportunities for wave energy that lie in Ireland.

While not a de-facto test site, Killard Point represents a significant source of commercially relevant wave data for the development of MRE technologies in Ireland, particularly given its focus on the collection of wave data specifically for assessment of a Marine Renewable Energy project. Waverider buoys have been

located in 33-35m water depth at the site since 2011. WECs will be installed in either nearshore or offshore areas, depending on the technology type.

2.1.1.4 ADCPs



FIGURE 10: TELEDYNE ADCP, TRIPOD BOTTOM MOORING DEVICE FOR ADCP, BOTTOM-MOUNTED ADCP IN-USE MEASURING WAVE PARTICLE VELOCITIES (OCEAN-INNOVATIONS.NET, MOORINGSYSTEMS.COM)

Acoustic Doppler Current Profilers (ADCP) are hydro-acoustic current meters, similar to sonar, which are used to measure water current velocities over a depth range using the Doppler effect of sound waves. ADCPs use the sound waves back-scattered from particles (typically sediment) within the water column to determine particle velocities. They have been widely used in the assessment of the tidal energy resource (USGS, 2007), however, they can also be used very effectively to determine wave conditions.

Directional wave spectra can be computed from the orbital velocities of passing waves, which are measured using high frequency pulses that are reflected by the moving water particles. The water surface elevation is measured by either a pressure sensor or an additional vertical beam. Comparisons between the measurements of co-located ADCPs and wave buoys have been shown to display good agreement, particularly for wave height parameters (Hydro International, 2005).

ADCPs for wave measurement are generally positioned on the seabed, and can be mounted in water depths of approximately 5 - 60m. An example mounting mechanism is shown in the centre panel of Figure 10. This mounting location has the advantage of reducing the risk of instrument loss due to extreme environmental conditions, or damage or movement due to passing vessels. With few exceptions, data storage for ADCPs is internal and is not transmitted to shore in real time. For

this reason, it is generally not possible to conduct real-time monitoring of wave conditions using ADCPs – a crucial differentiator from most buoy systems. Additionally, deployment durations are limited by battery life, and any loss of device during the deployment will also result in loss of data.

An ADCP was deployed at the Killard Point area in Co. Clare, as part of the WAVEMEASUREMENT project, focussing on uncovering the fundamental mechanisms underlying the physics of rogue waves. The aim was to define the quality of currently available wave measurements under extreme conditions, and this involved the concurrent deployment of a Sentinel V ADCP and Waverider buoy. (ERC and UCD, 2017)

2.1.1.5 Satellite

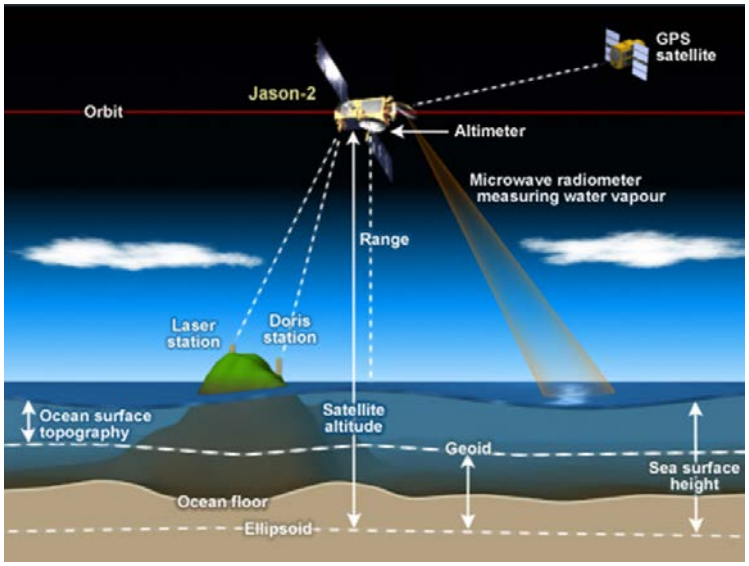


FIGURE 11: PRINCIPLES OF OPERATION OF SATELLITE ALTIMETRY (NOAA, NESDIS and STAR, 2017)

Satellite radar altimetry falls under the family of remote sensing techniques; these are instruments which are mounted above the water surface on a fixed or moving platform, and include observations from towers or platforms at sea, moving vessels, and airplanes. Satellite radar altimeters measure the ocean surface height by measuring the time taken for a radar pulse to make a round-trip from the satellite to

the sea surface and back (Figure 11). Satellite measurements, using either altimeter or synthetic aperture radar (SAR) systems allow wave data to be collected at a global scale, and have been used as input for assessments of the worldwide wave energy resource (Arinaga and Cheung, 2012).

Data covering the last 20 years is available from satellite remote sensing at a reasonably comprehensive level. However, satellites have the distinct dis-advantage of measuring only along predetermined ground tracks. Synthetic Aperture Radar (SAR) is, in principle, capable of providing full two-dimensional spectra, but this is still highly debated. Modern methods such as echo-tracking promise to introduce centimetre-level accuracy, but this is not readily available at present (Sui *et al.*, 2017).

Altimeters compute wave statistics by sending high frequency pulses which a sensor then detects at the ocean surface. Synthetic Aperture Radar systems record a high-resolution representation of the wave fields captured beneath their path, and produce a directional spectrum using this data (Holthuijsen, 2007). Long term studies of these satellite measurements are available and have undergone extensive quality control and validation (Globwave, 2012). These measurements have been used to analyse the influence of inter-annual variability in wave energy resource, and the impact it has on WEC power production (Mackay, Bahaj and Challenor, 2010b).

Seasat, deployed by NASA's JPL (Jet Propulsion Laboratory), was the first satellite system design specifically for remote sensing of earth's oceans. There have since been several satellites deployed for this purpose in Europe and America. These collect ocean wave and wind measurements. The current European Space Agency (ESA)'s Envisat is the primary source of satellite measured ocean data, joined by the American Jason 2 satellite.

The key operational difference compared to in-situ techniques is that large areas can be covered near-instantaneously. However, this needs to be balanced with the cost of such observations, and the fact that rotating satellites have a limited temporal window in which they can measure a site, making continuous deployment impossible.

2.1.2 Model Data

2.1.2.1 Wave Modelling History

Wave models contribute to our understanding of the oceans, and form the cornerstone of the available data on wave resource. Modelled wave datasets have greatly enhanced the wealth of available knowledge of the ocean environment, supplementing in-situ and remotely sensed data. Theorised to have seen first operational use in forecasting the wave conditions for the D-Day landings in 1944, these wave models have since been subject to significant development. In response to the growing need for accurate sea-state information for uses such as shipping, offshore operations, coastal and marine management, recreational and research activities, they have undergone rapid evolution from parameterised representations which related significant wave height and local wind speed - used to forecast information at short time-scales - to fully-spectral models capable of modelling the gamut of spectral wave parameters. Gelci and Cazalé are credited with introducing the spectral concept to numerical wave modelling (Gelci and Cazalé, 1953), and up to the late 1980's models used simple nonlinear interaction approximations, or made assumptions on the spectral shape. These were known as first and second-generation models. The Sea Wave Modelling Project (SWAMP) (The SWAMP Group, 1985) was a wave-model intercomparison study which identified and discussed the shortcomings of first and second generation models, and led to the development of the first third-generation wave model, the WAM model (WAMDIG, 1988). This contained explicit treatment of nonlinear interactions, not addressed until this point, and essentially replaced all previous models.

Third-generation spectral wave models are the current state of the art for wave climate modelling, and represent the underlying structure of the majority of wave transformation models such as WAM, SWAN, WW3 and Mike21 SW (Sections 2.1.2.4 – 2.1.2.7). These third-generation models are based on solving the spectral action balance equation, which determines the evolution of the action density in space and time. The action density is defined as energy density divided by wave frequency; and is used because, unlike energy density, it is conserved in the presence of currents; the energy density is specified using the linear two-dimensional (2D) wave spectrum, with the wave energy distributed over frequency and propagation direction.

$$\frac{d}{dt}E + \frac{d}{dx}C_x E + \frac{d}{dy}C_y E + \frac{d}{d\sigma}C_\sigma E + \frac{d}{d\theta}C_\theta E = \sum S \qquad (2.1)$$

Where E is the wave energy density,
t is the time,
x, y are the horizontal Cartesian coordinates,
σ is the wave frequency,
θ is the direction of wave propagation,
C is the speed of wave energy propagation (and the subscript the dimensional space in which the energy is propagating),
S refers to the energy sources/sinks.

The left-hand side of equation **(2.1)** represents the propagation terms of the model, which describe the propagation of the waves in both geographical space and the spectral space, whilst the right-hand side of the equation is the sum of energy sources/sinks, which represents all the physical process that generate, dissipate and redistribute wave energy.

The primary energy source term in third-generation spectral wave models is wave growth due to wind blowing across the ocean surface. Turbulent eddies in the wind field exert a fluctuating pressure on the water surface, causing small ripples to form. Friction between these ripples and the wind continues to transfer energy to the water. The model behaviour can be understood most easily by considering the case where waves propagate over a variable seabed slope with no sources or sinks of energy. In these circumstances, the solution of **(2.1)** leads to the well-known expressions for wave shoaling and refraction. Thus, the model kinematics can be viewed as an alternative representation of linear wave theory and the spectral energy balance equation is simply an extension of linear wave theory to include energy sources and sinks, albeit where some sources can redistribute the wave energy between individual spectral wave components (Folley and Whittaker, 2009).

Modelling of energy sinks is the predominant focus of these third-generation spectral wave models; with this often being handled differently by each of the models. These aspects of model-specific behaviour will be discussed for the primary third-generation models in Sections 2.1.2.4 to 2.1.2.7.

2.1.2.2 Model Inputs and Outputs

Wave models are driven by input information provided at the boundaries – lines defining known or estimated start conditions for the model. An example wave boundary (and mesh set-up) is displayed in Figure 12 below.

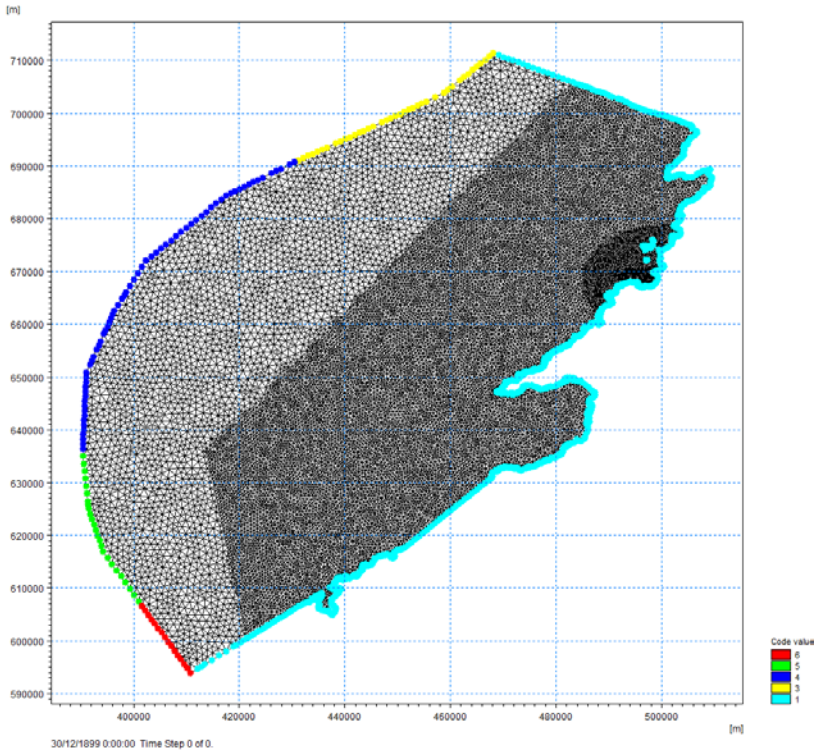


FIGURE 12: EXAMPLE WAVE MODEL INPUT BOUNDARY SHOWN IN MIKE 21 SW. RED, GREEN, BLUE AND YELLOW REPRESENT SEPARATE INPUT DATA DERIVED FROM GLOBAL WW3 MODEL AND INTERPOLATED ALONG BOUNDARY. LAND BOUNDARY SHOWN IN AQUA-BLUE.

There are two sources of potential wave input data at the model boundaries: measured data and the output from other models. Measured data, from sources such as wave buoys, Acoustic Doppler Current Profilers (ADP), satellite or radar measurements, provide the most accurate representation of the boundary conditions. For nearshore modelling applications however, data more commonly comprises point measurement outputs from a larger, global-domain, model, which must be estimated or interpolated along the boundary.

A spectral model requires full two-dimensional (frequency and direction) spectral information as the input at the offshore model boundaries. If 2D spectra are available from a large-scale wave model, these can be interpolated to the grid points of the local grid. Within the accuracy of the large-scale model this is the most complete and detailed possible input. Often, when dealing with the summary outputs or limited buoy information, only global parameters such as H_{m0}, T_p, T_z, Dir_p or 1D frequency spectra will be available. In these cases the full 2D spectra must typically be derived, with many models having the facility to generate this based on an assumed parametric formulation – the Bretschneider, Pierson-Moskowitz, or JONSWAP spectrum.

Models offer the option of output either in spectral files or as summary spectral parameter statistics. Spectral output is typically useful if a true spectrum was used as the input to the model. If the spectrum was generated based on a parametric shape, the output spectrum will similarly be based on the selected parametric spectral shape. For high level resource assessment studies for ocean energy developments, a set of parameters including significant wave height, energy period and direction will usually be sufficient, and will allow additional parameters such as the wave power to be calculated.

Figure 13 shows the output of a Wavewatch-III model, with summary wave height, wind speed and wind direction parameters displayed over the spatial domain.

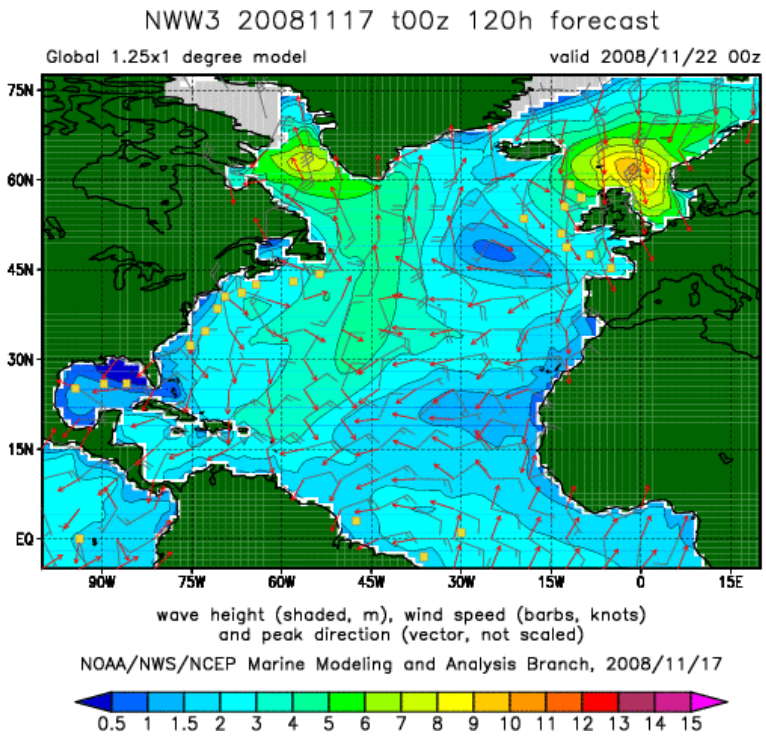


FIGURE 13: SAMPLE WAVEWATCH 3 GLOBAL MODEL OUTPUT DISPLAYING SHADED MAP OF WAVE HEIGHT (NOAA, 2008)

2.1.2.3 Wave Model Usage

Models require initial conditions, that is - information describing the sea-state, in order to run. An analysis of the sea or ocean can be created through data assimilation of observations such as buoy or satellite altimeter measurements, combined with a background "guess," from a previous forecast or climatology to create the best estimate of the current conditions. In practice, many forecasting system rely only on the previous forecast, without any assimilation of observations. (Tolman, 2009)

A critical input of wave models is the "forcing" by wind fields. This is provided in the form of a time-series of wind speed and directions. The most common sources of errors in wave model results are attributable to errors in the wind fields (Stopa *et al.*, 2016), as the wind field is the primary source of wave generation for these models,

and any error in the input will have subsequent effects on the accuracy of the model itself.

Although modelled data may lack the accuracy of recorded data, the use of output from other models as input for a nearshore model can often be a better option because of its spatial distribution. For this reason, the output of large global-domain wave models is often treated in the same way as point measurements, and used to provide input at intervals along the model boundaries for nearshore or finer resolution models. Alternatively, models can be "nested," which involves running a larger-scale, coarser resolution model to generate boundary conditions for a finer grid, and can be repeated on decreasing scales until the required scale is attained. SWAN, for example, is designed so that it can be nested in WAM and WaveWatch III, allowing global outputs to feed into nearshore models (EquiMar, 2010a).

It is difficult to over-state the utility of wave models. By providing a uniform and unbroken record of wave conditions, wave models alleviate many of the issues which are present with missing data common in the use of buoys and other physical measurement techniques. Wave models can provide information on the wave climate over long periods of time, and inform a broad gamut of essential parameters for resource assessment.

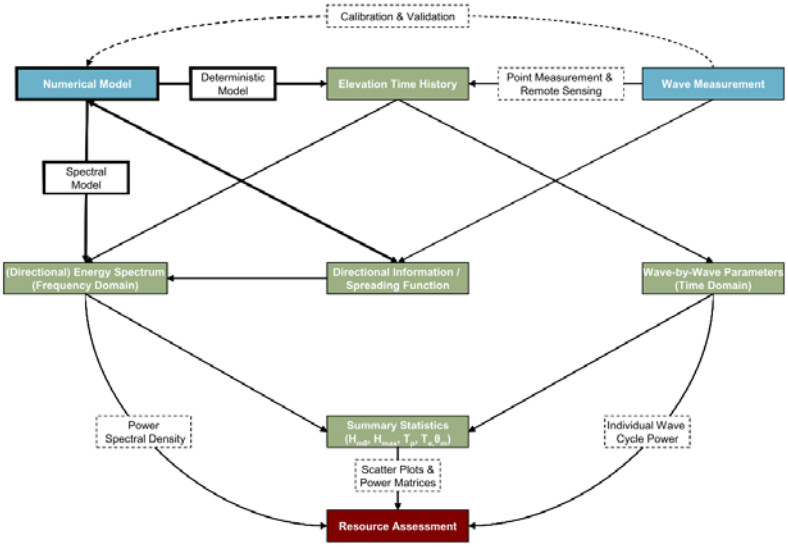


FIGURE 14: OVERVIEW OF THE ROLE OF NUMERICAL MODELS IN RESOURCE ASSESSMENT IN RELATION TO MEASUREMENT TECHNIQUES (EquiMar, 2010a)

2.1.2.4 WAM Model

The WAM model (WAMDIG, 1988) is one which has been widely adopted by the international community and has been validated on numerous occasions, proving to be remarkably reliable. (Janssen *et al.*, 1997). WAM is a third-generation wave model developed based on the collaborative findings of (The SWAMP Group, 1985) to resolve known issues with first generation models, which used a non-existent high-frequency equilibrium spectrum, and second generation wave models which could not properly simulate complex wave fields generated by rapidly changing winds, such as hurricanes.

The WAM model integrates the basic transport equation describing the evolution of a two-dimensional ocean wave spectrum without additional assumptions regarding the spectral shape. There are three explicit source functions which describe the wind input, non-linear transfer, and whitecapping dissipation. There is an additional bottom dissipation source function included, and refraction terms are included in the finite-depth version of the model. The model runs on a spherical latitude-longitude grid and can be used in any ocean region. The WAM model approach solves the left

side of the spectral energy balance equation (advection of wave energy), using an explicit scheme, without taking into account the source terms. The source terms on the right side are computed using a semi-implicit second-order method, and then added to the wave spectra. (Komen, 1994)

WAM predicts directional spectra along with wave properties such as significant wave height, mean wave direction and frequency, swell wave height and mean direction.

2.1.2.5 Wave Watch III

WAVEWATCH-III (WW3) is based on the spectral wave model that was initially developed by Tolman et al., (2002) at the Marine Modelling and Analysis Branch of the National Centers for Environmental Protection (Tolman, 2014). This code has been expanded into an open source community modelling framework, with the addition of many new features and options now available in version 4.18 that was recently made public.

WW3 predicts the wave evolution in two-dimensional physical space, x, and time, t, of the wave action density spectrum. This is expressed as a function of the wave number k, and wave direction θ. The governing balance equation for the wave action density spectrum $N(k,\theta,x,t)$ is given by:

$$\frac{\partial N}{\partial t} + \nabla_x \cdot \dot{x}N + \frac{\partial}{\partial k}\dot{k}N + \frac{\partial}{\partial \theta}\dot{\theta}N = \frac{S}{\sigma} \tag{2.2}$$

$$\dot{x} = c_g + U \tag{2.3}$$

$$\dot{k} = -\frac{\partial \sigma}{\partial d}\frac{\partial d}{\partial s} - k \cdot \frac{\partial U}{\partial s} \tag{2.4}$$

$$\dot{\theta} = -\frac{1}{k}\left[\frac{\partial \sigma}{\partial d}\frac{\partial d}{\partial m}\right] - k \cdot \frac{\partial U}{\partial m} \tag{2.5}$$

Where c_g is calculated from c_g and θ,
s is a coordinate in the direction of θ,

m is a coordinate perpendicular to s
The left-hand derivative in Equation **(2.2)** represents the local change and effects of wave propagation. The right-hand function, S, represents the net source term for wave growth and decay by wind action, exchange of action between components of the spectrum due to non-linear effects, losses due to whitecapping and shallow water processes.

In deep water, the net source term S consists of three parts: a wind-wave interaction terms S_{in}, non-linear wave-wave interactions term S_{nl} and a dissipation (whicapping) term S_{ds}. For model initiation, and to provide more realistic initial wave growth a linear input term S_{ln} is also considered. In shallow water additional terms for wave-bottom interactions S_{bot} is included. In extremely shallow water, depth induced breaking term S_{db} and triad wave-wave interactions term S_{tr} are included. The scattering of waves by bottom features is governed by the source term S_{sc} is also important. WW3 also includes a general purpose slot for user-defined source terms, S_{xx}. The collection of source terms can be written as:

$$S = S_{ln} + S_{in} + S_{nl} + S_{ds} + S_{bot} + S_{db} + S_{tr} + S_{sc} + S_{xx} \qquad (2.6)$$

2.1.2.6 Simulating WAves Nearshore (SWAN)

The SWAN (Simulating Waves Nearshore) model is a package developed at Delft University (Booij, Ris and Holthuijsen, 1999). SWAN is a free, open source, model which predicts wave conditions with a primary focus on shallow water coastal areas, lakes or estuaries. It utilises user-defined wind, bottom and current conditions and is based on solving the energy balance equation (**2**.**2**). This energy balance equations describes the surface gravity wave field in time and space. On the left-hand side of the equation, the terms describe the two-dimensional wave spectrum dependant on frequency and direction. The right-hand side represents the net source function; describing the energy input by the wind, propagation, non-linear wave interactions and dissipation. It calculates the non-linear energy transfers explicitly; though analytical and numerical approximations are required to accelerate the calculations.

In the SWAN model waves vary their shape, height, and direction as a consequence of wind action, wave breaking, energy transfer between waves, white capping, and variations in the seabed and currents. SWAN accounts for the following physics (Folley and Whittaker, 2009):

- Wave generation by wind.
- Wave propagation in time and space, refraction due to current and depth, shoaling, frequency shifting due to currents and non-stationary depth.
- Reflection, Refraction, Diffraction
- White capping, bottom friction and depth- induced breaking.
- Dissipation caused by aquatic vegetation, turbulent flow and viscous fluid mud. Reflection (specular and diffuse) against obstacles, and diffraction.

The initial wave conditions (wave height, wave direction and wave period) form the inputs to the model, which computes the wave changes as these conditions move toward the shore. The model provides output information in each cell of the numerically computed grid (typically 500x500m).

While WAVEWATCH III is used at global scale for offshore locations, linking meteorological parameters to the generation of ocean wave states, SWAN is used to accounts for the wave transformations that occur near the coast (whitecapping, bottom friction and depth induced wave breaking).

2.1.2.7 Mike 21 SW (Spectral Wave)

One of the most popular models for wave transformation in coastal and shallow water environment, and the model used for the study performed in Chapter 5 of this thesis, is Mike 21 SW (Spectral Wave). Mike 21 SW is a state-of-the-art third generation spectral wind-wave model developed by DHI that simulates the growth, decay and transformation of wind-generated waves and swells in offshore and coastal areas (Danish Hydraulic Institute, 2015). Mike 21 SW includes two different formulations; a fully spectral formulation and a directionally decoupled parametric formulation. The fully spectral formulation is based on the wave action conservation equation, while the directionally decoupled parametric formulation is based on a parameterisation of the wave action conservation equation. When establishing the

nearshore model for the Killard Pount site for the modelling exercise conducted in Chapter 5, both the fully spectral formulation and the directionally decoupled parametric formulation were trialled. The fully spectral formulation was found to be excessively computationally demanding, with run times exceeding three weeks to model just two weeks of hindcast data; while the accuracy ultimately did not prove significantly better than the directionally decoupled formulation. Thus, the directionally decoupled parametric formulation was ultimately utilised for the modelling exercise conducted in Chapter 5.

In MIKE 21 SW, the wind waves are represented by the wave action density spectrum N(σ,θ). The independent phase parameters have been chosen as the relative (intrinsic) angular frequency, σ = 2πf and the direction of wave propagation, θ. The relationship between the relative angular frequency and the absolute angular frequency, ω, is given by the linear dispersion relationship

$$\sigma = \sqrt{gktanh(kd)} = \omega - \bar{k} \cdot \bar{U} \tag{2.7}$$

where g is the acceleration of gravity,
d is the water depth,
U is the current velocity vector
k is the wave number vector with magnitude k and direction θ.
The action density, N(σ,θ), is related to the energy density E(σ,θ) by $N = \frac{E}{\sigma}$

2.1.2.7.1 Fully Spectral Formulation

The governing equation in MIKE 21 SW is the wave action balance equation formulated in either Cartesian or spherical co-ordinates. In horizontal Cartesian co-ordinates, the conservation equation for wave action reads:

$$\frac{dN}{dt} + \nabla \cdot (\bar{v}N) = \frac{S}{\sigma} \tag{2.8}$$

Where $N(\bar{x}, \sigma, \theta, t)$ is the action density,
t is the time,
$\bar{x} = (x, y)$ are the Cartesian co-ordinates,
$\bar{v} = \left(C_x, C_y, C_\sigma C_\theta\right)$ is the propagation velocity of a wave group in the four-dimensional phase space $\bar{x}$, σ and θ.
S is the source term for energy balance equation.
∇ is the four-dimensional differential operator in the $\bar{x}$, σ, θ-space.

The characteristic propagation speeds are given by the linear kinematic relationships:

$$(C_x, C_y) = \frac{d\bar{x}}{dt} = \bar{C}_g + \bar{U} = \frac{1}{2}\left(1 + \frac{2kd}{\sinh(2kd)}\right)\frac{\sigma}{k} + \bar{U} \tag{2.9}$$

$$C_\sigma = \frac{d\sigma}{dt} = \frac{d\sigma}{dd}\left[\frac{dd}{dt} + \bar{U} \cdot \nabla_{\bar{x}} d\right] - c_g \bar{k} \cdot \frac{d\bar{U}}{ds} \tag{2.10}$$

$$C_\theta = \frac{d\theta}{dt} = \frac{1}{k}\left[\frac{d\sigma}{dd}\frac{dd}{dm} + \bar{k} \cdot \frac{d\bar{U}}{dm}\right] \tag{2.11}$$

Here, s is the space co-ordinate in wave direction θ,

m is a co-ordinate perpendicular to s,

$\nabla_{\bar{x}}$ is the two-dimensional differential operator in the $\bar{x}$ – space.

The source function term, S, on the right-hand side of the wave action conservation equation is given by:

$$S = S_{in} S_{nl} S_{ds} S_{bot} S_{surf} \tag{2.12}$$

Here S_{in} represents the momentum transfer of wind energy to wave generation, S_{nl} the energy transfer due non-linear wave-wave interaction, S_{ds} the dissipation of wave energy due to white-capping (deep water wave breaking), S_{bot} the dissipation due to bottom friction and S_{surf} the dissipation of wave energy due to depth-induced breaking.

The default source functions S_{in}, S_{nl} and S_{ds} in MIKE 21 SW are similar to the source functions implemented in the WAM Cycle 4 model (Komen, 1994). The wind input is based on (Janssen, 1991). Janssen's quasi-linear theory of wind-wave generation, where the momentum transfer from the wind to the sea depends not only on the wind stress, but also the sea-state itself. The non-linear energy transfer is approximated by the Discrete Interaction Approximation approach, overcoming the limitations of the Local-Interaction Approximation (Hasselmann et al., 1985). The source function describing the dissipation due to white-capping is based on the

theory of (Hasselmann, 1974) and (Janssen, 1989). The influence of the bottom friction dissipation is modelled using the approach demonstrated by (Johnson and Kofoed-Hansen, 2000) which depends on the wave and sediment properties, and is modelled using the linearized bottom friction formulation. The source function describing the bottom-induced wave breaking is based on the well validated approach of (Battjes and Janssen, 1978).

2.1.2.7.2 Directionally Decoupled Parametric Formulation

The directionally decoupled parametric formulation is based on a parameterisation of the wave action conservation equation. Following the approach detailed in (Holthuijsen, Booij and Herbers, 1989), the parameterisation is made in the frequency domain by introducing the zeroth and first moment of the wave action spectrum as dependent variables. A similar formulation is used in the MIKE 21 SW. However, with MIKE 21 SW it is not necessary to set up a number of different orientated bathymetries to cover varying wind and wave directions.

The parameterisation leads to the following coupled equations:

$$\frac{d(m_0)}{dt} + \frac{d(c_x m_0)}{dx} + \frac{d(c_y m_0)}{dy} + \frac{d(c_\theta m_0)}{d\theta} = T_0 \qquad (2.13)$$

$$\frac{d(m_1)}{dt} + \frac{d(c_x m_1)}{dx} + \frac{d(c_y m_1)}{dy} + \frac{d(c_\theta m_1)}{d\theta} = T_1 \qquad (2.14)$$

Where m_0 (x, y, θ) and m_1 (x, y, θ) are the zeroth and first moment of the action spectrum N(x, y,σ,θ) respectively.

T_0 (x, y, θ) and T_1 (x, y, θ) are source functions based on the action spectrum.

The moments m_n (x, y, θ) are defined as:

$$m_n(x, y, \theta) = \int_0^\infty \omega^n N(x, y, \omega, \theta) d\omega \qquad (2.15)$$

The source functions T_0 and T_1 take into account the effect of local wind generation and energy dissipation due to bottom friction and wave breaking. The effects of wave-current interaction are also included. The source functions for the local wind generation are derived from empirical growth relations.

Solving the Equations

The steady-state solution to the quasi-stationary time integration can be solved using either of the following two methods:

- Modified Newton-Raphson method
- Iteration in the time-domain

Using a modified Newton-Raphson method, the solver attempts to solve a set of non-linear equations that describe the sea-state. The iteration procedure is stopped when a maximum number of iterations is performed or when the Root Mean Square error of the residual vector containing the increment in significant wave height between two iteration steps is smaller than the user specified tolerance.

For the approach which uses iteration in the time domain, the steady state solution is obtained by solving the instationary basic equations with steady boundary conditions and forcing. The time step used in the iteration procedure is determined automatically to satisfy the stability restriction. The iteration procedure is stopped when a maximum number of iterations is performed or when the Root Mean Square error of the vector containing the increment in significant wave height between steps is smaller than the user specified tolerance.

Numerical Methods

The frequency spectrum (fully spectral model only) is split into a prognostic part for frequencies lower than a cut-off frequency σ_{max} and an analytical diagnostic tail for the high-frequency part of the spectrum

$$E(\sigma,\theta) = E(\sigma_{max},\theta)\left(\frac{\sigma}{\sigma_{max}}\right)^{-m} \qquad (2.16)$$

Where m is a constant (=5).

Space Discretisation

The discretisation in geographical and spectral space is performed using cell-centred finite volume method. In the geographical domain an unstructured mesh is used. The spatial domain is discretised by subdivision of the continuum into non-overlapping elements, with both triangle and quadrilateral shaped polygons supported in MIKE 21 SW. The action density, N(σ,θ) is represented as a piecewise constant over the elements and stored at the geometric centres.

In frequency space either an equidistant or a logarithmic discretisation is used. In the directional space, an equidistant discretisation is used for both types of models. The action density is represented as piecewise constant over the discrete intervals, $\Delta\sigma$ and $\Delta\theta$, in the frequency and directional space.

Integrating the wave action conservation over an area A_i, the frequency interval $\Delta\theta_m$ gives:

$$\frac{d}{dt}\int_{\Delta\theta_m}\int_{\Delta\sigma_i}\int_{A_i} N d\Omega \mathrm{d}\sigma \mathrm{d}\theta - \int_{\Delta\theta_m}\int_{\Delta\sigma_i}\int_{A_i}\frac{S}{\sigma} d\Omega \mathrm{d}\sigma \mathrm{d}\theta \tag{2.17}$$

$$= \int_{\Delta\theta_m}\int_{\Delta\sigma_i}\int_{A_i} \nabla\cdot(\bar{v}N) d\Omega \mathrm{d}\sigma \mathrm{d}\theta \tag{2.18}$$

Where Ω is the integration variable defined on A_i . Using the divergence theorem and introducing the convective flux $\bar{F} = \bar{v}N$, the following equations are obtained:

$$\frac{dN_{i,l,m}}{dt} = -\frac{1}{A_i}\left[\sum_{p=1}^{NE}(F_n)_{p,l,m}\Delta l_p\right] \tag{2.19}$$

$$-\frac{1}{\Delta\sigma_l}\left[(F_\sigma)_{i,l+\frac{1}{2},m} - (F_\sigma)_{i,l-\frac{1}{2},m}\right] \tag{2.20}$$

$$-\frac{1}{\Delta\theta_l}\left[(F_\theta)_{i,l,m+\frac{1}{2}} - (F_\theta)_{i,l,m-\frac{1}{2}}\right] + \frac{S_{i,l,m}}{\sigma_l} \tag{2.21}$$

Where NE is the total number of edges in the cell,

$(F_n)_{p,l,m} = \left(F_x n_x + F_y n_y\right)_{p,l,m}$ is the normal flux through the edge p in geographical space with length Δlp.

$(F_\sigma)_{i,l+\frac{1}{2},m}$ and $(F_\theta)_{i,l,m+\frac{1}{2}}$ are the flux through the face in the frequency and directional space respectively.

The convective flux is then derived using a first-order up-winding scheme:

$$F_n = C_n(\frac{1}{2}\left(N_i + N_j\right) - \frac{1}{2}\frac{c}{|c|}(N_i - N_j) \tag{2.22}$$

where $C_n$is the propagation speed normal to the element cell-face.

Time Integration

The integration in time is based on a fractional step approach. Firstly, a propagation step is performed calculating an approximate solution N^* at the new time level (n+1) by solving the homogenous wave action conservation equation. Secondly, a source terms step is performed calculating the new solution N^{n+1} from the estimated solution taking into account only the effect of the source terms.

The propagation step is carried out by an explicit Euler scheme.

$$N^*_{i,l,m} = N^n_{i,l,m} + \Delta t\left(\frac{dN_{i,l,m}}{dt}\right)^n \tag{2.23}$$

To overcome the severe stability restriction, a multi-sequence integration scheme is employed. The maximum allowed time step is increased by employing a sequence of integration steps locally, where the number of steps may vary from point to point.

A source term step is performed using an implicit method.

$$N^{n+1}_{i,l,m} = N^*_{i,l,m} + \Delta t\left[\frac{(1-\alpha)S^*_{i,l,m} + \alpha S^{n+1}_{i,l,m}}{\sigma_l}\right] \tag{2.24}$$

Where α is a weighting coefficient that determines the type of finite difference method. Using a Taylor series to approximate S^{n+1} and assuming the off-diagonal terms in $dSldE = \gamma$ are negligible, this equation can be simplified as:

$$N_{i,l,m}^{n+1} = N_{i,l,m}^{*} + \frac{\left(S_{i,l,m}^{*}/\sigma_l\right)\Delta t}{(1-\alpha\gamma\Delta t)} \tag{2.25}$$

For growing waves ($\gamma > 0$) an explicit forward difference is used ($\alpha = 0$), while for decaying waves ($\gamma < 0$) an implicit backward difference ($\alpha = 1$) is applied.

2.2 Wave Data Analysis

Wave data analysis is used to extract useful parameters from measured wave data. These parameters describe the sea-states, and give information on the distribution of energy and of wave parameters within the given sea-state. This information is vital for characterising the wave energy resource and for predicting the performance of Wave Energy Converters (WECs) within that resource.

The first wave analysis recognisable by modern standards began with wartime studies during World War 2. The need to categorise, analyse and predict wave conditions drove a greater understanding of the methods used to analyse wave data. Shortly after the war, (Sverdrup and Munk, 1947) performed a study which informs a huge part of not only modern wave data analysis, but also developed the foundations of modern wave models. Sverdrup and Monk introduced the concept of "Significant Waves," characterised by a type of mean wave height and mean wave period. The concept of energy balance in a wave system was introduced to understand wave evolution, while empirical relations for the evolution of ocean surface waves were obtained using accumulated wave data.

Statistical theory of wind waves was greatly enhanced based on the theory of random process, particularly the work of Bell Telephone Laboratory, presented by (Rice, 1944). Following the introduction of the random noise theory, random waves began to be considered as a sum of an infinite number of superimposed sinusoidal waves of random phase. This informs much of the modern approach to the spectral analysis of waves which will be discussed in Section 2.2.2. Based on this statistical distribution, (Longuet-Higgins, 1952) gave the first theoretical derivation of the statistical distribution of wave-heights. Following this, significant attention was given to characterising and validating the spectral shape distribution in various seas, including

the Joint North Sea Wave Project (JONSWAP) and (Bretschneider, 1951); and efforts to understand wave interactions and non-linear effects began (Mitsuyasu, 2002).

This Section deals with how the necessary information for metocean data is derived through different analysis techniques, in both the time-domain and the frequency-domain.

Table 1 below provides a summary of the typical wave data inputs, their available analysis options, and the resultant output.

TABLE 1: SUMMARY OF TYPICAL WAVE DATA INPUTS, ANALYSIS OPTIONS, AND OUTPUTS

Input	Analysis Type	Output
Surface Elevations	Times series	A record of subsequent wave heights and periods, which can be used to determine local sea-state conditions ($H_{1/3}$, T_z etc.)
	Spectral	Local Sea state conditions (H_{m0}, T_p etc.)
	Wavelet	Visual output of spectral energy of a wave across frequency, direction and time domains.
Sea-state Parameters	Variability Analysis	Visual and statistical outline of wave conditions at site
	Weather Window	Probability of sites availability on a month by month basis
	Extreme Wave	Prediction of Extreme Wave heights

2.2.1 Time-series analysis

With a wave elevation record that has been obtained from surface following buoys, there are a number of analysis methods available to characterise the sea-state conditions. The most commonly used analysis technique is a time domain based analysis. This deals with describing the movements of the sea surface at one position. Time-series analysis takes a series of ocean surface elevations and breaks them down into a series of waves. To do so, individual waves must be defined. With a time-series signal of sufficient length (>100 distinct wave records typically recommended), the zero, or mean, point around which the signal oscillates is determined. Next, the

points where the water surface elevation crosses these zero points are determined, either by successive zero up-crossings, or zero down-crossings (Figure 15).

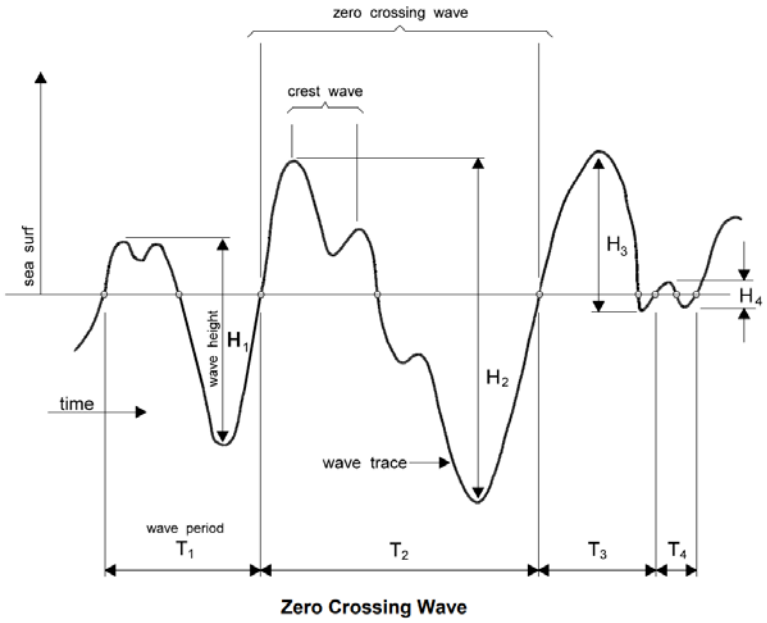


FIGURE 15: ZERO CROSSING WAVES. DIAGRAM DISPLAYS FOUR ZERO UP-CROSSING WAVES AND THEIR HEIGHT (H) AND PERIOD (T) (Manly Hydraulics Laboratory, 2017)

The most characteristic measure of a sea-state is the significant wave height, which can be determined via a number of methods. Primarily, this is taken as the mean height of the largest 1/3 waves, and denoted $H_{1/3.}$ The characteristic mean period of all the waves is determined via the zero-crossing method and denoted as the zero-crossing period, T_z. Commonly, the maximum wave height in the time-series, H_{max} and its corresponding period (but not necessarily the largest period), $T_{max,}$ are also defined. An alternative method of deriving the significant wave height is by determining the variance of the signal, σ; with H_s then defined as:

$$H_s = H_{var} = 4\sqrt{\sigma^2} \tag{2.26}$$

A further method of determining the significant wave height from its spectral moment definition is given in Table 2.

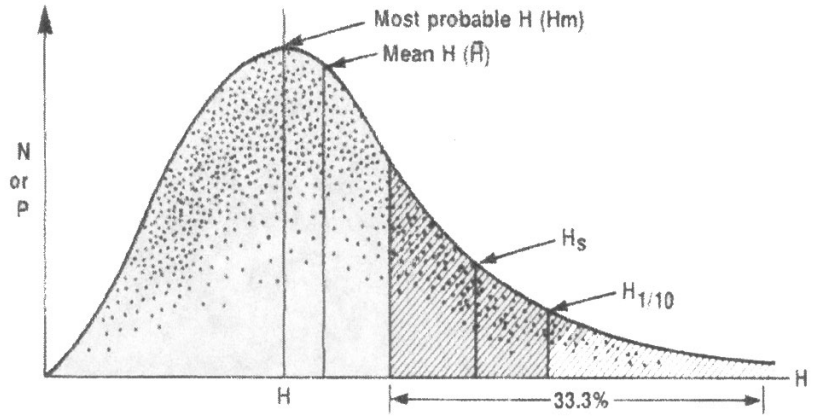


FIGURE 16: NON-DIMENSIONALISED HISTOGRAM OF WAVE HEIGHT BASED ON A RAYLEIGH DISTRIBUTION (Bretschneinder, 1964)

Figure 16 shows the statistical distribution of wave heights which can be seen to approximate to a Rayleigh curve. This statistical distribution is the basis of time from which important parameters are determined. The significant wave height (H_s) is determined analytically, as described before. From the H_s other wave parameters can be determined.

- H_m (Mean wave height) = 0.64 times H_s
- $H_{1/10}$ (Highest 10% wave height) = $1.27H_s$
- $H_{1/100}$ (Highest 1% wave height) = $1.67H_s$
- H_{max} (Max probable wave height) = ~ $2.0H_s$

2.2.2 Spectral Analysis

Analysis can also be carried out in the frequency domain, which presents a powerful tool for the analysis of wave data. A sea-state may be described as a summation of many individual waves with a given amplitude, propagation direction and frequency (Figure 17).

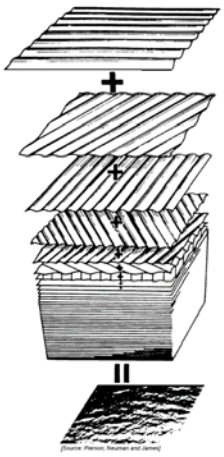


FIGURE 17: SUPERPOSITION OF SINE WAVES TO MAKE IRREGULAR SEA (St. Denis and Pierson, 1953)

The waves can then be represented as a function of distance from an origin point and time elapsed, as follows:

$$\zeta(x,t) = \sum_{n=1}^{N} \zeta_{an} \cos(k_n x - \omega_n t) \tag{2.27}$$

Where ζ is the harmonic wave at a position x and time t,
ζ_{an} is the wave amplitude,
ω the circular frequency of the wave component n,
k is the wave number, representing $\frac{2\pi}{\lambda}$ ($\lambda = Wavelength$)

By sampling the wave time-series at a suitably high frequency, sea surface elevations can be decomposed into combinations of their constituent harmonic components across the frequency domain. Fourier series expansion through an algorithm such as the Fast Fourier Transform (FFT) (Cooley and Tukey, 1965) is used to estimate the frequency and amplitude of discrete harmonics which make up the signal. At this step, the phase information of the waves is typically discarded. Figure 18 shows the process of time domain signal conversion to Energy Density Spectrum via Fourier analysis.

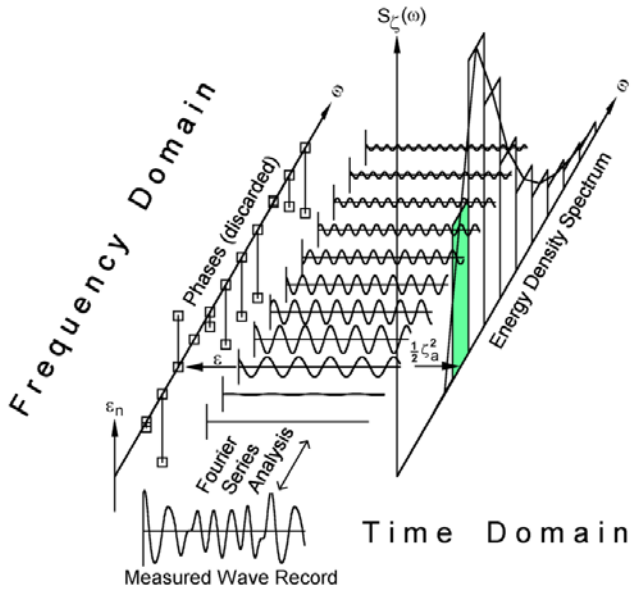


FIGURE 18: TRANSFORMATION OF TIME-DOMAIN INFORMATION TO ENERGY DENSITY SPECTRUM VIA FOURIER ANALYSIS (Journée and Pinkster, 2002)

The relationship between a component wave's amplitude and frequency is represented by the wave energy spectrum. The definition of the spectrum, commonly referred to as the "half-amplitude squared" spectrum, is provided by:

$$S(f)\Delta f = \sum_{1}^{n} \frac{1}{2} {a_n}^2 \tag{2.28}$$

Which can be used to determine the energy spectral density (commonly referred to as "wave spectral density") as follows:

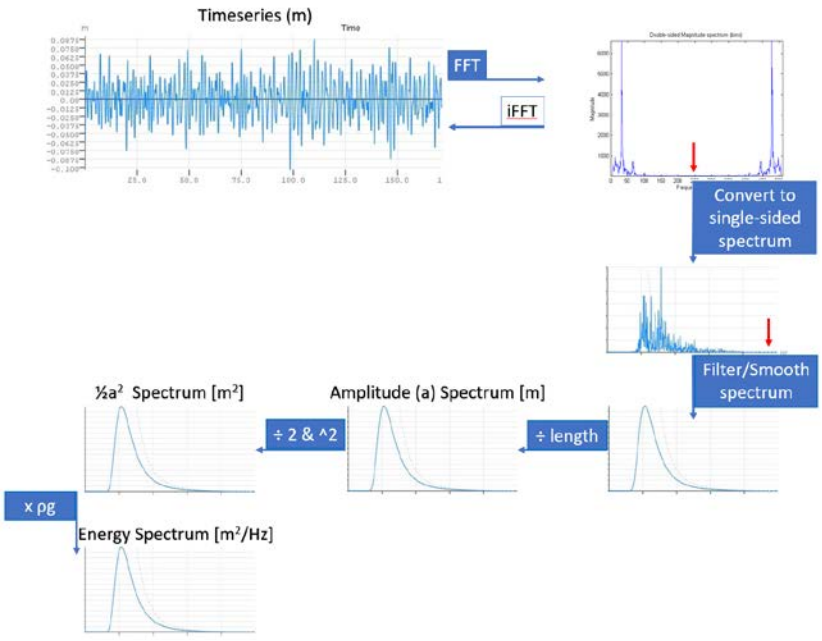


FIGURE 19: GENERATION OF WAVE ENERGY SPECTRUM FROM TIMESERIES

The process of generating a wave energy spectrum is illustrated in Figure 19. The terminology associated with the spectrum is often incorrect or absent, and one must be certain whether they are dealing with the half-amplitude squared spectrum or the energy spectrum.

Spectral moments

Determination of statistical parameters related to the specific wave spectrum revolve around the spectral moments. These moments are analogous in meaning to the physical concepts of centre of mass and first and second moments of area, that is, the moment represents the content of the spectrum at every frequency in the spectrum, weighted by the n^{th} power of the frequency, with the result summed across the entire spectrum. The n^{th} spectral moment is given by equation (**2.29**)

$$m_n = \int_0^\infty f^n S(f) df \tag{2.29}$$

Computing the moments of the wave spectrum provides a means to calculate summary statistics which describe the nature of a sea-state. The most commonly used parameter, H_{m0}, is an approximation of the H_s parameter derived from time-series analysis (and these terms may sometimes be used interchangeably). T_{02} is equivalent to the zero-crossing period T_z seen in time-series analysis. T_E, the energy period, is defined as being equivalent to the period of monochromatic wave whose height is equal to H_{m0}, and which has the same energy as the sea-state in question. The peak period, T_P, is given by $1/f_p$, where f_p is the frequency component with the highest value of Spectral Energy. Spectral bandwidth is an increasingly used parameter, with particular utility in studying spectral shape (Saulnier *et al.*, 2011). Two bandwidth parameters, ε_1 and ε_2 are defined as follows:

ε_1, which was first computed with studies of wave energy in mind (Smith, Venugopal and Wolfram, 2006):

$$\boldsymbol{\varepsilon_1} = \sqrt{\frac{m_1 m_{-1}}{m_0^2} - 1} \tag{2.30}$$

And the "Narrowness Parameter," ε_2 defined as:

$$\boldsymbol{\varepsilon_2} = \sqrt{\frac{m_0 m_2}{m_1^2} - 1} \tag{2.31}$$

These values of ε_1 and ε_2 range from 0 to 1, with narrow-banded spectra having the lowest values of spectral width.

The most common parameters and their moment definitions are given in Table 2 below.

TABLE 2: COMMONLY DERIVED WAVE PARAMETERS AND THEIR MOMENT DEFINITIONS (Tucker and Pitt, 2001)

Parameter (unit)	Symbol	Moment Definition
Significant Wave Height (m)	H_{m0}	$4\sqrt{m_0}$
Energy Period (s)	T_e / T_{-10}	m_{-1}/m_0
Zero-Crossing Period (s)	T_{02}	$\sqrt{m_0/m2}$
Mean Period (s)	T_{01}	$m0/m1$

Where only summary statistical parameters are available, parametric representations of these based on empirical trials are often used. The most commonly used are the JONSWAP and Bretschneider spectrum, which will be addressed in greater detail in Chapters 3 and 6.

2.2.3 Error Analysis of Wave Data

The most commonly used equations for the statistical analysis of wave data are outlined below. These are Correlation Coefficient (R), Root Mean Squared Error (RMSE), Bias and Scatter Index. These error parameters are commonly used in the field of signal processing and spectral analysis, and are also used frequently throughout wave energy research (Sakhare and Deo, 2009). These parameters allow for the determination of metrics for level of fit between modelled and recorded data, theoretical and empirical results, and numerous other statistical uses. Theses equations are presented here to introduce them prior to their use in this work.

These statistical measures include:

Correlation Coefficent (R): Indicates the strength of the linear relationship between corresponding data. R values close to 1 are an indicator of good correlation.

$$R = \frac{\Sigma_{i=1}^{N}(X_i - \overline{X})(Y_i - \overline{Y})}{\sqrt{\Sigma_{i=1}^{N}(X_i - \overline{X})^2 \Sigma_{i=1}^{N}(Y_i - \overline{Y})^2}} \tag{2.32}$$

Root Mean Squared Error (RMSE): A measure of the differences between values, commonly used as a measure of difference between values predicted (model) and observed (recorded).

$$RMSE = \sqrt{\frac{1}{N}\Sigma_{i=1}^{N}(X_i - Y_i)^2} \tag{2.33}$$

Mean Square Error may also be used where it is typical of the analysis type performed.

Bias: The bias represents the average error between data sets.

$$Bias = \frac{1}{N}\Sigma_{i=1}^{N}(X_i - Y_i) \tag{2.34}$$

Scatter Index (SI) The scatter index is a normalized measure of error, with lower values of SI indicating that the datasets are well matched.

$$SI = \frac{\sqrt{\frac{1}{N}\Sigma_{i=1}^{N}(X_i - Y_i - Bias)^2}}{\overline{X}} \tag{2.35}$$

2.3 Metocean Analysis

2.3.1 Overview

Metocean analysis refers to the combined analysis of meteorology and physical oceanography. It is the process of deriving a greater understanding of the conditions in which an offshore or coastal project will be undertaken.

A detailed understanding of the metocean environment and wave energy resource is crucial to examine the impact of site conditions such as wind speed and direction; wave amplitude, period, direction, extreme events, tides, bathymetry and many other factors on a proposed project. These factors are imperative for informing Site Selection and Feasibility, Development and Consenting; and the Design, Installation, Performance (Energy Production), Operations & Maintenance and Decomissioning of WEC concepts. The estimate of energy production from WECs will be a key focus of the work in this thesis; and its analysis will examine the biggest factors affecting the

energy production potential of projects. This includes the energy contribution of sea-sates, seasonal and inter-annual variability of resource, extreme events, as well as delving into the ability of current metocean standards to outline accurate analysis proceedures for determining device power production.

The process of a typical site selection and assessment is outlined in Figure 20 below.



FIGURE 20: SIMPLIFIED OVERALL DESIGN PROCESS FOR COMMERCIAL SITE SELECTION

This represents a real-world approach to the resource assessment problem, with the selection of sites and site parameters narrowed first by energy production, then by additional technoeconomic factors and environmental considerations. This often becomes an iterative process, whereby the available site details are continually updated as the project develops.

2.3.2 Scatter plots

Bi-variate scatter plots are amongst the most important and descriptive visualisations of site characteristics. These are plots of important summary statistics; typically, the H_{m0} – T_e pair. These provide a useful method of achieving an overall understanding of the wave climate and the energy resource at an area of interest. The “Assessment of Wave Energy Resource” (The European Marine Energy Centre

Ltd., 2009) and Equimar "Protocols for wave and tidal resource assessment" (EquiMar, 2010a), outline some standards and guidelines for the use of scatter plots, with comprehensive guidelines in the Equimar protocols on the definition of Wave Height and Period bin intervals, at 0.5m and 0.5s respectively. These are not strictly adhered to as industry standards, and the interval may vary depending on the analysis.

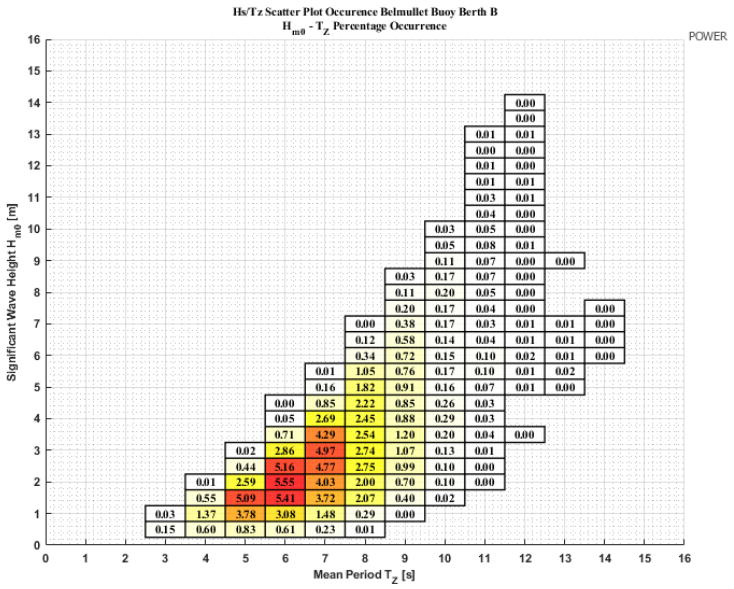


FIGURE 21: EXAMPLE H_S - T_Z SCATTERPLOT

2.3.3 Extreme prediction

Extreme Wave prediction, often called Extreme Value (EV) analysis, is the analysis of measured or hindcast data to determine the annual probability of failure, threshold exceedance, or return-period of extreme conditions.

These methods provide long term information for fatigue assessments, extreme loads and the prediction of energy production. Most marine structures are initially designed to withstand a specified set of extreme conditions. Further study may be conducted on the structure's design to ensure that issues, such as fatigue effects, will not cause damage over long time periods. The structure may also be subjected to risk

analysis which examines the statistics of the structure's ability to withstand the forces experienced in extreme conditions.

When designing offshore structures to withstand extreme conditions, the most important factor is the "Design Wave," This is the individual wave with a height which is exceeded on average only once in a specified "return period," which is conventionally either 50 or 100 years. Provided there is sufficient data the methods are equally applicable to any other value.

Extreme wave prediction is most commonly performed by approximating an extreme wave height through fitting observed values to a variety of different statistical curves. Determination of extreme wave height probability is based on methods such as those outlined by (Tucker and Pitt, 2001), (Battjes and Groenendijk, 2000), (Draper, 1972).

Storm waves can be considered as waves which exceed a defined height threshold. Extreme Wave analysis requires that each storm event be recorded as an individual occurrence, and be defined by its peak wave height. Recorded data from wave buoys tends to be at hourly intervals, and thus each storm occurrence typically contains many data points. It is therefore necessary to define a storm event as series of successive data points in which the peak wave value for an hour exceeds the defined threshold. Figure 22 below shows the selection of a threshold value which determines storm events.

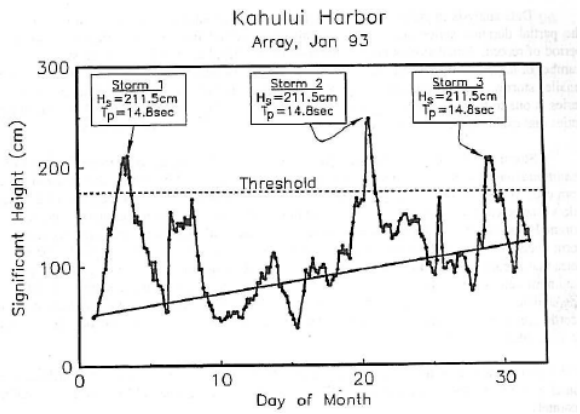


FIGURE 22: ILLUSTRATION OF THE SELECTION OF A THRESHOLD VALUE (THOMPSON 2001)

The definition of the storm duration and peak wave height are extremely subjective. A change in the threshold value utilized can change the duration of a storm event, and result in a single storm event becoming two or more shorter storm events. Conversely, a reduced threshold can also combine multiple storm events into a single event. There is no clear consensus on the best method of threshold selection, and the optimal strategy is often dependent on the quantity of data, duration of recording, and the extreme prediction method which will be used. The most common amongst these techniques include the Peak over Threshold (POT) method, Annual maxima, and n-maxima techniques.

In the application of the Peaks Over Threshold method, only wave events with a height greater than a defined threshold are ranked and analyzed. This threshold can be mathematically defined using a multiple of significant wave height, or user defined to match an existing off-shore structure or coastal defense feature.

The n-maxima method uses a defined number, n, of storm events which will be considered in determining the extreme wave distribution. While this method offers flexibility in the selection of storm events, it requires prior experience and knowledge of the underlying physics and typical conditions at the site in question to achieve accurate results.

For datasets of longer duration, the Annual maxima method is often used. With this approach, the peak value from each year of the dataset is selected for use in the analysis. This method of extreme analysis is intuitive and widely used, but does have a number of drawbacks. It assumes that for n years, you have a storm with an n-year return period. Where there are multiple years with low peak wave values, the analysis will not accurately depict the trend for waves which are indicative of extreme values at the site.

It is possible to perform a statistical analysis on recorded data to derive the predicted height of a wave which has a certain return period. In theory, the wave height for an infinite return period can be calculated using any set of data; however, for an n-year return period it is advised to have a minimum of n/5 years of data. One such method of defining the return period is using the Weibull formula to assign a return period and probability to each wave and rank them, as follows.

$$T(x) = \frac{n+1}{m} \tag{2.36}$$

And

$$P(x) = \frac{m}{n+1} \tag{2.37}$$

Where T(x) is the return Period, and P(x) is the probability of an annual maximum equaling or exceeding the height value h in any given year. To simplify the curve fitting, the reduced variate is calculated. The reduced variate, y, is given by:

$$y = -\ln\left\{-\ln\left[1 - \frac{1}{T(x)}\right]\right\} \tag{2.38}$$

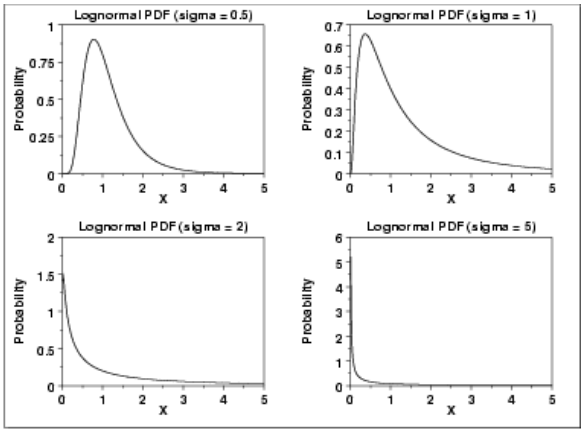


FIGURE 23: ILLUSTRATION OF LOGNORMAL PROBABILITY DISTRIBUTION FUNCTION

The data points are then plotted on a graph of h vs. y where y is plotted on a logarithmic scale horizontal axis. A curve is then fitted using the least squares method and the predicted heights for any return period can be obtained.

Methods for the determination of Extreme Waves and their associated return period are explored in greater detail in Chapter 4.

2.3.4 Weather Windows

Weather Windows are a period during which the sea-state, usually defined by its significant wave height, does not exceed a certain desired value.

Weather Windows are critical to any offshore operation involving installation, construction or maintenance, and often have a large bearing on the economic viability of projects. It is now common practice to thoroughly determine Weather Windows before the commencement of any major offshore operation. Weather Windows are not easily predicted, as doing-so requires highly accurate prediction of wave behavior, which a threshold-based analysis such as weather window analysis is particularly sensitive to. However, a study can be performed on past data to determine the probability of the duration and occurrence of weather windows; which vary depending on the significant wave height and the conditions at the site in question.

Weather Window prediction is similar to Storm Prediction in its application. However, in place of determining a period of exceedance and peak height; a period of non-exceedance (of, for example, the worst possible weather conditions in which the operation can take place) and the duration of that period are determined.

This probability is returned as a percentage or fractional likelihood of the weather window event occurring. It is determined by taking the number of periods for which the limiting threshold is not exceeded for a defined duration, and dividing by the total number of possible weather windows available across the entire dataset.

2.3.5 Power Production Estimates

Power production estimates form one of the most important project economic inputs. They are crucial to determining the most profitable device and site; as well as in determining the variability of electricity production, pay-back time, grid-integration and load balancing requirements, and other more granular details affecting project outcomes (Dalton, Alcorn and Lewis, 2012) (Teillant *et al.*, 2012).

The estimated power output from a WEC is most commonly presented as a function of two variables – typically H_{m0} and T_e. These are referred to as Power Matrices, and allow estimates of device energy production to be determined using available wave data. These Power Matrices are usually derived from numerical models of devices,

or produced following scaled-device performance testing and analysis in a wave basin.

The use of Power Matrices is widely accepted as the de-facto method of determining device power output, and their use is common in a number of large-scale resource assessments, such as that carried out for the Accessible Wave Energy Resource Atlas: Ireland (Sustainable Energy Authority Ireland, ESBI and Marine Institute, 2005). A sample power matrix for the Wavebob self-reacting WEC is provided in Figure 24 below:

Significant Height Hs [m] \ Wave Period [s]	4	5	6	7	8	9	10	11	12	13	14	15	16
1	6	11	19	25	30	44	50	53	44	34	22	20	17
1,5	13	25	43	55	68	90	102	92	91	66	65	45	37
2	24	45	65	100	121	153	175	151	122	126	87	61	58
2,5	0	65	104	141	191	179	243	255	190	181	135	99	83
3	0	96	137	205	244	357	293	353	260	248	184	137	120
3,5	0	0	192	254	291	431	385	424	314	285	239	222	172
4	0	0	256	366	403	551	536	531	473	420	289	268	179
4,5	0	0	327	418	574	678	708	665	509	415	386	244	249
5	0	0	358	514	658	824	828	618	638	512	452	384	333
5,5	0	0	0	610	774	880	936	905	805	603	456	397	311
6	0	0	0	711	952	974	1000	838	886	648	501	503	396
6,5	0	0	0	788	1000	1000	1000	979	1000	727	577	435	424
7	0	0	0	871	1000	1000	1000	1000	1000	959	748	574	472

FIGURE 24: EXAMPLE POWER MATRIX FOR WAVEBOB WEC (Babarit *et al.*, 2012)

The power matrix for a Hinged-Flap type WEC is used in this thesis to determine the potential energy production at the Killard Point site (Chapter 5); and in the analysis of Machine Learning model performance in improving energy estimates through improvement of wave parameter estimation (Chapter 3).

While Power Matrices are a useful tool for determining the scale of energy output that can be expected with a wave energy device, and are indeed used extensively in aspects of this work, many authors have suggested that H_{m0} and T_e alone are insufficient to accurately estimate device power output. As well as losing finer detail such as the spectral bandwidth, mean wave direction and directional spreading, which would assist in informing and accurate energy production estimate, it has been observed that it is readily possible for slight variations in observations of H_{m0} and T_e to result in large variations in energy production due to the granularity of the selected divisions in Power Matrix cells.

WEC performance is also influenced by the spectral shape distribution of the incident wave spectrum. Previous studies have shown that variability in the spectral shape has a significant impact on device power production (Barrett, Holmes and Lewis, 2007), (Saulnier *et al.*, 2011). The work in Chapter 6 will show that sea-states with similar summary parameters will often display distinctly different spectral shapes; and through physical and numerical testing will demonstrate that this has a major impact on the resultant energy production.

2.4 Standards for assessment of Marine Renewable Energy Projects

The earliest attempts to detail and standardise ocean wave analysis methods began with USACE (Engineers, 1995), and afterward were predominantly concerned with application to the Oil & Gas industry. A number of standards attempting to standardise metocean analysis for the assessment of Marine Renewable Energy have emerged in recent years (The European Marine Energy Centre Ltd., 2009), (EquiMar, 2010b), (International Electrotechnical Comission, 2015); with the IEC TS 62600-100 standards providing the most comprehensive treatment to-date. These standards are implemented and assessed in relation to their applicability to a commercial wave energy development in Chapter 5.

The IEC 62600-101 TS: Marine Energy – Wave, Tidal and other Water Current Converters – Part 101: "Wave Energy Resource Assessment and Characterisation", (henceforth referred to as IEC-TS) has been created with the aim of establishing a set of standards for estimating, analysing and reporting the wave energy resource at sites which are suitable for the installation of WECs; together with defining a standardised methodology with which this resource can be described (International Electrotechnical Comission, 2014).

(Ramos and Ringwood, 2016) assessed the utility and effectiveness of the IEC standards for wave energy resource characterisation using 3 different models with increasing spatial resolution in order to fulfil the requirements of the IEC-TS standards. They found that the IEC-TS offered a robust and coherent methodology, featuring recommendations and rules to carry out a precise wave resource characterisation. However, it was also found that some of the minimum requirements needed for validation of the more stringent design stages were

excessively demanding considering current best available wave modelling techniques; finding too that the increase in accuracy of key wave parameters was relatively small in comparison to the processing and time constraints imposed by using the more refined mesh stipulated for these design & feasibility stage requirements.

2.5 Machine Learning

Machine Learning is a field of computer science that evolved from the study of pattern recognition and computational learning theory found in Artificial Intelligence. The field covers the study and construction of algorithms which allow the user to learn from and make predictions on data. The unique aspect lies in the construction of the models. In place of static values and programming instructions; Machine Learning models build a model from example inputs in order to make data-driven predictions or decisions. The two primary types of learningare supervised and unsupervised learning. In supervised learning, the computer is presented with example inputs and their desired outputs, and learns a general rule that maps inputs to outputs. In unsupervised learning, no labels are given to the learning algorithm, and the model is left to determine the structure and relationships within the data itself. As an example, this approach could be used to determine whether or not a relationship exists between wave parameters such as H_{m0} and T_p at extreme wave conditions, or it could determine the precise wave period ratio between T_e and T_{02} at a given site. These methods invoke techniques from linear regression and weighted models, to classification algorithms that can learn to classify based on test value-prediction pairs.



FIGURE 25: FAMILIES OF MACHINE LEARNING ESTIMATORS, CLASSIFIERS, AND ASSESSMENT TECHNIQUES

The machine learning approach has been adopted in weather forecasting (Lu *et al.*, 2015), solar energy prediction (Sharma *et al.*, 2011) and the promising performance of an Artificial Neural Network in estimating one wave parameter from the specified value of another was shown by (Agrawal and Deo, 2004), in which the generated model proved to be more accurate than the statistical non-linear regression methods compared. Machine Learning has also been used to optimise the positioning of Wave Energy Converters (Sarkar and Dias, 2015), and thus there is some precedent for its application in Marine Renewable Energy.

The numerical techniques presented in this work will be approached from a practical, in-use, perspective as they can be applied to create solutions in Renewable Energy, rather than from a purely theoretical viewpoint.

2.5.1 k-fold cross validation

Cross-fold validation is a method of assessing the performance and accuracy of a model. This approach partitions a dataset into two or more parts. Each part is used once as a training set and once as a validation set. Generally, it is desirable to perform k-fold validation as many times as the size of the dataset and number of features will

allow. Three to Ten-fold cross validation is generally preferred and is commonly used in many fields.

Nested k-fold cross-validation is a common adaptation of this. This method partitions the dataset into k-folds. One fold is kept as the test set, while the remaining data is then partitioned again into k folds. One of these folds is kept as the validation set. The remaining data is used for training. The model is allowed to learn on the training dataset; and its performance is then trialled on the test dataset. This process iterates through each section of the dataset, as a new fold, lessening the impact of any bias in the dataset on the predictions.

The model is further allowed to select the best hyper-parameters by iteratively assessing each fold of the dataset and determining the parameters which give the lowest training error. The model is then tested on the outer (validation) data fold kept as test set. This process is then repeated - a different outer fold becomes the test set; and k-fold cross-validation is run on the remaining data to find another best value for the hyperparameter.

The dataset is partitioned into k disjoint equal-sized subsets, T1, T2, … , Tk.

This process is illustrated in Figure 27 below:

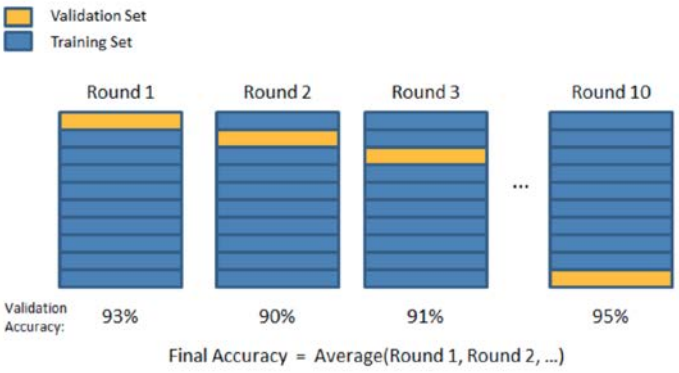


FIGURE 26: CROSS-VALIDATION APPROACH ILLUSTRATED

With the dataset creation, model learning, and testing outlined as pseudo-code below:

For u_1=1 to k, let D' be $D \setminus T_{u_1}$
Partition D' into k disjoint equal-sized subsets, S_1, S_2, …, S_k
For u_2=1 to k
    For v=1 to numvals
    Train on $D' \setminus S_{u_2}$ with the vth hyperparameter value
    Make predictions for S_{u_2}
    Measure validation error (e.g. MSE)
    Get the mean of the errors for each hyperparameter value
    Select the model (hyperparameter value) with lowest mean mse
Use the selected model to make predictions for T_{u_1}
Measure test error (e.g. MSE)
Report the means of the test errors

2.5.2 Leave One Out Cross Validation (LOOCV)

Leave One Out Cross-Validation involves leaving one section of data as a validation set, and training on the remaining data. The model is thus evaluated on the data point that has been left out, avoiding a biased model which carries overestimated accuracy as a result of testing on the data which has been used to train the model.

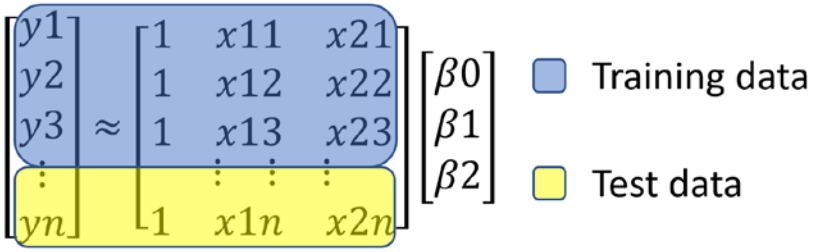


FIGURE 27: LEAVE ONE OUT CROSS-VALIDATION (LOOCV) APPROACH ILLUSTRATED

The blue box represents the data which is left out for testing purposes. The yellow box represents the remaining data. This process proceeds iteratively, choosing new data to leave out each time. This process can be generalised to "leave P out", where multiple data points are iteratively left out to ensure proper validation of the accuracy of the model.

2.5.3 Ordinary Least Squares

Ordinary Least Squares (OLS) forms the basis for a large number of methods used to estimate unknown parameters in a linear regression model. OLS is a method for estimating the unknown parameters in a linear regression model, with the aim of

minimizing the square error between observations and the approximation predicted by the linear approximation of the data. It is an intuitive model which measures the average lack of fit, and aims to achieve the best linear fit. The linear regression model has the form:

$$\mathrm{f}(x) = \beta_0 + \sum_{j=1}^{p} X_j \beta_j \qquad (2.39)$$

Figure 28 provides an intuitive geometric understanding of the operation of the linear regression model. The OLS estimation can be viewed as a projection of each coefficient times the associated training data onto a linear space.

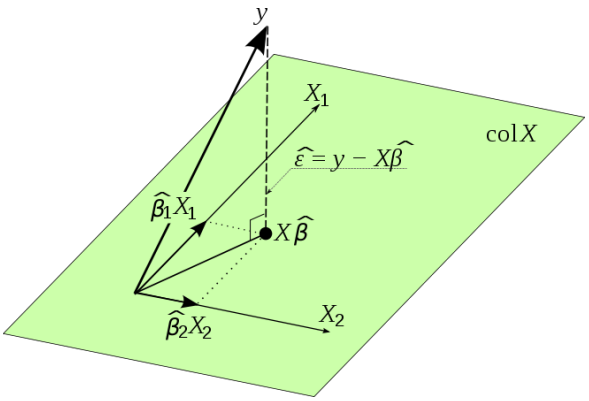


FIGURE 28: OLS ESTIMATION VIEWED AS A PROJECTION ONTO THE LINEAR SPACE SPANNED BY THE REGRESSORS

The basis of the linear model is that the regression function $E(Y|X)$ is either linear, or that a linear model is a reasonable approximation for the function. In the linear regression model expression, the β_j's represent the unknown parameters, and the X_j's are typically quantitative inputs.

Typically, there is a set of training data (X_1,Y_1) .. (X_N,Y_N) from which the parameters (β) are estimated. Each X_i= $\left(X_{i1}, X_{i2}, .., X_{ip}\right)^T$ is a vector of feature measurements for the *i*th case. The most commonly used estimation method for training the model is least squares, in which the coefficients β are selected to minimize the residual sum of the squares according to:

$$\mathrm{RSS}(\beta) = \sum_{i=1}^{N} (Y_i - f(X_i))^2 \qquad (2.40)$$

2.5.4 Other Methods

Methods other than ordinary least squares are also applied, as Least squares estimates often have low bias, but large variance. Prediction accuracy can sometimes be improved by shrinking or setting some coefficients to zero. By doing so; some accuracy, as defined by bias, is sacrificed, but results in a reduction of variance of the predicted values. This gives the possibility of improved overall prediction accuracy, especially with regard to analysis that is more sensitive to the variable nature of wave parameters.

With a large number of predictors, it can be useful to determine a smaller subset of parameters that exhibit the strongest effects, therefore covering the majority of the variance in the overall dataset while minimizing the number of inputs required for future models to achieve an accurate prediction.

2.5.5 Selection of best subset

Best subset regression finds for each $k \in \{0, 1, 2, \ldots, p\}$, the subset of size k which gives the smallest residual sum of squares. Deciding how to choose a k value involves a trade-off between bias and variance, as well as the complexity and size of the model. It is typically desirable to choose the smallest model that minimizes an estimate of the expected prediction error. Cross-validation is often used to estimate prediction error and select a value for k, while the Akaike Information Criterion (AIC), discussed in Section 2.5.9.2, is a popular alternative.

2.5.6 Shrinkage Methods

By retaining a subset of the predictors and discarding the rest, subset selection produces a model that is more easily interpreted and used in future work. It also carries the potential to produce lower prediction error than a full model. However, because it is a discrete process and variables are either retained or discarded it often exhibits high variance, and so doesn't reduce the prediction error of the full model. Shrinkage methods apply some variation of a shrinkage term to parameters to reduce

the effect of those which do not improve model prediction accuracy. Shrinkage methods are more continuous, and don't suffer as much from high variability.

2.5.7 Ridge regression model

Ridge regression is a commonly used method of regularization for ill-posed problems, also known as the method of linear regularization. Ridge regression becomes useful in the case where a standard approach (e.g. Ordinary Least Squares) cannot be used as no x, or more than one x value satisfies the equation – leaving no unique solution. In such cases, Ordinary Least Squares estimation leads to an overdetermined (aka over-fitted) or, commonly, an underdetermined system.

Ridge regression shrinks the regression coefficients by imposing a penalty on their size. The ridge coefficients minimize a penalized residual sum of squares:

$$\widehat{\beta}\,\text{ridge} = \text{argmin}_{\beta}\left\{\sum_{\text{i}=1}^{\text{N}}(yi - \beta_0 - \sum_{j=1}^{p} x_{ij}\,\beta_j)^2 + \lambda\sum_{j=1}^{p}\beta_j{}^2\right\} \quad (2.41)$$

Where λ $(\lambda \geq 0)$is the complexity parameter that governs the amount of shrinkage. In the ridge regression model, the coefficients are shrunk towards zero, using a penalization method based on the sum of the squares of the parameters. The ridge regression method contains an explicit size-limit on the parameters, which can be shown by writing the ridge equation as:

$$\widehat{\beta}\,\text{ridge} = \text{argmin}_{\beta}\sum_{\text{i}=1}^{\text{N}}(yi - \beta_0 - \sum_{j=1}^{p} x_{ij}\,\beta_j)^2 \quad (2.42)$$

$$\sum_{j=1}^{p}\beta_j{}^2 \leq t \quad (2.43)$$

Where t is the size constraint for the coefficients. In the case where many correlated variables exist in a linear regression model, their coefficients can become poorly determined (I.E.) exhibit high variance. Imposing a size constraint on the coefficients can prevent a large positive coefficient on one variable from being cancelled by a

similarly large negative coefficient on a correlated variable, thereby alleviating this problem.

2.5.8 Lasso Model

The Lasso (Least Absolute Shrinkage and Selection Operator) (Tibshirani, 1996) model is a shrinkage method regression analysis that performs both variable selection and regularization to improve the prediction accuracy and interoperability of the statistical models it produces. In signal processing literature, the Lasso is also known as basis pursuit. Lasso was originally formulated for least squares models, which informs a substantial amount of the behaviour of the estimator. Namely, its relationship to ridge regression and best subset selection. Despite being formulated for least squares, lasso regularization is easily extended to a wide variety of statistical models including Generalized Linear Models, generalized estimating equations, and M-estimators (of which least-square estimators are a subset). The lasso estimate is defined by:

$$\widehat{\beta}\,\text{lasso} = \text{argmin}_{\beta} \sum_{\text{i}=1}^{\text{n}} (yi - \beta_0 - \sum_{j=1}^{p} x_j \beta_j)^2 \tag{2.44}$$

$$\text{subject to} \sum_{\text{j}=1}^{\text{p}} |\beta_j| \leq t \tag{2.45}$$

The constant β_0 can be re-parameterized by standardizing the predictors. The solution for $\widehat{\beta}_0$ is $\hat{y}$, and a model can therefore be fit without an intercept.

Computing the lasso solution is a quadratic programming problem, for which a number of efficient algorithms exist. Because of the nature of the constraint of the lasso penalty $\sum_{\text{j}=1}^{\text{p}} |\beta_j|$, making t sufficiently small will cause some of the coefficients to be exactly zero, and thus the lasso model uses a method of continuous subset selection, and translates each coefficient by a constant factor λ, truncating at zero. This is known as “soft-thresholding”. (Hastie, Tibshirani and Jerome, 2009)

2.5.9 Selection of Alpha parameter

2.5.9.1 Coordinate descent

Coordinate descent is an optimization algorithm based on the idea that multivariate functions can be minimized by minimizing it along one direction at a time. Essentially, a line search is performed along one coordinate direction at each point in an iterative fashion. Different coordinate directions are applied cyclically throughout the procedure.

Beginning at an initial guess, x_0 for a local minimum of F, using a sequence x^1, x^2, x^3 … and performing a line search in each iteration will yield x^1, x^2, x^3, $F(x_0, x_1, x_2)$

With round k+1 defining, x^{k+1} from x^k by iteratively solving the single variable optimization problems:

$$x_i^{k+1} = \arg\min f(x_1^{k+1}, \dots, x_{i-1}^{k+1}, \text{y}, x_{i+1}^{k}, \dots, x_n^{k})\ y \in R \qquad (2.46)$$

For each variable x_i of x, for i from 1 to n

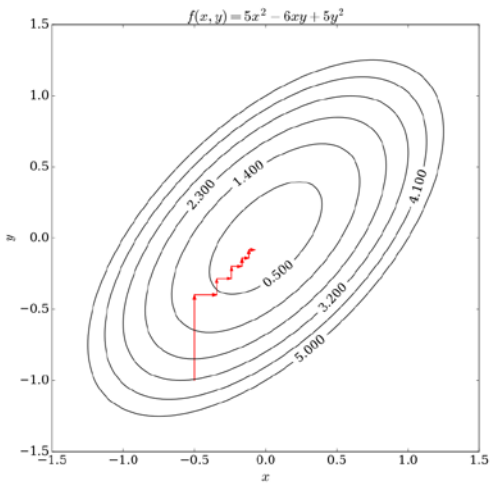


FIGURE 29: COORDINATE DESCENT PATH ILLUSTRATION

2.5.9.2 Akaike information criterion (AIC)

The Akaike information criterion provides a measure of the relative quality of a statistical model for a given set of data. Given a collection of models available to fit the data, AIC gives an estimate of the quality of each model relative to each other, thus providing a means of model selection. The AIC gives a representation of the relative balance of goodness of fit of the model and the complexity of the model. It does not tell us anything about the quality of the model in an absolute sense, and is therefore best used to differentiate between the performance of various numerical models. AIC can be used to determine the optimal Alpha value for a model.

$$AIC = 2k - 2\ln(\widehat{L}) \tag{2.47}$$

2.5.9.3 Bayes information criterion (BIC)

The Bayes information criterion, also known as the Schwarz criterion, is another criterion that can be used to choose among a finite set of models. It is based on the Likelihood function and thus is a similar approach to the AIC. Both AIC and BIC aim to resolve the problem of overfitting by introducing a penalty term to the number of parameters in the model. This penalty term is larger in BIC than in AIC.

$$BIC = \ln(n)\, k - 2\ln(\widehat{L}) \tag{2.48}$$

2.5.9.4 Least-Angle Regression (LARS)

Least-Angle regression is an algorithm for fitting linear regression models to high-dimensional data. LARS is used when a response variable is expected to be determined by a linear combination of a subset of potential covariates. The LARS algorithm is used as a means of producing an estimate of the variables to include, as well as their coefficients. The LARS solution consists of a curve denoting the solution for each value of the L1 norm of the parameter vector. It is similar to forward stepwise regression, but estimated parameters are increased in a direction equiangular to their correlation with the residual. The LARS method is advantageous as it produces a full, piecewise linear solution path, which is highly useful in cross-

validation for attempting to tune the model. It is also easily modifiable to produce solutions for the Lasso estimator.

2.6 Literature Review Summary

This literature review has covered the Wave Data sources that will be used throughout this thesis to perform an analysis of wave conditions on the West Coast of Ireland. These data sources will be also be used as case studies to investigate novel data and metocean analysis methods (used in addition to those in Section 2.3) that are developed in this thesis; additionally including an introduction to the novel Machine Learning methods which will be developed in Chapter 3. This review details some of the standards for the assessment of Marine Renewable Energy, including the newly-formed IEC-TS for Wave Resource Characterisation, which will be implemented in a first-of-kind case study in Chapter 5.

Commented [AB6]: Is this a suiable summary of the liteature review chapter?

3 Machine Learning Applied to Wave Parameters

3.1 Introduction

Wave Parameter relationships have long been determined using methods that give non-standard and often inaccurate results. With increased commercial activity in the marine sector, the importance of accurate wave parameter relationship determination has become increasingly apparent. The outputs of many numerical models and buoy datasets do not include all requisite wave parameters, and a typical approach may be to use a constant conversion factor or relationship based on defined spectra, such as the Bretschneider or JONSWAP spectrum, to determine these parameters.

Given that relationships between wave parameters vary significantly over both short scales (hourly) and longer scales (seasonal and annual variation), the currently employed methods are lacking, as subtleties are missed by the simpler approach.

The work in this Chapter addresses the determination of wave parameter relationships using a Machine Learning (ML) based model, and aims to identify and select the optimal method for the conversion of wave parameters (T_e, T_{01}) in coastal Irish Waters. This approach is then validated at two sites on the West Coast of Ireland.

It is the aim of this work to highlight the utility of ML in determining the relationship between wave parameters; using both buoy and modelled data, and mapping the predicted outcomes for a Wave Energy Converter (WEC) based on a variety of ML and Measure Correlate Predict (MCP) approaches.

There are a number of specific issues to tackle that ML can help with in the context of the overall goal for this thesis; namely:

- Conversion of T_{01} period to T_e for accurate energy production estimates using modelled data from the Killard Point and Belmullet sites.
- Conversion of T_{01} to T_{02} to better facilitate comparison of numerical models with recorded data.
- Calibration of modelled data to fit site conditions. In this case, taking three Killard Point buoy deployments and the concurrent output of the MIKE21

model and using machine learning to alter the MIKE21 model outputs to better represent the conditions at the site.

3.2 Machine Learning

This work is motivated by the desire to improve the accuracy of energy production estimates for the marine renewables industry. It is common industry practice to use modelled hindcast data to extend the utility of measured data at the site, or in cases where no proper data measurement campaign has taken place (Gallagher *et al.*, 2016). Despite the availability of online datasets of wave conditions such as IOWAGA (Rascle and Ardhuin, 2013) and NOAA (Tolman, 2002) WAVE-WATCH III derived models which cover large swathes of the globe, there remains a lack of high temporal and spatial resolution data suitable for studying the nearshore environment in which many wave energy converters will be deployed (Hughes and Heap, 2010). This paucity of quality wave data, particularly spectral data containing detailed information on wave parameter relationships, necessitates theoretical assumptions to infer some of the required parameters (Mackay, Bahaj and Challenor, 2010a). This approach can result in inaccuracies if the results are not correctly calibrated to the actual conditions at the site, or are based on fixed conversion factors which are not representative of the local wave conditions. Additionally, for particular wave models, such as the MIKE21 SW spectral wave module (Danish Hydraulic Institute, 2015), the output of wave parameters does not include the Energy Period (T_e) which, along with Significant Wave Height (H_s) is used in determining the incident wave energy and thus the potential output of a WEC device. Other models suffer from similar shortcomings, often owing to a reduced range of output parameters as an effort to decrease computation time. A chief motivation of the creation of the ML model developed in this work is to generate an accurate T_e parameter estimate from other available parameters, ultimately to improve the estimate of energy production.

Inaccurate Wave Period Ratios (WPRs) are a problem that has been highlighted by the work of Cahill in (Cahill, 2014), where he has shown that standard WPR relationships derived from the Bretschneider Spectrum have been calculated incorrectly, but still used in studies to determine available energy resource (Reikard, 2009) , (Dalton, Alcorn and Lewis, 2010), including the production of the Accessible

Wave Energy Resource Atlas (Sustainable Energy Authority Ireland, ESBI and Marine Institute, 2005). Furthermore, adopting a constant wave period ratio approach, where the ratio is derived based on short duration trials of just a number of weeks to months, can cause significant skew in the results due to seasonal variability in wave parameters and general variation in the parameters over shorter timescales. The outcome of this impacts the value of the resulting wave parameters, which has a knock-on effect on the prediction of device energy production.

The work done in this section will allow for more accurate use of Modelled and Buoy data (such as from the Mike21 model or M-buoys maintained by Marine Institute Ireland). It will display this accuracy by means of a real-world scenario using buoy data and the characteristic power matrix of a real wave energy converter, displaying the improvement in prediction accuracy of energy production using a ML based approach.

Making use of a straightforward method of utilising ML, such as the Least Absolute Shrinkage and Selection Operator (LASSO) (Tibshirani, 1996), this work demonstrates how the prediction of wave parameter relationships can be improved.

The work in this chapter will further show the required duration to train a machine learning model to accurately predict WPRs, informing the duration of deployment campaign required to produce accurate estimates of energy resource. With validation across multiple sites on the West Coast of Ireland, this will give confidence to end users that the summary statistics produced via the measurement campaign will be of real value to the project.

3.2.1 Background and Development

Section 2.5 of this thesis deals with a broad introduction to the field of Machine Learning, however a specific definition which explains the motivation behind its application to this particular problem is now provided:

Machine Learning is a field of computer science that evolved from the study of pattern recognition and computational learning theory as used in artificial intelligence. Machine learning has recently seen a rise in popularity, and has come to prominence with speech and handwriting recognition, online recommendation systems, fraud detection and more; which are all now commonplace (Jordan and

Mitchell, 2015). The field covers the study and construction of algorithms which allow the user to learn from and make predictions on data. The unique aspect lies in the construction of the models. In place of static values and programming instructions; ML models ”learn” from example inputs in order to make data-driven predictions or decisions (Marsland, 2015). The two primary types of learning are supervised and unsupervised learning. In supervised learning, the computer is provided with example inputs and their desired outputs, and learns a general rule that maps inputs to outputs. In unsupervised learning, no labels are given to the learning algorithm, and the model is left to determine the structure and relationships within the data itself. As an example, this approach could be used to determine whether or not a relationship exists between wave parameters such as H_{m0} and T_p at extreme wave conditions, or for the purposes of this work, can determine the precise WPR between T_e and T_{01} at a given site. These Machine Learning methods invoke techniques from linear regression and weighted models, to classification algorithms that can learn to classify based on test value-prediction pairs. The utility offered by ML is relatively unparalleled, with the capability for computationally efficient, highly accurate, tailored results that learn based on the conditions of the particular site being studied.

3.2.2 Machine Learning as a WPR estimator

The results presented here will show a Machine Learning approach based on the Lasso Model (Tibshirani, 1996) and show its utility in the field of renewable energy. ML has been used in similar fields before: A ML approach has been adopted in solar energy prediction (Sharma *et al.*, 2011), weather forecasting (Lu *et al.*, 2015), optimisation of the positioning of Wave Energy Converters (Sarkar and Dias, 2015), to reconstruct H_s from adjacent buoys with a hybrid genetic algorithm (Alexandre *et al.*, 2015)**,** and these models have been applied to Marine Renewable Energy, making use of neural networks to estimate wave parameters (Agrawal and Deo, 2004). On a broader scale, the ML work in this work has been inspired by (Cuadra *et al.*, 2016), (Fernández *et al.*, 2015), the latter of which used Artificial Neural Networks to predict significant wave height at an offshore site on the east coast of India. Here, ML will be used to estimate the relationship between two wave parameters; T_e (Energy Period) and T_{01} (Mean Period), specifically considering the case of the conversion between these parameters for measured buoy datasets off the west coast of Ireland.

3.2.3 Existing Approaches

To date, the most commonly used approach for determining the WPR has been to use the ratio suggested by the distribution of energy in the sea-spectrum, for which many empirical models exist; such as the Bretschneider or JONSWAP Spectrum. Ratios relating the WPR have been derived for these in many previous works, and their use is common throughout the industry. However, given that any real sea will not correspond perfectly to one of these generalized spectra, this approach will introduce inaccuracies, as shown in (Cahill, 2014). For Atlantic Seas off the West Coast of Ireland, the WPR is typically higher than these theoretical relationships. The work has also produced up-to date estimates for the conversion of wave period parameters, using Average Annual Values of WPR in real sea states. A comparison will be made to the constant wave period ratio approach in this work, as well as the derivation and use of the $T_e : T_{01}$ ratio based on the Bretschneider Spectrum.

3.2.4 Approach Taken

The determination of wave energy resource in locations with a lack of real wave measurements necessitates assumptions of the relationship between certain wave parameters. Measurements of wave resource in Ireland, such as those provided by the M-Buoy network maintained by the Marine Institute (Marine Institute, 2015), provide values for average zero-crossing period (T_z or T_{02}); however, wave energy resource assessment frequently relies on additional parameters such as peak period (T_p), mean spectral period (T_{01}) and energy period (T_e). Conversely, the wave period information output from numerical modelling, such as that detailed in Chapter 5, includes only T_{01} and T_p wave period information. In these models the outputs are constrained due to the time and processing cost of producing the full spectral formulation output necessary to obtain T_{02} and T_e information. Furthermore, determining these parameters for the entire hindcast in the case of the modelling undertaken in this work would have added significant complexity and delays to the commercial project. In order to fully assess the conditions at the site according to industry standards, and to produce reliable estimates for power production in particular; additional wave parameters, such as T_{02} and T_e, are necessary.

In this work, a number of different methods will be applied in the determination of the wave parameter relationships. These include:

- "Direct division" approach which simply provides the average WPR between two wave period parameters.
- Approach whereby The WPRs $T_z(T_{02})$: T_{01} and T_e : T_{01} will be derived based on the Bretschneider Spectrum via the method of computation of spectral moments suggested by (Tucker and Pitt, 2001).
- An increased fidelity method will be used whereby the WPR is determined across a combination of wave height and period conditions, and this applied as a "mask" to convert period values according to their wave height and period.
- A Machine Learning model which will be established and trialled to examine the value it will offer in the conversion of wave parameters in the context of the estimated power produced by a WEC power matrix combined with the values of H_{m0} and T_e derived through these methods. This model will use a LASSO method linear regression with k-fold cross-validation to train the model, and a number of alternative parameter selections and approaches will be trialled to unearth the optimally performing model configuration for this specific implementation.

Commented [AB7]: Updated to include all the required information in one go, and negate the need for further explanation of the methods later.

Each method has distinct advantages and drawbacks in terms of effort, complexity, time cost and accuracy, and these will be explored in detail. For the above methods, there follows a pattern of increasing accuracy and reduced uncertainty, accompanied by an increase in complexity and time cost; with an arithmetic average method offering a base point of acceptable accuracy, and Artificial Neural Networks/ML offering unparalleled accuracy at the expense of an increase in implementation time and complexity for the analyst.

A new method for determining wave parameters from associated wave parameters is developed in this chapter that provides vastly improved performance compared to existing methods. The importance of accuracy in these determinations will be highlighted through a power production comparison which shows the effect of increasing accuracy upon the power production estimates.

Commented [AB8]: Rephrased to highlight that a new method has been developed that is superior

Section 3.3 and 3.4 detail the development and application of the Machine Learning (ML) model via two test cases, which take place at two distinct sites; the Atlantic

Marine Energy Test site near Belmullet (Test Case 1), and the Killard Point site in County Clare (Test Case 2).

3.3 Test Case 1

3.3.1 Belmullet Introduction

The Atlantic Marine Energy Test Site (AMETS) is currently under development by the Sustainable Energy Authority of Ireland (SEAI) near Belmullet, Co. Mayo on the West Coast of Ireland. AMETS offers a harsh, energy-rich wave climate that is typical of exposed, Atlantic facing sites in Ireland. The data used to test this approach has been obtained from records for Belmullet "Berth A", monitored by a Waverider buoy positioned at Latitude: 54.2847° Longitude: -10.2703°. The Berth A buoy is positioned at the 100m depth contour. The data spans the period 01/09/2012 to 16/10/2014, containing 34564 data points at half-hourly intervals. Some 20 parameters are included in the output of the Waverider buoy. T_e has been generated for the spectral record using the relationship:

$$T_e = \frac{{T_{dw_2}}^2}{T_{01}} \tag{3.1}$$

Where,

$T_{dw2} = \sqrt{m_{-1}/m_1}$

m_{-1} = -1th Spectral moment

m_1 = 1st Spectral moment

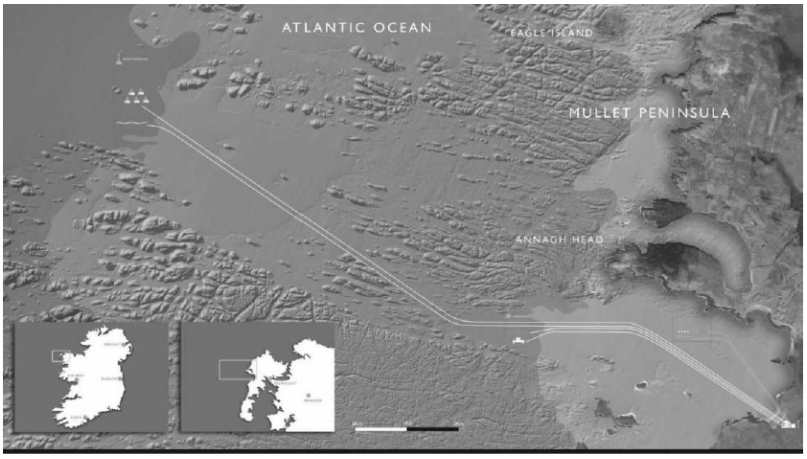


FIGURE 30: LAYOUT OF THE ATLANTIC MARINE ENERGY TEST SITE (IMAGE COURTESY OF SEAI)

3.3.2 Model development for Belmullet

The work in this chapter is motivated by the desire to improve estimates of wave parameters from limited datasets, with the overarching goal of improving energy production estimates for Marine Renewable Energy projects. The development of these novel methods for estimating wave parameters using a Machine Learning approach will focus on sites on the West Coast of Ireland, which represent an enormously energetic environment that has huge potential for the development of Marine Renewable Energy projects. These sites will require accurate predictions of energy production as part of their bid to achieve bankability, and the development of a Machine Learning model is a crucial step in providing this level of accuracy.

Commented [AB9]: Removed confusing forward and backward references, and strengthened the case for the need for these types of models.

WPR is not a linear relationship across all sea-states or over time. While it is possible to generalize the behaviour of the WPR across sea states, it is difficult to capture all of the variability and the influence of additional parameters such as wave direction using traditional approaches. To combat this, two Machine Learning approaches have been developed to map the relationship between wave parameters at Irish sites, and to enhance the prediction of associated wave parameters given a limited dataset. This work is primarily concerned with the conversion between T_{01}, T_{02}, T_p and T_e periods, but it is expected that the utility of the model developed will extend to adding certainty to the prediction of H_{max}/H_s ratio for the purposes of extreme H_{max} prediction. It is, ultimately, the aim of this work to highlight the utility of

Machine Learning in approximating the relationship between wave parameters; using both buoy and modelled data, and mapping the predicted outcomes for a WEC based on a variety of Machine Learning and MCP approaches.

Making use of the data provided by the Marine Institute for Belmullet Berth A, which is representative of conditions off the West Coast of Ireland, serves as a test case for the use of Machine Learning based approaches for Renewable Energy developers. Before application to the more limited-in-time Killard Point buoy dataset at three deployment locations is used in the context of the WestWave development.

3.3.3 Determination of T_e

The following outlines the method by which the T_e period parameter has been determined. T_e was determined via four distinct methods outlined previously in Section 3.2.4.

To ensure a fair and consistent approach from which real conclusions can be drawn, every effort has been made to implement best-practice data analysis and statistical analysis methods. Each approach will include a training/test split, with multiple tests, to determine the level of training data required to accurately predict the relationship. This approach will also be used to see how using a constant WPR compares to the ML model developed.

The accuracy of the model is to be determined using as standard suite of statistical methods common to both this field of computer science and engineering research in this field, those being Mean Average Error (MAE), Mean Square Error (MSE), Root Mean Square Error (RMSE), Cross-Correlation of variance (Rcorr) and Scatter Index (SI).

3.3.4 Python scikit-learn Workflow

The programmatic approach to the Machine Learning model development is complex and covers a large codebase of several thousand lines of code (LOC), and thus is not presented directly. Instead, the key elements of the code are illustrated below, with a granular version of the Python scikit-learn workflow provided in lieu of detailing the full code base:

3.3.5 Programmatic method

1. Import required dependencies

2. Read Prepared CSV database
3. Get an overview of the data
4. Describe the dataset
5. Feature selection
6. Get feature values and target values into separate numpy arrays
7. Plot the learning curve to demonstrate amount of data required
8. Perform Model selection. Choose between Ordinary Least Squares (OLS), Least Absolute Shrinkage and Selection Operator (Lasso), Ridge Regression, K-Nearest Neighbours (KNN) by performing 10-fold cross-validation using Mean Square Error as the scoring metric
9. Report model performance and choose model based on needs
10. Run the final model using a train/test split

Some specific adaptations pertaining to the Belmullet site were conducted as follows

- Belmullet Data extracted for 2012-2014 from .his files.
- Data records processed to correct format.
- Model run and optimal learning rate (alpha) determined for Belmullet.
- Holdout ratio effect on training score and cross validation score determined.
- Model input parameters altered from the basic set (H_S, T_1) to (H_S, T_1, T_p, PeakDir) to test the accuracy increase in prediction by adding additional parameters to the prediction.
- Lasso Model, CWPR model and BRET model run.
- Training time determined, including the seasonal variability in training time for the model
- Model run multiple times to ensure consistency and accuracy.
- Results compared to CWPR and BRET.

3.3.6 Comparison of models

Two models, a Constant Wave Period Ratio (henceforth CWPR) determination and a Bretschneider Spectrum derived ratio (BRET), form the basis of industry best practice. The two main alternative approaches to the ML model will be detailed here, along with a derivation of the $T_{01} : T_{02}$ and the $T_e : T_{01}$ ratio from the Bretschneider Spectrum.

3.3.6.1 Constant Wave Period Ratio:

The Constant Wave Period Ratio (CWPR) model is the most basic form of linear model, which takes the average ratio of the desired period to another period – in this case $T_e : T_{01}$, and uses this ratio to transform the existing value to the desired period type for unseen data

This is performed as follows:

$$CWPR = \frac{1}{N}\sum_{i=1}^{N}\frac{(T_e)_i}{(T_{01})_i} \quad (3.2)$$

Where,

T_e = Energy Period (s)

T_{01} = Mean Period (derived by method of spectral moments)

N = Number of datapoints

i = data-point index

3.3.6.1.1 T_{01}/T_{02}

In order to obtain an estimate of T_{02} which corresponded to that of the MIKE21 model data, it was necessary to determine the relationship between T_{01} and T_{02}. As an initial approach, this was determined empirically by determining the arithmetic ratio between T_{01} and T_{02} from the history of spectral parameters in the buoy data obtained during three separate deployments at Killard Point. The archived values of summary statistics were used to obtain the arithmetic WPR in the recorded data, with the same CWPR approach as 3.3.6.1

$$CWPR = \frac{1}{N}\sum_{i=1}^{N}\frac{(T_{01})_i}{(T_{02})_i} \quad (3.3)$$

3.3.6.2 Bretschneider derived approach:

The WPR can also be derived for the Bretschneider Spectrum by introducing a constant, αB to represent the relationship between the periods desired and the period contained within the deployment records.

3.3.6.2.1 T_{01}/T_{02} Derivation

Using the method of spectral moments, a derivation using the formulation of the spectral moments for the Bretschneider Spectrum was used to formulate a constant wave period relationship factor for T_{01}:T_{02}. The relationship between T_{01} and T_{02} was derived for the Bretschneider Spectrum as follows:

$$T_{01} = \alpha_A T_{02} \tag{3.4}$$

Rewritten in terms of spectral moments, this relationship becomes:

$$\frac{m_0}{m_1} = \alpha_A \sqrt{\frac{m_0}{m_2}} \tag{3.5}$$

Squaring both sides gives:

$$\frac{{m_0}^2}{{m_1}^2} = {\alpha_A}^2 \frac{m_0}{m_2} \tag{3.6}$$

Which simplifies to:

$$\frac{m_0}{{m_1}^2} = \frac{{\alpha_A}^2}{m_2} \tag{3.7}$$

The spectral moments can be generated in terms of A and B using the following formula based on the approach outlined in (Tucker and Pitt, 2001), where A and B are dependent on the modal frequency, ω_m and the variance of the spectrum $M_0 = \sigma_2$ as follows:

$$B = \frac{5\omega_m^4}{4} \tag{3.8}$$

$$A = 4\sigma^2 B \tag{3.9}$$

$$m_n = \frac{1}{4} A B^{\frac{n}{4}-1} \Gamma\left[1 - \left(\frac{n}{4}\right)\right] \tag{3.10}$$

Giving:

$$\frac{4}{0.0938534 \frac{A}{B^{\frac{3}{4}}}} \times 0.443 = {\alpha_A}^2 \tag{3.11}$$

$$\alpha_A{}^2 = 1.180032 \tag{3.12}$$

$$\alpha_A = 1.086293 \tag{3.13}$$

$$T_{01} = 1.086293 T_{02} \tag{3.14}$$

The relationship derived for T_{01}:T_{02} for the Bretschneider Spectrum gives an average relationship of 1.086, versus 1.134 based on the arithmetic average method of determining this ratio. This variation occurs due to the both the seasonal bias in the recorded data, and the deviation from the Bretschneider Spectrum in the recorded data which is explored in greater detail in Chapter 6.

3.3.6.2.2 T_e/T_{01} Derivation

The relationship between T_e and T_{01} was derived for the Bretschneider spectrum as follows:

$$T_e = \alpha_B T_{01} \tag{3.15}$$

Rewritten in terms of spectral moments, this relationship becomes:

$$\frac{m_{-1}}{m_0} = \alpha_B \frac{m_0}{m_1} \tag{3.16}$$

We can generate the spectral moments in terms of A and B, again following the approach of (Tucker and Pitt, 2001) and the derived equations (**3.8**) - (**3.10**), Giving:

$$\frac{0.2266 \frac{A}{B^{\frac{3}{4}}}}{\frac{A}{4B}} = \frac{\alpha_B \frac{A}{4B}}{0.30635 \frac{A}{B^{\frac{3}{4}}}} \tag{3.17}$$

$$\frac{0.0694189 A^2}{B^2} = \alpha_B \frac{A^2}{16 B^2} \tag{3.18}$$

$$\alpha_B = 1.1107 \tag{3.19}$$

Resulting in:

$$T_e = 1.1107 T_{01} \tag{3.20}$$

The T_e:T_{01} ratio derived is slightly greater than the T_{01}:T_{02} ratio. This wave period ratio is applied as a linear transform to the predictor value in the same fashion as the CWPR method to obtain the energy period.

3.3.6.3 Lasso Model

The Lasso (Least Absolute Shrinkage and Selection Operator) model is a shrinkage method regression analysis that was created with the aim of combining the favourable aspects of ridge regression and subset selection. It performs both variable selection and regularization to improve the prediction accuracy and interoperability of the statistical models it produces (Tibshirani, 1996). In its simplest terms, this regularisation is a tuning of the level of model complexity so that the model is better at predicting, and avoids overfitting or underfitting which would result in inaccurate predictions. Lasso was originally formulated for least squares models, which informs a substantial amount of the behaviour of the estimator. The Lasso model is the primary ML model used to make predictions in this work. The Lasso estimate is defined by:

$$\hat{\beta}\text{lasso} = \text{argmin}_{\beta} \sum_{i=1}^{n} (yi - \beta_0 - \sum_{j=1}^{p} x_j \beta_j)^2 \tag{3.21}$$

$$\text{subject to} \sum_{j=1}^{p} |\beta_j| \leq t \tag{3.22}$$

Where,

$\hat{\beta}$ is the Lasso estimate

yi is the predicted value

x_j the predictor

β_0 the intercept value

β_j the coefficient for the predictor

t $(>> 0)$ the standard tuning parameter

The constant β_0 can be re-parameterized by standardizing the predictors. The solution for $\hat{\beta}_0$ is $\hat{y}$, and a model can therefore be fit without an intercept. Because of the nature of the constraint of the Lasso penalty $\sum_{j=1}^{p}|\beta_j|$, making t sufficiently small will cause some of the coefficients to be exactly zero, and thus the Lasso model uses a method of continuous subset selection, and translates each coefficient by a constant factor λ (Hastie, Tibshirani and Jerome, 2009). This behaviour of the Lasso model provides a balance of Bias and Mean Square Error (MSE) with computation time when a large number of input parameters are used.

Computing the Lasso solution is a quadratic programming problem, for which a number of efficient algorithms exist. Various options and their respective merits will be discussed in this chapter.

3.3.7 Determination of T_E using Lasso based method

The determination of the relationship between T_e and T_{01} utilising the ML model requires a number of steps to complete the initial setup. The dataset of wave parameters is first imported and pre-processed. Some preliminary feature selection occurs, using domain specific knowledge to ensure that the parameters used are valid, free from errors, and, additionally, are typical of the parameters which will be available when the model is in use for its ultimate application. This process includes the removal of the predictant value and its subsequent assignment to a separate array, such that the model has no a-priori knowledge of the correct "guess," for the parameter value. Model selection is then performed via cross-validated error estimation, using Mean Square Error as the metric of assessment in determining the optimal model and alpha parameter. Repeated holdout testing is then performed with the selected models to ensure an unbiased determination of the model accuracy across the dataset. The final model is then used to predict the T_e value for an unseen portion of the dataset and these results are used to determine additional error metrics, as well as the power production accuracy when using the data produced by the models.

The accuracy of the model is determined using Mean Absolute Error (MAE), Mean Square Error (MSE), Root Mean Square Error (RMSE), R correlation coefficient (R_{corr}), and Scatter Index (SI).

3.3.8 Method of Alpha Selection

A number of methods exist to determine the optimal alpha parameter (a tuning hyperparameter which controls the degree of regularisation) for the model, and we search for the parameter which successfully minimizes the L1 norm, providing the best fitting model for the dataset. These methods include Akaike and Bayes information criterion to determine the relative accuracy of the proposed models, and coordinate descent and LARS (Least Angle Regression) which are more specifically applicable to the Lasso model. The Akaike and Bayes information criterion approaches rely on correct estimation of degrees of freedom. It is also necessary that the data be derived from a large sample. Further, these approaches require that the data is actually generated by the model, and the information criterion based approach tends to fall over for poorly conditioned problems. The Akaike and Bayes information criterion are examined below. Only the Bayes information criterion manages to select an alpha value for the problem which minimises error.

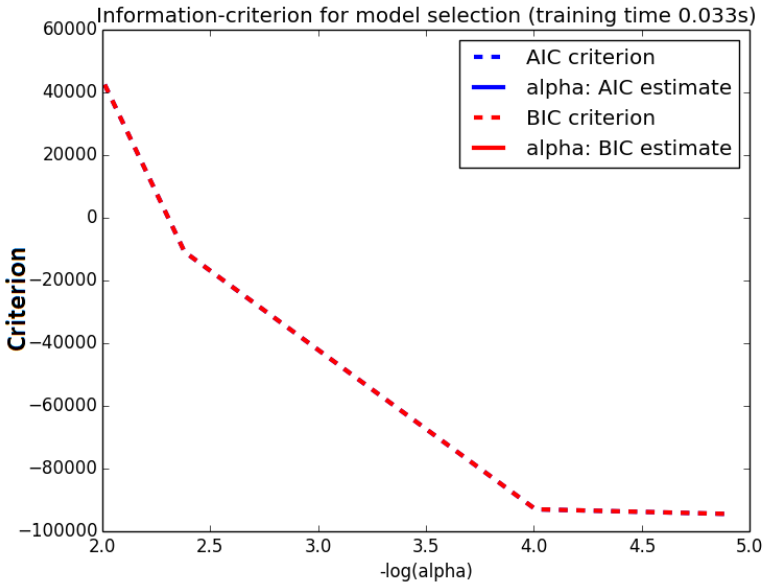


FIGURE 31: AIC AND BIC USED TO SELECT OPTIMAL VALUE OF REGULARIZATION PARAMETER OF LASSO ESTIMATOR

The Akaike Information-Criterion based model selection is extremely quick, reaching alpha value stability after only 0.033s. The Bayes Information-Criterion approach, however, fails to produce an estimate, and thus is not visible in Figure 31. Ultimately, it will be shown that there are simpler and more effective methods of selecting the optimal alpha value for this analysis.

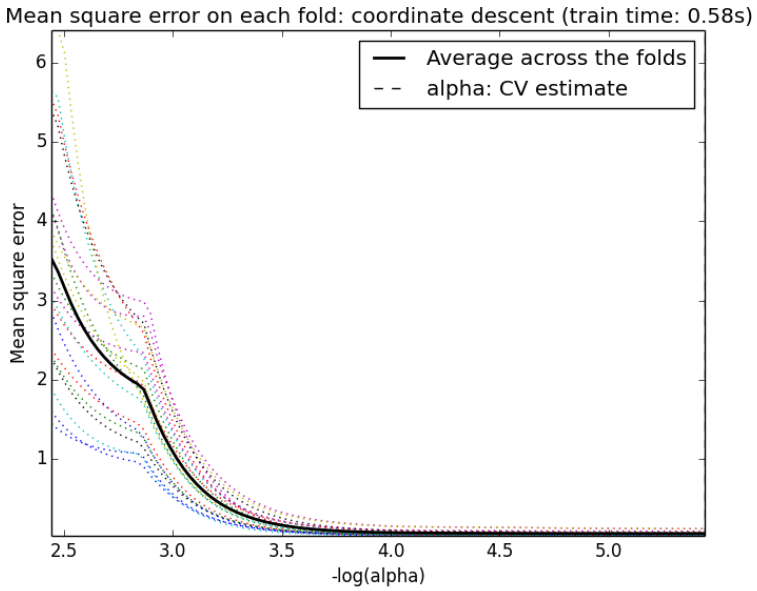


FIGURE 32: COORDINATE DESCENT ESTIMATION OF ALPHA PARAMETER FOR LASSO MODEL

Coordinate descent computes the path points on a pre-specified grid, and is thus more efficient if the number of grid points is smaller than the number of kinks in the path. This approach is typically used in cases where the number of features is very large. For the Lasso model at the Belmullet site, the MSE of the model rapidly reduces across all folds as alpha value decreases. Particularly apparent in the plot is that the MSE is hugely different across the folds initially; highlighting the value in repeated crossfold validation. The mean square error is effectively minimized in this case for (-log) alpha values above 4.5.

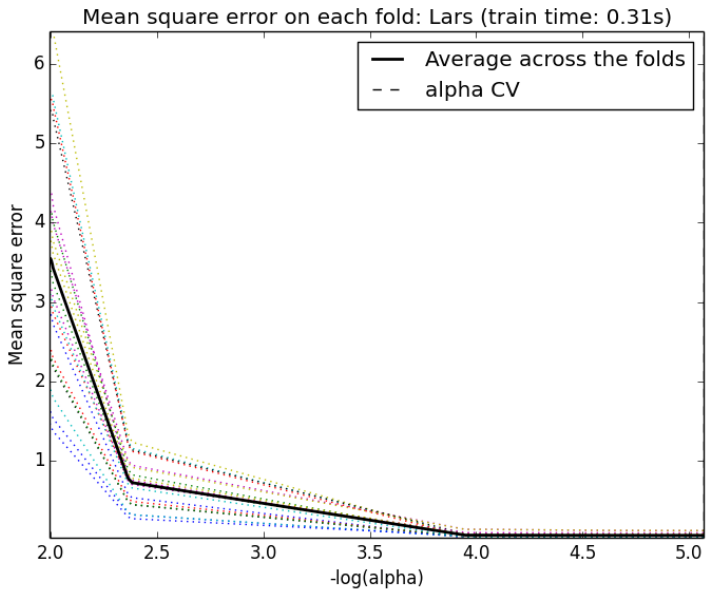


FIGURE 33: LARS SELECTION OF OPTIMAL ALPHA PARAMETER

For this case, the LARS method provides a quicker approximation of the alpha value than the coordinate descent approach. Given its similarity to the Lasso model, the LARS approach is most applicable to the determination of the alpha value for use in a Lasso model.

Despite the variety of options for the selection of the alpha parameter, there is a need to have an automatable, repeatable and transparent metric by which to assess the best regularization of the model. To implement this in an achievable way, the selection of alpha parameters has ultimately been made using repeated holdout for regression and training the model to minimize the MSE parameter.

3.3.9 Parameter Selection

Typically, in the formation of the ML model, feature selection would be left entirely to results of the repeated testing. However, the need to manually intervene and select parameters arises when there is a need to have a generally applicable model which will have a known subset of input parameters which have been determined to be important a-priori. In this case the parameters that will typically be available are known, as well as which of these are likely to influence the prediction of energy

period. Preliminary parameter selection was performed by means of Lasso path analysis, which was run on the entire dataset. This analysis allowed a thorough examination of the parameters which affected the prediction of T_e.

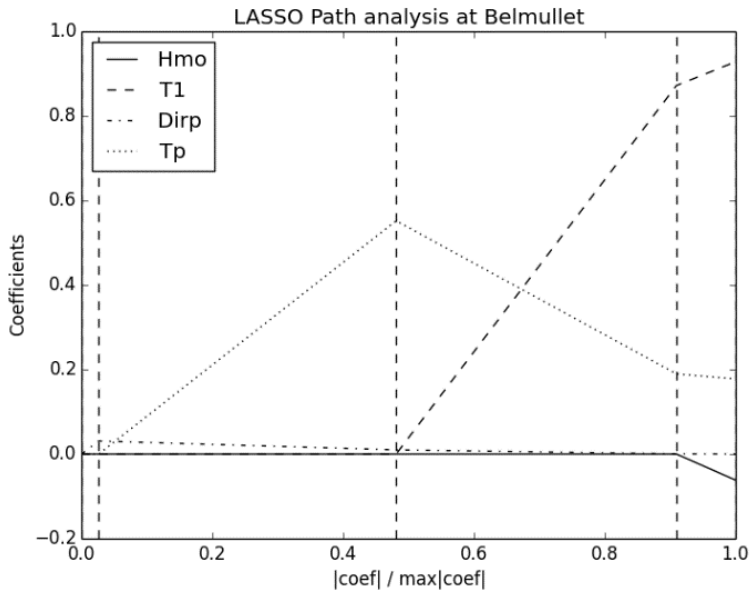


FIGURE 34: LASSO PATH COEFFICIENT ANALYSIS FOR BELMULLET DATASET

Figure 34 shows the Lasso coefficients for a reduced subset of the most commonly available parameters, as the standardized tuning parameter $s = \frac{t}{\sum_1^p |\hat{\beta} j|}$ is varied. At s = 1 (right-hand-side of x-axis in Figure 34), these are least squares estimates, and moving left on the plot indicates a reduction of the coefficients, $\hat{\beta} j$, which decrease to 0 as s → 0. At the first step it identifies the variable most correlated with the response. Least Angle Regression then moves the coefficient of this variable continuously toward its least squares value of error. Additional parameters are introduced as indicated by the vertical dashed lines along the x-axis. As soon as another variable equals the existing variable in terms of correlation with the residual, the second variable then joins the active set and their coefficients are moved together in a way that keeps their correlations tied and decreasing. This process is continued until all the variables are in the model, and ends at the full least-squares

fit. This Lasso path analysis helps to identify the parameters which have the greatest influence on producing an accurate prediction.

T_1 and T_p have the highest influence as coefficients throughout the range of tuning parameters, while the influence of H_{m0} becomes apparent only as $s \rightarrow 1$. Dashed vertical lines denote the introduction of new parameters to the model. The identification of parameters with a high influence on the predicted value is merely one aspect of the selection of parameters. Domain expertise must be utilized to ensure that the results are useful and applicable to real world scenarios in which the model would see deployment. The utilization of a limited set of parameters informed by domain expertise in this fashion allows the selection of a smaller number of parameters which will typically be sufficient to get satisfactory results, while lowering the computational requirements for wave models producing this data. The results are summarised in Table 3 below. Note that the Bretschneider and Constant Wave Period methods continue to rely on a single parameter relationship and are thusly not affected by the parameter selection ongoing in the ML model. However, given that the dataset which is used for testing is randomly assigned, the values vary with each repeated holdout test. The result of each analysis type has been included for each parameter selection to ensure that no large discrepancy in predictability of the dataset exists. It can be seen, however, that the results are quite repeatable despite the varying partitioning and random selection of elements from the dataset.

TABLE 3: MEAN SQUARE ERROR FOR REPEATED HOLDOUT ANALYSIS OF PREDICTORS AS FEATURE SELECTION FOR ANALYSIS AT BELMULLET

Model	Parameter Selection for ML Model			
	T_1	H_s, T_1	H_s, T_1, T_p	H_s, T_1, T_p, D_p
ML	0.13006	0.13037	0.06341	0.06385
CWPR	0.15194	0.15107	0.15300	0.15089
BRET	0.31557	0.31424	0.31701	0.31453

Using T_1 alone as a predictor results in a MSE of 0.13. This improves upon the performance of the CWPR and BRET models. The addition of H_s as a predictor does not produce a significant benefit in terms of MSE. However, based on the Lasso path analysis in Figure 34 there is a suggestion that the benefit to the inclusion of H_s for prediction appears at greater H_s values/coefficient values, with H_s negatively

correlated with the predicted T_e value; suggestive of a physical limit – such as the limiting wave steepness, whereby the importance of H_s for the prediction increases for increasing H_s.

The addition of T_p was found to provide significant benefit to the prediction of T_e values, in this case resulting in a MSE of 0.06341 for the ML model, 50% less than that of model using only T_1.

No significant benefit was derived from the addition of peak direction as a predictor. However, the Lasso path analysis shows that the influence of the parameter is almost immediately removed from the prediction and thus has no negative bearing on the MSE of the T_e estimate.

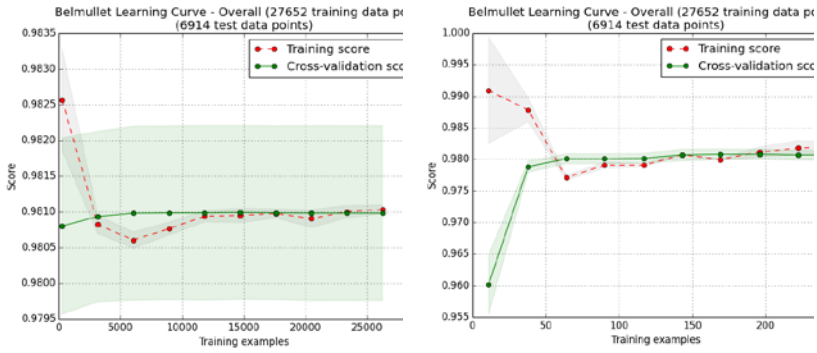
Therefore, the determination of the parameter selection is that H_s, T_1, T_p and D_p should be used where available to minimize mean squared error, and these wave parameters represent a sufficient set upon which to generate an ML model.

3.3.10 Learning Curve: Analysis of required training time

To determine the time required to train the ML model, a learning curve analysis has been performed. The learning curve displays the accuracy score of the model against the number of training examples. The score is determined both for the direct analysis of training data, and as an average of cross-validated results across 10 data folds. This method gives additional insight that allows us to see the rate of learning for data which may be heterogeneous (training score) and for data that is more likely to be discrete (cross-validation score). This has been performed across the entirety of the dataset and additionally for a 10x restricted subset. There are two questions at play; what is the required duration of data recording to achieve sufficient accuracy, and what is the effect of seasonality and short buoy deployments on the training of the model?

The learning curve analysis will additionally inform the benefit that can be derived from additional training data; and whether the estimator suffers more from variance or Bias Error. Learning curve analysis utilising the Naive Bayes classifier estimation is shown for the Belmullet dataset in Figure 35 below. The training score and cross-validation score can both be classified as very good. The shape of these curves is typical of more complex datasets - the training score is initially very high and

decreases (as the likelihood of highly correlated data decreases), while the cross-validation score increases with increasing data. As the number of elements in each fold of the cross-validation array increases. The high value to which both training and testing data converge in this instance is indicative of good model fit.



A B

FIGURE 35: NAIVE BAYES CLASSIFIER LEARNING CURVE FOR BELMULLET DATA. NUMBER OF CROSS-FOLDS =10

A. TEST DATA SIZE FROM 0 TO 27652 DATAPOINTS

B. TEST DATA SIZE 10 TO 250 DATAPOINTS TO SIMULATE LESS AVAILABLE TRAINING DATA

Figure 35b displays the naive Bayes classifier estimation for a reduced number of samples, simulating a reduction in available training data. The primary effect is that the variance in the training score is increased, while the cross-validation initially exhibits a lower score than in Figure 35a. at 0.96; subsequently stabilising at 0.98 after approximately 60 training examples.

It appears that with cross-validation, approximately 150 data-points are sufficient to appropriately validate the model to a cross-validation training score >0.98. At half-hourly data collection interval for a Waverider buoy, this would appear to indicate that an accurate approximation of WPRs could be obtained in as little as 75 hours of data collection. However, it must be noted that this does not match with the continuous recording duration that would be needed to achieve this fit. In practice,

due to the natural clustering of correlated sea conditions, it is likely to take much longer. In Section 3.3.11 the impact of training the model on consecutive data is analysed through analysis of contiguous sections of data derived from each season.

3.3.11 Seasonal variability

The effect of seasonality in biasing the learning of the ML and other models is important to quantify. The following table provides a breakdown of the respective capture periods of the buoy deployments:

Season	Start No	End No	Start Date	End Date	Notes
Winter	2767	7000	01/11/2012 00:21	31/01/2013 9:21	
Spring	7001	10985	01/02/2013 00:21	30/04/2013 23:51	
Summer	10986	15224	01/05/2013 00:21	31/07/2013 23:33	
Autumn	15225	19321	01/08/2013 00:04	31/10/2013 22:03	
Winter 2	19322	22025	01/11/2013 00:33	25/01/2014 03:53	Data gaps / Timestep changes

TABLE 4: DATA RECORD DETAILS BY SEASON FOR BELMULLET BERTH A DATASET

The primary aim of this investigation is to determine the suitability of data gathered in a single season for providing a prediction for the entire year/entire dataset. This has a particular focus on data gathered solely during summer months, as many deployment campaigns select this time due to ease of deployment and retrieval.

This analysis will be performed in a Leave One Out Cross-Validation (LOOCV) fashion, with the models' calibrated based on data for a given season, then used to predict the wave period relationship for the remaining data. This approach ensures that prediction on the training data does not take place, which would artificially inflate the estimate of model accuracy; and that there is no resulting bias to the accuracy measures of the predictions.

Often, due to weather conditions, battery life, and access constraints, buoys are deployed for a limited duration (Gorman, Bryan and Laing, 2003) (Zheng *et al.*, 2016) It is important, therefore, to examine the changes in WPR across months and in harsher and calmer conditions. The Belmullet dataset exhibited a different T_{01}:T_e WPR for the Spring months in particular, with a ratio of 1.1865, it distances itself from the other months which carry an average ratio of 1.163. Using a CWPR approach and training using this data will thus clearly result in a large Bias error. A key advantage of using an ML based model that is evident here is its ability to negate this issue by adapting to the changing conditions without additional user input.

The following work attempts to quantify the ability of the model to learn based on limited training data for each season; with the primary aim of this investigation being the determination of the suitability of data which is gathered predominantly in a single season for providing a prediction for the entire year. The four seasons are independently analysed as if they were the sole source of training data to discern the potential effect on MSE, Bias and Wave Period Ratio. This additionally allows for an analysis of the model training time when using contiguous data, rather than random cross-validation segments which may be spread throughout the dataset. Prior to this analysis it will be useful to examine the WPR variability at the Belmullet site by season.

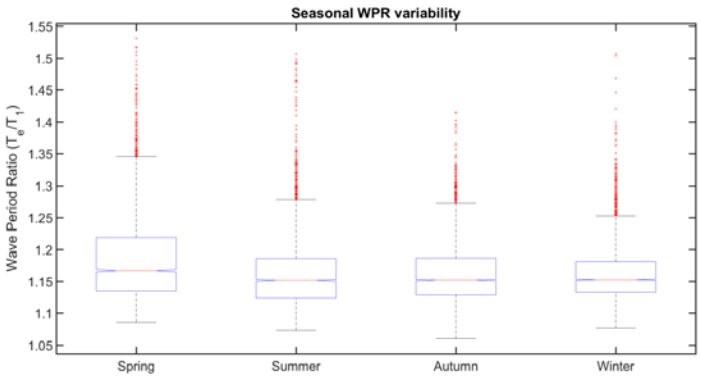


FIGURE 36: SEASONAL T_E/T_1 WAVE PERIOD RELATIONSHIP AT BELMULLET

Looking at the 95% confidence intervals; these being defined by the outer extents of the blue lines at the top and bottom of each box, there is clearly a greater degree of variability in both the Spring and Summer data than for the Autumn and Winter seasons. The effect of this variability will be investigated in the forthcoming analysis.

3.3.11.1 Winter

Beginning with an analysis of the model behaviour when trained exclusively on winter data, the model is used to predict the T_e period for the other three seasons of available data. The ML model appears to perform very well, with low MSE and Bias values, though an increase in Bias error is found as a direct consequence of the reduction in training data available.

TABLE 5: ERROR METRICS FOR WINTER TRAINED WAVE PERIOD ESTIMATION MODELS.

Metric	Machine Learning Model	Constant Wave Period Ratio Model	Bretschneider Derived Relationship
Mean Square Error	0.07295	0.15459	0.31084
Bias	-0.36555	1.24945	1.55446

Given that the determination of the WPR by both the CWPR and BRET models is based on a mostly constant factor, it is unsurprising that the Mean Square Error metric does not suffer much in the seasonal LOOCV approach. The MSE for the machine learning model worsens by approximately 0.01 versus using the entirety of the dataset. The bias of the ML model remains low with the SLOOCV approach, while the CWPR and BRET models suffer more through inaccurate determination of the WPR and spectral relationship. The WPR for $T_1 : T_e$ has been determined to be 1.1641 for the winter Months, which is in line with the yearly average value.

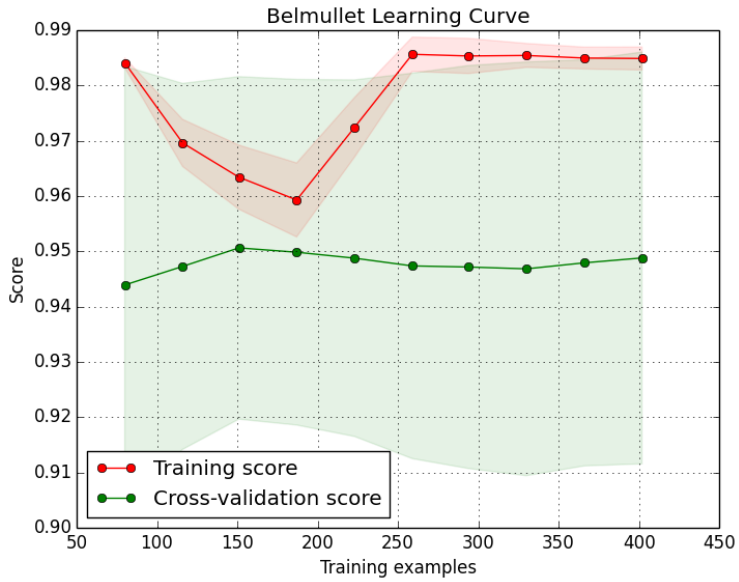


FIGURE 37: WINTER TRAINED LOOCV LEARNING CURVE FOR BELMULLET

The effect of the limited data capture duration is evident in the analysis of the winter-trained model, with larger uncertainty in the confidence of the model score (MSE determination) when compared to training on all months.

3.3.11.2 Spring

Next, the model was trained exclusively on spring buoy data, and subsequently tested on the remainder of the data. For this case, the MSE error of the ML model is relatively unchanged, while the Bias suffers significantly. For the CWPR approach, the MSE worsens from ~0.150 to 0.188, while the Bias improves slightly over the winter trained result; to 1.118. The advantage of the Machine Learning model is clear here, as it is able to adapt to site specific conditions, and will be able to adapt to varying conditions throughout the year, rather than relying on a fixed conversion factor. The Bretschneider-derived relationship approach sees a small decrease in MSE over both the yearly (randomised) dataset selection and the winter-trained data. The CWPR value was determined to be 1.187 for the spring data, and the variation in this from the yearly average value is likely the contributing factor in altering error metrics for the two constant wave period ratio approaches. The Machine Learning model,

meanwhile, likely suffers due to the lack of a diverse range of wave conditions – preventing it from learning the characteristics associated with the WPR at higher wave conditions.

TABLE 6: ERROR METRICS FOR SPRING-TRAINED WAVE PERIOD ESTIMATION MODELS.

Metric	Machine Learning Model	Constant Wave Period Ratio Model	Bretschneider Derived Relationship
Mean Square Error	0.07662	0.18800	0.28103
Bias	-0.72630	1.11828	1.55446

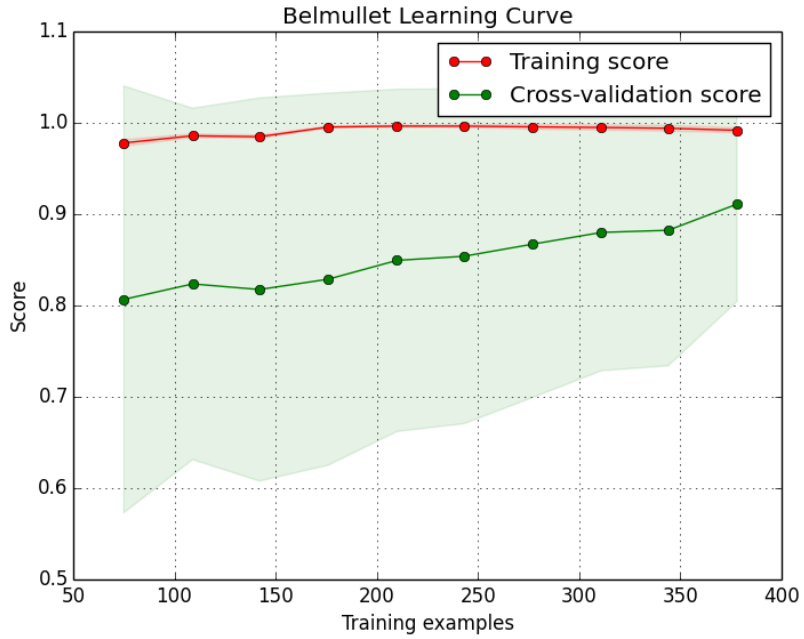


FIGURE 38: SPRING TRAINED LOOCV LEARNING CURVE FOR BELMULLET

The learning curve for the spring dataset is anomalous in that the training score is particularly low. The confidence intervals for the cross-validation score are very large, possibly owing to wide variation in the relationship between wave parameters during the spring portion of the dataset. The variability of the WPR, seen in Figure 36, provides some explanation for the reduced performance of the model. The spring

data has the widest confidence intervals, and contains a large number of outliers occurring above the 1.35 $T_e : T_{01}$ ratio. This effectively increases the difficulty for the model in predicting the correct WPR. The model score is low at ~0.8 at 75 training examples, rising to just over 0.9 at 375 training examples. This season is the lowest performing of all tested, and it indicates that Spring may be a poor time for buoy deployment if the goal is to be able to predict the wave period relationships throughout the year; with the caveat being that there is also a significant benefit to other areas of site characterisation in capturing this variability information.

3.3.11.3 Summer

When trained during summer months, there is a moderate increase in the MSE of the ML model over utilising the entire dataset. The Bias, however, is very significantly reduced compared to training in any of the other seasons. The CWPR and Bretschneider approaches perform in line with what has been seen from training on the entire dataset.

TABLE 7: ERROR METRICS FOR SUMMER-TRAINED WAVE PERIOD ESTIMATION MODELS.

Metric	Machine Learning Model	Constant Wave Period Ratio Model	Bretschneider Derived Relationship
Mean Square Error	0.093790	0.157986	0.32986
Bias	-0.127161	1.250567	1.55446

The Constant Wave Period Ratio value was determined to be 1.162 for the summer dataset, which is in line with the average value exhibited at the Belmullet site throughout the year.

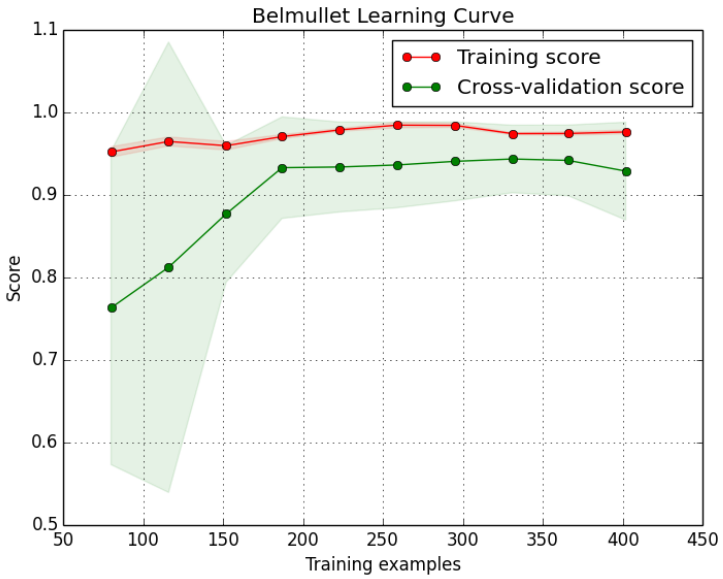


FIGURE 39: SUMMER TRAINED LOOCV LEARNING CURVE FOR BELMULLET

The learning curve for Belmullet when trained on summer data exhibits wide confidence intervals where a low number of training examples are used. This may be attributable to generally calm and benign conditions which do not exhibit much variation in H_s, but bring with them a highly variable WPR – typical of summer months. The model does successfully achieve a cross-validation score in excess of 0.9 after 150-200 training examples, showing that an extended training duration is capable of compensating for the increased variability in WPR.

3.3.11.4 Autumn

Training the model exclusively in autumn results in a very slight increase in MSE for the ML model; while the Bias error result achieved is amongst the lowest of all seasonal training period options tested. The CWPR and Bretschneider derived approaches also fall broadly in line with the error metrics when training is performed on the entire dataset.

TABLE 8: ERROR METRICS FOR AUTUMN-TRAINED WAVE PERIOD ESTIMATION MODELS.

Metric	Machine Learning Model	Constant Wave Period Ratio Model	Bretschneider Derived Relationship
Mean Square Error	0.08258	0.15919	0.32772
Bias	-0.15632	1.25255	1.55446

The Constant Wave Period ratio value was determined to be 1.162 for the Autumn Dataset, in line with the overall average of the entire dataset.

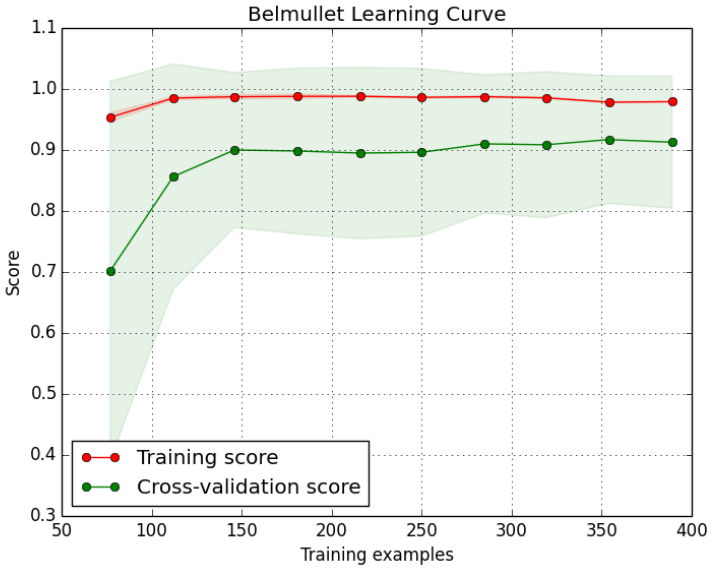


FIGURE 40: AUTUMN TRAINED LOOCV LEARNING CURVE FOR BELMULLET

The learning curve when using Autumn training data shows very broad confidence intervals for the Cross-Validation score, reaching below 0.40 for 75 training examples. This rapidly improves as more training data is added, achieving an average 0.9 training score, with a lower-bound confidence interval of 0.78 after just 150 training examples.

3.3.11.5 Overview of seasonal effect

There is a significant variation in the model's learning ability at the Belmullet site based on the season from which data is obtained. Figure 41 displays the learning curve for the entirety of the seasonal data at Belmullet. Here, the learning curve data has been truncated to 1/10th of the dataset to better display the learning progression. There exists a significant difference in the training and cross-validation scores across all seasons used as training data examples. The training score for the winter dataset peaks at 0.985, with a trough at 0.960. The cross-validation score increases from 0.945 at 75 data-points to 0.950 at 150 data-points and remains relatively stable beyond this. The training score for the spring period is high due to the relatively changeable WPR. The cross-validation score improves consistently as more data points are examined, reaching just above 0.900 at 375 test data points.

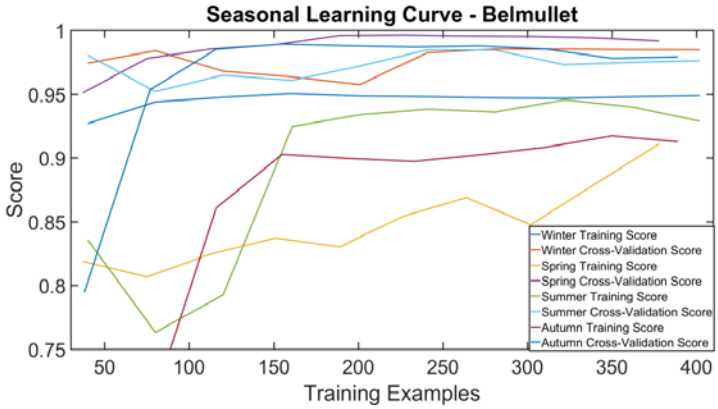


FIGURE 41: LEARNING CURVE FOR BELMULLET SEASONAL DATA

The summer training score varies between 0.950 and 0.980 across 400 data points. The cross-validation score stabilizes beyond 200 data points at a level of approximately 0.930. Rather anomalously, the prediction accuracy of the model when trained on the Autumn data is very high for the training dataset, while the cross-validation score is very low below 150 data points, and does not increase markedly beyond 0.9. A plausible explanation for the effect of the WPR variability, as well as the variety of conditions "seen" in the training data on the model's predictive ability have been discussed alongside the results for each individual season; with the

broad consensus being that the winter months provide the best opportunity for training the model to predict WPRs throughout the remainder of the year.

3.3.12 Error Assessment for Seasonal LOOCV approach

Through the Seasonal Leave-One-Out Cross-Validation (SLOOCV) approach, we can estimate the required duration of deployment to appropriately train a ML model for wave parameter conversion. There are notable differences amongst the seasons where learning time is concerned. The winter data stands out as providing the quickest learning, while summer and autumn conversely display the worst results; with low cross-validation scores. The frequent storm conditions, and greater variance in conditions during winter, is thought to be instrumental in this rapid learning. Additionally, it has been shown by (Cahill, 2014) and others that the relationship between wave parameters becomes more defined and less variable in larger, fully developed sea-states; much as sea spectra such as the Pierson-Moskowitz rely critically on the assumption of a fully developed sea.

TABLE 9: MEAN SQUARE ERROR FOR LOOCV SEASONAL EVALUATION OF MODELS AT BELMULLET

Model	*Seasonal Training Effect*			
	Winter	Spring	Summer	Autumn
ML	0.07295	0.07662	0.09379	0.08258
CWPR	0.15459	0.18800	0.15799	0.15919
BRET	0.31084	0.28103	0.32986	0.32772

TABLE 10: BIAS ERROR FOR SEASONAL LOOCV EVALUATION BY BIAS ERROR OF MODELS AT BELMULLET

Model	*Seasonal LOOCV*			
	Winter	Spring	Summer	Autumn
ML	-0.36555	-0.72630	-0.12716	-0.15632
CWPR	1.24945	1.11828	1.25057	1.25255
BRET	1.55446	1.55446	1.55446	1.55446

The MSE and Bias Error are detailed above for each of the 3 models: ML, CWPR and BRET. Table 9 displays MSE across all seasons. For the ML model, winter training provides the best MSE at 0.073, while this worsens to 0.094 when the model is trained on summer data only. For the CWPR model, winter training resulted in an

MSE of 0.155, while spring training resulted in an MSE of 0.188. The spring period had a WPR of 1.187, which was significantly higher than the average of 1.163 throughout the remaining seasons; and this is likely to have contributed to the increased error. Table 10 gives the Bias Error for each model across all seasons. The bias for the CWPR and BRET models, based on a constant factor, remain relatively consistent across all seasons, with little variation. The CWPR method, which exhibited the poorest seasonal result in spring, sees its best Bias Error result in spring, at 1.118.

Most notably, while there is little to separate the models given the MSE results shown, the difference in Bias Error shown in Table 10 is considerably larger, and displays a key advantage of the ML model. Bias of upwards of 1.5 seconds has the potential to significantly impact the energy prediction accuracy of the model, whereas the ML performs markedly better than either the CWPR or BRET approaches according to Bias Error, with the largest bias being -0.72630 in spring.

Given that the determination of the WPR by both the CWPR and BRET models is based on a mostly constant factor, it is unsurprising that the MSE metric does not suffer much in the seasonal LOOCV approach. The bias of the ML model remains low with the SLOOCV approach, while the CWPR and BRET models suffer more through inaccurate determination of the WPR and spectral relationship.

3.3.13 Prediction accuracy

To verify the analysis performed in the Sections above, the accuracy of the three models when predicting on an unseen dataset has been characterised according to MSE, RMSE, Bias, MAE, Max error and R^2 correlation coefficient. Below are the model performance results after repeated cross-validation, utilising the entirety of the unseen testing dataset, which represented 6914 data-points, corresponding to a recording period of approximately 144 days. This served as an approximation of a real-world implementation of the ML model.

TABLE 11: MODEL ERROR COMPARISON FOR BELMULLET (TEST) DATASET.

Model	MSE	RMSE	Bias	MAE	Max Error	Rcorr
ML	0.0641	0.2532	0.0031	0.1889	1.9482	0.9903
CWPR	0.1536	0.3919	-0.0326	0.2965	2.751	0.9802
BRET	0.3151	0.5614	0.4272	0.4364	3.1551	0.9802

The ML model is superior in every tested error metric, providing more accurate results than either the CWPR or BRET based approaches. In particular, the MSE metric is adept at highlighting the improvement in accuracy that is possible using an ML based approach. Where the ML model is trained for a sufficiently long period of time, the bias in the prediction approaches 0. The MSE achieves a very low value of 0.0641.

3.3.14 Prediction accuracy for energy production

The performance of the models was next evaluated in a typical Wave Energy Development scenario, undertaking a calculation of energy prediction using a device power matrix in combination with the test data timeseries corrected by the respective models. The actual power consumption determined using the correct values of T_e in the dataset was 6.4618 x 10^5 kWh, while the results using the 3 models are displayed below.

The power production was determined using a device power matrix which specified a power output for a given (H_s,T_e) Tuple according to the formula:

$$\sum P_{i,j}(x) = \frac{1}{2}\sum {H_{s_i}}^2 \times T_{e_j} \tag{3.23}$$

TABLE 12: MODEL PREDICTION ACCURACY: ESTIMATING 5 MONTH ENERGY.

Model	Power Production (kWh)	Power Production Error (kWh)	Power Production Error (%)
ML	6.4775 x10^5	1.5743 x10^3	0.24
CWPR	6.1658 x10^5	-2.9597 x10^4	4.58
BRET	6.9535 x10^5	4.9174 x10^4	7.61

For the test dataset, representing approximately 3500 hours of sea time, the ML model had the lowest power production error. This serves to highlight the improvements that can be made using the ML model that may not be made immediately obvious by standard error metrics alone, and represents a significant improvement in the ability to accurately characterise the energy production at the Belmullet site.

3.3.15 Detailed comparison of model error

As a final examination of the prediction characteristics of the three model approaches, the performance of the three models was explored across the range of period test values. In Figure 47 & Figure 48, A histogram of the occurrence of values in each bin is present on the leftmost y-axis as a guide to the relative importance of the accuracy of prediction at that test value. The Bias/SE of the models occupies the rightmost axis.

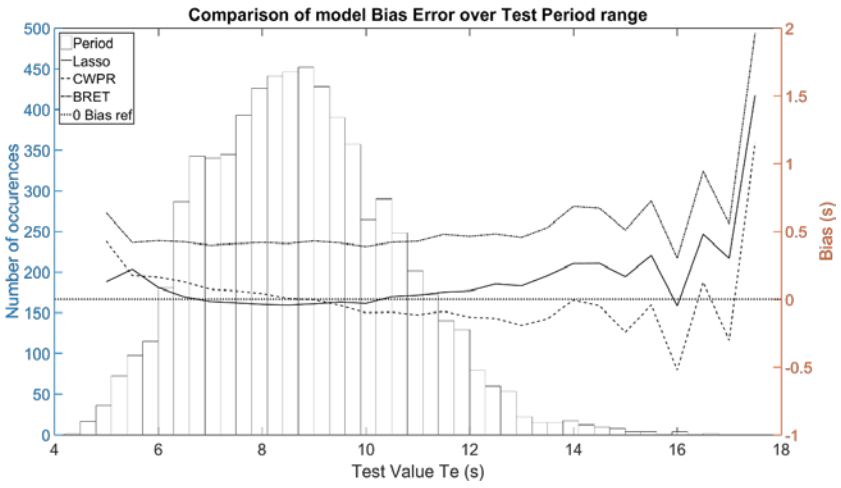


FIGURE 42: COMPARISON OF MODEL BIAS ERROR ACROSS TEST PERIOD VALUES. HISTOGRAM OVERLAID REPRESENTING DATA AVAILABILITY FOR EACH BIN OF TEST VALUE

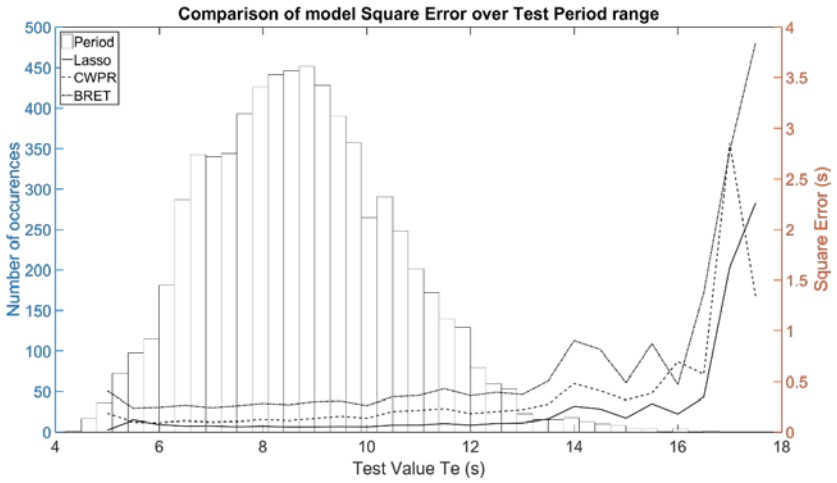


FIGURE 43: COMPARISON OF MODEL SQUARE ERROR ACROSS TEST PERIOD VALUES. HISTOGRAM OVERLAID REPRESENTING DATA AVAILABILITY FOR EACH BIN OF TEST VALUE.

The Lasso model performs best across the entire range of test values, followed by CWPR and BRET models. The divergence in accuracy of the models as measured by Square Error becomes particularly apparent beyond 14 seconds. Beyond 14 seconds, the CWPR and BRET based models begin to perform poorly, whereas the Lasso model maintains a significant advantage in all cases where sufficient data is available. The BRET model exhibits high Bias Error throughout the range of test values, demonstrating that the wave period relationship suggested by the Bretschneider spectrum is not especially applicable to this location during this time period.

3.4 Test Case 2

3.4.1 Killard Point Introduction

To provide further validation for the model and prove the wider reach of its applicability, the procedure documented above was repeated for the Killard Point Site (Section 2.1.1.3) in County Clare. Data was obtained through partnership with ESB, and provided in the form of Waverider ".his" files, spanning the period: 19-11-2011 to 30-4-2014 at three separate locations. The results of testing and validation on deployment location 3 (situated at 52.774 ° Lat, -9.5865 ° Long) are presented here. This dataset represents the longest unbroken deployment at the site, spanning 15-10-2013 to 30-04-2014 (9286 data-points at half-hourly intervals). Buoy data was obtained, and pre-processing was performed to remove the influence of erroneous

and missing values, and to provide a single cohesive dataset. In addition, the dataset was synchronised with a 24 year hindcast dataset produced by a MIKE 21 SW model which contains hourly output data. This resulted in an additional timestep occurring each hour for the buoy data. This was produced using a standard linear interpolation approach.

Similar to the Belmullet location, Killard Point faces the full force of the Atlantic Ocean. The buoy was located in 33-35m water depth, considerably shallower than the placement of the Belmullet buoy. As a result of the seasonal distribution of the buoy deployment, and the directional sheltering at the site, the average T_1 period is approximately 1.5 seconds higher for the duration of the Killard Point deployment, with a greater standard deviation. The mean H_{m0} condition for the Killard point deployment was 3.6m, indicative of considerably more energetic conditions than the 2.89m mean H_{m0} at Belmullet.

3.4.2 Model Development

The model development process was more involved for the Killard Point site than the approach taken for the Belmullet site in the work contained above. The key differentiator in the approach was that the Belmullet approach was performed in-situ on a single dataset, which was sub-divided using train-test sets and cross-fold validation to provide both the training data. For the Killard Point site, however, there was an additional requirement to correct the full hindcast dataset produced as part of the modelling exercise in Chapter 5. The Killard point hindcast dataset does not contain a T_1 or T_e period, and it is therefore necessary to generate this information by calibrating with the buoy dataset.

The additional requirements were therefore addressed by introducing a Three-Stage model with the following workflow:

- The model generates a T_1 estimate from the MIKE21 data, using the relationship between T_1 and T_z derived by learning from concurrent buoy and model data.
- An estimate of the equivalent buoy T_e value is generated using all model parameters available and the generated T_1 values from the first step for the model dataset, which has been synchronised with the available buoy data.

- T_e is predicted for the entire hindcast dataset using all model parameters with the addition of the corrected model T_1 information.

The result is a full hindcast dataset containing T_1 period data which has been corrected based on the buoy data available, and T_e period data for the entire hindcast which has been corrected based on the model trained on the corrected $T_1 : T_e$ relationship at each of the deployments.

3.4.3 Parameter Selection

A number of input parameter combinations were trialled to determine the impact on the accuracy of the model predictions. These parameter combinations were primarily selected based on an assessment of the most likely available wave data for a Waverider or similar buoy deployment.

TABLE 13: MEAN SQUARE ERROR ASSESSMENT FOR KILLARD POINT USING H_s, T_1 PARAMETERS

Parameters	Machine Learning Model	Constant Wave Period Ratio Model	Bretschneider Derived Relationship
T_1	0.13006	0.15194	0.31557
H_s,T_1	0.13037	0.15107	0.31424
H_s,T_1, T_p	0.06341	0.15300	0.31701
H_s,T_1, T_p,Dir_p	0.06385	0.15089	0.31453

It is clear that both T_1 and T_p are integral to the ultimate accuracy in the prediction of T_e. T_p significantly improves the Mean Square Error in the prediction of T_e, while H_s does not significantly impact the prediction accuracy of the model as originally expected. It is possible that in cases where limiting steepness is a factor that the H_s would provide additional information about the wave period relationship, but this is not the case in general. Going forward, all typically available input parameters (H_s, T_1, T_p, Dir_p) are fed to the model to achieve the most accurate prediction.

3.4.4 WPR analysis at Killard Point

An analysis of WPR was conducted at Killard Point to determine what differences, if any, existed between the deployment locations and the effect of seasonality on the WPR and its variability.

TABLE 14: T01/T02 WAVE PERIOD RATIO AT KILLARD POINT DEPLOYMENTS

WPR by Deployment	DL1	DL2	DL3	All Deployments
Min	1.0795	1.0446	1.0634	1.0446
Max	1.2259	1.5356	1.4329	1.5356
Average	1.1241	1.1271	1.1403	1.1338
Standard Deviation	0.0202	0.0481	0.0422	0.0433

Table 14 above shows some that noticeable differences exist in the wave period relationships across each deployment location. To assist in processing the significance of the variation between locations, it is useful to know that the recording time-periods differ for each of the deployment locations, introducing an additional affect due to seasonal variation of wave conditions.

A seasonal bias is evident in the recordings. Despite the spectral parameter history consisting of almost a full year of wave records, the deployments took place predominantly during autumn, winter and early spring which typically represent the most energetic conditions. While this represents an intelligent deployment selection for the determination of accessibility, survivability and extreme wave survival for wave energy devices at the site, it influences the variability of the conditions experienced at the site and may have an impact on the relationship of WPR determined. The Killard Point deployments covered the following time periods:

TABLE 15: KILLARD POINT BUOY DEPLOYMENT SUMMARY DETAILS

Deployment	DL1	DL2	DL3	All Deployments
Start Date	19/11/2011	23/08/2012	15/10/2013	-
End Date	13/01/2012	12/12/2012	30/04/2014	-
Duration	1323.5 hrs	2657.5hrs	4742.5hrs	8723.5
No. of records	2647	5315	9485	17447

Deployment location 1 covers a particularly energetic period from November to January, Deployment Location 2; August to December, and Deployment Location 3; October to end of April.

The maximum WPR varies significantly across the deployments, with DL1, which experiences the most energetic wave conditions – with an average Hm0 of 4.57m and a maximum of 11.42m, having a notably lower maximum WPR than Deployment Location 2 and 3, with average Hm0 values of 2.42m and 3.46m respectively. This trend is indicative of another physical limit of wave period ratio which occurs at higher values of H_{m0} and T_{01}/T_{02}. It makes intuitive sense that there is less room for variation at the upper extremes of wave height and period, but this will be further investigated in Section 3.4.4 and the occurrence binned value approach to determining WPR (Section 3.4.8).

The average WPR is broadly the same across each of the deployments, with a minimum of 1.124 Maximum of 1.140, with a resultant average of 1.134.

The minimum WPR is also broadly similar, bounded at 1.045 and 1.080 for the lower and upper limits respectively, with an average across all deployments of 1.045. This indicates that there seems to be a physical "limit," to the lower bound relationship between the respective wave period parameters.

It was necessary to determine the T_e/T_{01} relationship to provide an accurate estimate of T_e using the modelled wave data. To provide an initial estimate for the T_e/T_{01} relationship, the series of 17210 data points, covering the three deployment locations was analysed, dividing each successive T_e entry by the corresponding T_{01} entry. This resulted in an average WPR of 1.1762, with a minimum of 1.0668 and maximum of 1.8276.

This average WPR was used as a linear multiplier to produce an estimate of T_e from the T_{01} record in the output of the Mike21 dataset.

TABLE 16: T_E/T_{01} WAVE PERIOD RATIO AT KILLARD POINT DEPLOYMENTS

WPR by Deployment	DL1	DL2	DL3	All Deployments
Min	1.0939	1.0706	1.0668	1.0668
Max	1.3826	1.8118	1.8276	1.8276
Average	1.1577	1.1858	1.1760	1.1762
Standard Deviation	0.0299	0.0758	0.068	0.0668

It is evident that the relationship between T_e/T_{01} differs from that of T_{01}/T_{02} by location. The highest average ratio occurs at DL2 for T_e/T_{01}, whereas the highest average T_{01}/T_{02} ratio occurs during the DL3 deployment. The variance is greater for the T_e/T_{01} relationship, with a greater maximum ratio between T_e/T_{01} relative to the average WPR present. This occurs most notably for deployments 2 and 3.

3.4.5 Parameter Selection

As with the Belmullet site, many methods for determining the optimal parameter and regularisation values were trialled at the Killard Point site. Based on the information obtained during the Belmullet analysis, these were restricted to the more useful – Least Absolute Regression and Shrinkage and Lasso Path analysis.

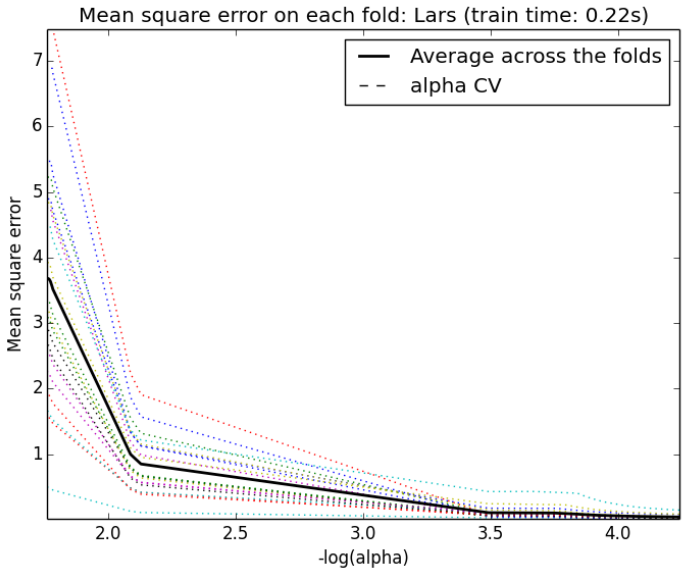


FIGURE 44: LEAST ABSOLUTE REGRESSION AND SHRINKAGE PLOT FOR KILLARD POINT TEST SITE

Analysis of the LARS path for the Killard Point site reveals that the majority of folds converge to a low MSE value rapidly, being effectively minimized at –log(alpha) value of 4.0 or above. Additionally, we see that one of the folds contains a path with 5 kinks, highlighting that certain parameters may have more predictive effect in certain conditions than others. This highlights the need to select and analyse multiple folds when determining the optimal model complexity.

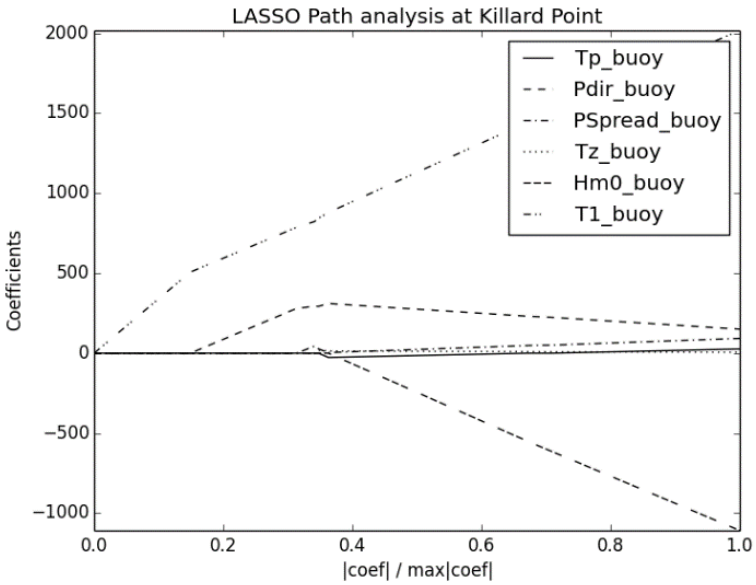


FIGURE 45: LASSO PATH ANALYSIS AT KILLARD POINT SITE

Figure 45 above shows the Lasso coefficients for a reduced subset of the most commonly available parameters. It is evident that the T_{01} parameter is the strongest predictor of T_e, while the peak direction parameter is also correlated with concurrent T_e value. As the standard tuning parameter "s," equivalent to the ratio of the coefficient to the maximum coefficient value, (shown on the x-axis), which represents the aggressiveness of the penalisation that is applied, tends towards 1, the effect of H_{m0}, suggestive of a physical limitation such as maximum wave steepness, on the prediction continues to increase, while the effect of Peak Direction begins to decrease.

3.4.6 Learning Curve Analysis

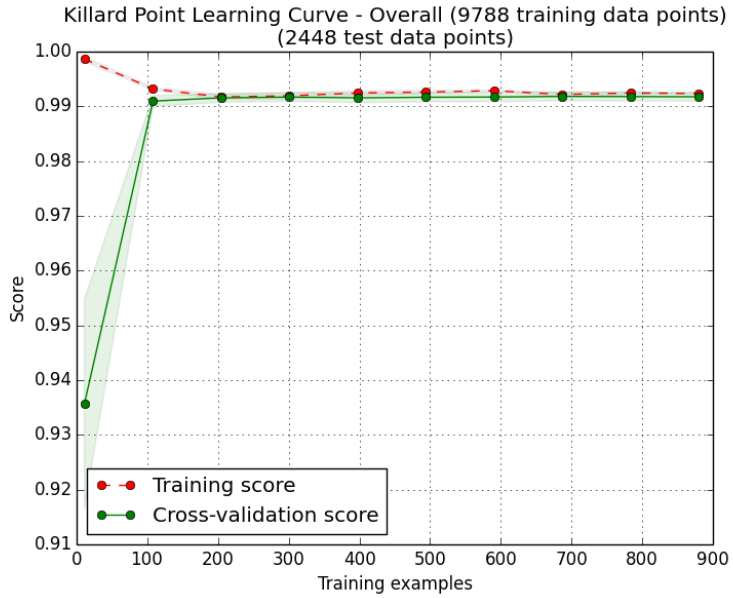


FIGURE 46: LEARNING CURVE AT KILLARD POINT. TEST SET RATIOS FROM 0.1 TO 1.0

Examining the Naïve Bayes Classifier Learning curve analysis for Killard Point in Figure 46 above, it is evident that the model learns its target rapidly, with both a training and cross-validation score in excess of 0.99 after 100 data points. The shape of these curves is typical of complex datasets, with a training score that is initially very high and decreases (as the likelihood of highly correlated data decreases), while the cross-validation score increases with increasing data. The high value to which both training and testing data converge in this instance is indicative of good model fit.

For the Killard Point site, approximately 100 data-points are sufficient to appropriately validate the model to a training score in excess of 0.99. This figure compares very well with the 75 hours of data collection found to be required with the Belmullet analysis. This serves as preliminary evidence that these results are replicable across sites on the West Coast of Ireland.

3.4.7 Error Analysis

TABLE 17: BIAS AND MEAN SQUARE ERROR METRICS PRODUCED THROUGH REPEATED HOLDOUT TESTING FOR ML, CWPR AND BRET APPROACHES

Model	Bias		MSE	
	Training Set	Test Set	Training Set	Test Set
ML	-0.0197	-0.0076	0.0293	0.0296
CWPR	-0.0621	0.0101	0.2372	0.2371
BRET	0.5112	0.5352	0.4951	0.4929

The bias and MSE Values for the ML model are extremely low, demonstrating excellent prediction performance. The CWPR method results in MSE values which are approximately an order of magnitude greater, while these MSE values approach 0.5 for the BRET model.

TABLE 18: MODEL ERROR COMPARISON FOR KILLARD UNSEEN TEST DATASET.

Model	MSE	RMSE	Bias	MAE	Max Error	R_{corr}
ML	0.0286	0.1691	-0.0015	0.1185	1.2275	0.9960
CWPR	0.2339	0.4836	-0.0553	0.3536	3.2039	0.9756
BRET	0.4922	0.7016	0.553	0.557	3.8025	0.9756

Taking the test portion of the dataset and performing additional error analysis, the skill in prediction of the ML model is further highlighted, demonstrating the lowest error metrics across all tests by a considerable margin. Additionally, examining the Mean Average Error (MAE) and the maximum error shows a clear benefit of the ML model, with greatly improved accuracy for both mean and extreme conditions. The R_{corr} value for the ML model approaches a "perfect" 1.0 result.

3.4.8 Comparison of model error across test value range.

As a final examination of the prediction characteristics of the three model approaches utilized at the Killard Point site, the performance of the three models was explored across the range of period test values. A histogram of the occurrence of values in each bin is present on the leftmost y-axis (Figure 47 & Figure 48) as a guide

to the relative importance of the accuracy of prediction at that particular test value. The Bias and MSE of the models occupies the rightmost axis. The Lasso model performs best across the entire range of test values, offering a distinct improvement over the CWPR and BRET approaches. For MSE, the CWPR and BRET based models perform relatively poorly below 7.5 seconds and above 15 seconds, whereas the Lasso model maintains a significant advantage, exhibiting very low MSE values throughout the test range. Examining Figure 48, the BRET model exhibits high Bias error throughout the range of test values, demonstrating that the WPR suggested by the Bretschneider Spectrum is not especially applicable to this location during this time period. The CWPR approach performs far better, but suffers particularly when the occurrence of conditions that it is attempting to predict are less common. The Lasso model maintains a minimal bias error throughout the test range, maintaining a bias value below 0.25 seconds even when examining conditions with fewer than 5 occurrences.

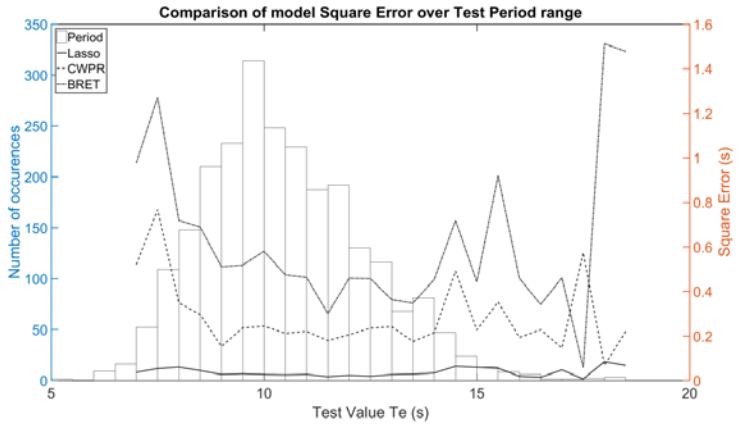


FIGURE 47: COMPARISON OF MODEL SQUARE ERROR ACROSS TEST PERIOD VALUES. HISTOGRAM OVERLAID REPRESENTING DATA AVAILABILITY FOR EACH BIN OF TEST VALUE.

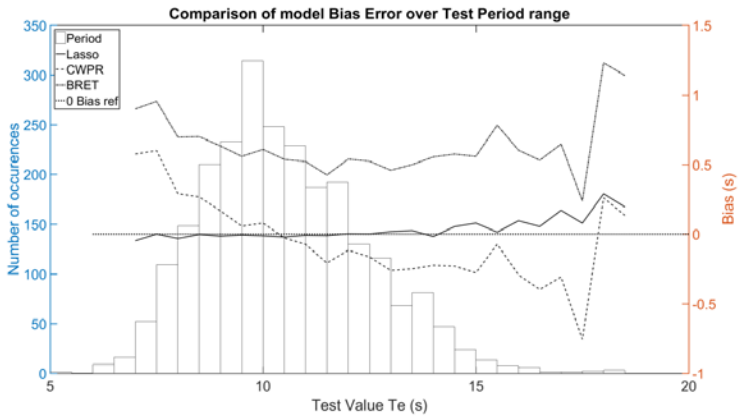


FIGURE 48: COMPARISON OF MODEL BIAS ERROR ACROSS TEST PERIOD VALUES. HISTOGRAM OVERLAID REPRESENTING DATA AVAILABILITY FOR EACH BIN OF TEST VALUE.

TABLE 19: POWER PRODUCTION ACCURACY AT KILLARD POINT

Model	Power Production (kWh)	Power Production Error (kWh)	Power Production Error (%)
ML	1.3519 x10^5	-4.8260 x10^3	-3.45%
CWPR	1.2950 x10^5	-1.0520 x10^4	-7.51%
BRET	1.8270 x10^5	4.2709 x10^4	30.50%

The improvement in power production accuracy at the Killard Point site provided by the ML model proves significant. The ML model provides approximately 4% lower absolute error than the CWPR method, and 27% lower than the BRET approach.

3.5 Conclusions

A machine learning model has been created which enhances the accuracy of wave parameter conversion and wave parameter estimation using a combination of recorded and modelled data. This model allows for improved WPR estimation, and hence greater accuracy in the characterisation of the resource available at candidate wave energy test sites. This benefit has been shown to extend to the power production estimate for WECs.

The WPR for both T_{01} : T_{02} and T_e : T_{01} has been derived for the Killard Point and Belmullet sites using both Arithmetic methods based on the history of spectral parameters, and derivations based on the Bretschneider Spectrum.

The results above demonstrate that the ML model offers significant improvement in the prediction accuracy of the T_e : T_{01} and T_{01} : T_{02} wave period relationship, and this can be used to create a more reliable assessment of Wave Period Ratio. This has a significant impact on the accuracy of wave power estimates produced using the modelled data.

This work has been conducted at two sites on the West Coast of Ireland, and has been shown to have large consequences when used in the determination of WEC power production. The main findings of this work are analysed below.

3.5.1.1 Improvement in accuracy with machine learning model over existing approaches

The prediction accuracy has shown to be much improved in the ML model in comparison to the existing CWPR and Bretschneider models, even under relatively ideal conditions for all models.

MSE, RMSE, Bias, MAE and Maximum Error are all lowest for the ML model, while it also displays the best R^2 correlation coefficient. These findings were consistent across the two sites studied, as well as at different time scales and accounting for seasonal variability.

This is perhaps best displayed in Figure 42 & Figure 43 (Belmullet) and Figure 47 & Figure 48 (Killard Point), where the extent of the ML model's predictive power is highlighted, and the lack of influence of the amount of data collected on the predictive result is evident.

3.5.1.2 Improvement in prediction of energy production

The improvement in the prediction accuracy for the model had a considerable impact on the prediction of energy production for the ML model, resulting in approximately a 4% improvement over the constant Wave Period Ratio method, and approximately a 7-27% improvement over the Bretschneider method dependant on the site. This finding is significant, and suggests that current methods used are not optimal for the prediction of energy production using an estimated T_e parameter. This improvement

in the prediction of energy production should offer a significant benefit for developers in improving the certainty of energy production at the site.

It is important to note that these results have been obtained using a power matrix that is graduated in 0.5s T_e steps. There can be significant variation in the energy production of a device across a 0.5s step, something that is discussed in detail in Chapter 6, and therefore there is potential for greater accuracy improvements depending on the power matrix granularity used, the location and the frequency of occurrence of values that are examined. Furthermore, this highlights the importance of a spectral based approach to energy production determination, which will be examined using spectral weighted basis in future work.

3.5.1.3 Learning Time required

The analysis in 3.3.10 answers a crucial question. How long a deployment is necessary to accurately train a ML model? For both the Belmullet and Killard Point sites, it has been determined that 100-150 data points (corresponding to 50-75 hours of deployment) are sufficient to train the model when the data is sampled throughout the year. To guarantee a well-trained model that is effective at predicting conditions in all seasons, an extended deployment covering all seasons is still preferable and will certainly result in reduced MSE and Bias Error. Winter months appeared to provide the quickest training for the model, and this is thought to be as a consequence of the variance in conditions, and the stability of WPRs offered by the increase in spectral energy density at a defined peak and the absence of bi-modal conditions during larger storm events.

The accuracy of the model continues to improve as more training data is used, with Bias Error approaching 0 with a sufficiently large training dataset. This is important, as it will inform the deployment strategy for new measurement campaigns at potential site locations. This learning time is far quicker than was anticipated, and should expand the potential utility of short buoy deployments when used in conjunction with this method of determining WPRs; offering large benefits in terms of time savings and easing the burden of an extended data capture campaign significantly.

3.5.1.4 Potential for use in other locations

It is important to assess these findings in the context of multiple sites. The model appeared to perform equally well at both the Killard Point and Belmullet locations, with equivalent accuracy and training times. Previous work in (Cahill, 2014) has shown significant differences in WPRs between Atlantic Irish sites and Pacific sites on the west coast of the United States. It would be useful to characterise the impact of this relationship on the learning ability of the model. This future work should assess the difference in alpha value, training time and seasonal variability between this location and the Irish coastal sites.

The work of Cahill has suggested that appropriate WPR should be calculated from measurements from a nearby buoy or wave model grid point if spectral data is unavailable at the point of interest, rather than using an assumed value from a theoretical spectrum, noting that nearby buoys returned similar WPR values despite their physical separation. Likewise, this work would suggest that the ML model would be eminently applicable to the prediction of WPRs at nearby locations, and this information could be used to improve the availability of summary statistics within the limited datasets that exist off the Irish West Coast. (M-Buoy network).

3.5.1.5 Potential for use in other ratios

There is huge potential for the application of this model to other wave parameter relationships. A crucial relationship for use in the determination of the maximum height of extreme waves is the Anomaly Index / Abnormality index (AI), which is the H_{max} : H_s ratio. (Barker and Murphy, 2015) examined the use of a linear regression model on the 95-99th percentile waves to determine the AI. This approach was required to filter the effect of large AIs at lower H_s wave heights which skewed the results, but the removal of these results resulted in lower confidence intervals for predictions at the extremes. With a Machine Learning approach, we can use more parameters and have more certainty in predictions at the extremes, without the need to introduce user bias by arbitrarily selecting only results above a defined threshold. This is just one of the many potential applications for this ML model in relation to Marine Renewable Energy. It is also possible to implement this to perform a number of other crucial tasks such as calibration of satellite altimeter data with buoy data,

giving the ability to accurately predict the conditions at the buoy site with a limited duration calibration alongside the satellite data; to correlate between adjacent or related sites and make predictions based on one dataset or to convert large scale model data to an accurate estimate for a local site, bypassing the need for intermediate WW3, SWAN, or Bousinessq modelling.

4 Extreme Wave Assessment Techniques

4.1 Introduction

Extreme wave parameters are used for engineering design in our seas and oceans to assess the survivability of structures and devices, yet the methods used to determine them are non-standardized and can give highly variable output. With increased commercial activity in the marine sector, the importance of accurate extreme wave parameter determination has become increasingly apparent. This is particularly the case for marine renewable structures where even small over-predictions in design parameters can affect the feasibility of the project. This chapter addresses the methods of extreme wave prediction currently in use, determining the optimal method for the prediction of extreme wave conditions (H_s, H_{max} and T_z) in coastal Irish waters. This work identifies pitfalls and drawbacks of current extreme prediction methods, with particular attention given to the use of buoy data with limited recording duration from coastal locations where development is to take place. In addition, a new methodology of determining extreme wave periods, that is the wave periods occurring coincidentally with the most extreme wave heights, is created.

This is important for design purposes as the energy of a wave is dependent on the wave period. The clear potential for the application of modern programming techniques to the estimation of extreme wave parameters will be highlighted, using auto-regressive techniques to quickly and accurately determine the best fitting distribution. By estimating the extreme wave energy and significant wave height, as well as performing regression analysis on the AI and Slope of wave conditions, it is possible to formulate a method to reliably estimate the wave period coincident with the extreme H_s value, as well as lending greater certainty to the prediction of H_{max} values.

Knowledge ofthe wave climate and design wave conditions isfundamental to any structural design, yet recent analyses have highlighted shortcomings in termsof the input wave data and the analysis methods, notably in the use of basic Extreme Value techniques and tools, the lack of use of covariates, and lack of application of Bayesian Inference (Jonathan and Ewans, 2013). This can impact significantly on the final design;with incorrect estimation of the design wave condition resulting in an over-

designed and expensive structure, or a structure that is unsafe. To achieve accurate predictions of extreme climate, a systematic approach must be applied to determining the factors which have the greatest influence on extreme predictions. These include parameters such as those related to the probability distribution, i.e. the shape factor and location factor, the method of curve fit chosen andthe criteria for storm event selection.

Extreme prediction methods typically rely on empirical curve fitting and extrapolating from these curves to give estimates of future conditions. These models are often used with theoretical coefficients which do not fit the distribution of the dataset well. The reliability ofa prediction made in this manner is questionable and can expose a contractor to significant risk. Further, the choice of the fit is left to the analyst, who may choose an inappropriate distribution to make the prediction. The human selection element in this analysis is sometimes undesirable, and it is prudent to have a statistical backing on which to select an appropriate prediction. There are a number of options available to improve the selection of data and fit of the distribution used to make extreme predictions proposed in (You and Callaghan, 2013), such as the use of Extreme Value quantile functions, and ensuring the use of statistically independent data using the Peaks Over Threshold (POT) method, Annual Maxima method; or the use of other techniques to determine the homoscedasticity and heteroscedasticity of data which will be examined in this chapter.

A number of other pieces of work have informed the analysis that has taken place in this chapter. The work in (Jonathan and Ewans, 2013) raised the issue of covariate effects in extreme prediction in their paper “Statistical modelling of extreme ocean environments for marine design: A review,” They commented that interest may lay in estimating EV models for each variable independently (marginal modelling) or in joint modelling. The specific case given raises the desire to have associated values for T_p at the extreme value of H_s. In other work cited by Jonathan & Ewans, (Coles, Heffernan and Tawn, 2000), on dependence in extreme value data; it is said that a standard method for multivariate extremes is based on distributions for which the variables are asymptotically independent. Given this asymptotic independence, it was necessary to find a method to reliably predict the accompanying T_z value for an

extreme H_s value when performing an extreme wave analysis at sites on the West Coast of Ireland.

The work in this chapter develops a method, using a linear regression model, which allows the determination of the associated period for extreme events. By comparing the estimated wave steepness given by the predicted maximum H_s and T_z, a sense of the behaviour of the regression model can be derived; and this used in conjunction with the limiting steepness value seen at extreme conditions of H_s as a sanity check in determining realistic extreme values. In (Bell, 1972), it was found that the measured period of the highest individual wave is longer but has a wide range of values relative to T_z, which is consistent with the results determined by the regression model, as shown in Figure 55, and this research guided some of the assumptions made in determining period values associated with extreme H_s conditions. (Carter and Chaellenor, 1990) found that Fischer-Tippett Type 1 and Weibull 1 give a good fit in British waters, which informed their inclusion here as part of the default options for the automatic curve selection method.

The average conditional exceedance rate (ACER) method is applied to the prediction of extreme wave heights using a cross-validation method to obtain an insight into its behaviour. This will also examine the influence of variability, and of the data selection method, on prediction variability in a long-term dataset.

4.2 Method

4.2.1 Current Extreme Prediction Methods

In the field of extreme analysis, threshold selection remains a much-debated topic. The selected set of data must cover the variance of the extremes, but the inclusion of too much data below what can be considered an extreme wave will skew the distribution and result in a lower prediction of extreme wave height. The work of (Mathiesen *et al.*, 1994) describes the recommended practice for extreme wave analysis methods, with particular focus on data selection process. A number of the methods suggested therein will be applied in this study, including methods for data selection, sample selection, and the use of model distributions and fitting methods. The work of (Mazas, Garat and Hamm, 2014), however, has examined replacing the distribution used for the analysis (as was encouraged originally by Mathiesen et. Al.).

They have replaced the Maximum Likelihood Estimated two-parameter distributions by L-Moments estimated 3 parameter distributions to good effect. In this Chapter, alternative distributions will be used based on the Generalized Extreme Value (GEV) approach, a family of continuous probability distributions within Extreme Value theory, to achieve a better fit for the data at the extreme quantiles. In addition, regression and covariate analysis are used to attempt to tie together all sea state parameters at the extremes and give a better understanding of the extreme values of Wave Power and Period.

Defining storm duration must take into account that most extreme predictions require the data to be discrete and independent. For this reason, storm events must have at least 3 days between them to qualify as independent storms in this analysis. This threshold was chosen based on the typical length of storm events at sites on the West Coast of Ireland, and chosen to ensure statistical independence (Cid *et al.*, 2016).

Though this chapter will not delve deeply into each of these topics, it will give an insight into the controllable factors which can be adjusted to create the best predictions at a given location.

4.2.2 Proposed Analysis

The analysis undertaken focused on determining an improved method for the prediction of wave parameters during extreme conditions, the likely return periods of these conditions, and the relationship between parameters during concurrent conditions. The focus is on achieving greater certainty in the extreme conditions that will face Marine Renewable Energy devices while deployed. The novel aspect of this work lies in the combination of regressive and correlative techniques used to determine the extreme wave prediction. This primarily involves an investigation of the selection of the best distribution for a given dataset; using autoregressive techniques which make the assumption that current time-series values depend on past values from the same series. Homoscedastic / Heteroscedastic assessment techniques perform analysis based on the assumption of equal variance and unequal variance in the relationship of the predicted variable, respectively. This is performed with the aid of the AMEVA statistical toolbox version 1.32 and version 1.41 (IH

Commented [AB10]: Is this acceptable for highlighting what is new?

Cantabria, 2014). Extensive extreme analysis and data selection methods will also be employed using MATLAB, utilising the expanded capabilities and data processing options to achieve greater knowledge of the relationships between parameters at the extremes, and to enable automated parameterisation of extreme value functions.

The Generalized Extreme Value (GEV) analysis was used to determine H_s values, H_{max} and Wave Power at 5, 10 and 20-year return periods. The commonly used 50 year return period was not determined here, given the limited duration of the dataset.

The Anomaly Index (AI)was analysed across all wave conditions. Establishing the relationship between these parameters is critical for safe design in extreme conditions, and additionally gives greater insight into the likely values of H_{max} when this information is not directly available.

Wave Steepness values at the extreme values of H_s are determined. This is done using regression techniques and the best fit 3-part regression model is used to estimate the likely steepness at the predicted extreme wave heights.

The most appropriate T_z value to use at extreme H_s values is determined. These values are estimated using regression analysis, and with a new method based on the estimated wave power at the extremes.

Period Correlation to wave height at extremes is examined. Extreme predictions provide more definitive information on wave height than on wave period (Mercier J. A., 1982), and it is normal to determine the associated wave period by assuming a wave steepness. The steepness of extreme waves, however, will often be markedly different to the average climate, as will the wave with maximum period. Where there is a dynamic response involved, the wave period can in some cases be equally or more important than wave height. Thus a joint probability of height and period was assessed, providing additional information on the characteristics of waves at the extremes.

4.2.3 Location & Data Sources

The data used for the analysis was acquired from the Marine Institute, and consists of Waverider buoy measurements acquired at Berth B of the Atlantic Marine Energy

Site (AMETS) at Belmullet in Ireland (shown in Figure 30). It spans a time period from December 2009 to August 2013 and consists of 50173 records at 30-minute intervals. Spectral records are logged every 30 minutes by the Waverider buoy with the output of the spectral analysis computed and logged 6 minutes later. This output also includes the time-series output of $H_{1/3}$, $H_{1/10}$ and H_{max}. Spectral data includes the significant wave height (H_{m0}) and mean wave period (T_z). Missing and invalid entries due to buoy or logging error were removed from the dataset along with their associated values at that timestamp. Such anomalies as these are not ideal, but in this case, consist of 1588 records. This represents a meagre (3%) of the dataset and further, these anomalies were mostly confined to more benign sea states. It is expected that the removal of false/missing data in this manner provides optimal error prevention without compromising the outcome of the extreme analysis. An occurrence scatter plot for the dataset used is given in Figure 49.

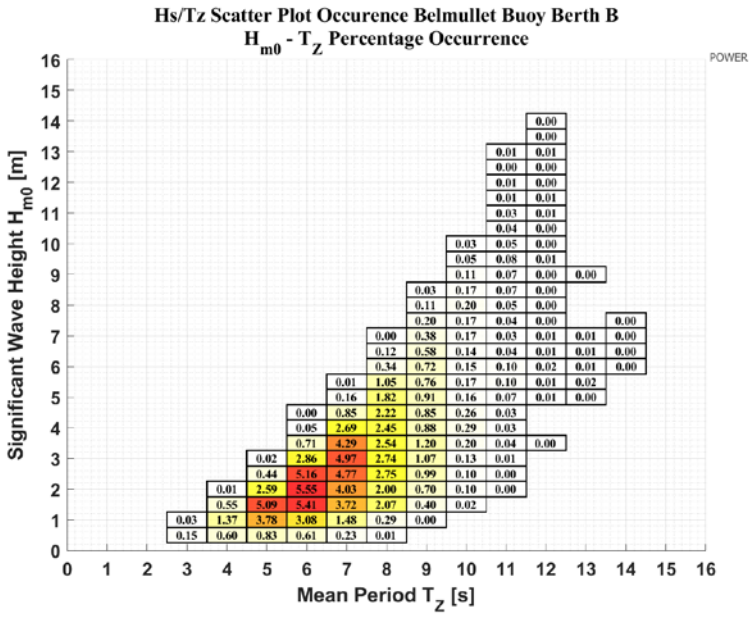


FIGURE 49: HS/TZ OCCURRENCE SCATTER PLOT AT AMETS BERTH B

The Belmullet Berth B site is demonstrably energetic, with the most commonly occurring conditions in the range 1.75-4m H_s and 5-7s T_z, and with waves records in

excess of 14 meters during the span of the recorded data. Thus, Belmullet presents an excellent test-case for extreme wave analysis.

4.3 Analysis

Analysis is now conducted on the recorded data from the Belmullet site to determine the optimal prediction of conditions during extreme wave events, beginning with the identification of the best fitting distribution for Hs. This is performed using 98th percentile data to identify and isolate the effect of the most extreme wave conditions.

Extreme Wave Determination Methodology:

- Identification of best fitting distribution
    - 98th percentile values to identify extreme values.
    - Identification of best fitting distribution.
    - Identification of distribution descriptors and confidence intervals using AMEVA tool.
    - Quantile-Quantile plot to identify any skew in distribution or tendency to over or under-estimate and validate the selection of percentile threshold.
    - Identification of best fitting distribution for H_S
- Alternative method if too many datapoints use progressively more restrictive percentiles
    - Use Monthly maximum Hs data.
    - Dual function of isolating storm events and reducing dataset.
    - Quantile-Quantile plot of adjusted dataset of monthly maximum values, accompanied by confidence intervals.
- Identification of Extreme H_s and H_{max} Values
    - Identify Extreme Hs values at defined Return Periods.
- Determination of Anomaly Index from H_{max}/H_s
    - Determine AI using Regression analysis.
    - Determine AI using predicted max H_{max} / H_s values.
    - Sanity Check using AI values.
- Determination of Wave Steepness at Extremes
    - Determine Wave Steepness using regression analysis.
    - Check steepness values at predicted extreme waves.
    - Perform regression analysis on T_z/H_s relationship.
    - Use predicted T_z values from regression analysis to determine slope at extremes and check agreement with steepness regression analysis

4.3.1.1 Using 98th Percentile H_s values

The H_s, H_{max}, and wave power parameters were fitted to an optimum distribution function for the dataset using auto-regression to identify the shape, location and

scale parameters which best fit the data. The data selection process began by selecting the 98th percentile values of each dataset to remove the effect of lower values on the fit of the distribution. This effectively removed wave events with a H_s below 7 meters. The best fitting distribution was found to be the Weibull minimum distribution, with a probability distribution function defined as follows:

$$F(x;\mu;s;\mathrm{a}) = \frac{a}{s}\left(\frac{x-\mu}{s}\right)^{-1-a} \mathrm{e}^{-\left(\frac{x-\mu}{s}\right)^{-\mathrm{a}}} \quad (4.1)$$

Where:

μ is location parameter

s is the scale parameter

a (>0) is the shape parameter

The resultant best-fit had the following parameters:

TABLE 20: DISTRIBUTION DESCRIPTORS FOR H_S.

Mean	8.245
Log likelihood	-1329.600
Location factor (μ)	6.9 ± 6.504e-08
Shape Factor (a)	1.14 ± 0.079
Scale Factor (s)	0.87 ± 0.046

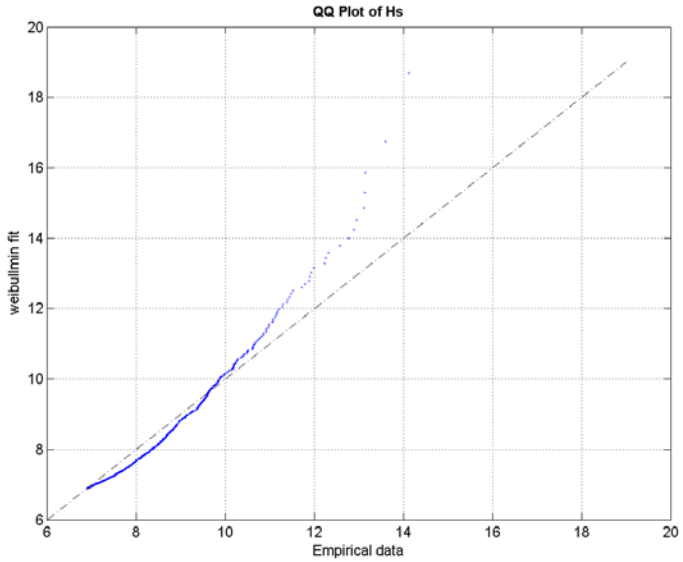


FIGURE 50: QUANTILE-QUANTILE PLOT HS 98TH PERCENTILE VALUES AT BELMULLET BERTH B

The Quantile-Quantile plot, which shows the probabilistic fit of the distribution to the fitted curve - with the theoretical quantiles on the x-axis and fitted quantiles on the y-axis - displays an upward concavity at higher quantiles, displaying a tendency to overestimate extreme values. This is evidence that a more rigorous data selection process is needed to identify only the storm condition maximum values which contribute to the extreme wave estimate. There is a clear variation in the fit of the weibullmin curve to the empirical data when wave conditions exceed 10m. In place of arbitrarily continuing to select more restrictive percentile thresholds in an effort to isolate the behaviour of the most extreme waves, the methods proposed by (Mathiesen *et al.*, 1994) are used; selecting the monthly maximum values. For this approach storms are additionally not considered unless they are separated by 3 days. This ensures discrete data and heteroscedasicity of the model.

4.3.1.2 Using Monthly Maximum H_s data

The monthly maximum values for H_s were determined, and used to examine the level of fit with the available distributions in comparison to the use of the 98th percentile H_s data. Given the range of the monthly values would be expanded due to seasonal

variation, and the GEV distribution has the form of an exponential function, the data was first normalised.

The best fit found for the data was a GEV distribution whose cumulative distribution takes the form:

$$F(x;\mu;\sigma;\xi) = \exp\left(-\left[1+\xi\left(\frac{x-\mu}{\varphi_1}\right)\right]^{\frac{1}{\xi}}\right) \tag{4.2}$$

Where:

$\mu \in R$ is the Location parameter

$\sigma > 0$ The Scale parameter.

$\xi \in R$ The Shape parameter.

And where scale parameter of the model is assumed to follow the physical description:

$$\sigma(t) = exp\left(\alpha_o \sum_{i=1} [a_{2i-1}\cos(i\omega t) + a_{2i}\sin(i\omega t)] + \beta_{T2}t + \sum_k \varphi_k\, n_{k,t}\right) \tag{4.3}$$

With

$$\mu(t) = \beta_0 = 5.844 \tag{4.4}$$

$$\alpha_0 = 0.726 \tag{4.5}$$

The Quantile-Quantile plot shown in Figure 51 below shows a marked improvement in the level of fit, though there is still a noticeable deviation from the expected value at higher wave heights. Additionally, the confidence intervals are displayed, indicating the 95% percentile confidence interval in the prediction of extreme H_s. The empirical data falls inside these confidence intervals for each of the monthly maximum values.

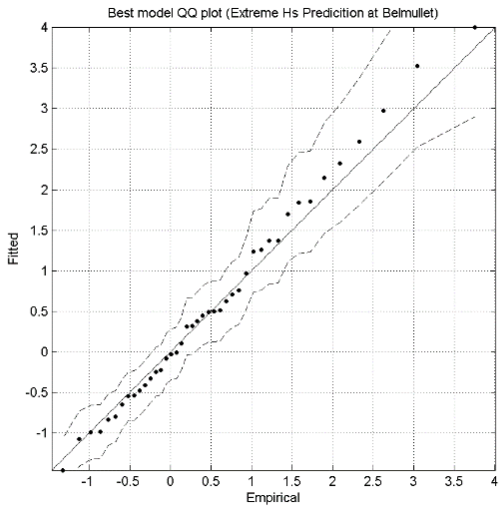


FIGURE 51: QUANTILE-QUANTILE PLOT OF ADJUSTED DATASET OF MONTHLY MAXIMUM VALUES AT BELMULLET BERTH B.

The extreme H_s analysis was then conducted with the newly reduced dataset. The maxima encountered in each month show the highly seasonal nature of the test site and the influence that seasonality has on the prediction of extremes.

The results show that the annual maximum data contribute the most to the extreme prediction. As expected, the most extreme events occur during winter months and make up the largest component of the maximum wave estimation.

TABLE 21: EXTREME HS VALUES AND ASSOCIATED UNCERTAINTY AT 5, 10, 20 YR. RETURN PERIOD

Return Period (Years)	**Expected H_s (m)**	**95% Confidence interval bounds for H_s (m)**
5	14.1	[11.8-16.4]
10	15.6	[13.0-18.3]
20	17.1	[14.1-20.1]

Wide separation for 95% confidence intervals is observed. Benign data can be seen to be contributing significantly to this uncertainty in the estimate, with summer monthly maximums seen to be much lower and therefore affecting the fit. It is evident then that even with great care taken in the data selection process, a limited dataset in a seasonal site will still present a challenge with regards to the certainty of the prediction.

Monthly maximums at this site include waves with a height as low as 2.8m, and these should perhaps not be considered extreme waves. Further analysis is performed by introducing an additional wave height threshold to determine storm events. This was run after the selection of monthly maximum values, with an additional threshold value of 6.5m set as the minimum H_s to be considered a "maximum," value. This analysis (not shown) revealed that an imposition of an additional wave height limitation in a short duration dataset such as this served to decrease confidence in the upper estimates of extreme wave height due to decreased sample size. Thus, for this case it can be said that a human selection element was not necessary – and acted to reduce certainty in the prediction. This result displays the importance of threshold selection and it was found that the selection of the most extreme waves by monthly maximum selection was superior to the quantile method for this particular dataset and location. A point that will be examined in subsequent work is whether the distribution that gives the best fit with the data provides the best prediction of extremes. The expected H_s values indicated in Table 21 are higher than what has been normally used at the AMETS site, so further analysis is required to understand the sensitivity of the extreme predictions to distribution type, threshold selection and data length.

4.3.1.3 H_{max} Data

Using monthly maximum data from the wave buoy, the H_{max} extremes were determined using the same methods as the H_s extreme values, by selecting the monthly maximum values. This is performed to provide comparable results between the H_s and H_{max} analyses. These extreme H_{max} values will be used in the determination of AI values in section 5.4

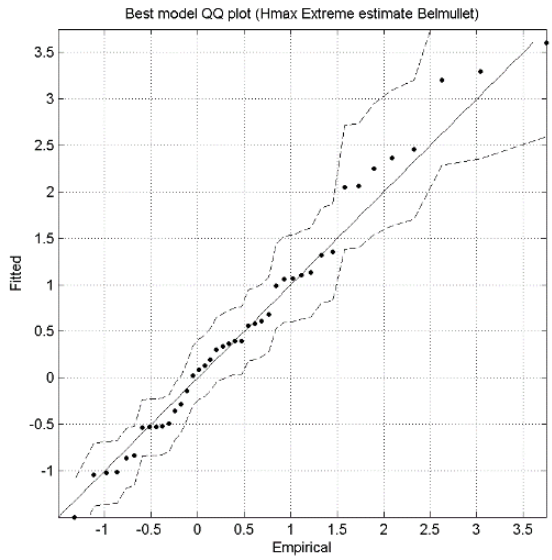


FIGURE 52: QUANTILE-QUANTILE PLOT OF DISTRIBUTION FIT FOR H_{MAX} EXTREME ESTIMATION

The distribution selected for H_{max} fits quite well at the average conditions but begins to show increased variability at the upper quantiles. Nevertheless, the distribution and results were determined using the GEV model (Equations (**4.2**) and (**4.3**))

With:

$$\mu(t) = \beta_0 = 9.849 \tag{4.6}$$

$$\alpha_0 = 1.1216 \tag{4.7}$$

And using the GEV model, the expected maximum H_{max} results were determined to be the following:

TABLE 22: EXTREME H_{MAX} VALUES USING A GEV MODEL WITH MONTHLY MAXIMUM VALUES AT BELMULLET BERTH B.

Return Period (years)	Expected H_{max} at RP (m)	95% Confidence interval bounds
5	23.3	[19.6-27.0]
10	25.8	[21.6-30.1]
20	28.3	[23.4-33.1]

These H_{max} values are bounded by wide confidence intervals due to the limited sample size available, as well as the variability of the maxima encountered from month to month.

4.3.2 Analysis of Anomaly Index from H_{max}/H_s

The Anomaly Index (AI) parameter is an important and commonly used parameter which reflects the relationship between the Maximum Wave Height encountered, H_{max}, and the Significant Wave Height, H_s. It is often used in offshore industries such as Oil & Gas for determining the likely H_{max} for a given value of H_s. These values are typically determined empirically, and generally range from a value of 1.65 to 2.0 (H_{max} : H_s). This wide spread in values of AI leaves some uncertainty asto the exact expected H_{max} value. As will be shown in Section 4.3.2.1, the AI is not a constant relationship, and indeed changes significantly as waves approach the maximum extreme wave height. The result of this assumption is likely to be a structure or device that is under or overdesigned.

4.3.2.1 Anomaly Index to H_S Correlation from H_{max}/H_s AI regression analysis

The correlation between Anomaly Index (AI) and H_s is measured using a 3-parameter regression analysis and is found to trend towards mean AI values governed by the following equation.

$$\mu(t) = p1 + p2t + p3t^2 \qquad (4.8)$$

With p1= 2.453, p2= -0.166, p3= 0.007

Confidence in the mean value diminishes with increasing wave height due to decreased data availability at this level. This is a significant drawback of the limited nature of the dataset. The Confidence Interval for the model values overall, however, narrows appreciably at more extreme wave heights. Future work should look at the behaviour over a much longer period to establish a firmer relationship, but this behaviour is indicative of a constraint on the variability and maximum value of the AI at extreme wave heights. Figure 53, below, demonstrates that the variability of AI outliers decreases as H_S increases.

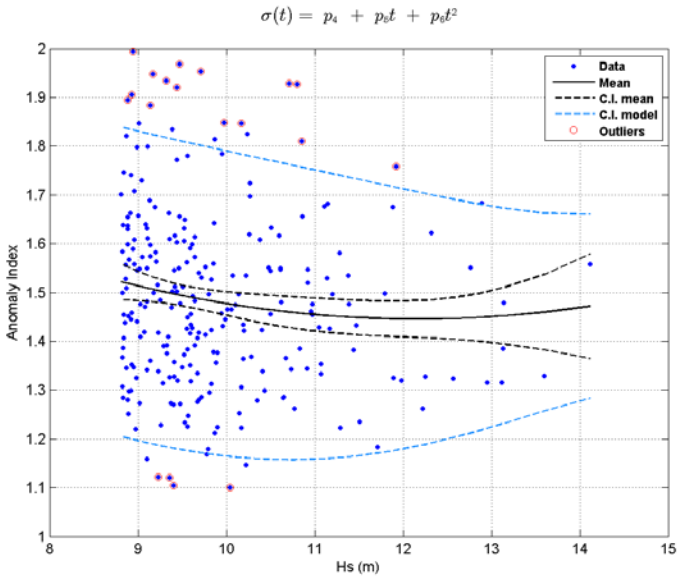


FIGURE 53: REGRESSION ANALYSIS OF AI USING 98TH PERCENTILE H_S/H_{MAX} DATA

Predicting the expected mean value of the AI at the 5, 10 and 20-year Return Period extreme wave heights (as determined in Section 4.3.1.2) gives the following estimates for AI values at the 5, 10, 20-year return periods.

TABLE 23: REGRESSION DERIVED AI VALUES AT EXTREME VALUES OF H_S

Return Period (years)	H_S (m)	Expected AI at RP
5	14.1	1.503
10	15.6	1.569
20	17.1	1.662

4.3.2.2 AI to H_S Correlation obtained at predicted extreme values

As an alternative method of determining the AI at extreme values, the AI was also calculated by comparing the concurrent values of H_{max} and H_s for extreme values of H_s. The maximum predicted H_s and H_{max} as shown in tables Table 23 & Table 24 respectively were used to determine values of AI. The results, shown in Table 24, in all cases show the AI Value to be relatively constant with a value of about 1.65. This appears to be a more consistent measure of AI at extreme values than can be derived using a regression based analysis, and while the values agree well with the values determined in Table 23 for a return period of 20 years, the confidence intervals attached would suggest that the values of AI derived through direct arithmetic division of H_{max} and H_s values carry more certainty. It is likely that the values in Table 23 are less accurate given the sensitivity of the equation to the limited available data at the high values of H_s. While it is difficult to draw firm conclusions based on a limited analysis, it appears that the industry accepted 1.65 H_{max}/H_s ratio is realistic for the determination of maximum H_{max} values at the Belmullet site, and that ratios of 1.87 and 2.0 as are often recommended would give a large factor of safety in the determination of the H_{max} value.

TABLE 24: AI INDEX VALUES DETERMINED USING EXTREME H_{MAX}/H_S VALUES

Return Period (Year)	Expected AI at RP	95% Confidence interval bounds
5	1.654	[1.661-1.650]
10	1.652	[1.659-1.648]
20	1.651	[1.657-1.646]

4.3.3 Determination of wave steepness at the extremes

Regression analysis was performed for the 98th percentile H_s and accompanying wave steepness values to determine a link between H_s and wave steepness at the extremes. This will enable a better estimate of the T_z associated with the extreme H_s to be determined. For this analysis, the steepness reciprocal value (I.E. L/H) was used for improved numerical precision and improved legibility.

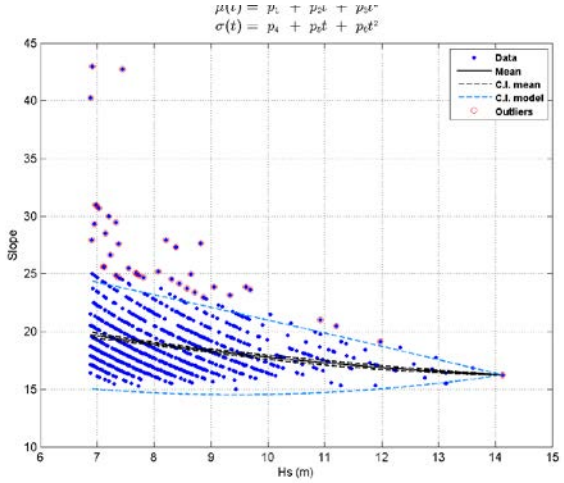


FIGURE 54: WAVE STEEPNESS (RECIPROCAL) REGRESSION ANALYSIS AGAINST H_S

It is evident from Figure 54 that there is an obvious trend of convergent wave steepness values at extreme values of H_s, suggesting that there is a limiting wave steepness which governs the behaviour of the wave at the extremes. Tabulated results of this regression analysis are as follows:

TABLE 25: RESULTS OF WAVE STEEPNESS RECIPROCAL REGRESSION ANALYSIS

Mean	18.8707
Standard Deviation	2.6898
Log likelihood	-2122.1926

According to the regression analysis, the mean steepness for the 98th percentile waves is given by the following equation.

$$\mu(t) = p1 + p2t + p3t^2 \tag{4.9}$$

Where the *p* values were determined to be as follows:

TABLE 26: EQUATION PARAMETERS DETERMINED FOR WAVE STEEPNESS RECIPROCAL FROM REGRESSION ANALYSIS AT BELMULLET

p	Value	Upper	Lower
p1	26.380	28.658	24.103
p2	-1.207	-0.767	-1.647
p3	0.035	0.054	0.015

The resulting wave steepness reciprocal predicted using regression analysis converges to a value of approximately 16, decreasing only fractionally for increasing predicted H_s values. (Table 27). From this result it is proposed that a limiting wave slope at the extremes of H_s can be applied as a method of determining associated T_z values. This means that a methodology can be developed to determine related parameters such as T_z given an extreme H_s value. From this work it is possible to state that a wave steepness reciprocal of 16 is a reasonable assumption at the extreme values of H_s in Eastern Atlantic Waters, and tends to hold across increasingly large H_s events – assuming deep water conditions.

TABLE 27: WAVE STEEPNESS RECIPROCAL VALUES AT EXTREME H_S VALUES DETERMINED FROM REGRESSION ANALYSIS AT BELMULLET

Return Period (Years)	Predicted H_s (m)	Wave Steepness (Reg. Model)
5	14.1	16.324
10	15.6	16.065
20	17.1	15.975

4.3.4 Calculation of extreme T_z using regression analysis

Linear Regression analysis was performed on the T_z and H_s concurrently, and was found to provide a good fit for the relationship at increasing values of H_s. In determining the best fit, outliers above a 95th percentile threshold were removed, and confidence intervals were set at the 90th percentile of values (Figure 55).

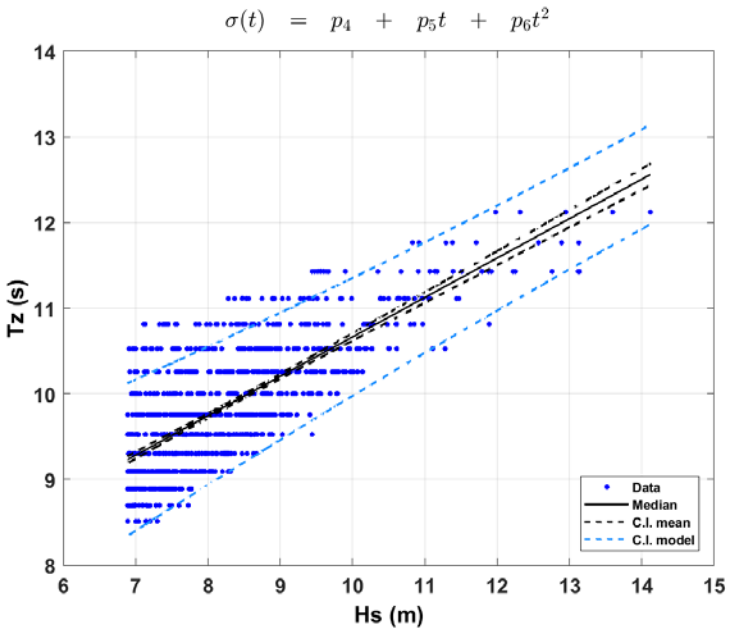


FIGURE 55: REGRESSION ANALYSIS TO DETERMINE T_z/H_s RELATIONSHIP AT AMETS

While there is a broad spread of H_s to T_z relationships at lower values of H_s, the relationship begins to approximate a linear fit for increasing values of H_s. While confidence in the mean value estimate decreases with increasing H_s values due to lack of available data matching these conditions, the strengthening of the overall relationship between H_s and T_z has the effect of continued narrowing the confidence intervals, indicative of better certainty in the estimate. With increasing values, the relationship approximates a linear fit, with P-Values governing the plotting of the curve as follows:

$$\mu(x) = p1 + p2x \tag{4.10}$$

TABLE 28: EQUATION PARAMETERS DETERMINED FOR WAVE PERIOD DETERMINED FROM REGRESSION ANALYSIS

p	Value	Upper	Lower
p1	6.026	6.196	5.856
p2	0.465	0.485	0.445

Using the result of this regression analysis, the values of T_z for extreme H_s values at 5, 10 and 20-year return periods were estimated as follows:

TABLE 29: T_z VALUES AND WAVE STEEPNESS RECIPROCAL VALUES PREDICTED BY T_z/H_s REGRESSION AT BELMULLET

Return Period (Years)	H_s (m)	T_z (s) Reg. Model	Wave Steepness
5	14.1	12.5	15.57
10	15.6	13.3	15.22
20	17.1	13.9	14.93

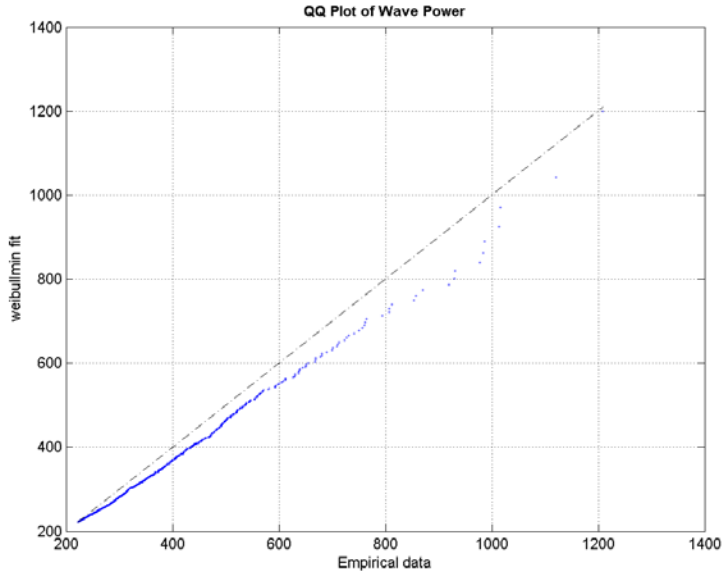
The wave steepness reciprocal results shown in Table 27 and Table 29 broadly agree, and they indicate that a relatively reliable prediction can be achieved for wave steepness at the extremes using either method, or, conversely, a value for T_z at extreme H_s can be determined using knowledge of the likely maximum wave steepness value. Wave periods will continue to increase with the H_s value for higher return periods. This result is significant in terms of increasing certainty in the determination of the most appropriate T_z value concurrent with extreme values of H_s.

4.3.5 Calculation of extreme Wave Power

A novel method of determining extreme T_z by first determining the extreme wave power is trialled here. The distribution of extreme wave power values was found to conform best to a Weibull min curve with:

Location factor	222.79
Shape Factor (a)	100.46 +- 6.78
Scale Factor (s)	0.89 ± 0.045

TABLE 30: QUANTILE - QUANTILE PLOT FOR 98TH PERCENTILE VALUES OF WAVE POWER AT BELMULLET



Making the assumption that the upper bound to the sea-state is the extreme energy, we can use the fact that:

$$P = \frac{pg^2}{64\pi} H_{m0}{}^2 T_e \approx \tfrac{1}{2} \times H_s{}^2 \times T_z \qquad (4.11)$$

Gives the wave power, and work backwards to determine the associated T_z value.

TABLE 31: DETERMINATION OF EXTREME T_z VALUES USING EXTREME WAVE POWER AS AN UPPER BOUND TO THE SEA-STATE CONDITIONS

Return Period (Years)	Wave Power	H_s	$T_z = 2P/H_s^2$	Wave Length	Slope	Steepness (Slope Reciprocal)
5	1204 kW/m	14.08 m	12.15 s	208.72 m	0.067458	14.82
10	1368 kW/m	15.63 m	11.20 s	183.49 m	0.085183	11.74
20	1514 kW/m	17.11 m	10.34 s	160.48 m	0.1066185	9.38

The resulting values for T_z and wave slope do not match those suggested by the regression analysis shown in Figure 54 and Figure 55, with the T_z values lower than have been shown previously in this chapter, and decreasing with increasing Return Period. The analysis also examined the determination of the extreme wave power values, but this proved difficult due to the nonlinearity of wave power with increasing wave height. It was concluded that there was no added benefit to doing such an analysis in this case as the output was substantially different to power values determined using the predicted H_s and T_z values, which is determined below:

TABLE 32: PREDICTED EXTREME WAVE POWER VALUES AT BELMULLET

Return Period (Years)	H_s	T_z (Regression Model)	Wave Power
5	14.10 m	12.5 s	1225 kW/m
10	15.63 m	13.3 s	1625 kW/m
20	17.11 m	13.9 s	2035 kW/m

These values are considerably larger than those determined by direct extreme wave power estimation, but given the strength of the wave slope and regression analysis, these appear to represent realistic values of expected extreme wave power at Belmullet.

4.4 Cross-validated ACER approach

4.4.1 Purpose

The ACER method - (Naess, Gaidai and Karpa, 2013) "Estimation of Extreme values by the Average Conditional Exceedance Rate Method," has shown promise in determining the extreme values of wind speeds in real, empirical trials. The goal of the work in this chapter is to apply the ACER method using wave conditions in Atlantic seas as a test case, and to study the transferability of the model to prediction of extreme wave conditions. The method is based on constructing a cascade of ACER functions which allow the capture of the effect of statistical dependence in data on the extreme value distribution. When the ACER functions have converged, an exact representation of the extreme value is said to have been obtained. Depending on the relevant type of asymptotic extreme value distribution, these empirical ACER

functions are combined with a class of parametric functions to achieve high return level predictions. This leads to a procedure that is claimed to be less restrictive and more flexible than the ones based on asymptotic theory. In particular, it has the capability to capture statistical dependence and sub-asymptotic behaviour of the data (Statistics for Innovation, 2013). This claim to be able to deal with sub-asymptotic data is something which would be of huge benefit in improving the usability of and certainty in extreme value predictions, as well as conferring the benefit of removing the need to de-cluster data prior to prediction to ensure independence, as is common in use of the Peak Over Threshold methods. The aim of this Section is to obtain a more accurate estimate of extreme conditions occurring at the M3 buoy (as a representative of sites on the West Coast of Ireland); this being characterised by tighter confidence intervals and less dependence on user selection of values of fit. The benefits of such a method for extreme wave prediction are multitudinous, but the work done in this chapter is particularly focused on the use of extreme wave data for the design of marine structures.

A further aspect of this study is the implementation of a cross-validation approach, which is pursued to ensure homogeneity of the extreme wave predictions based on sub-asymptotic data. Moreover, this approach allows for an examination of the effects of limited data duration upon the ultimate prediction of extreme wave events, and a method of validating the accuracy and variability of predictions which extends beyond curve-fitting. The primary motivation is in the prediction of an extreme H_s value only, though the authors of the method claim that ACER can (non-trivially) be applied to multi-variate predictions also.

4.4.2 Introduction to Average Conditional Exceedance Rate extreme function

The method described in the paper is used for extreme value prediction based on a sampled time series. It is specifically designed to account for statistical dependence between the sampled data points and to do so precisely. It claims to provide statistical estimates of the exact extreme value distribution. It further avoids the problem of having to de-cluster data to ensure independence, which is a pre-requisite for methods such as POT (Peaks Over Threshold). The ACER method uses

sub-asymptotic data to improve prediction accuracy, defining a "level of interest" parameter to determine the influence of data:

$$\text{Level of interest} = \frac{duration\ of \frac{observations}{N-k+1}}{time\ horizon} \tag{4.12}$$

Where:

duration of observations is the total time over which the observations were obtained.

N is the number of data points

time horizon is the desired target return period (Units must be the same as the duration of observations)

4.4.3 Method

The ACER method will be analysed for its ability to accurately predict extreme values of H_s at the M3 wave buoy. Three aspects are analysed for this review of the extreme prediction ability of the ACER function:

- The influence of data length on the accuracy of prediction.
- The choice of threshold and the impact on the prediction – In this case, specifically for the ACER function.
- The utility of cross-validation in providing an alternative means of statistical calibration to curve-fitting for extreme wave determination.

4.4.3.1 Site Location

Buoy data has been obtained from the M3 buoy, maintained by Met Eireann, which spans 13 years. This results in 98337 data points recorded at hourly intervals. The M3 buoy sits off the South-West coast of Ireland (Figure 5), a particularly energetic wave environment. This study was performed in conjunction with a project which seeks to analyse the siting of offshore floating wind platforms at the site, giving rise to this analysis.

4.4.3.2 Choice of threshold

The choice of threshold has a significant impact on the result of the ACER function, which is a finding that is also commonplace in methods such as POT. There are no clear guidelines provided on the selection of a threshold. The user is told to choose a

point where the function “has stabilized,” but this is highly open to interpretation. This is a problem which is common to all forms of extreme prediction, and is especially applicable to the POT method. Here the effect of threshold on the resulting prediction is quantified.

The threshold value for determining an extreme wave condition is selected by percentage of the maximum value contained within the test data fold, with the threshold additionally selected by percentile of the maximum value contained within the test data fold to ensure there are enough data points for the algorithm to achieve a good fit. The data above the selected percentile will be used for the extreme predictions; and the expected Extreme Value prediction, minimum and maximum confidence intervals quantified. The threshold selection will be plotted against the predicted value, minimum and maximum confidence interval to show the change in the prediction and the associated confidence intervals based on the choice of threshold.

4.4.3.3 Influence of data length

The influence of data recording duration is a contentious issue in the determination of future extreme wave conditions. Typical rules of thumb utilised in the industry suggest prediction of return periods no greater than 5 times the length of the current dataset. This study aims to provide a more accurate characterisation of the influence of data length on the prediction accuracy, as defined by the predicted confidence intervals, and as determined by the restricting the analysis to a subset of the data and analysing the individual accuracy of the prediction against the likelihood as determined by the remainder of the dataset.

To perform this analysis, the dataset will be randomly partitioned into k-folds, with the k value chosen according to the reduction in dataset size desired for testing. i.e. a selection of a k value of 10 will result in 10 folds of 9539 data points, corresponding to approximately 1.09 years of data. This will be done from 10->1 folds to determine the increase in accuracy of the model based on increased length of data capture. A secondary fold technique involves segmenting the data by defined one-year intervals, to include a more realistic representation of seasonal effects within a 1-year timespan.

A cross-validation approach will be taken, separating the data into k-folds to ensure independence, and then using the ACER approach to provide an approximation of the 5-year return period event based on the data in each fold. The relative fit of the extreme prediction at this return period will be compared to the determined probability of occurrence in the entire dataset.

The ACER function is then used to determine the 1, 2, 3, 4, 5-year extreme events based on this data. With a sample size of 10, the minimum, maximum, and average predictions can be assessed, as well as the width of the confidence intervals.

Using this approach, the point at which the prediction accuracy of the function begins to break down can be determined. This is useful to assess the length of data truly needed to provide an accurate prediction, from an empirical standpoint, and can inform future work at similar sites. The length of data vs. prediction accuracy (as defined by spread in CI and RMSE values) will be plotted to give a representation of the effect of data length on prediction accuracy.

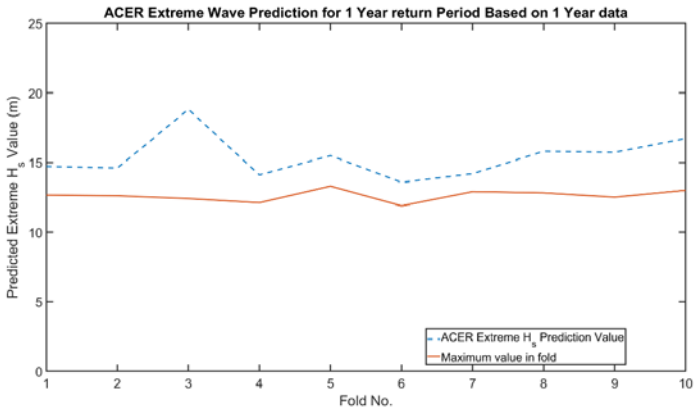


FIGURE 56: VARIATION IN ACER EXTREME H_S PREDICTION ACROSS 10 FOLDS CONSISTING OF 1 YEAR OF DATA AT M3.

Figure 56 displays an analysis of the variation of predicted extreme H_s values across 10-folds of randomly selected 1-year intervals from the M3 buoy data records,

generating a prediction for a 1-year return period at the M3 buoy site. The standard deviation in the predictions is 1.54m, while the spread between the largest and smallest predicted extreme events is 5.25m. Thus, the impact of the data that is selected, or by extension, the recording period from which the buoy data is obtained, has a significant impact on the prediction of extreme values; even when utilising a method that claims to work effectively when using sub-asymptotic data. This level of standard deviation and range of predicted values was found to be mostly uniform across 1 to 5-year return periods, and thus the impact is predominantly from the selection of data records and not the return period. It will be shown in Figure 60 and the associated analysis below, however, that the return period does have a significant impact on the variation that can be expected in the upper confidence intervals of extreme wave predictions.

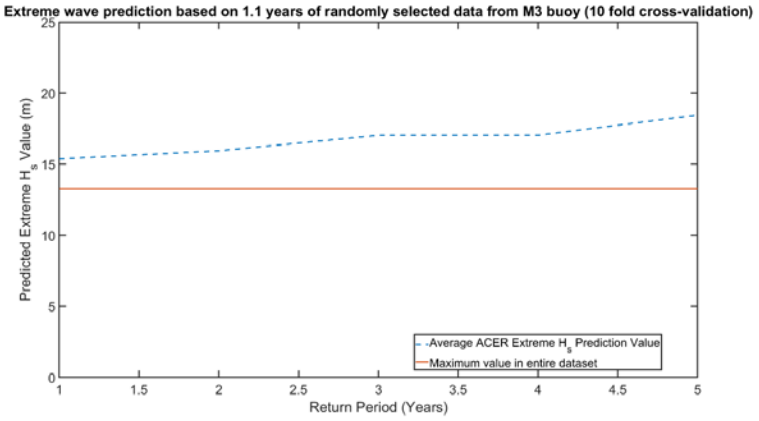


FIGURE 57: AVERAGE ACER EXTREME H_S PREDICTION FOR 1-5 YEAR RETURN PERIOD AT M3 USING 1 YEAR DATA.

Figure 57 displays the Extreme H_s prediction for return periods from 1-5 years using a short dataset of 1.09 years for prediction. The prediction of extreme values beyond 5 years (approximately 5x dataset duration) becomes unruly, with the normalized confidence interval spread (Figure 58 - Figure 60) increasing as the return period increases. This widening of the confidence intervals as longer return period intervals are used indicates a declining ability to predict these events beyond the 5x time horizon.

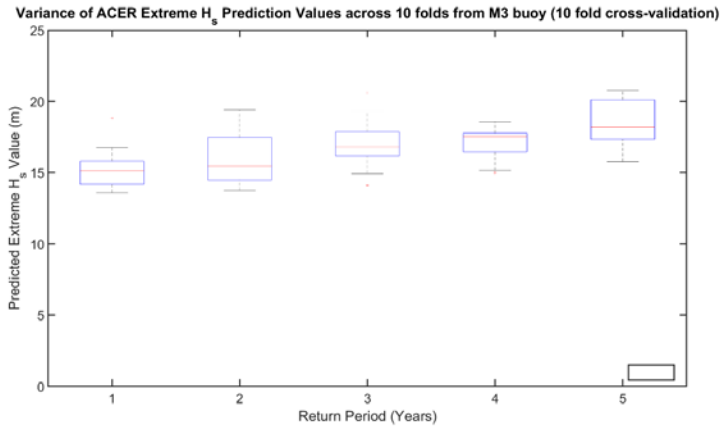


FIGURE 58: VARIANCE OF ACER EXTREME H_S PREDICTION ACROSS 10 FOLDS FOR 1-5 YEAR RETURN PERIOD AT M3 USING 1 YEAR SEGMENT OF PREDICTION DATA

The variation in the prediction value of H_S, and particularly the extent of the outliers, rises with increasing return period, though the selection of data is still seen to be significant.

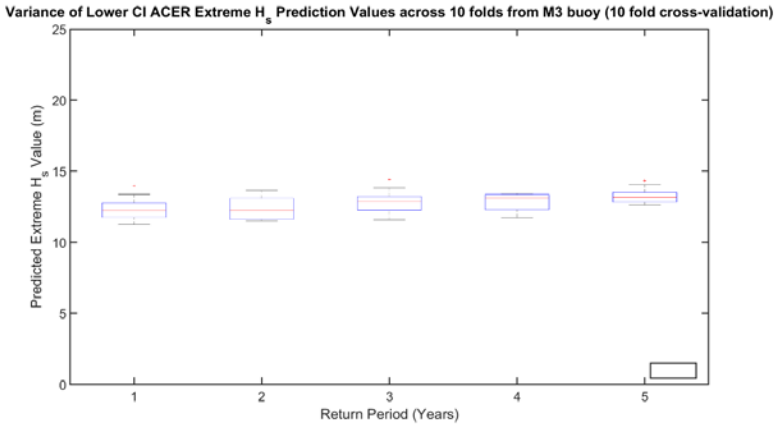


FIGURE 59: VARIANCE OF LOWER CONFIDENCE INTERVAL FOR ACER EXTREME H_S PREDICTION FOR 1-5 YEAR RETURN PERIOD AT M3 USING 1 YEAR SEGMENT OF PREDICTION DATA

The spread of lower 95% confidence intervals for extreme H_S prediction is found to be far lower than that of the primary prediction value, indicative of greater

confidence in the prediction of the lower confidence interval. Here the variation in predictions across a 1 to 5-year Return Period interval is seen to be less significant than the impact of the selected data for producing the prediction.

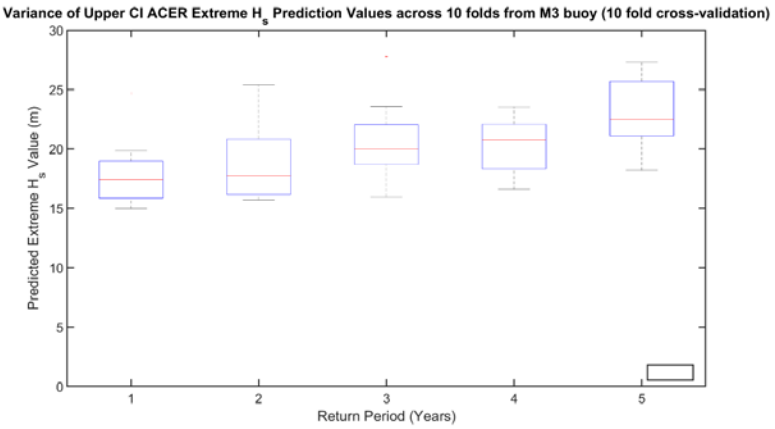


FIGURE 60: VARIANCE OF UPPER CONFIDENCE INTERVAL FOR ACER EXTREME H_S PREDICTION FOR 1-5 YEAR RETURN PERIOD AT M3 USING 1 YEAR SEGMENT OF PREDICTION DATA

The variance in upper 95% confidence interval using the ACER approach is found to be extremely large. At just a 1-year return period, there is a spread of 9.72m between the largest and smallest upper confidence intervals, while the maximum difference between the largest encountered wave height across all folds was just 1.42m. This indicates a large degree of uncertainty in the upper bound confidence of the ACER function. Any project which is cognisant of these in selecting an extreme wave height is likely to struggle with achieving a realistic upper bound based on the use of this function.

4.5 Conclusions

The motivation for the work performed in this chapter comes primarily from the offshore renewable energy sector, whose sustainability is dependent on reducing both cost and risk. By the provision of more accurate design information there can be more certainty in terms of the survivability of a structure and thus a de-risking of the proposed project.

The work performed here has succeeded in providing greater accuracy in extreme wave design information. This increase is achieved through an improved

understanding of the influence of selection thresholds on the resultant extreme wave prediction, through automated selection of the best-fitting distribution for wave conditions at the site, and via greater knowledge of the relationships between wave parameters at these extreme conditions.

The method proposed in Sections 4.1 - 4.4 is an extension of the type of analysis already undertaken to determine extremes; with the goal of providing more certainty in terms of the predicted values achieved, and the relationship between wave parameters during extreme wave conditions. By establishing a methodology involving the use of linear regression techniques for relating wave period and wave height, more certainty has been brought to the prediction of wave periods corresponding to extreme H_s values. Additionally, the analysis of wave steepness has suggested a limiting wave steepness value can be determined for extreme conditions, and this will aid an understanding of the relationship between wave height and period for extreme events.

Significantly, the relationship between H_s and H_{max} or T_z magnitudes can be determined for conditions defined as extreme wave events; these defined by either monthly maxima selection, or Peaks Over Threshold selection. With this relationship tailored to a particular site, an improved estimate of wave parameters coincident with future extreme H_s events can be determined. This relationship has been derived for Belmullet Berth B data, finding that the AI reaches a value of approximately 1.65 during extreme H_s conditions, which is consistent with the lower-end of many industry assumptions for this ratio. H_{max} values coincident with extreme H_s events for 5, 10 and 20-year Return Periods at the Belmullet site have been determined, and these values will be found to be significantly lower than those produced by the theorised 1.87-2.00 AI which is often used in extreme analysis in the industry.

The value of T_z was found to increase at a rate of approximately $0.46H_s$ for extreme wave conditions defined by the 98^{th} percentile or greater H_s, while the wave steepness at extreme wave conditions was found to continually decrease and become less variable with increasing H_s, converging to a value of 16 at the highest recorded H_s value. Utilising a combination of this $H_s : T_z$ relationship, and a relatively defined bound for the wave steepness during extreme wave conditions, it is possible

to have much greater certainty in the prediction of the coincident values of these parameters for future estimates of extreme conditions at the Belmullet site.

A further advantage to the determination of these relationships is the ability to build a model which improves with each tranche of data gathered, rather than assuming values of the anomaly index and wave steepness that have been derived empirically elsewhere.

From this work, the following methodology is proposed for the optimization of the prediction of extreme conditions at sites in Coastal Irish Waters (whose behaviour likely extends to all Eastern Atlantic sites):

- Select the monthly extremes of H_s, H_{max} values and the accompanying T_z and H_{max} values for the H_s results.
- Determine the best fitting distribution for the data.
- Using regression analysis, identify trends in AI, Slope, and Wave Period.
- Estimate H_s and H_{max} extreme values using GEV or similar techniques.
- Estimate corresponding extreme T_z and AI values using the results of the regression analysis.
- Ensure correlation between results using wave steepness at the extremes as a guiding value.

Using this methodology, it has been found that the identification of extreme wave events above a defined percentile threshold results in more accurate predictions of extreme values versus utilising the entire dataset available; while selection and fitting of monthly maxima to an extreme curve results in more realistic prediction of extreme wave events for longer return periods. This additionally carries the benefit of inherently selecting independent and heteroscedastic data due to the temporal separation of the selected extreme wave events. Contrasting this method to the selection of extreme wave event by percentile threshold; it was found that while the percentile method did not provide the same accuracy in mean extreme value estimates, there were benefits conferred by the increased number of sampling points, which resulted in increased statistical confidence in the range of extreme conditions which are likely to be encountered. It carries additional value by retaining

a far greater number of data points in data-limited scenarios, making it a preferred option for shorter buoy deployments.

The analysis of ACER as a prediction method for H_s at the M3 buoy has shown that the method provides reasonable estimates of predicted extreme wave heights, and does so using sub-asymptotic data that does not require that extreme events occur in the recorded data to make a prediction. However, it was also found that even amongst 1-year segments of the dataset with similar maxima encountered, there was significant variation in the predicted value. This was particularly the case for the upper confidence intervals of the resulting predicted values.

The use of a cross-validated approach allowed for additional insight into the influence of the selected data on the resulting prediction, while highlighting aspects of the prediction that were particularly affected by either the variation in conditions encountered in the dataset, or the length of return period for which extreme values were predicted.

The elements which affect the prediction of extreme events are multifactorial; typically requiring a choice of distribution, choice of threshold, and an analysis of the influence of data length. The ACER method implemented with cross-validation approach allows for a more consistent and informative prediction of extremes.

5 Metocean Assessment to IEC standards

5.1 Introduction

Increased activity in the Offshore Renewable Energy sector has ensured that knowledge of the wave climate, including accurate modelling and forecasting of wave conditions in locations suitable for Marine Renewable Energy projects has become increasingly important.

In Ireland, renewable energy strategies such as the Offshore Renewable Energy Development Plan, which outlines the Irish government's target of 40% of electricity from renewable sources by 2020, highlight commitment to the long term economic potential of Ireland's wave and tidal resources (Department of Communications and Resources, 2014). Given Ireland's huge natural wave resource, with an accessible capacity estimated at over 11.72Twh/year (Sustainable Energy Authority Ireland, ESBI and Marine Institute, 2005), the need for a standardised and thorough assessment of potential sites for Marine Renewable Energy has never been greater. Rapid development is taking place globally, with advancements in device design, testing methodologies and project planning. There remain, however, a number of issues surrounding the proposed deployment of WECs, with two of the most prominent being assessment of energy production and survivability (Jager *et al.*, 2011). These issues, in a rapidly growing and highly promising field, give rise to the need for detailed metocean analysis methodologies, as well as standards governing the analysis of sites for Marine Renewable Energy.

This Chapter builds on the work performed in Chapters 3 and 4, using comprehensive numerical modelling and characterization of the site conditions at Killard Point as a test case for the development of improved tools to tackle two of the outstanding issues in the development of wave energy projects; namely, energy production and survivability. The novel Machine Learning methods developed in Chapter 3 are applied to improve the correlation and the prediction of wave parameters, while the Extreme Wave techniques developed in Chapter 4 are applied to improve estimates of Extreme Waves on the West Coast of Ireland.

In addition to this, the wave resource characterisation is performed to the IEC 62600-101 standards for Wave Energy Resource Assessment and Characterization (henceforth IEC-TS), which represents a first-of-kind study, and will enable an exploration of the validity, cost and practicality of implementing these standards for Marine Renewable Energy projects.

Section 5.2 gives an overview of the IEC-TS requirements and recommendations, as well as the details of the WestWave project, which serves as the test case for the application of the novel metocean analysis methods that have been developed.

Section 5.3 details the process of generating a 24 year hindcast, numerical wave data, dataset at the Killard Point site to the IEC-TS standards. It will highlight the difficulties that are found in meeting the stringent requirements outlined therein.

The wave climate and resource modelling methodology and validation processes undertaken will be detailed in Sections 5.3 - 5.4. Issues associated with data acquisition of hindcast boundary conditions, validation of data sources and modelling of the area in MIKE 21 SW software will be highlighted.

Section 5.4 implements the novel methods developed in Chapters 3 and 4 to improve power production accuracy in line with the requirements of the IEC-TS, and to highlight the utility these newly developed methods have in moving toward the accuracy required for the Marine Renewable Energy industry to have “bankable” projects.

Section 5.4.7 deals with the predictability of wave conditions on the West Coast of Ireland and quantifies the impact that inaccuracies in available numerical forecast models have on energy production of WEC farms.

Finally, potential opportunities for further work to improve upon best practice in terms of validity, cost and the practicality of implementing the IEC-TS will be outlined. This work represents an important development for the future of Marine Resource assessment.

5.2 Background and Development

This Section is intended to give background on both the IEC-TS and the WestWave project case study. Though these have been described previously in Chapter 2, this

Section gives additional information that is pertinent to their use in the context of a first-of-kind utilisation of the IEC-TS for a commercial wave energy development. It further outlines the motivations of the WestWave project, as well as the specific site data and site characteristic details relevant to the modelling, characterisation, and implementation of novel methods for characterisation and energy production estimation.

5.2.1 IEC-TS

The IEC 62600-101 TS: Marine Energy - Wave, Tidal and other Water Current Converters - Part 101: Wave Energy Resource Assessment and Characterisation provides guidance relating to the measurement, modelling, analysis and reporting of the wave energy resource, and the linkages between these activities.

It provides a uniform methodology that will ensure consistency and accuracy in the estimation, measurement and analysis of wave energy resource at sites that could be suitable for the installation of WECs, together with defining a standardised methodology with which this resource can be described. It is intended that it be applied at all stages of site assessment (initial investigations to detailed project design) and in conjunction with the IEC technical specification on WEC performance (IEC TS 62600-100).

These standards are targeted at Project developers, Device Developers, Utilities/Investors, Policy-makers and Consultants producing resource data.

It is important to remember that wave climate analysis and modelling will shape design decisions and commercial outcomes, thus it is important that these observations be held to high standards.

The standards are currently in published in “Technical Specification” format, with a stability date of 2020, after which it will be replaced by a revised edition. It is hoped that work such as that done in this Chapter will act as a feedback mechanism for the future development of these standards, and act as a test-case for the implementation of these standards.

The utility and effectiveness of the IEC standards for wave energy resource characterisation has been assessed using three different models with increasing

spatial resolution in order to fulfil the requirements of the IEC-TS standards in (Ramos and Ringwood, 2016). They found that these standards offered a robust and coherent methodology, featuring recommendations and rules to carry out precise wave resource characterisation. However, it was also found that some of the minimum requirements needed for validation of the more stringent design stages were excessively demanding in light of current best available wave modelling techniques; finding too that the increase in accuracy of key wave parameters was relatively small in comparison to the processing and time constraints imposed by the use of a more refined mesh stipulated for the "design" & "feasibility"-stage requirements.

5.2.1.1 Requirements and Recommendations

Three distinct types of studies: Reconnaissance, Feasibility and Design, are defined by the IEC-TS (shown in Table 33); with Class 1 studies typically conducted at low to medium resolution, spanning a large area and producing estimates with considerable uncertainty. Resource assessments conducted to investigate the feasibility of a particular site or to support the design of a specific project will focus on a smaller area and employ a greater resolution, aiming to generate greater certainty in estimates of the wave energy resource.

TABLE 33: CLASSES OF RESOURCE ASSESSMENT – IEC 62600-101 ("TABLE 1")

Class	Description	Uncertainty Wave Resource	Longshore Extent (km)
Class 1	Reconnaissance	High	>300
Class 2	Feasibility	Medium	20-500
Class 3	Design	Low	<25

Note that the class of resource assessment does not explicitly limit the longshore extent of the model, it is merely indicative of the expected reduction in area owing to the focus on a specific area of the domain.

Table 34 covers the model setup recommendations for the three classes of assessment, outlining the physical processes, boundary conditions and numeric modelling factors of the wave model that are permitted or recommended, while Table 35 provides the IEC-TS recommendations for model validation.

TABLE 34: IEC-62600-101 MODEL SETUP RECOMMENDATIONS

Component	Class 1	Class 2	Class 3
Physical Processes			
Wind-wave growth	●	●	●
Whitecapping	●	●	●
Quadruplet interactions	●	●	●
Wave breaking	○	●	●
Bottom friction	○	●	●
Triad interactions	●	●	●
Diffraction	●	●	●
Refraction	●	●	●
Wave reflections	●	●	●
Wave-current interactions	●	●	●
Numerics			
Parametric wave model	○	★	★
2nd generation Spectral wave model	○	○	★
3rd generation Spectral wave model	*	*	*
Mild-slope wave model	○	○	○
Spherical coordinates	●	○	○
Non-stationary solution	○	○	○
Min. spatial resolution	5 km	500 m	50 m
Min. temporal resolution	3 h	3 h	1 h
Min. num. wave frequencies	25	25	25
Min. num. azimuthal direction	24	24	24
Boundary Conditions			

Parametric boundary	○	★	★
Hybrid boundary	○	○	★
Spectral boundary	∗	∗	∗

★ = Not Permitted ○ = Acceptable ∗ = Recommended ● = Mandatory

Further requirements of the, such as those for input wind conditions, can be found in the IEC-TS documentation.

TABLE 35: IEC-62600-101 VALIDATION RECOMMENDATIONS

Criteria	Class 1	Class 2	Class 3
Data coverage			
Min. Num. of cell data points	3	5	5
Min. coverage by validation data	90%	90%	95%
Sig. wave height, Hm0	10%	5%	2%
Energy period, T_e	10%	5%	2%
Omni-directional wave power, J	25%	12%	5%
Dir. of max dir. resolved power, θ_{Jmax}	–	10°	5°
Spectral width, ε0	–	12%	5%
Directionality coefficient, d	–	12%	5%

These validation requirements include a number of additional elements to ensure proper coverage and appropriate analysis. These include the stipulation of a minimum data coverage of 70% for each month, a minimum of 1 year of validation data to accompany the modelling results, the construction of an omnidirectional scatterplot, and the evaluation of normalised error, systemic error and random error.

5.2.2 Test Case: WestWave Project, Killard Point

5.2.2.1 Overview

The WestWave (see Section 2.1.1.2) project is Ireland's first commercial wave energy project, under development by ESBI.

The goals of the WestWave project are to:

- Demonstrate Technology Readiness.
- Develop Capability and supply-chain.
- Gain Public acceptance for Wave Energy.
- Prove Opportunities for Wave Energy in Ireland
- Disseminate Learnings.

The WestWave site, then, represents a key source of resource data and commercial development data for Irish West Coast MRE projects. It is used in this work as a test case for the development of the novel ML and extreme wave characterisation techniques developed in Chapter 3 and 4, as well as a test case for the development of a first-of-kind characterisation methodology to IEC-TS standards, developed in this Chapter.

5.2.2.2 Buoy Data Resource

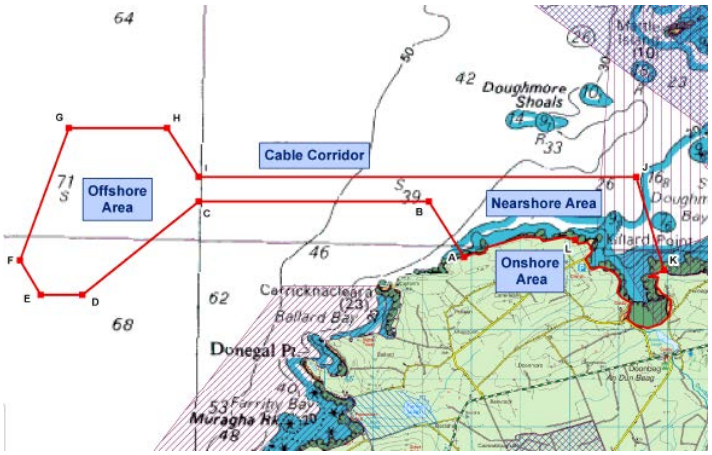


FIGURE 61: KILLARD POINT DEVELOPMENT AREA

Wave Buoy data was available from three buoy deployments made during the measurement campaign for the WestWave project. Data was collected by means of

a Datawell Waverider Directional wavebuoys, and post-processed and analysed to produce a half-hourly record of timeseries and spectral parameters. Deployment locations are outlined in Table 37, with Deployment durations and dates outlined in Table 37.

TABLE 36: BUOY DEPLOYMENT LOCATIONS / HINDCAST MODEL EXTRACTION POINTS AT KILLARD POINT

Location	Latitude	Longitude	Easting	Northing
DL1	52.762	-9.61	90500	169050
DL2	52.766	-9.58	93511	169483
DL3	52.774	-9.59	92965	170349

TABLE 37: KILLARD POINT BUOY DEPLOYMENT SUMMARY DETAILS

Deployment	DL1	DL2	DL3	Total
Start Date	19/11/2011	23/08/2012	15/10/2013	-
End Date	13/01/2012	12/12/2012	30/04/2014	-
Duration	1,323.5 hrs	2,657.5hrs	4,742.5hrs	8,723.5
No. Records	2,647	5,315	9,485	17,447

The IEC-TS validation requirements include 70% coverage for each month, and a minimum of one year duration for validation. This requirement is not fully met by the measurement campaign, with no coverage between May and late August, and a total of 8,723.5 hours falling short of the 8,760 hour requirement, though the remaining months do feature greater than 70% coverage. Fortunately, the magnitude and variability of wave parameters in the Atlantic is much larger during winter months (Young, 1999), thus the predictability of ambient conditions will not be majorly affected by the absence of calibration data during this timeframe.

5.2.2.3 Killard Point Site Characteristics

It was important to accurately characterise and achieve a better understanding of the conditions at the Killard Point site before beginning the numerical modelling. This was done using the available data from the three buoy deployments. Performing this analysis prior to beginning the numerical modelling exercise gave the baseline characteristics of the site; informing the general levels of available resource, while providing an insight into idiosyncratic conditions at the site which may have warranted further investigation during the detailed analysis which followed. This

analysis also serves to enable the calibration of the numerical wave model to recorded site conditions.

This characterisation includes an examination of the occurrence of wave conditions; with the distribution plotted for individual parameters. Histogram plots are provided to view the distribution of single parameters (H_{m0}, T_{01}, T_p for modelled data and H_{m0}, T_z, T_p for buoy data), and an occurrence matrix defined by sea-states consisting of combined $H_s - T_p$ and $H_s - T_{02}$ parameters is provided to view the joint distribution of sea-state parameters. The directionality of the site is also characterised on both an overall, and a seasonal basis.

This section serves mainly to demonstrate the process of performing data acquisition and resource analysis in line with the IEC-TS requirements.

Given the length of dataset for each, there were some key differences between the analysis methods employed for the buoy and model data analysis. The analysis of the buoy data was somewhat constrained due to the limited availability of data, particularly with regard to the inability to perform a full seasonal or monthly analysis. Using the buoy data to perform the initial characterisation of the site, overall plots representing the magnitude and distribution of each wave parameter were produced for each deployment location. In addition, both mean and peak period was used in defining a scatter plot of occurring sea-states.

The distribution of the occurrence of wave height and period parameters has been compared between buoy data recorded during buoy deployments 1-3 and the output of the Mike 21 model to ensure parity between the representation of the climate produced by the model and its actual behaviour.

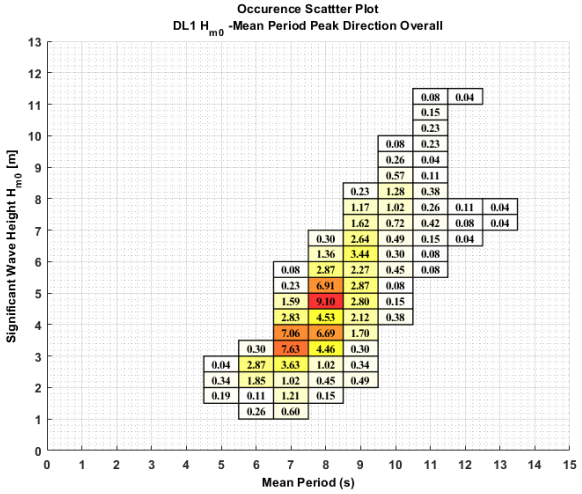


FIGURE 62: PERCENTAGE OCCURRENCE SCATTER PLOT FOR H_{M0} / T_{02} (MEAN PERIOD) AT KILLARD POINT DL1

The prevailing climate during Deployment 1, which covered the period 19/11/2011 – 13/01/2012 with 2647 records, is shown in Figure 62. Metocean conditions during this period are visibly energetic, as heavy storms were experienced. A number of sea states with an H_{m0} greater than 6m occurred and typically have an accompanying period in the range 8-11s; while a number of outlier storm events are evident in the upper right quadrant of Figure 62. The most commonly occurring bin, representing a spread of sea states, with an occurrence percentage of 9.1%, has a significant wave height between 4.5-5m and a mean wave period between 7.5 and 8s.

Figure 63 shows the distribution of H_{m0} is shown for Deployment Location 1. The energetic conditions are evident, given that the most commonly occurring H_{m0} is 4m.

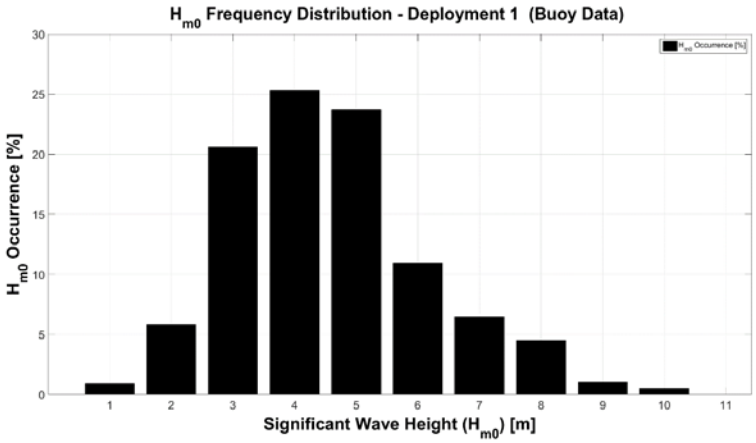


FIGURE 63: HISTOGRAM OF H_{M0} DISTRIBUTION FOR BUOY DATA AT DEPLOYMENT LOCATION 1.

The histogram of T_z distribution in Figure 64 shows that the most commonly occurring Tz is 8s, representing approximately 37% of the overall Tz Period occurrence.

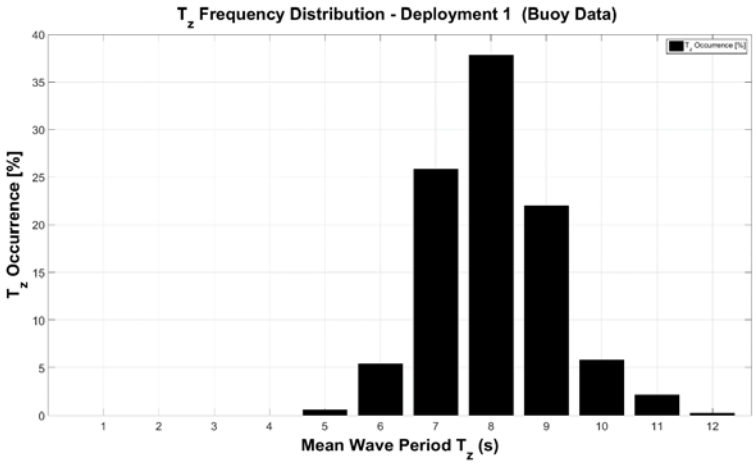


FIGURE 64: TZ HISTOGRAM OF BUOY DATA AT DEPLOYMENT LOCATION 1.

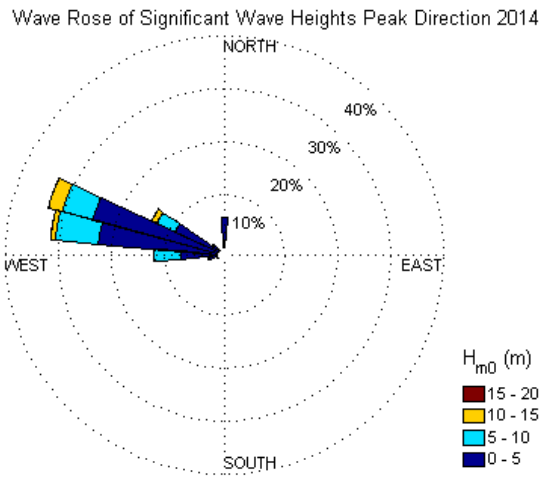


FIGURE 65: WAVE HEIGHT DISTRIBUTION ACROSS 30 (PEAK) DIRECTIONAL SECTORS FOR BUOY DATA IN 2014 (1ST JANUARY – 30TH APRIL)

It is important to note that the figures shown for the buoy deployment data are generated using a dataset of limited duration, and are thus likely to present a biased representation of conditions at the site. However, it will be shown in Section 5.3.3.2 that the hindcast data coincides well with the buoy data at concurrent times, and thus there can be confidence that the extended hindcast provides a good picture of the site conditions over a longer duration.

5.3 Metocean Modelling

5.3.1 Introduction

Meteocean modelling plays a key role throughout all aspects of the Ocean Renewable Energy project lifecycle. It is required for Site Selection and Feasibility, Development and Consents, Design, Installation, Operations and Maintenance and Decomissioning.

This section details the methodology, calibration, correction and error analysis of the modelling exercise performed for the Killard Point site. It covers the selection of domain output points, selection of input data used to achieve optimum accuracy and

establishes the level of accuracy of the modelling and its compliance with the IEC-TS modelling error and validation requirements.

The standards produced by Technical Committee (TC) 114 specifically address resource assessment requirements, design and survivability; and the evaluation and mitigation of environmental impacts. This section represents the first real-world application of the IEC TC114 62600-101 standards governing wave modelling and metocean assessment and the adherence of the modelling process to these standards.

The primary focus will be addressing the challenges associated with obtaining quality wave model input data and with the selection of an appropriate domain resolution that balances accuracy and computation time. The suitability of the accuracy limits proposed by the standards is to be examined, and the impact of the application of these standards on resource characterisation elucidated.

This modelling exercise additionally represents the cornerstone of producing reliable resource data for the WestWave Project, with the results of the analysis driving the work of device developers and informing decisions on O&M and operational strategy for the Killard Point site.

An overview of the work in this Chapter is as follows:

- Detail of wave model setup including acquisition and processing of:
    - Bathymetry Data
    - Numerical Model Boundary Data
    - Wind Data
    - Tidal Elevation Data
- Computational Grid setup from bathymetry detailed.
- Mesh Creation process in MIKE 21 SW described, including calibration to available recorded data..

5.3.2 Wave Model Setup

The analysis was primarily undertaken in MIKE21 (DHI) Spectral Wave Module described in Section 2.1.2.7. For a Class 1 IEC-TS assessment, the directionally decoupled parametric formulation available in MIKE21 SW is acceptable, and has been used in this case to greatly reduce the computational load and time involved in generating the hindcast dataset. The computational demand of the fully-spectral formulation was analysed using a preliminary model at the Killard Point, and it was found to take over three weeks to produce two weeks of hindcast data, while the accuracy of the output was not appreciably better than that achieved with the directionally decoupled parametric formulation. In addition, the fully spectral model was found to be more prone to convergence errors.

The required wind, wave, tidal and bathymetry datasets were compiled from a variety of sources which will be described. In this Section, the model set up and input parameters are presented, along with both visual and statistical model validation performed across MIKE21, MATLAB, and Python software packages.

The process for establishing and running the Numerical Wave Model is outlined in Figure 66.

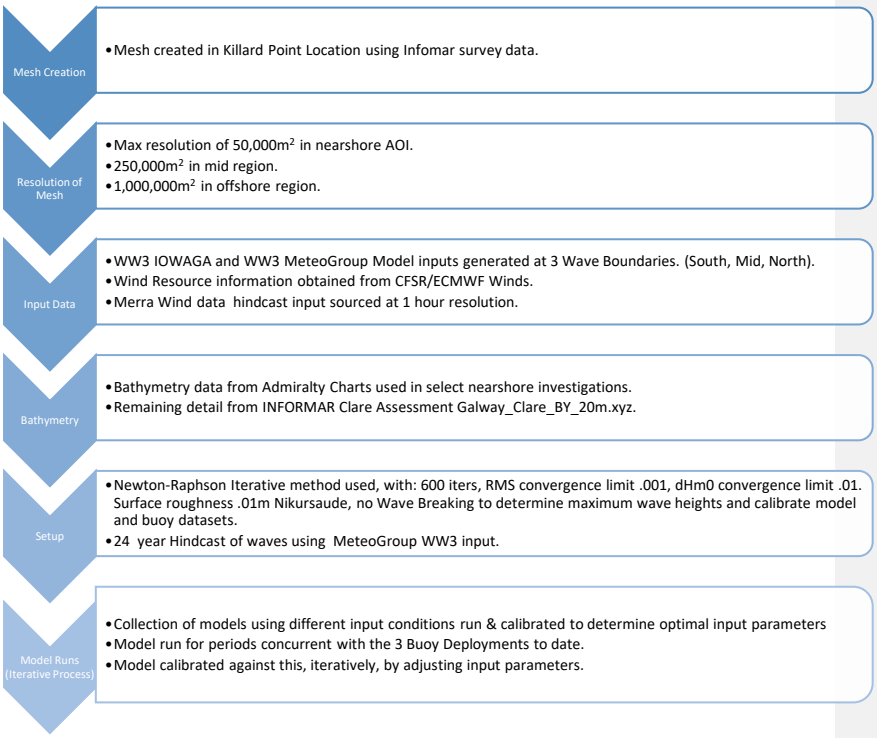


FIGURE 66: PROCESS AND SETUP OF MIKE 21 NUMERICAL MODEL AT KILLARD POINT



FIGURE 67: SITE ASSESSMENT HIERARCHY FOR KILLARD POINT AND WESTWAVE PROJECT

Figure 67 details the analysis process once a site has been chosen for detailed analysis. In IEC-TS terms, there would then follow a Class 1, Class 2 and Class 3 analysis to determine the true energy production capability and overall site characteristics in terms of operations and maintenance.

5.3.2.1 Input Data

A large number of input datasets were used during the calibration period of the model run. For simplicity and brevity, only the options which would feasibly make the final model run, and reasonably comply with the IEC-TS regarding wave modelling and resource assessment are referred to in this work.

The final model run consisted of three time-series inputs:

- MeteoGroup wave data comprising H_s, T_p, Peak Direction and Spreading Index at 4 defined Wave Boundaries in the model, which roughly correspond to South, Mid and North Boundaries. For these, information was extracted from a global WW3 model.

- Wind resource information from the M6 Weather Buoy, IOWAGA WW3 model (Rascle and Ardhuin, 2013) which includes both CFSR and ECMWF winds), and MERRA wind data.
- Tidal Elevation data, produced from a MIKE21 tidal elevation simulation based on recorded tidal gauge data at Carrigaholt, and expanded to cover the duration of the hindcast assessment

5.3.2.1.1 Bathymetry Data

In setting up the Mike21 SW wave model, using accurate bathymetric data of the local area was of paramount importance in obtaining optimal results. Great effort was made to collate bathymetry data from the best available sources, as well as ensuring that the data was consistent, reliable and as accurate as could be determined by a bench study. This involved data retrieval from several datasets, online portals and from data provided by ESBI for specific use with the WestWave Project. The data was adjusted to a uniform projection to ensure consistency amongst dataset, and accuracy and replicability in the output of the model. Measures were additionally implemented to ensure consistency in the datum used and similarity of adjoining points from disparate datasets.

Coastline data was obtained from an EU coastline dataset sourced from the Canadian Hydraulics Centre, which covered the entirety of Ireland, including the location of interest, at a suitable resolution. This was obtained in UTM-29 format, containing x, y, z coordinates, and was subsequently transformed to Irish Transverse Mercator Projection for compatibility with other inputs to the project, and ultimately for the compatibility of the model outputs run with other mapping and modelling software. Bathymetry data was obtained chiefly from a 2013 SEAI funded INFOMAR survey which covered the majority of the area of interest with a resolution of 20m. The shaded relief overlay map of the survey can be seen in Figure 68.

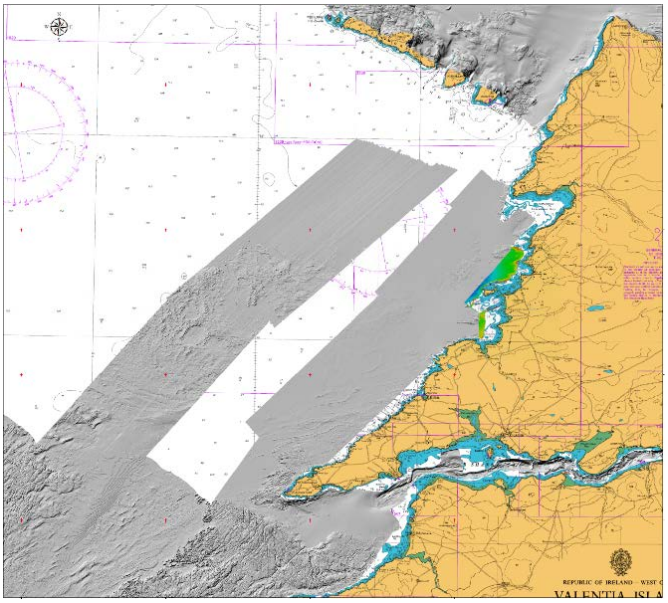


FIGURE 68: INFOMAR SURVEY OF COUNTY CLARE AREA AT 20M RESOLUTION.

The grey markings indicate the bathymetry collected as part of the INFOMAR survey. Evident in the map of the survey are missing areas in both the nearshore and offshore locations which have not been covered. The scatter data was linearly interpolated onto the computational grid (Figure 69).

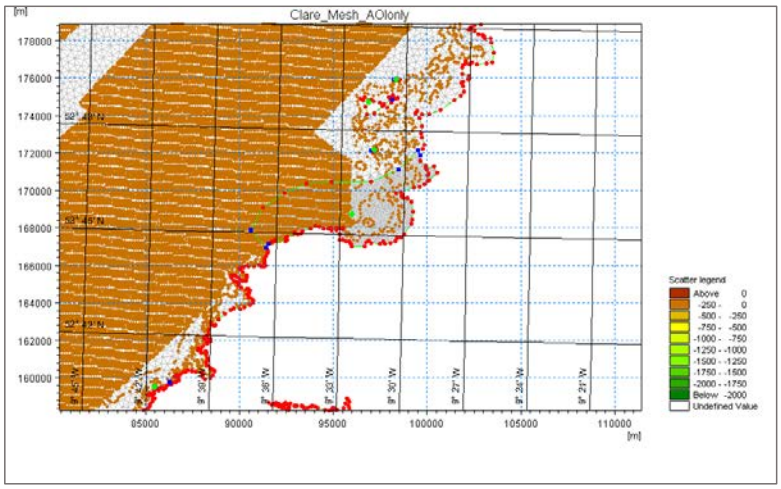


FIGURE 69: KILLARD POINT MESH CREATION IN MIKE 21 SW

In order to establish a suitable bathymetry for modelling, it was necessary to infill missing areas in the INFOMAR dataset. These were provided by digitised admiralty data that was checked against neighbouring INFOMAR survey data to ensure compatibility of datum and elevation level. The neighbouring points agreed closely, and it was not necessary to weight or otherwise manipulate the interaction of either bathymetry dataset. Figure 69 gives a view of this data infill using the admiralty data. The INFOMAR survey is the large block of ordered line surveys in the offshore area, while the admiralty data are the scattered points visible nearshore.

The INFOMAR survey was an ensemble of multiple surveys acquired between 2004 and 2013, as follows:

- EM1002 data (multibeam) acquired during Surveys CV07_01 (2007) and CE04_01 (2004).
- EM3002 data (multibeam) acquired during Surveys CV13_SEAI_1 (2013), CV13_SEAI_2 (2013),
- CV13_SEAI_3 (2013), CV12_SEAI (2012), KRY11_03 (2011), CV11_02 (2011), CV09_01 (2009) and CV08_02 (2008).
- LiDAR (airborne laser) data acquired during Aurvey LI08_01 (2008).

Acquired survey data and leg reports can be found at www.infomar.ie.

The Geodetic Control was a projection to Universal Transverse Mercator, Zone 29 N, CM 9° W and the WGS-84 Spheroid. Horizontal Control was provided by two distinct methods for survey data obtained pre and post 2011. From 2011 onwards the Positioning system was a C-Nav 3050 receiver with DGNSS corrections. Pre-2011, this came in the form of a Primary Positioning System - Fugro Starfix 3100LRS receiver with Fugro Starfix HP corrections, and a Secondary Positioning System – The Seatex Seapath 200 using Fugro Starfix Spot DGPS corrections.

The following details were available for the Celtic Voyager & Celtic Explorer vessels used for the surveys:

Positioning System

- Applanix POS-MV with DGPS corrections

LIDAR System

- Digital Surveying System: Tenix LADS Mk II Airborne System.
- Primary Positioning System: Ashtech GG24 GPS receiver with WADGPS corrections from Fugro OmniSTAR.
- Secondary Positioning System: Ashtech PNAV.

Vertical Control

- Source data is reduced to Vertical Offshore Reference Frame (VORF).

5.3.2.1.2 Numerical Model Boundary Data

The Mike 21 model's external boundary is provided in parametric form via MGWave data from the Metocean Pro model, which has been run by MeteoGroup with CFSR (NOAA) "reanalysed winds & ice" model winds. This model is based on WW3 model (v3.14) (Tolman and Tolman, 1991) fed by ensemble wind sources including CFSR from NOAA, ERA-Interim from ECMWF and altimeter data from the globwave project, ESA. It has proven to be reasonably accurate for storm conditions (Padilla-Hernández *et al.*, 2007).

There is a global model at 1° and several nests including a regional nest around Europe with a resolution of 15'x10'. The European domain has been validated against

satellite and in situ stations. The calibration performed by MeteoGroup has been focused on ambient conditions, with validation data at the M6 Weather buoy showing that severe conditions are very well captured until 12m, “beyond which there is a characteristic overestimation of wave conditions.” This was not, however, seen in a number of storm events exceeding 12m during the calibration window at the Killard Point site. The raw data is a timeseries of date, Significant Wave Height (H_s) (m), Peak Wave Period (T_p) (s), Mean Period (derived from first moment) (T_{01}) (s), Mean Wave Direction (°) and Peak Wave Direction (°) at 1-hourly intervals.

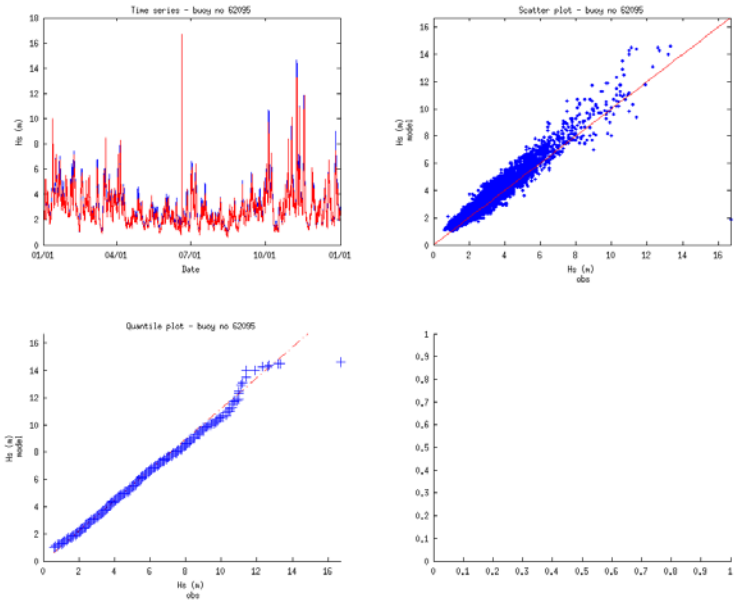


FIGURE 70: MODEL CALIBRATION DATA AT M6 WEATHER BUOY PROVIDED BY METEOGROUP

The calibration of this model, performed by MeteoGroup at the M4 weather buoy in Donegal Bay, can be seen in Figure 71 below

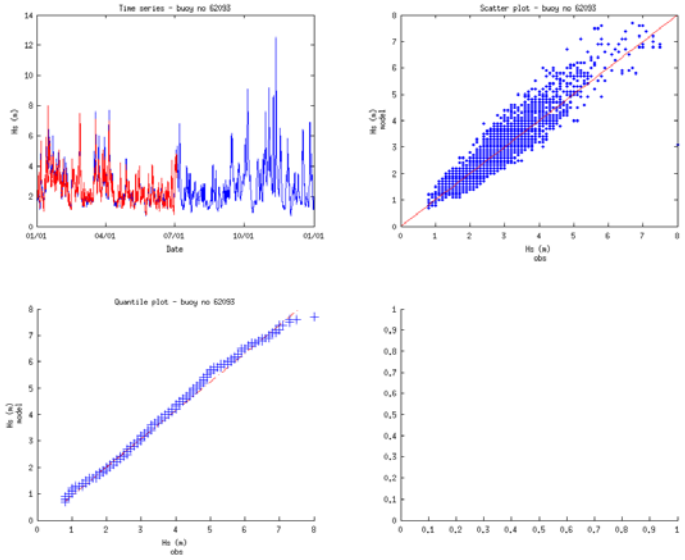


FIGURE 71: MODEL CALIBRATION DATA AT M4 WEATHER BUOY PROVIDED BY METEOGROUP

The Timeseries, scatter and Quantile-Quantile (Q-Q) plots give us a greater understanding of the degree of accuracy of the input data, and allow us to identify any potential areas for concern when using this as the basis of our parametric input wave condition.

In Figure 72 below, the same analysis is performed for the M3 Weather Buoy, located 30 Nautical Miles Southwest of Mizen Head, at 51.13N 10.33W, and again the results can be considered very accurate, with some minor deviations in the modelled Hs accuracy appearing for wave conditions in excess of 10 meters visible particularly when examining the Q-Q plot.

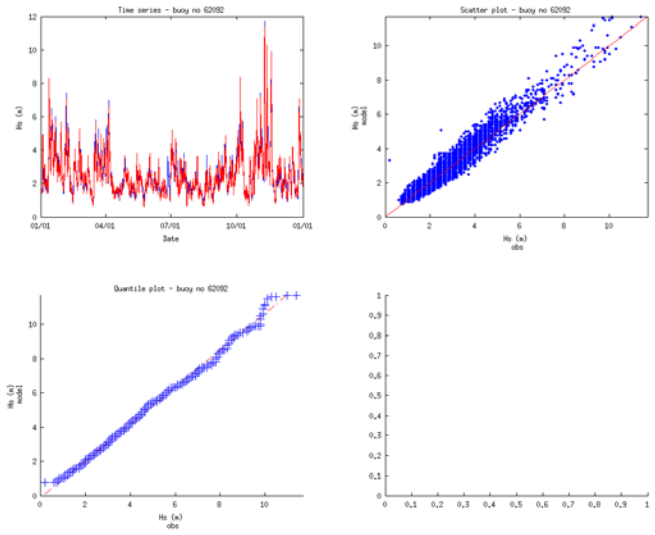


FIGURE 72: MODEL CALIBRATION DATA AT M3 WEATHER BUOY PROVIDED BY METEOGROUP

The MeteoGroup model is the primary data source for the boundary data of the MIKE 21 SW model. 24 Years of data have been obtained spanning 01/01/1991 – 31/12/2014. This data has been extracted at three locations shown in Table 38 which were chosen as source points for the south, mid and north points of the MIKE 21 SW model boundary. These locations are:

TABLE 38: EXTRACTION LOCATIONS FOR METEOGROUP WW3 WAVE DATA

Location	Latitude	Longitude	Latitude	Longitude
South	52°20'N	10°50'W	52.33°	10.83°
Mid	52°40'N	10°40'W	52.67°	10.67°
North	53°00'N	10°10'W	53.00°	10.17°

The input boundaries within the MIKE 21 SW model domain for these conditions are shown in Figure 73.

5.3.2.1.3 Wind Data

Wind data has been obtained from ensemble sources. MERRA hindcast wind data at 1-hourly intervals was the primary source used to drive the hindcast model. Additional wind data was obtained from the M6 weather buoy operated by Marine Institute Ireland, IOWAGA WW3 model (which includes both CFSR and ECMWF forcing winds) for comparison and calibration of the model.

5.3.2.1.4 Tidal Elevation Data

Tidal elevation data has been generated using a MIKE 21 SW tidal elevation model, with recorded input data from the nearby tidal gauge data at Carrigaholt. The data was recorded over a period of approximately 1 year, and a tidal harmonic analysis perfomed in the MIKE software was used to extract the constituents of the tidal behaviour and to make a prediction for the water surface elevation at Killard Point for the hindcast.

5.3.3 Modelling Methodology

5.3.3.1 Mesh Creation

A mesh consistent with IEC-TS Class 1 and 2 requirements was implemented in the study area, spanning 14,000 km^2. The mesh setup is shown below in Figure 73.

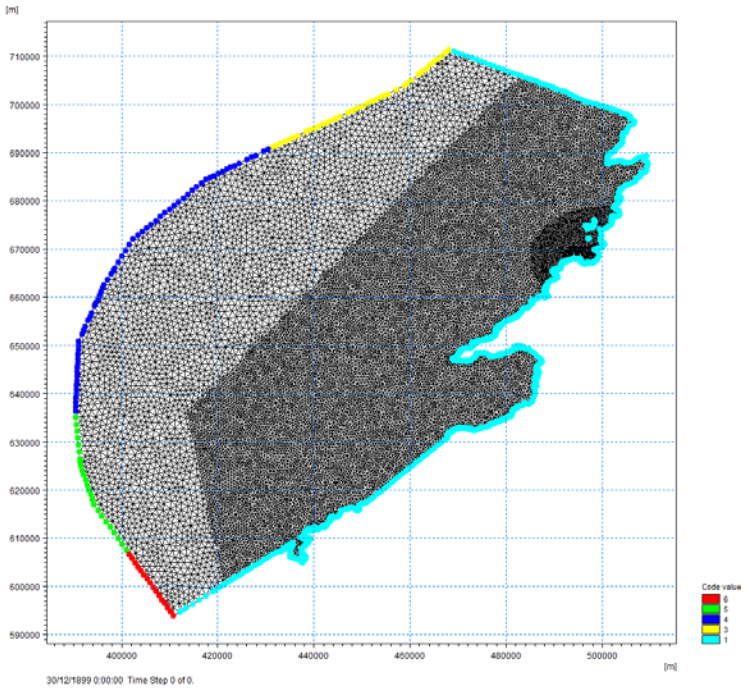


FIGURE 73: KILLARD POINT STEPPED TRIANGULAR MESH (MIKE 21 SW)

The area of interest covers the Killard Point location with high resolution triangular mesh of 50,000m^2 maximum area. Expanding from this inner mesh is a 100,000m^2 mesh and an outer mesh, at two progressively increasing resolutions of 250,000m^2 and 1,000,000m^2. The computational domain covers a large area of the western coastline of Ireland, and extends outwards to the location of the best available input boundary data, which occurs in an area where wave conditions and bathymetry are reasonably homogenous.

For this modelling exercise, the stepped grid implemented allowed for a much better representation of wave conditions in the wider environment, and sufficient distance for the stabilisation of wind and wave conditions between the boundary conditions and the nearshore site. It also preserved the high resolution required to ensure validation of wave conditions within the environment of interest according to the IEC-TS requirements.

The model domain consists of 38,045 elements, 20,093 nodes, and spans 390354m – 509452m Easting and 593951m – 711375m Northing, encapsulating an area of approximately 14,000km^2.

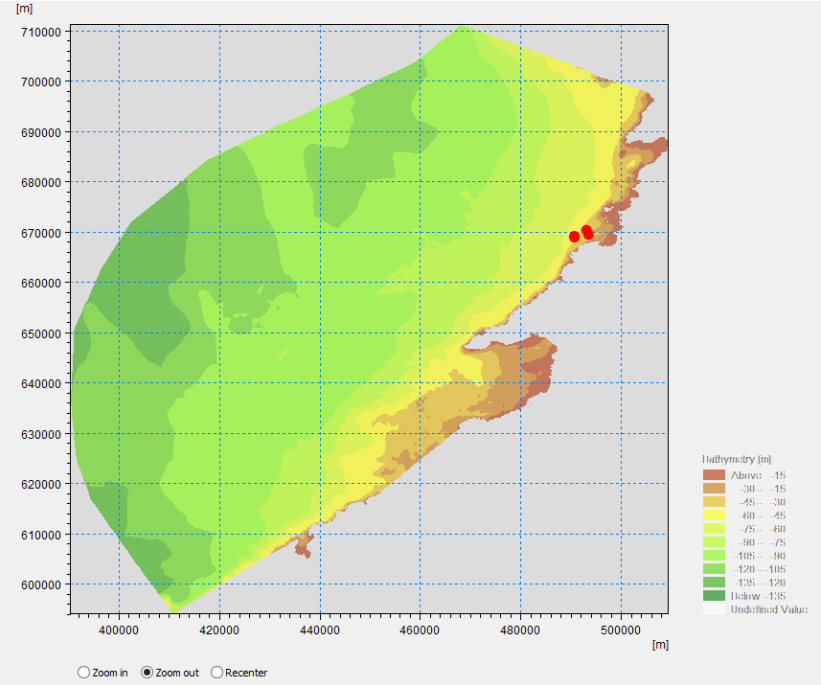


FIGURE 74: MODEL DOMAIN (BUOY DEPLOYMENT 1-3 LOCATIONS USED FOR INITIAL CALIBRATION HIGHLIGHTED - DEEP RED)

Figure 74 shows the domain of the MIKE 21 SW model at Killard Point, after the mesh has been interpolated and smoothed. The locations of three buoy deployments, spanning 2011 – 2014 are highlighted (dark red circles). These points are used as the reference in the initial model calibration. The model extraction points, corresponding to the three buoy deployment locations, are shown in Table 36.

The complexity of the mesh and features within it was altered a number of times to optimise the resolution of the output, while keeping model run-times at a sustainable level. Aside from creating four defined mesh areas with varying resolution from 50,000m^2 to 1,000,000m^2 in deeper water, a number of changes to the mesh and

node points were required to ensure even transition of mesh size and bathymetry to prevent convergence issues during the modelling process.

All data sources with a spatial component were standardised to an ITM projection to ensure the consistent location of features and the utility of the project outputs for the developer by using a projection consistent with that chosen for other relevant project elements.

Figure 75 below outlines the location of the Mike21 SW model extraction points. These correspond to five Nearshore locations, and one Offshore location that represent potential sites for the future deployment of WEC devices as part of the WestWave project. Coordinates of these locations are given in Table 39.

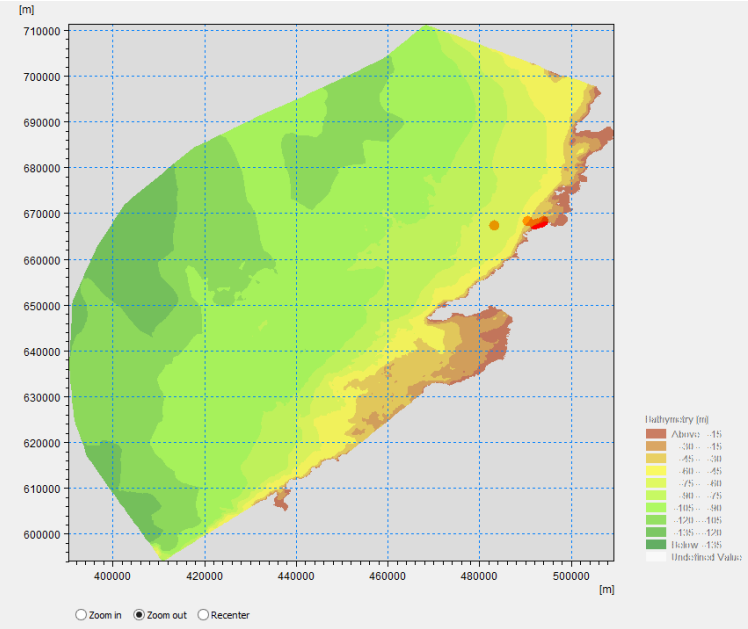


FIGURE 75: MODEL DOMAIN (NEARSHORE AND OFFSHORE MODEL OUTPUT POINTS HIGHLIGHTED)

TABLE 39: MIKE 21 MODEL OUTPUT POINTS (NEARSHORE AND OFFSHORE LOCATIONS FOR STATISTICAL ANALYSIS HIGHLIGHTED)

Model Output Location	Easting	Northing	Latitude	Longitude
Nearshore	90500	168357	52.76	9.62
Offshore	**83214**	**167321**	**52.74**	**9.73**
Nearshore 2	**94000**	**168357**	**52.76**	**9.57**
Nearshore 3	93410	168000	52.75	9.58
Nearshore 4	92650	167750	52.75	9.59
Nearshore 5	92000	167500	52.75	9.60

The Nearshore 2 point is taken as the primary "Nearshore" location for the purposes of this report, and is referred to as-such from now on. It is located in approximately 16m water depth, in line with the expected deployment depth for the bottom-mounted WEC device. In addition to the marked points, the hindcast model also outputs a subset of parameters at a more limited temporal resolution over the entire domain shown.

5.3.3.2 Model Calibration

5.3.3.2.1 Initial Model Calibration

A statistical analysis and comparison of model output and wave buoy data was performed at Deployment Locations 1-3 (Figure 74 and Table 36) to verify the integrity of the data and ensure proper setup of the model.

Undertaking a Class 1 modelling exercise at Killard Point, three validation points were used. The minimum data coverage of 70% stipulated for each month, however, was not possible due to the timing of the measurement campaign which was carried out - and the resultant lack of data from April - August. This is an important consideration for projects which will follow the IEC-TS, as it will necessitate that buoy deployments for measurement campaigns achieve high availability across each month.

During initial calibration, IOWAGA WW3 model data was used to drive the model boundary conditions; and statistical comparisons showed that it matched the mean conditions at the Killard Point site with very good accuracy. A visual inspection and extreme wave analysis, however, revealed that the IOWAGA data resulted in under-prediction of wave heights during large storm events.

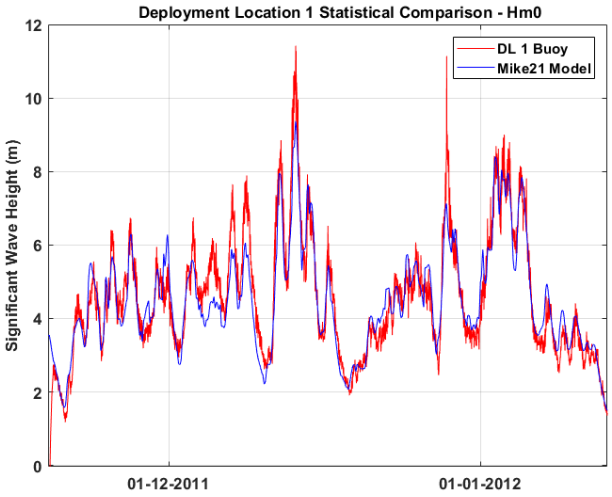


FIGURE 76: UNDER PREDICTION OF H_{M0} CONDITION DURING STORM EVENTS USING IOWAGA WW3 INPUT

MeteoGroup data was obtained due to concerns with the IOWAGA data regarding the prediction of extreme wave events. Calibration tests at DL1-3 were run again with MeteoGroup data input, which was archived at 1 hourly intervals. It was found that the MeteoGroup data gave approximately equal statistical fit to the buoy dataset, while better representing the storm conditions. The correlation of mean wave period was greatly improved in comparison to the 3-hourly IOWAGA data. Additionally, this change fully satisfy the requirements of the IEC-TS, which stipulate that the minimum time interval for the numerical model output cannot be less than that of the data used for the numerical boundary input.

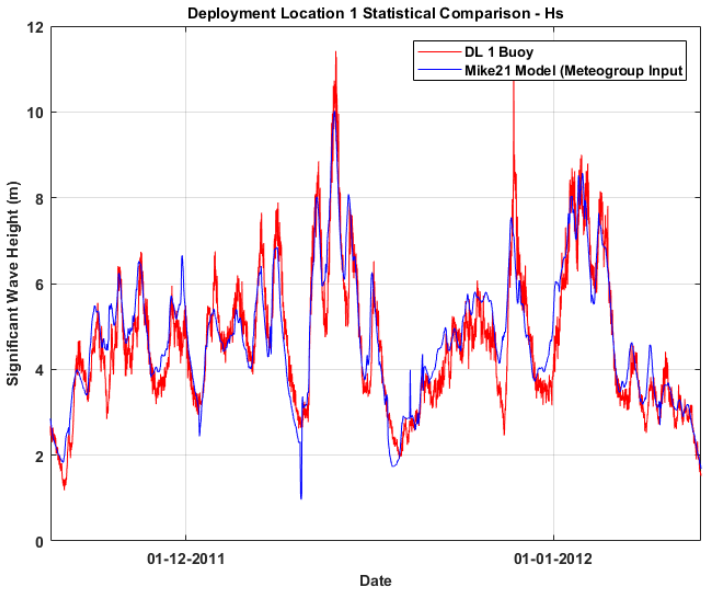


FIGURE 77: H_S COMPARISON - MIKE21 MODEL HINDCAST USING METEOGROUP DATA AT DEPLOYMENT LOCATION 1

Comparing Figure 76 and Figure 77, it is evident that the hindcast model using MeteoGroup input performs better for the prediction of storm events, not exhibiting the same level of under-prediction as the IOWAGA data.

5.3.3.2.2 Final Model Calibration

The calibration of the model at the 3 deployment locations is displayed below. Figure 78, Figure 79 and Figure 80 show the model's accuracy in estimation of H_S at the Killard Point site, matching the mean conditions very closely, while underestimating wave heights during large storm events. No time lag was observed in the model across all deployments, but a visible time lag is introduced in Deployment Location 2 and 3 below, caused by missing buoy data. This time lag was corrected during database creation for the statistical comparison of wave parameters. The difference in the sample time between recorded and modelled data generally does not present any issues, though the modelled data is "smoothed" to a greater degree. In synchronising the two datasets, the Hampel filter is applied to the input vector, x, to detect and remove outliers. For each sample of x, the function computes the median

of a window composed of the sample and its six surrounding samples, three per side. It also estimates the standard deviation of each sample about its window median using the median absolute deviation. If a sample differs from the median by more than three standard deviations, it is replaced with the median.

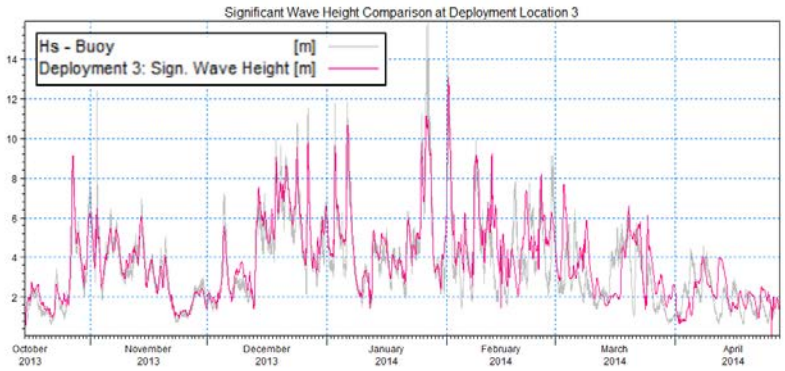


FIGURE 78: H_S CALIBRATION AT DEPLOYMENT LOCATION 1

H_s correlation between buoy and model is excellent (Figure 78), with both ambient and storm conditions represented by the model. Under prediction of large storm events is evident at a number of points, which can be attributed in part to the longer averaging period of the input model data (1 hour) vs the buoy (half-hourly). H_s prediction at deployment location 1 accurately mirrors that recorded by the buoy for the same period. The model shows no visible timelag, minimal bias, and very good correlation overall. There is a notable rounding of storm events, with the model showing a tendency to "smooth," and underpredict storm events, and rapid changes in H_s in general. This results in a maximum underprediction of approximately 1m H_s (discounting outliers) during deployment 1. The impact of this is likely limited to extreme analysis, and the calibration proves that the input data and modelling setup are more than adequate to produce output data to a high standard.

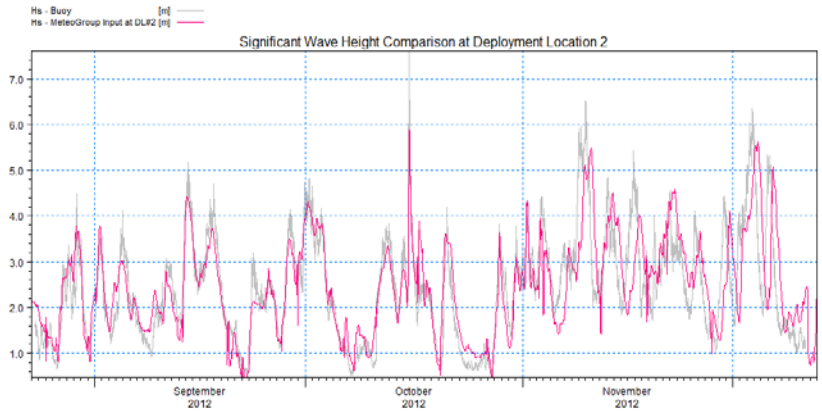


FIGURE 79: H_S CALIBRATION AT DEPLOYMENT LOCATION 2

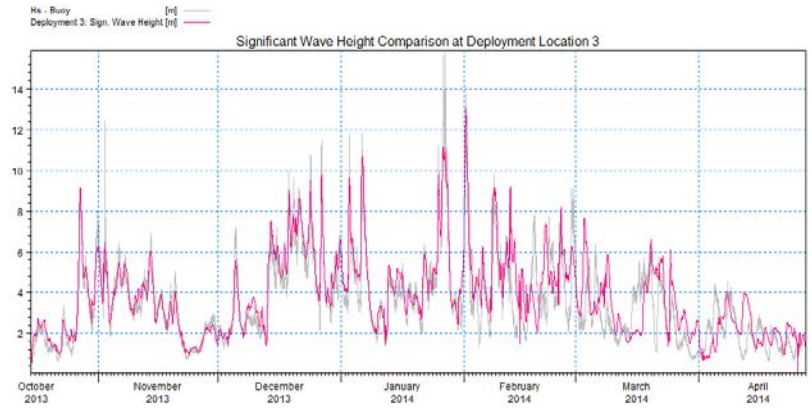


FIGURE 80: H_S CALIBRATION AT DEPLOYMENT LOCATION 3

The H_S calibration results for deployment Locations 2 & 3 mirror those of deployment location 1, exhibiting the same high accuracy in both magnitude and phase. There is, however, a notable time lag introduced towards the end of October 2012 and January 2014 due to missing buoy data for these periods. This is visible in Figure 79 and Figure 80, but is corrected by synchronising the model and buoy datasets prior to the statistical analysis performed; the results of which are presented in Table 40.

The model represents the mean wave direction well, capturing both magnitude and temporal variations with some skill. There is, however, a constant bias of approximately negative 5-10 degrees when compared to the recorded data.

Commented [A11]: The averaging of 3 wave boundary inputs in the south, mid and north likely gives rise to this behaviour. Why?

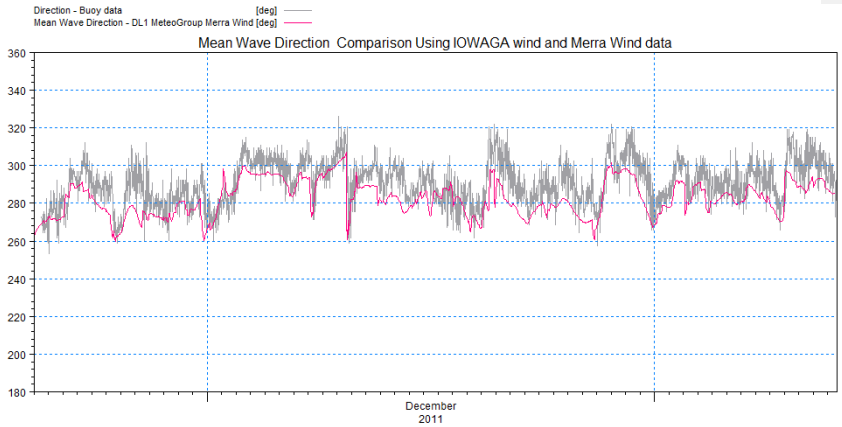


FIGURE 81: MEAN WAVE DIRECTION CALIBRATION AT DEPLOYMENT LOCATION 1

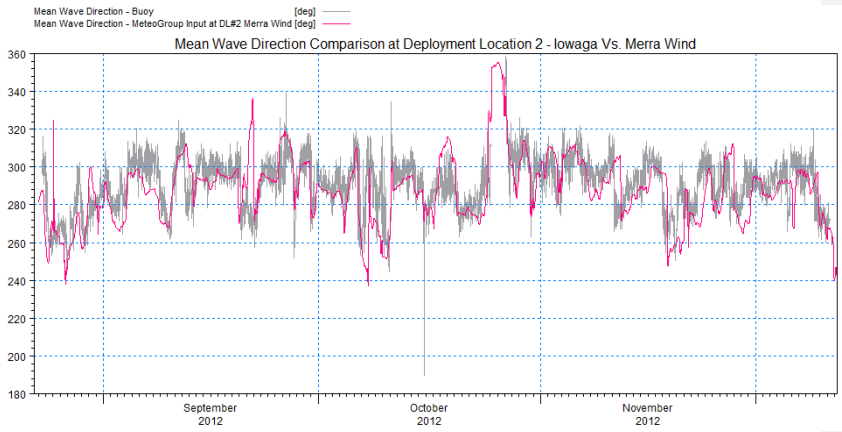


FIGURE 82: MEAN WAVE DIRECTION CALIBRATION AT DEPLOYMENT LOCATION 2

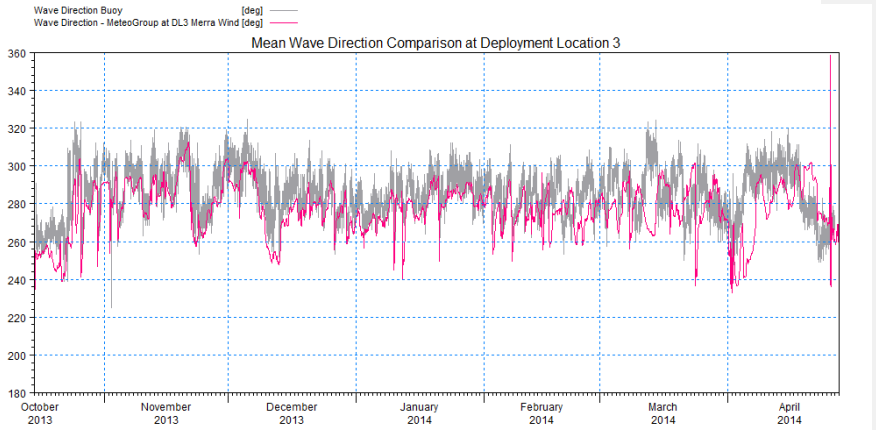


FIGURE 83: MEAN WAVE DIRECTION CALIBRATION AT DEPLOYMENT LOCATION 3

The overall granularity of the model is far lower than the buoy data, exhibiting far fewer mean wave directions, likely due to the longer averaging periods of both the input wind data for the model, and the 1 hour temporal resolution of the model output vs. the 30 minute resolution of the Waverider buoy output.

Peak Period is very well represented by the MIKE21 model, showing excellent correlation, lack of apparent time-lag, and magnitude which is very well represented. It does exhibit some smoothing when compared to the buoy data; similar to the behaviour of mean wave direction displayed in the section above. Further, the model has a tendency to under predict the extremes of Peak Period. This is particularly visible in Figure 84 and Figure 85 below. This under prediction, combined with underprediction in the values of H_s does present difficulty in the analysis of extreme wave events, and particular caution should be exercised in the interpretation of the results, as they may suggest lower values of extreme wave height than are likely to occur.

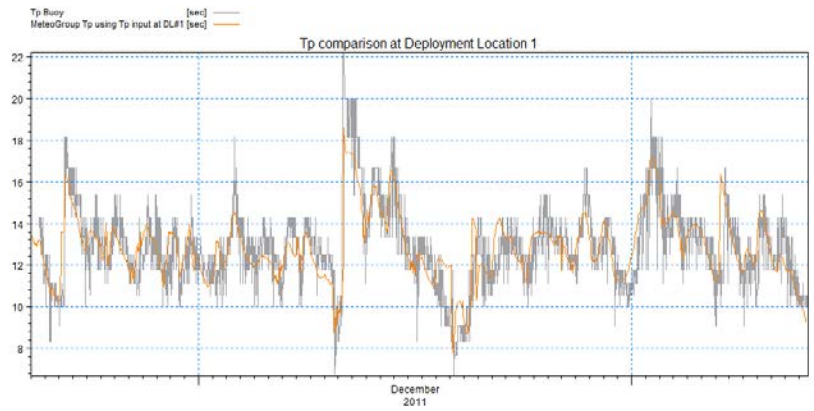


FIGURE 84: T_P CALIBRATION AT DEPLOYMENT LOCATION 1

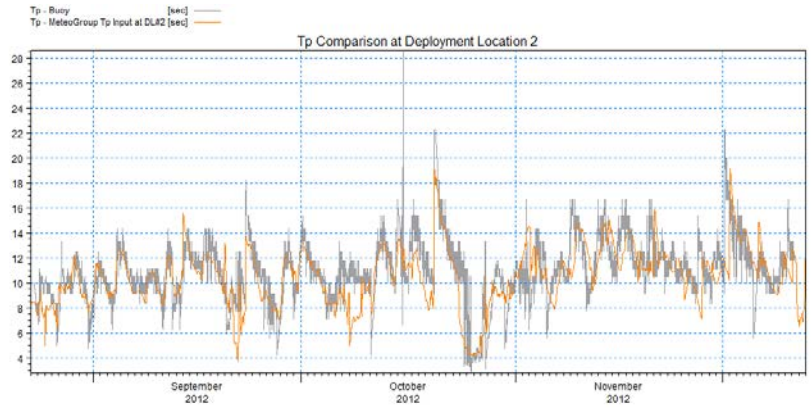


FIGURE 85: T_P CALIBRATION AT DEPLOYMENT LOCATION 2

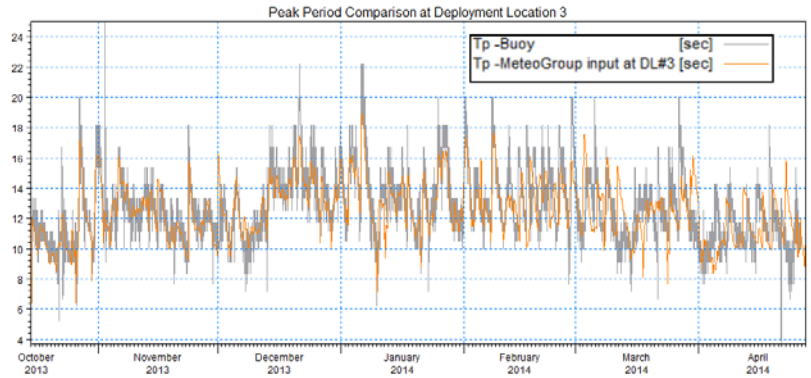


FIGURE 86: T_P CALIBRATION AT DEPLOYMENT LOCATION 3

The Peak Period parameter changed rapidly throughout the duration of the Deployment Location 3 deployment. The model coped admirably, exhibiting the same low bias and RMSE errors as for Deployment Location 1 & 2.

Calibration results for deployment locations 1-3 were as follows:

TABLE 40: STATISTICAL ANALYSIS OF MIKE21 MODEL USING METEOGROUP INPUT - AGAINST BUOY DEPLOYMENT DATA

Location		DL1	DL2	DL3
Parameter	**Metric**			
H_s	Bias (m)	0.1466	0.0369	0.2789
	RMSE (m)	0.6575	0.4925	0.9687
	Rcorr	0.9185	0.9057	0.9057
T_p	Bias (s)	-0.0762	-0.4128	-0.1103
	RMSE (s)	0.7739	0.7143	0.6824
	Rcorr	0.9185	0.9057	0.9057

The model produces results which compare favourably with the data obtained from the buoy deployments, having very low bias and RMSE, with an Rcorr value of above 0.9, indicative of good model fit.

The IEC standards stipulate that statistical analysis results be presented in terms of percentage. These are presented in Table 41 below, with the addition of T_e and Power calibration results.

TABLE 41: STATISTICAL ANALYSIS OF MIKE 21 SW MODEL USING METEOGROUP INPUT - AGAINST BUOY DEPLOYMENT DATA (POST-CALIBRATION).

Location		DL1	DL2	DL3
Parameter	**Metric**			
H_s	Bias (%)	10.84	15.48	13.33
	RMSE (%)	14.19	19.76	18.59
	Rcorr	0.92	0.91	0.95
T_p	Bias (%)	8.09	13.38	8.66
	RMSE (%)	10.90	18.03	12.23
	Rcorr	0.74	0.73	0.79
T_e	Bias (%)	6.20	9.71	6.83
	RMSE (%)	7.96	12.85	8.81
	Rcorr	0.86	0.82	0.87
Power (J)	Bias (%)	22.68	10.30	26.38
	RMSE (%)	34.36	13.26	56.57
	Rcorr	0.91	0.90	0.93

Table 41 displays the statistical analysis results for the three model extraction locations analysed alongside concurrent buoy data. Correlation Coefficient results are excellent for H_s, Power, and T_e, while inherent difficulties with the correlation of "peak" parameters produced by disparate sources reducing the correlation coefficient to 0.74 – 0.79 for T_p. R Correlation values in excess of 0.9 for H_s and Power are indicative of good model performance, while a bias of 10 – 15% for H_s is very good, despite falling marginally outside the requirements of the IEC-TS.

Overall, the calibration results reveal model performance that is in line with the current state-of-the-art.

5.3.3.3 Model Output

A first of kind Class 1 model assessment was performed according to the IEC-TS, using parametric wave data inputs (H_s, T_p, Peak Direction) and a 3rd generation spectral wave model. 24 years of high quality hindcast data was produced, with output at multiple validation points indicative of likely locations of WEC deployment. Attempts were

made to follow the guidelines for a Class 3 model assessment according to the IEC-TS where possible, but a number of relaxations were made according to Annex A of the standards, which specify that model components found not to have greater than a 5% threshold difference can be omitted. This included the omission of a fully spectral formulation input approach, as the memory and computational requirements were deemed excessive.

After repeated A/B testing on a validation dataset, the ultimate parameters chosen were the best attainable in terms of balance of cost, practicality, adherence to time constraints, and accuracy. The chosen parameters ensured that the model benefitted from drastically improved computation times, while maintaining a desirable level of accuracy. The methodology for selecting parameters in this work will inform future commercial projects seeking to follow the IEC-TS. The model output has been validated against in-situ buoy measurements at three separate locations for a total duration of approximately one year. The accuracy of the results compare favorably to state-of-the-art nearshore hindcast models for Ireland, e.g. (Gallagher *et al.*, 2013).

This hindcast data has been analyzed to determine summary statistics of key wave parameters according to the proposed IEC standards. This includes an assessment of the monthly and annual variation of the key parameters, H_s, T_e and wave power, giving a greater understanding of the characteristics of this energetic site. The analysis of wave power variability is of particular value to a site developer, informing them of both the magnitude and expected variability of the resource. The stringent requirements for validation accuracy were difficult to attain, and do not mirror what is currently achievable by state-of-the-art models. The accuracy of the wave model produced in this work is in the region of 10 – 15% bias and 15 – 20% RMSE for H_s, and 10 – 26% bias and 13 – 56% RMSE for wave power (Table 7). Despite displaying very encouraging statistical metrics and correlation with the buoy data at concurrent deployments, this falls outside the standards defined for even a Class 1 (Reconnaissance)— assessment. These standards, while admirable, are particularly onerous, and are unlikely to be met by most existing models with the majority of available data sources. Only after calibration can results reach below a 10% bias or

RMSE error. In this case, the validity of MCP and calibration methods used become increasingly important, and thus are found to be too lightly covered by the IEC-TS standards. This Class 1 analysis has served its purpose in highlighting

Some general statistics derived from the resource characterisation are presented (in part) below. This is not intended to be an exhaustive report of the analysis, but to present a summary of the results derived from performing an analysis to IEC standards and to give a basis for a full discussion of the site characteristics. The results derived from the characterisation of the resource based on the 24 years of hindcast data produced through the modelling exercise are shown below (Table 42).

TABLE 42: SUMMARY STATISTICS FOR HINDCAST DATASET

Hindcast Model Parameter	H_s (m)	T_1 (s)	T_e (s)	Wave Power (kW/m)
Std Dev	1.49	1.63	1.87	71.08
Median	2.19	1.64	8.83	20.47
Mean	2.55	7.59	8.94	45.52
10th Percentile	1.05	7.47	6.71	3.80
90th Percentile	4.58	5.65	11.41	113.79
Maximum Value	14.04	9.79	16.45	1,536.75
Minimum Value	0.11	14.76	2.78	0.00

With a mean Hs value of 2.55m and a maximum of 14.04m, the Killard Point site is clearly energetic, and thus represents a promising location for the deployment of WECs. A mean wave power value of 45kW/m at the nearshore location is in line with the values expected at a West Coast Site in approximately 20 meter water depth, and represents a suitable resource for the deployment of the typical nearshore wave energy converter. The standard deviation of the Wave Power is very large, and the maximum value of wave power recorded is in excess of 30 times the mean wave power value. Taking this alongside the 90^{th} percentile value of wave power highlights the sporadic nature of high energy generation periods in Wave Energy, with colossal chunks of energy present during storm conditions, and far reduced wave power during more benign conditions. To further this analysis prior to final design of the site for the deployment of WECs, it would be extremely prudent to examine the

extractable wave power for a given device, with the presumption that a typical device would not be operable in such extreme conditions.

The following Section 5.4 will characterise the Wave Resource available using the results of the modelling in greater detail.

5.4 Wave Resource Characterisation

This section focusses on the important characteristics of the Killard Point site in relation to commonly occurring conditions, extreme values, seasonal and annual variability, and a multitude of factors which are commonly used in the determination of energy production potential and accessibility for operations and maintenance. The general nature of the wave energy resource is characterized, allowing the identification of energy-rich sea-states, and the methodologies devised in Chapter 3 and 4 are implemented here. This resource assessment is the first to be conducted at a "Class 1" IEC-62600-101 standard, and elements of a "Class 2" or "Class 3" assessment have also been assessed and integrated where possible.

The metocean analysis includes Scatter Plots, Variability of Wave Height and Period parameters, Power Production, Directional Wave Rose analysis, Weather window analysis and an Offshore/Nearshore directional dependence analysis, and the analysis has been performed for the gamut of conditions defined in Figure 89 below.

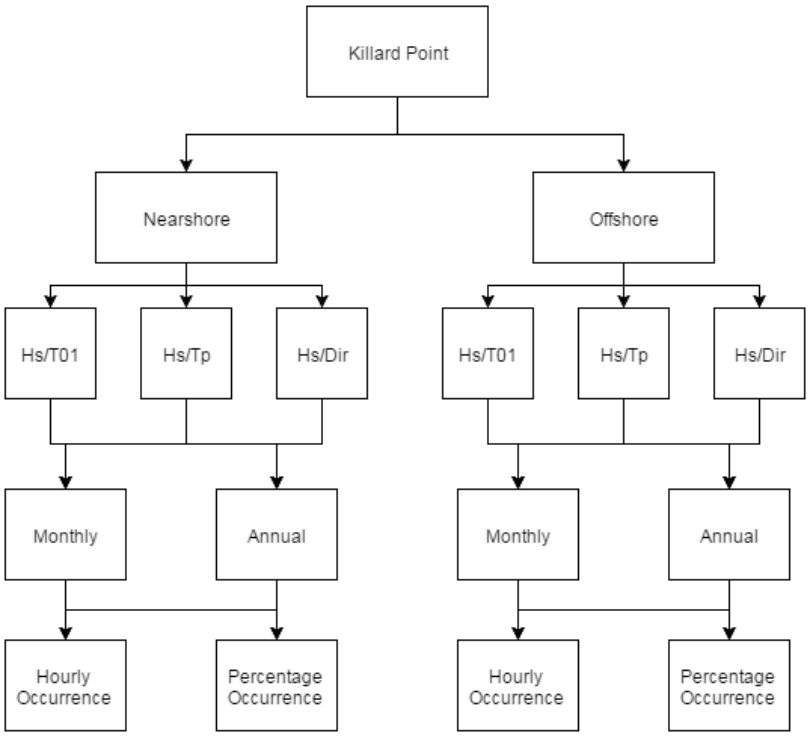


FIGURE 87: HIERARCHY OF CONDITIONS ASSESSED FOR EACH ANALYSIS AT KILLARD POINT SITE

Each assessment contained within the Metocean assessment was analysed for each of the conditions as indicated in the Tree Hierarchy Diagram (Figure 66). The volume of analysis produced does not lend itself to reproduction here, but further detail and additional results will be provided in the appendix documents. Particular cases of interest and broad trends rendered using the resulting analysis will be presented.

5.4.1 Magnitude and Variability of Wave Resource at Killard Point

The variation in resource on a monthly, seasonal and annual basis is an important consideration in the planning and development of a WEC development, as it has wide ranging influence on the energy output, which has a direct impact on the economic viability of any proposed project. Predicting, or at minimum accurately characterising the level of variability that can be expected at a site, is crucial in reducing the uncertainty associated with the project, and will allow for more detailed and comprehensive financial modelling for the developers.

The long term hindcast produced by the model for the Killard Point Dataset is used here to assess the variability of the average climate statistics for monthly and yearly time periods. Adding to the analysis of site conditions performed using buoy data in Section 5.2.2.3, the increased duration of the hindcast model dataset produced allowed for a larger focus on seasonal and inter-annual variations, and a full breakdown of each is provided. The results for both the inter-annual and monthly variability are presented, with these statistics reflective of the variation in conditions that can be expected at the site over both short and longer time-scales; examining wave height and period variation, most commonly and least frequently occurring conditions, and offering an assessment of the distribution of these parameters over the 24 year period, allowing an overview of the impact that changing weather conditions will have upon accessibility. This is crucial to provide information for installation and maintenance, for O&M and to serve as a guide for the average annual energy production at the site.

Given the current awareness and increasing discussion of Global Warming, it would be remiss not to mention here that there was no significant trend with regards to positive or negative movement of any parameter over inter-annual timescales, and any such movement would be out-weighed by the significant yearly variation which exists; however, climate change has the ability to be particularly influential over a longer time scale, and it is certainly conceivable that it's influence would be felt over the lifetime of a wave farm, which would typically be expected to be 25-50 years. Apart from changes in the overall magnitude of parameters, it has been suggested that climate change may elicit an increase in the occurrence of instances of both calm and extreme sea-states (Reeve *et al.*, 2011), effectively increasing difficulty in operating a WEC farm.

The summary statistics of the main wave parameters for the hindcast dataset are shown below. The output parameter validation required includes T_e Wave Period, which was not available from the MIKE 21 SW model. This parameter was generated using a number of Measure Correlate Predict (MCP) methods, including a simple linear relationship based on the Bretschneider spectrum, and a machine learning model whose creation is detailed in Chapter 3 and in (Barker and Murphy, 2016). The

diagram below summarises the approach which was used to generate the T_e wave period.

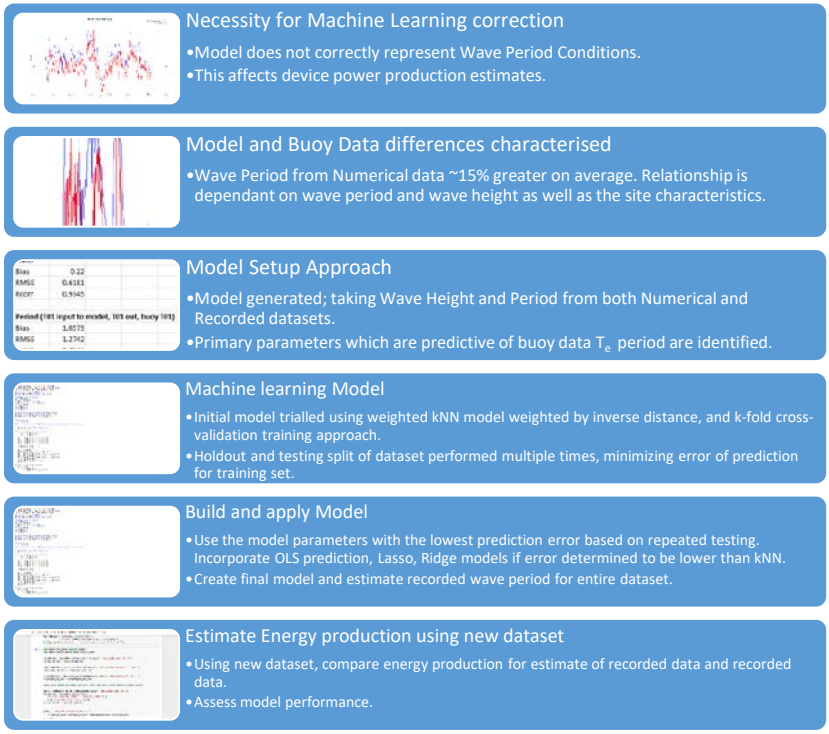


FIGURE 88: MACHINE LEARNING MODEL DEVELOPMENT OVERVIEW

T_{01} and T_e period have been calibrated and corrected against the buoy data to reduce the high bias and Root Mean Square Error (RMSE) values, while H_s has not been altered, and T_p is left unaltered due to the inherent variability associated with the prediction of "peak" parameters.

5.4.1.1 Annual Variability

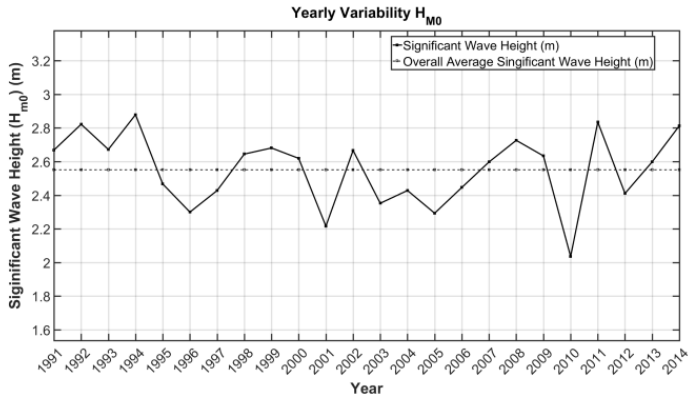


FIGURE 89: ANNUAL MEAN H_S AND VARIABILITY AT KILLARD POINT

The annual mean H_s (shown in Figure 89) exhibits significant inter-annual variability. The overall average value of 2.55m is indicative of energetic conditions at the site, while the minimum value of 2.04m occurring in 2010 and maximum of 2.88m occurring in 1994 respectively bound a particularly variable resource. There is an overall trend towards decreasing H_s, but the magnitude of this change is small and it cannot be considered a significant linear trend ($p = 0.536$, $p > 0.95$). The maximum H_s noted in the hindcast was 14.04m.

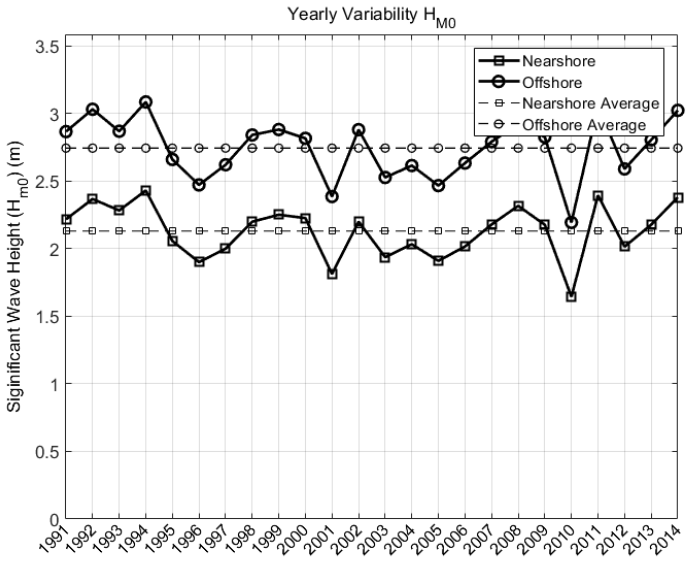


FIGURE 90: ANNUAL MEAN H_S AND VARIABILITY (NEARSHORE AND OFFSHORE) AT KILLARD POINT

Figure 89 displays the annual variability of the H_{m0} parameter over the period 1991-2014, separated into the nearshore and offshore sites. The average nearshore H_{m0} is 2.13m, and the yearly standard deviation is 0.21m. The average offshore H_{m0} is 2.74m and the yearly standard deviation is 0.23m. The average H_{m0} in the nearshore environment visibly mirrors the H_{m0} offshore, albeit at a magnitude approximately 22% lower.

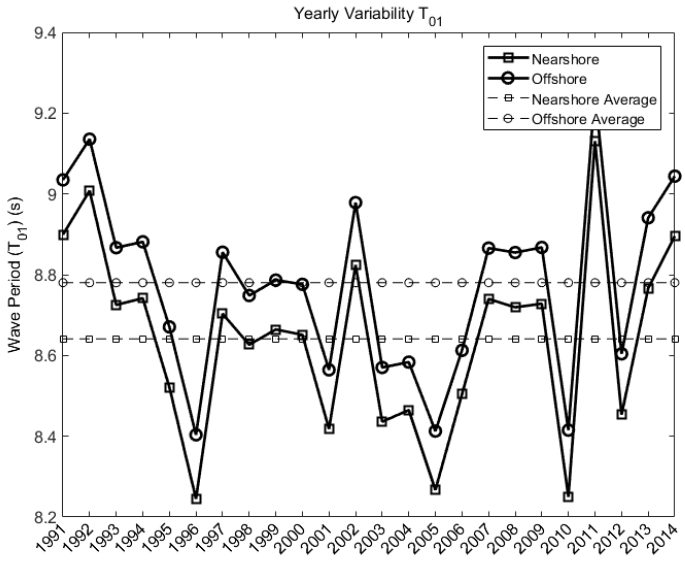


FIGURE 91: ANNUAL T_{01} VARIABILITY AT KILLARD POINT SITES

Figure 91 displays the annual variability of the spectral wave period, T_{01}. The average nearshore T_{01} is 8.64s, and the yearly standard deviation is 0.237s. The average T_{01} in the offshore environment is 8.78s, with a yearly standard deviation of 0.229s. The offshore site exhibits minorly less variability in wave period condition than the nearshore site.

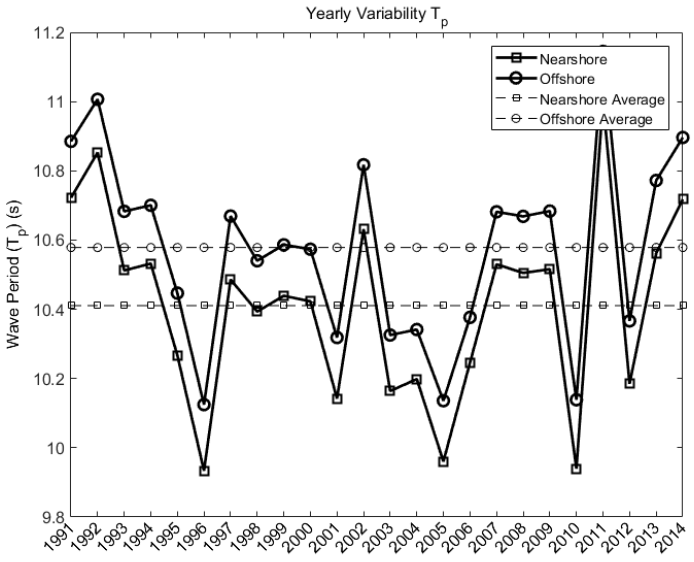


FIGURE 92: ANNUAL T_P VARIABILITY AT KILLARD POINT SITES

Figure 92 displays the annual variability of the spectral wave period, T_p. The average nearshore T_p is 10.41s, and the yearly standard deviation is 0.285s. The average T_p in the offshore environment is 10.58s, with a yearly standard deviation of 0.275s. The offshore site again exhibits minorly less variability in wave period condition than the nearshore site.

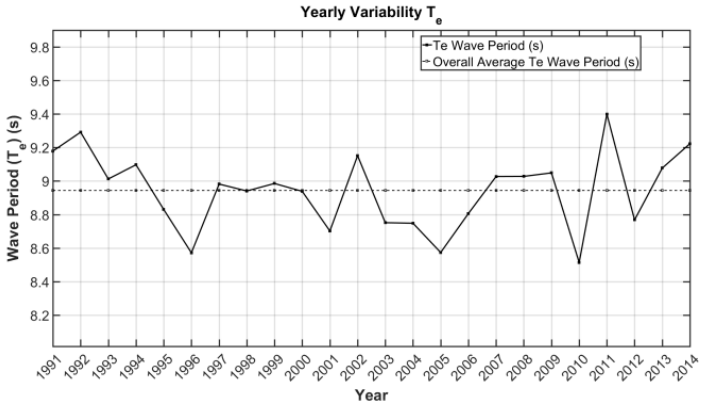


FIGURE 93: ANNUAL MEAN T_E WAVE PERIOD

Annual variation of the mean energy period, T_e, (Figure 93) is more tightly bounded than other parameters, with less than 1s between the minimum and maximum annual values, at 8.51s and 9.40s respectively.

Taking the wave parameters as a whole, the wave period and H_{m0} values exhibit similar variability and tend to be correlated throughout the 24 year timespan. The more energetic years exhibit both higher H_{m0} and T_{01}/T_p values, while the less energetic years see a corresponding decrease in all three parameters.

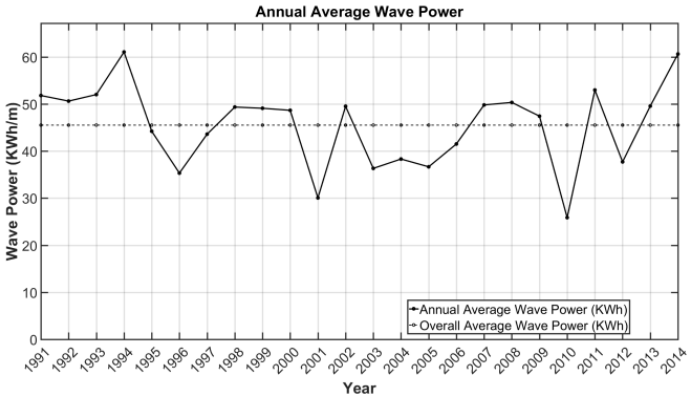


FIGURE 94: ANNUAL MEAN OMNI-DIRECTIONAL WAVE POWER

The annual average wave power, as characterised at the nearshore location, is 45kW/m. A maximum value of approximately 61 kW/m is seen to occur twice; in 1994 and 2014, consistent with the occurrence of the maximum values of annualised H_s. The minimum value, occurring in 2010, is just 26 kW/m, less than half that of the maximum value. This level of variability is sure to have an impact on the overall operation of a wave energy project at Killard Point.

Table 43 and Table 44 below provide the tabulated Mean and Standard Deviation of the annual average H_s, T_{01} and T_p values at the nearshore and offshore locations respectively.

TABLE 43: ANNUAL VARIABILITY SUMMARY STATISTICS FOR THE NEARSHORE SITE AT KILLARD POINT

Parameter	H_s	T_{01}	T_p
Mean	2.13m	8.64s	10.41s
Standard Deviation of annual average	0.215	0.237	0.285

TABLE 44: ANNUAL VARIABILITY SUMMARY STATISTICS FOR THE OFFSHORE SITE AT KILLARD POINT

Parameter	H_s	T_{01}	T_p
Mean	2.75m	8.79s	10.59s
Standard Deviation of annual average	0.229	0.229	0.275

5.4.1.2 Monthly Variability

Equally important to characterise is the variation in Wave Parameters over monthly timescale, with these values determining the yearly energy production profile at the site. Figure 95, Figure 96, Figure 97 represent the Monthly Average values of H_{m0}, T_{01} and T_p parameters respectively, across the 24 year hindcast model dataset.

A clear seasonal variability is present in the data in which a number of trends exist. All parameters are at their lowest during the summer months, May-August. Wave height and both wave period parameters increase during the winter months, with the highest values recorded during December, January and February. The average significant wave height during December-February is almost double that of June-August, at both the nearshore and offshore sites. The monthly standard deviations are much greater than on an annual basis, indicative of the level of seasonal variation present.

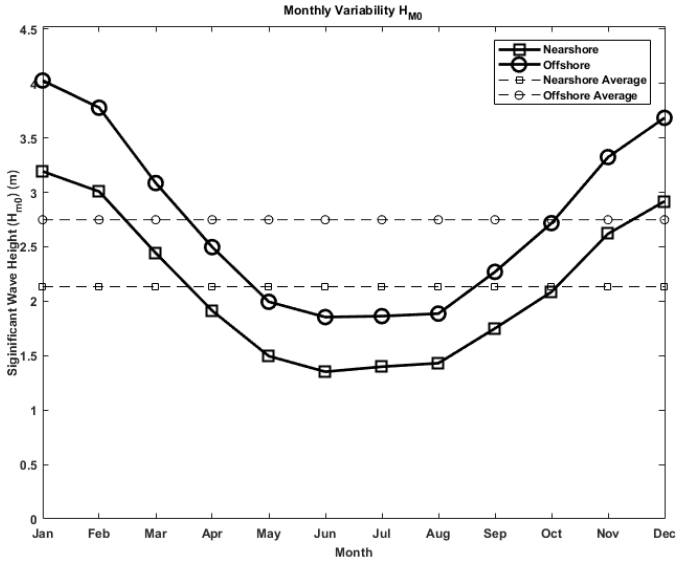


FIGURE 95: MONTHLY H_{M0} VARIABILITY AT KILLARD POINT SITE

The relative deviation between the monthly values of H_{m0} and the average annual value is far larger than that seen on an inter-annual basis. Interestingly, where the annual values at the nearshore and offshore sites tended to mirror each other, with a relatively uniform difference of ~22% throughout, the difference between nearshore and offshore H_{m0} on a monthly time-scale can be seen to grow in winter where there is a predominance of storm conditions, and reduce during the more benign summer months. It is likely that sheltering effects of the nearshore environment, and the wave breaking that is experienced in the nearshore environment, tend to have more influence at larger wave heights. The maximum value, averaged over 24 years, occurs in January. This significant wave height of 4 meters is over double that of the minimum monthly value of 1.48m occurring in June.

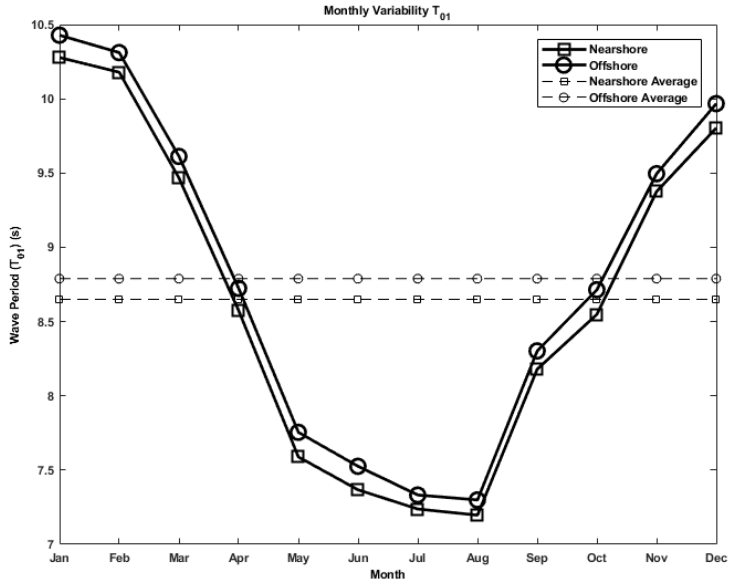


FIGURE 96: MONTHLY T_{01} VARIABILITY AT KILLARD POINT SITE

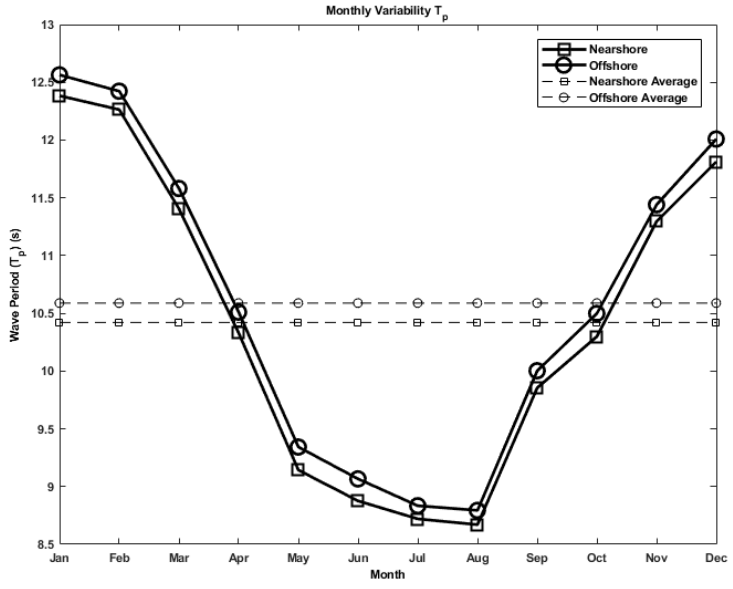


FIGURE 97: MONTHLY T_P VARIABILITY AT KILLARD POINT SITE

The monthly standard deviations are much greater than on an annual basis, indicative of the level of seasonal variation present, and present a clear case for the need for developers to consider not just their roadmap for energy production over the project lifecycle, but the level of variation that will be experience due to seasonal factors, and how this may impact energy supply, scheduling of maintenance, and various economic factors related to the sale of energy.

TABLE 45: MONTHLY VARIABILITY SUMMARY STATISTICS FOR THE NEARSHORE SITE AT KILLARD POINT

Parameter	H_s	T_{01}	T_p
Mean	2.13m	8.65s	10.42s
Standard Deviation	0.731	1.1405	1.374

TABLE 46: MONTHLY VARIABILITY SUMMARY STATISTICS FOR THE OFFSHORE SITE AT KILLARD POINT

Parameter	H_s	T_{01}	T_p
Mean	2.75m	8.79s	10.59s
Standard Deviation	0.809	1.161	1.4

The impact of the variability of these parameters on power production is illustrated in Section 5.4.2

5.4.1.3 Scatter Plots

Bi-variate scatter plots of important summary statistics have been produced. These are a representation of the occurrence of various sea-state combinations of Wave Height and Period and provide a useful method of ascertaining an overall understanding of the wave climate and the energy resource at the area of interest. The scatter plots are produced according to the suggested conventions of the Equimar Protocols (EquiMar, 2010b).

- Each bin displays the cumulative occurrences of the H_{m0}-T_{01}/T_{02}/T_p pair. The total number of data points have been provided for normalized scatter plots (e.g. scatter plots displaying percentage occurrence).
- H_{m0} bins are defined in intervals of 0.5m over the range 0.5m – Maximum H_{m0} value in the dataset.
- T_{01}/T_{02}/Tp Bins are defined in intervals of 0.5s over the range 0.5s to Maximum Period Value in the dataset.
- In addition, Scatter plots are produced for H_{m0} bins in intervals of 0.5m over the range 0.25- maximum H_{m0} value to satisfy the convention used by the Power Matrix, as these values are used to determine characteristic device performance at the Killard Point site.

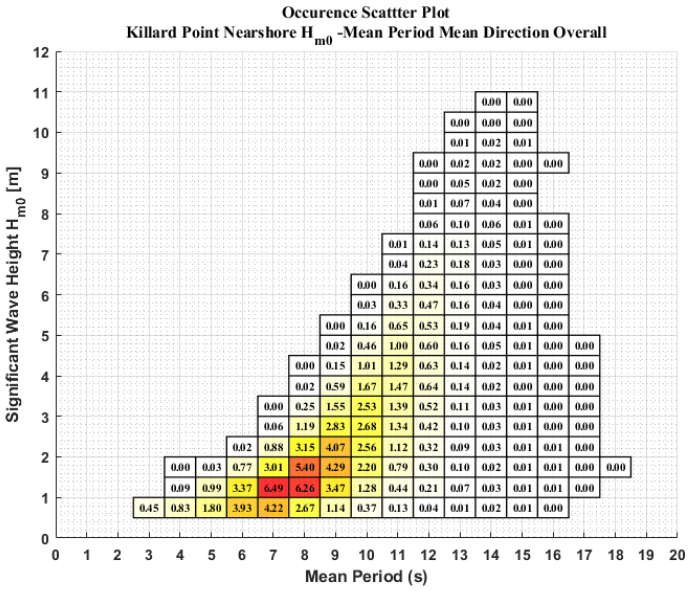


FIGURE 98: H_{M0} – T_{02} SCATTERPLOT OF OCCURRENCE PERCENTAGE FOR 24 YEAR HINDCAST.

The scatter plot (Figure 98) shows the percentage occurrence of wave conditions at 0.5m x 1s defined bins of H_s and T_p. The most commonly occurring wave conditions are clustered around 1 – 3m H_s and 7 – 10s T_e, with evidence of the highly energetic nature of the site found in the number of occurrences of waves in excess of 10m.

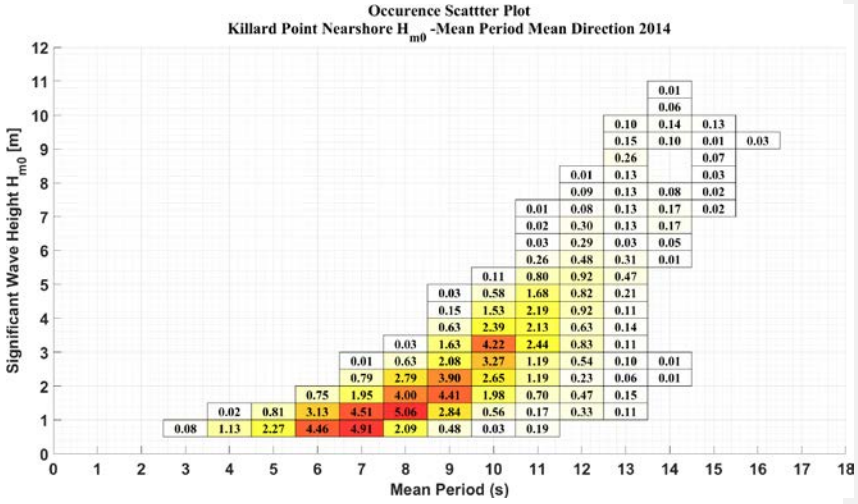


FIGURE 99: H_{M0} - T_E PERCENTAGE OCCURRENCE SCATTER PLOT FOR 2014 USING OUTPUT OF MIKE21 MODELLED DATA (8760 MEASUREMENTS)

Figure 99 displays the metocean conditions during 2014 as produced by the Mike 21 model. The percentage occurrence is shown, with the colour scale indicating the sea states which occur most frequently; allowing the typical sea states to be identified.

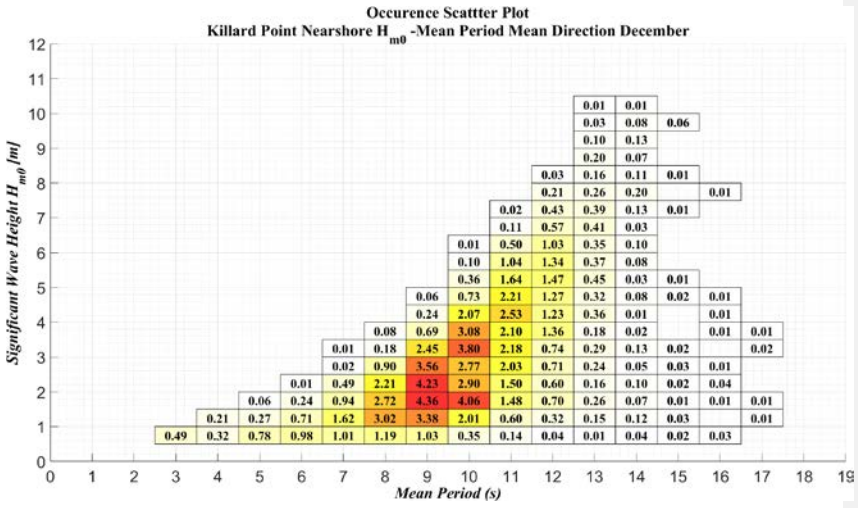


FIGURE 100: PERCENTAGE OCCURRENCE SCATTER PLOT FOR AVERAGE DECEMBER CONDITIONS USING OUTPUT OF MIKE21 DATA (744 MEASUREMENTS)

Figure 100 displays the percentage occurrence for December at the nearshore Killard Point site. There is an obvious upward shift in the positions of the most commonly

occurring sea-states, correspondent with the seasonal variation seen in the wave conditions. A number of events with H_{m0} greater than 10m are identifiable.

5.4.1.4 Histogram Plots

To represent the distribution of Wave Parameters over the duration of the modelled data, histogram plots have been produced which characterise distribution of the H_s and T_{01} parameters over the course of the 24 year hindcast.

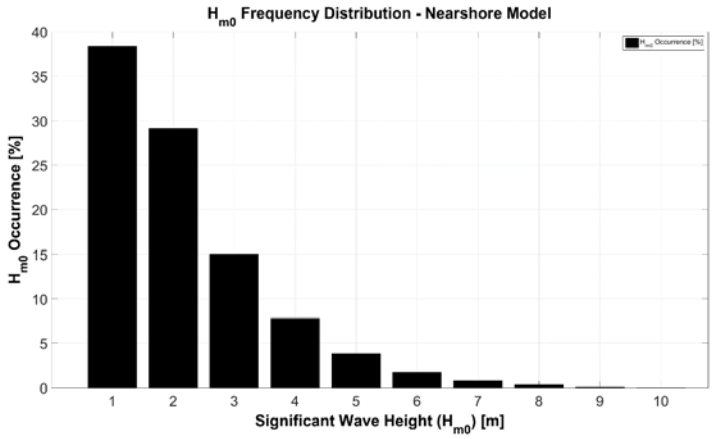


FIGURE 101: HISTOGRAM OF H_{M0} DISTRIBUTION FOR NEARSHORE MODEL 24 YEAR HINDCAST.

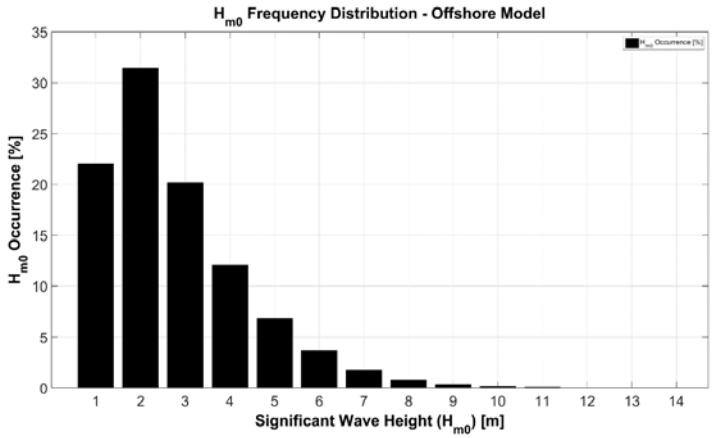


FIGURE 102: HISTOGRAM OF H_{M0} DISTRIBUTION FOR OFFSHORE MODEL 24 YEAR HINDCAST.

A change in the distribution of H_{m0} is seen between nearshore and offshore modelled data, with a reduction in the occurrence of wave heights between 1-2m H_{m0}, and an

increase in the occurrence of wave heights in all bins greater than 2m. The effect of this can be seen in the weather window calculations which follow in Section 5.4.6. The most commonly occurring waves at the nearshore site are in the range 1-2m, and this increases to 2-3m at the Offshore site, which here represent approximately 31% of the H_{m0} occurrence.

The greater duration of records within the modelled data results in an increased spread of Wave Period versus that of the limited buoy data recordings. However, the most commonly occurring period remains 8 seconds in both the Buoy and Modelled data, and appears to be the dominant condition at the site. The nearshore site sees an average T_{01} of 8.64s across the 24 years of hindcast data.

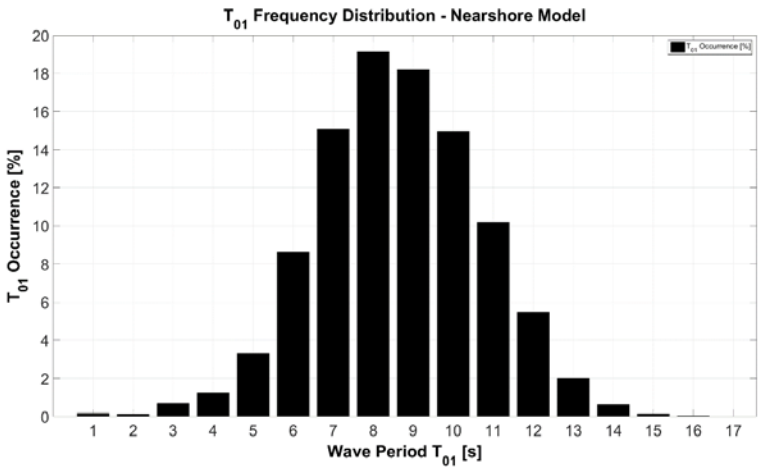


FIGURE 103: T_{01} HISTOGRAM OF NEARSHORE MODELLED DATA.

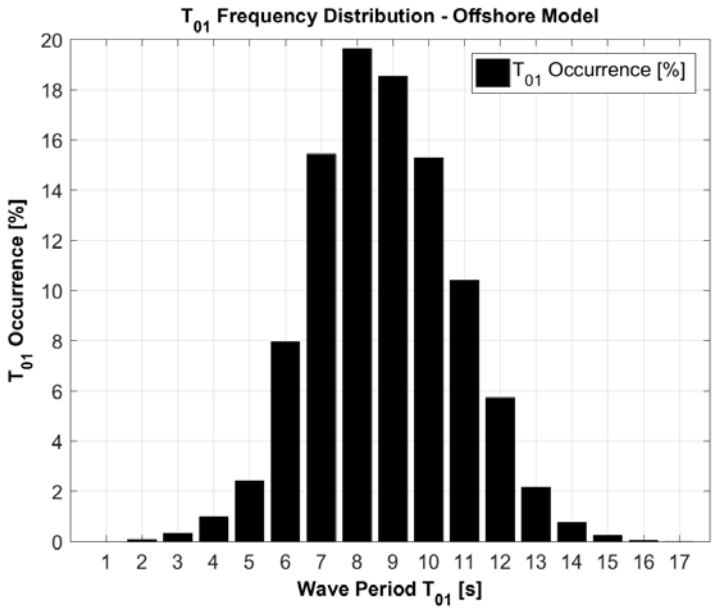


FIGURE 104: T_{01} HISTOGRAM OF OFFSHORE MODELLED DATA

The distribution of T_{01} at the offshore site is relatively unchanged in comparison to the nearshore data, with marginally reduced occurrence of conditions below 7 seconds, and marginally increased occurrence above this threshold.

5.4.1.5 Spatial Variability

The spatial variability is assessed using the modelled wave data at the Killard Point site, with this including an analysis of the variation in wave direction as waves travel from the offshore to the nearshore site. The distance between the sites is minimal but the water depth drops from greater than 50 meters to below 20 meters at the nearshore site, and this, coupled with the directional sheltering off waves from the south-west, causes a noticeable directional shift as the waves travel towards the shore. The conditions are analysed as if they were occurring simultaneously at the nearshore and offshore sites, which, given the low variability of conditions on a (less than) hourly scale, is a reasonable assumption.

5.4.1.5.1 Wave Rose

Wave Roses have been produced to show the monthly and yearly average directional distribution of wave height and wave period against wave direction. Wave Period,

Peak Wave period and Wave height have been analysed at 12 degrees directional separations, resulting in 30 total directional segments.

In Figure 105 to Figure 110 below, the most commonly occurring directions and the distribution of the Significant Wave Height and Mean Period parameters within each direction are shown. The length of each bar represents the percentage of sea-states within each directional division, while the coloured bars represent the distribution of intensity of the parameters within this directional sector.

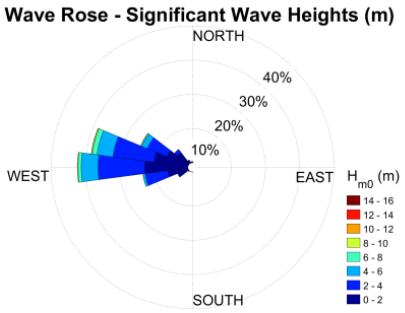


FIGURE 105: WAVE ROSE OF H_{M0}

An overall analysis of the entire dataset shows that the predominant wave direction is from the west, with the largest waves also originating from this segment. A slight disposition towards the 285° directional segment (west north-west) owes itself to the local topography, with waves from the predominant south-west direction being blocked by land and effectively "turned" before reaching the nearshore site.

Taking a representative year, 2014, in Figure 106 and Figure 107 below, the difference in distribution of Significant Wave Height according to Mean and Peak Direction is analysed.

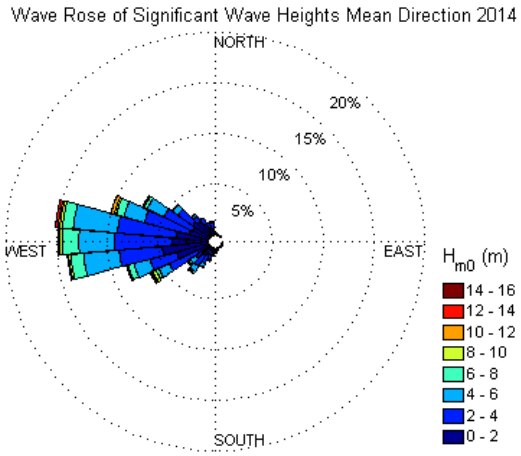


FIGURE 106: WAVE HEIGHT DISTRIBUTION ACROSS 30 (MEAN) DIRECTIONAL SECTORS FOR METEOGROUP BOUNDARY INPUT WAVE DATA IN 2014.

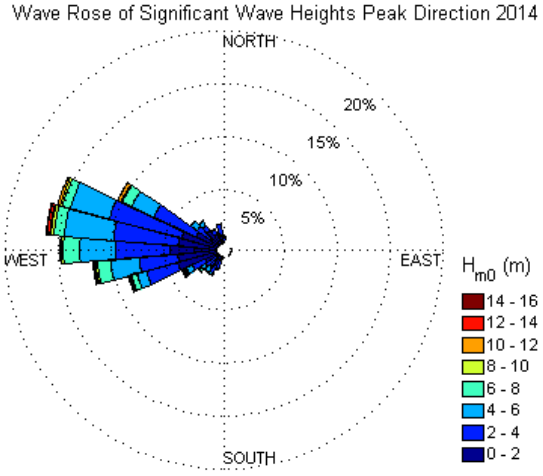


FIGURE 107: WAVE HEIGHT DISTRIBUTION ACROSS 30 (PEAK) DIRECTIONAL SECTORS FOR METEOGROUP BOUNDARY INPUT WAVE DATA IN 2014.

The peak direction plot shows a reduction in wave occurrence from more southerly directions.

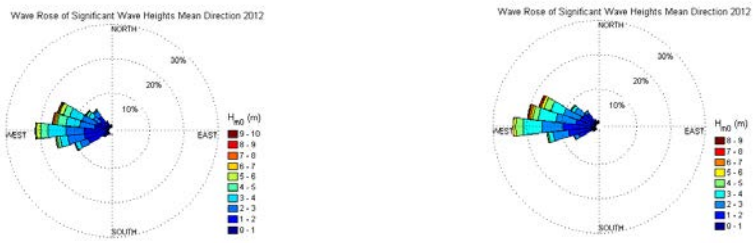


FIGURE 108: SIGNIFICANT WAVE HEIGHT OFFSHORE (LEFT) AND NEARSHORE (RIGHT) AT KILLARD POINT IN 2012

Figure 108 demonstrates the change in directional distribution and wave intensity between the offshore site and the nearshore site. Moving from the offshore to the nearshore site, waves are effectively "turned" as they feel the seabed, and as a result there is an increase in the occurrence of waves from more northerly directions at the nearshore site. Coupled with the sheltering of the nearshore site from the south-west, there is also a reduction in the magnitude and occurrence of waves from the South, while the overall magnitudes of Significant Wave Height are also lowered.



FIGURE 109: MEAN WAVE PERIOD OFFSHORE (LEFT) AND NEARSHORE (RIGHT) AT KILLARD POINT IN 2012

Figure 109 shows the same analysis for the Mean Wave period. The reduction in this parameter is not so severe, but there is a noticeable narrowing of the directional sectors, with an increase in the occurrence of west to north-westerly wave

conditions, and a decrease in the occurrence of conditions at the extrema of the experienced directions.

Peak Wave direction was found to be approximately 10 degrees more northerly in the resulting modelled data than the records in the buoy for deployment locations 1 and 2. Analysing the boundary data provided by MeteoGroup revealed that this deviation is more than likely owing to the seasonal distribution of the buoy data, being predominantly during winter months, during which there is an increase of storms predominating from northerly directions. This can be seen when the aggregate June and November months are compared below:

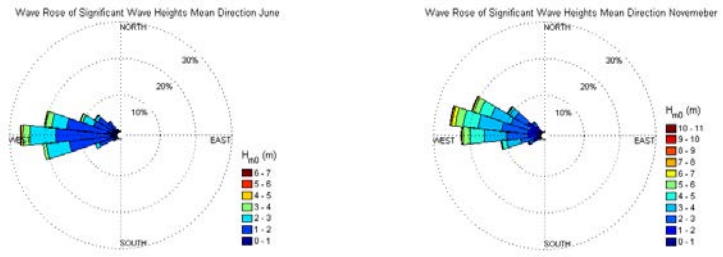


FIGURE 110: SIGNIFICANT WAVE HEIGHT DISTRIBUTION AT KILLARD POINT FOR SUMMER AND WINTER: JUNE (LEFT), NOVEMBER (RIGHT)

There is a significant difference in the distribution and intensity for summer and winter months, as evidence here. The predominant direction, and the direction of the largest storms is shifted northwards for during winter months, while the occurrence of more extreme storm conditions grows.

Of note was that the Peak Direction parameter output was found to be unreliable from MIKE21 solver, with a number of “gaps” occurring between certain segments. This was an unavoidable issue, and it is recommended that the mean directional output of the Mike 21 model be used if ultimate precision in wave direction is required as it does not exhibit these gaps in the data.

5.4.1.5.2 Directional Dependence

A directional analysis has been undertaken to study the effects of the wave direction on the propagation of waves to the shore. This analysis shows that incident waves coming directly from 270 degrees (West) are the largest, and proportionally see the least reduction when propagating from the offshore to nearshore environment. However, due to the larger waves which typically originate from these directions, the largest absolute losses in wave height are registered between offshore and nearshore conditions.

Figure 111 and Figure 112 below show a plot of the relative change in significant wave height from the offshore to nearshore site location for each wave direction. Each dot represents the reduction in significant wave height (H_{m0}) for a given Sea state (H_{m0} and incident Direction at the offshore site). The coloration of the dots represents the frequency of occurrence of a given sea state and associated significant wave height reduction, with lighter areas (enclosed) representing the most commonly occurring states.

Commented [LK12]: Need to describe what we are seeing in the diagrams more. Graphs are also unclear due to text size and colouring so better off spelling it out for people.

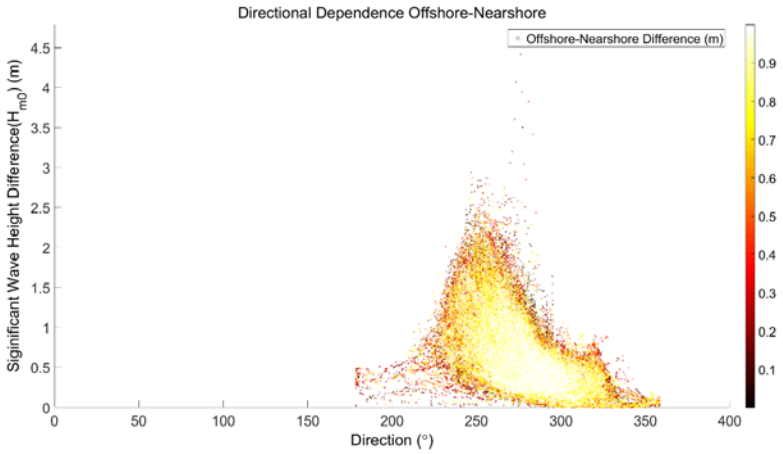


FIGURE 111: ABSOLUTE CHANGE IN OFFSHORE TO NEARSHORE H_{M0} ACROSS ALL DIRECTIONS

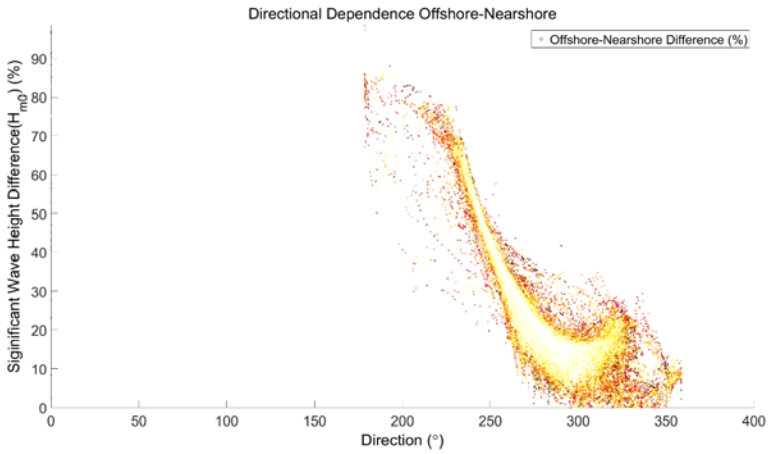


FIGURE 112: RELATIVE CHANGE IN OFFSHORE TO NEARSHORE H_{M0} ACROSS ALL DIRECTIONS

The change in wave height based on the direction of incident wave was analysed, with the finding that the 270 - 325 degree prevailing wave direction saw the least proportional reduction between the nearshore and offshore sites. The site is unsheltered from these directions and this direct path along the prevailing wave direction offers the shortest shallow-water path for wave to traverse. Waves at 180-250 degrees experience the largest relative reduction in wave height.

There wave front aligns itself to the shore due to refraction of the waves in the nearshore environment. The standard deviation of mean direction was seen to reduce from 21.92 degrees to 13.65 degrees from the offshore to nearshore environment, with the average mean wave direction increasing from 277.45 to 296.07 degrees; the waves in effect “turning” to align themselves with the shore.

5.4.2 Power Production

Power production is a primary factor in the WestWave Project. This analysis uses the resource scatter plot occurrence information; along with the power matrix for the a bottom-mounted, hinged-flap type device to assess the monthly-average and yearly power production using the Mike21 model information from the 24 year hindcast. A correction of the energy period output of the model was necessary to achieve the level of power production accuracy outlined in the IEC-TS, and a detailed treatment of this process is presented in Chapter 3.

5.4.2.1 Wave Periods

First, a brief note is required on the method used to determine the Energy period, T_e, used to generate estimates of power production. In order to obtain an estimate of T_e correspondent to the Mike 21 model data, it was necessary to determine the relationship between T_e/T_{01}. As an initial approach, this was determined using a derivation based on the Bretschneider spectrum, using the method of spectral moments (Section 3.3.6.2.2). An alternative method, determining the arithmetic ratio between T_{01} and T_e from the history of spectral parameters in the buoy data obtained during 3 separate deployments at Killard Point, was found to agree closely with the value obtained through the derivation. This average WPR was used as a linear multiplier to produce an estimate of T_e from the T_{01} record in the output of the Mike21 dataset.

5.4.2.2 Available Wave Resource

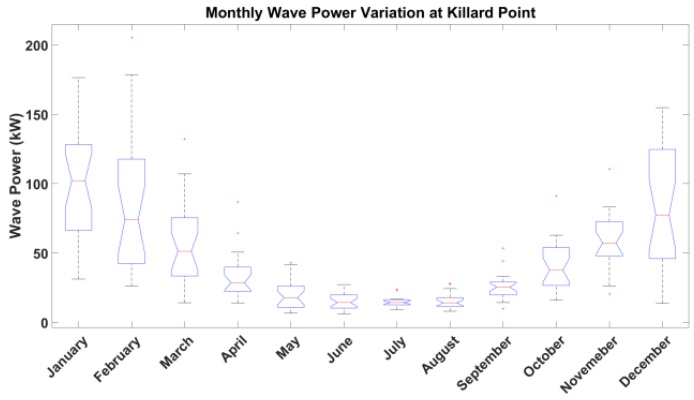


FIGURE 113: MONTHLY VARIATION OF WAVE POWER AT KILLARD POINT

The annual mean omni-directional wave power (Figure 94) follows the trend of H_s, showing considerable inter-annual variation. Figure 113 builds upon this by examining the monthly mean, variation, 95% confidence intervals, and outliers of available wave power. This reveals that the magnitude, but also the variability, of wave power during winter months is much greater than that of summer months. The minimum aggregate monthly value of 41 kW/m during the 24-year dataset occurs in June, with a very similar mean occurring in July. It is in July however, that the overall variation of the available wave power is lowest. February shows the largest variability

in available wave power, with 95% Confidence Intervals at 45 kW/m and 115 kW/m respectively. This is valuable information in informing the level of variability that can be expected from the available wave power at the Killard Point site.

5.4.2.3 Nearshore Power Production Study using a hinged-flap WEC

The figures below represent the monthly and annual power production estimates using a hinged flap, bottom-mounted WEC, at the near-shore Killard Point site.

This has been computed using the occurrence statistics for each month, and each year of the hindcast dataset; combined with a provided preliminary power matrix for a pre-production device. For this analysis, given the sensitivity of device power production to the energy period parameter discussed in Chapter 6, the Machine Learning method developed in Chapter 3 has been applied in 3-step fashion to the determination of Energy period. First, correcting the existing T_{01} period by training the machine learning model using the concurrent buoy data recordings, then using the corrected dataset alongside concurrent buoy data T_e measurements to enable the mapping and generation of T_e in the hindcast dataset. As demonstrated in Chapter 3, this method shows great accuracy improvements over traditional methods of WPR determination and Wave Parameter conversion.

The average Annual Power Production is 838MWh, with a standard deviation of 96MWh. The minimum calculated value of 590 MWh occurred in 2010 due to benign average conditions – 1.64m Average H_s. The maximum calculated value of 1013MWh occurred in 1992, where the average H_s was 2.37m.

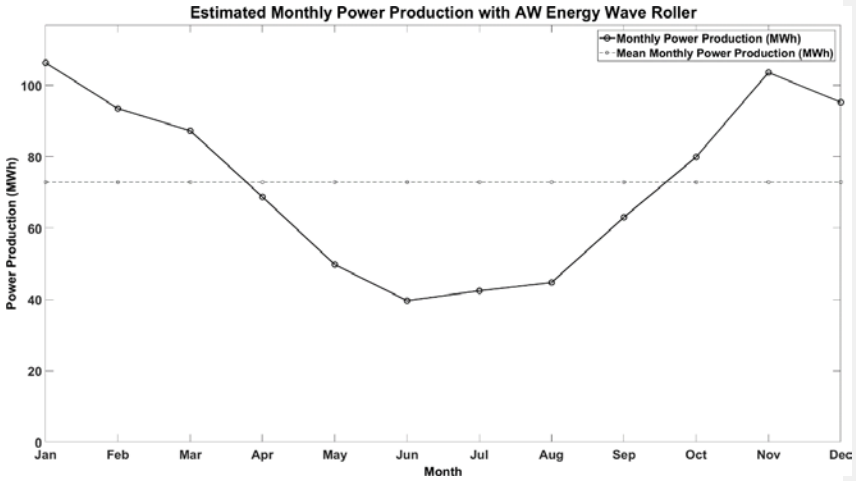
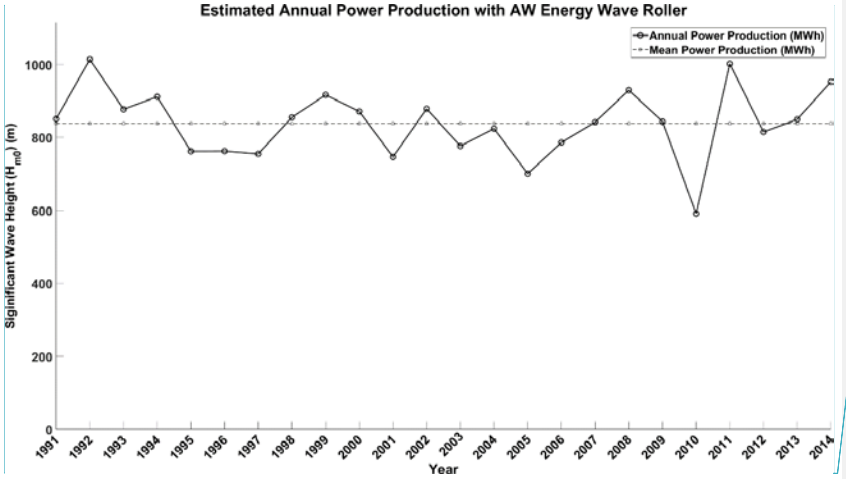


FIGURE 114: THEORETICAL MONTHLY POWER PRODUCTION AT KILLARD POINT SITE FOR WEC DEVICE



Commented [A13]: Need to change y axis label without messing up the aspect ratio

FIGURE 115: THEORETICAL ANNUAL POWER PRODUCTION AT KILLARD POINT SITE FOR WEC DEVICE

The average Monthly Power Production is 72.86MWh, with a standard deviation of 24.71MWh. The minimum estimated value of 39.67 MWh occurs in the month of June, which also carries the lowest average H_{m0} of 1.35m. The maximum estimated value of 106.34MWh occurs in November.

5.4.3 Extreme Analysis

Extreme analysis has been conducted at the Killard point using industry standard curve fitting methods across a number of directional sectors to determine the design conditions for device design and site assessment.

An examination is made using the buoy data, which, though limited in time, contains a number of events that could be defined as "extreme events". The largest recorded H_{m0} event, occurring during buoy deployment 3 on the 27th of January 2014, is 15.88m (Figure 116).

A more detailed extreme wave prediction has been made using the 24 years of modelled hindcast data, with the Extreme Wave height at return periods of 1-100 years extrapolated based on the hindcast data. This has been performed for both the nearshore and offshore sites. The R^2 value of the best fitting extreme curves used to derive estimates of the extreme H_{m0} are provided in Figure 121.

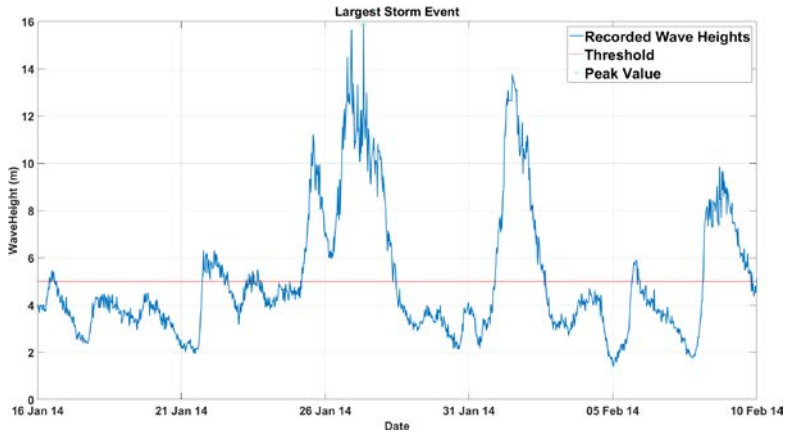


FIGURE 116: LARGEST STORM EVENT RECORDED DURING BUOY DEPLOYMENTS AT DEPLOYMENT LOCATION 3 - JANUARY 2014

Commented [A14]: Increase font size for all images in this section

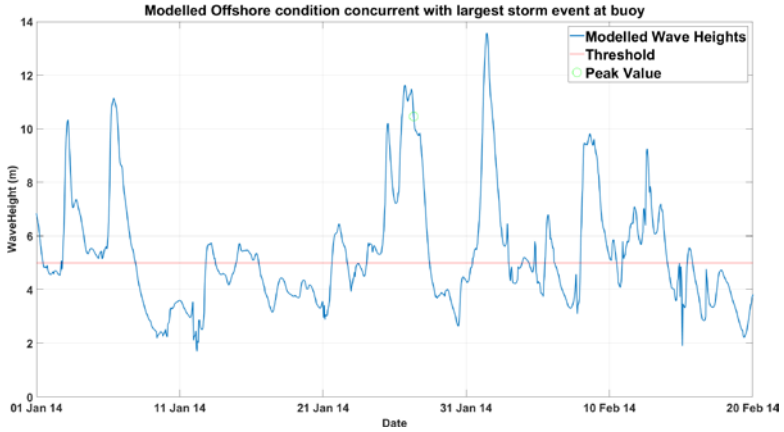


FIGURE 117: HINDCAST MODEL CONDITIONS OFFSHORE DURING LARGEST RECORDED WAVE AT BUOY – JANUARY 2014

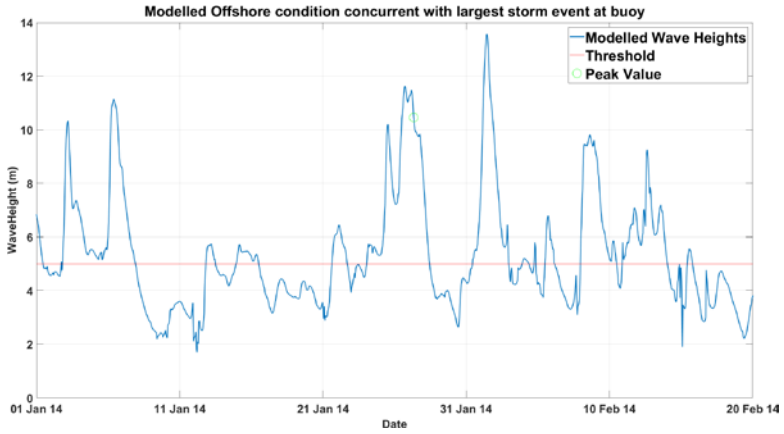


FIGURE 118: HINDCAST MODEL CONDITIONS NEARSHORE DURING LARGEST RECORDED WAVE AT BUOY - JANUARY 2014

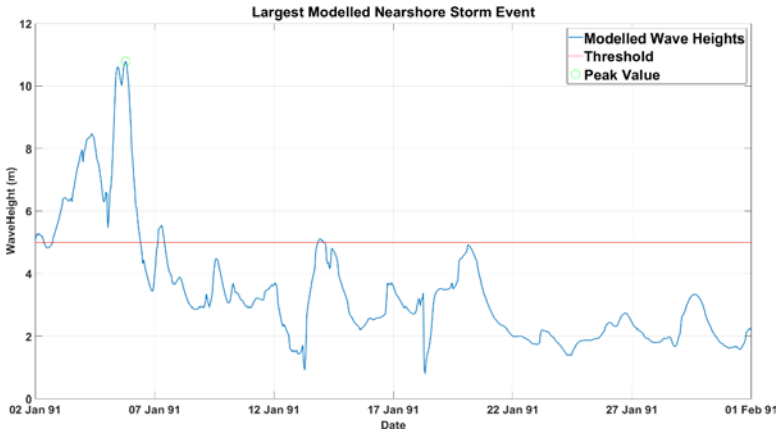


FIGURE 119: LARGEST NEARSHORE STORM EVENT IN 24 YEAR HINDCAST - OCCURRING DURING FEBRUARY 1991.

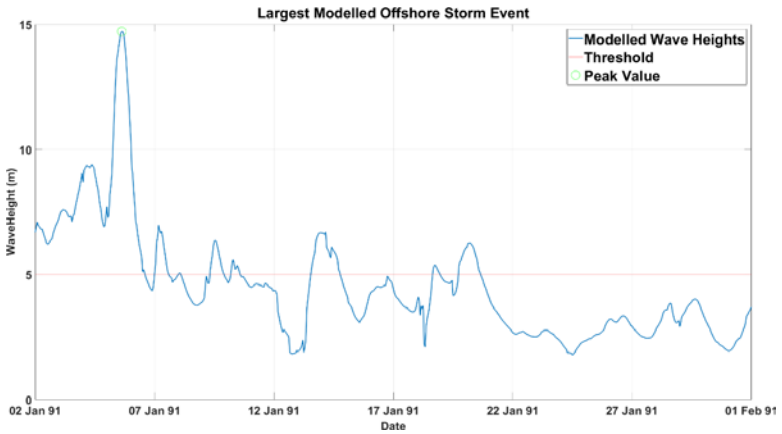


FIGURE 120: LARGEST OFFSHORE STORM EVENT IN 24 YEAR HINDCAST - OCCURRING DURING FEBRUARY 1991

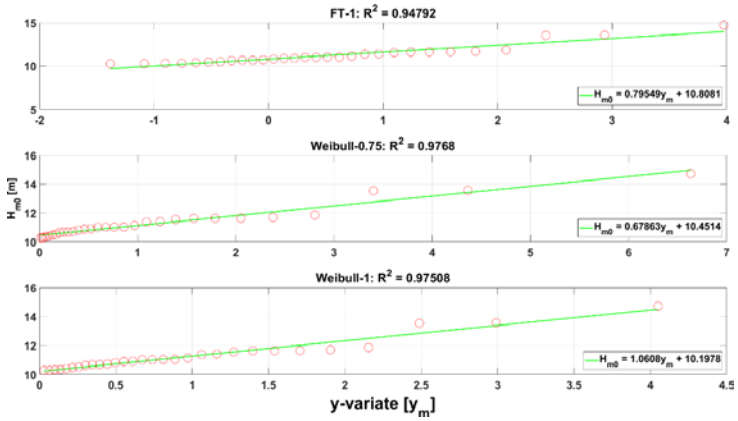


FIGURE 121: EXTREME WAVE CURVE FITTING R^2 VALUES FOR FISHER-TIPPETT AND WEIBULL CURVES. NEARSHORE MODELLED DATA, USING N_{MAX}=30. FT-1 CURVE SELECTED AS BEST FIT.

5.4.3.1 Nearshore

The nearshore site experiences large extreme waves, but sees a reduction in the largest extreme waves due to decreased water depth and proximity to the shore versus the offshore location.

TABLE 47: EXTREME WAVE HEIGHT (EXTREME H_{M0} (M)) NEARSHORE AT RETURN PERIODS 1-100 YEARS FOR BEST 3 FITTING CURVES USING KILLARD POINT HINDCAST MODEL DATA.

Curve Choice	Return Period	1 Year	5 Year	10 Year	20 Year	50 Year	100 Year	R^2
FT-1		**8.82**	**9.96**	**10.33**	**10.70**	**11.17**	**11.53**	**0.978**
Weibull .75		8.94	9.76	10.23	10.74	11.48	12.07	0.902
Weibull 1		8.85	9.89	10.34	10.78	11.38	11.82	0.953

Water depths at the nearshore have a nominal value of 16.6m compared to datum. Values in model simulation range from 18 - 24m depth, giving sufficient space for large extreme waves to occur.

5.4.3.2 Offshore

It appears that the extreme event in January 2014 during buoy deployment 3 represents a greater than 1 in 20-year return period event as predicted by extreme modelling of the offshore site, taking the Weibull – 1 curve estimate of the extreme wave height. Additionally, the magnitude of storm events in the model is less than concurrent events in the buoy data, thus it may be prudent to take the extreme

predictions using model data as a lower bound estimate of the extreme conditions at the site.

TABLE 48: EXTREME WAVE HEIGHT (EXTREME H_{M0} (M)) OFFSHORE AT RETURN PERIODS 1-100 YEARS FOR BEST 3 FITTING CURVES USING KILLARD POINT HINDCAST MODEL DATA. WEIBULL 1 CURVE SELECTED AS BEST FIT.

Curve Choice	Return Period	1 Year	5 Year	10 Year	20 Year	50 Year	100 Year	R^2
FT-1		9.86	11.76	12.57	13.38	14.46	15.27	0.981
Weibull .75		10.27	13.51	15.02	16.60	18.76	20.47	0.975
Weibull 1		**10.26**	**12.72**	**13.78**	**14.84**	**16.25**	**17.31**	**0.997**

5.4.3.3 Directional Extreme Wave analysis

5.4.3.3.1 Nearshore

TABLE 49: EXTREME WAVE HEIGHT (EXTREME H_{M0} (M)) AT RETURN PERIODS 1-100 YEARS FOR BEST 3 FITTING CURVES USING KILLARD POINT NEARSHORE HINDCAST MODEL DATA (270 DEGREES)

Curve Choice	Return Period	1 Year	5 Year	10 Year	20 Year	50 Year	100 Year	R^2
FT-1		3.57	3.59	4.11	4.40	4.73	4.97	0.916
Weibull .75		3.53	3.80	3.99	4.27	4.71	5.09	0.905
Weibull 1		**3.00**	**3.72**	**4.03**	**4.33**	**4.74**	**5.05**	**0.922**

TABLE 50: EXTREME WAVE HEIGHT (EXTREME H_{M0} (M)) AT RETURN PERIODS 1-100 YEARS FOR BEST 3 FITTING CURVES USING KILLARD POINT NEARSHORE HINDCAST MODEL DATA (300 DEGREES)

Curve Choice	Return Period	1 Year	5 Year	10 Year	20 Year	50 Year	100 Year	R^2
FT-1		**9.87**	**9.89**	**10.35**	**10.59**	**10.88**	**11.09**	**0.929**
Weibull .75		9.87	10.09	10.25	10.48	10.84	11.15	0.862
Weibull 1		9.42	10.02	10.27	10.53	10.87	11.13	0.899

5.4.3.3.2 Offshore

Directional extreme wave analysis has been conducted across 12 directional segments (30° increments). Extreme waves were found to come almost exclusively from the 255 - 315 degree segments, with very few waves of notable magnitude coming from outside these directions.

TABLE 51: EXTREME WAVE HEIGHT (EXTREME H_{M0} (M)) AT RETURN PERIODS 1-100 YEARS FOR BEST 3 FITTING CURVES USING KILLARD POINT OFFSHORE HINDCAST MODEL DATA (240 DEGREES)

Curve Choice	Return Period	1 Year	5 Year	10 Year	20 Year	50 Year	100 Year	R^2
FT-1		6.96	6.99	7.82	8.27	8.78	9.15	0.957
Weibull .75		**6.86**	**7.30**	**7.62**	**8.07**	**8.80**	**9.42**	**0.994**
Weibull 1		6.04	7.18	7.68	8.17	8.82	9.32	0.985

TABLE 52: EXTREME WAVE HEIGHT (EXTREME H_{M0} (M)) AT RETURN PERIODS 1-100 YEARS FOR BEST 3 FITTING CURVES USING KILLARD POINT OFFSHORE HINDCAST MODEL DATA (270 DEGREES)

Curve Choice	Return Period	1 Year	5 Year	10 Year	20 Year	50 Year	100 Year	R^2
FT-1		**11.20**	**11.27**	**12.98**	**13.91**	**14.98**	**15.75**	**0.950**
Weibull .75		11.17	12.02	12.61	13.47	14.84	16.01	0.896
Weibull 1		9.49	11.74	12.71	13.68	14.96	15.93	0.926

TABLE 53: EXTREME WAVE HEIGHT (EXTREME H_{M0} (M)) AT RETURN PERIODS 1-100 YEARS FOR BEST 3 FITTING CURVES USING KILLARD POINT OFFSHORE HINDCAST MODEL DATA (300 DEGREES)

Curve Choice	Return Period	1 Year	5 Year	10 Year	20 Year	50 Year	100 Year	R^2
FT-1		10.53	10.56	11.38	11.83	12.35	12.72	0.934
Weibull .75		**10.41**	**10.86**	**11.18**	**11.64**	**12.38**	**13.01**	**0.984**
Weibull 1		9.58	10.74	11.24	11.74	12.40	12.90	0.973

5.4.3.4 H_{max} Analysis using Calculated AI (H_{max} : H_s ratio)

The method developed in Section 4.3.2 is used here to derive the expected extreme values of H_{max} at the Killard Point site.

The .RAW data files from the Killard point buoy deployment are imported and pre-processed. A time-series analysis is then run to determine the H_s and H_{max} values for each .RAW file which corresponds to a 30 minute duration recording. The Anomaly Index, or ratio of H_{max} : H_s, is determined for the mean condition and for each cell of

an occurrence matrix for all the conditions during the November recordings. This ratio is used to determine the likely extreme H_{max} at the Killard Point site.

	Lower	Pnew	Upper
P_1	1.366	1.538	1.709
P_2	-0.071	0.010	0.090
P_3	-0.010	-0.001	0.008
P_4	-0.002	0.116	0.234
P_5	-0.051	0.005	0.062
P_6	-0.007	-0.000	0.007

FIGURE 122: REGRESSION MODEL OF ANOMALY INDEX VS H_S. DETERMINED EQUATION PARAMETERS OUTPUT

A 6-parameter function, with values shown in Figure 122, above was found to provide the best estimate of H_{max} for a given H_s at the Killard Point site.

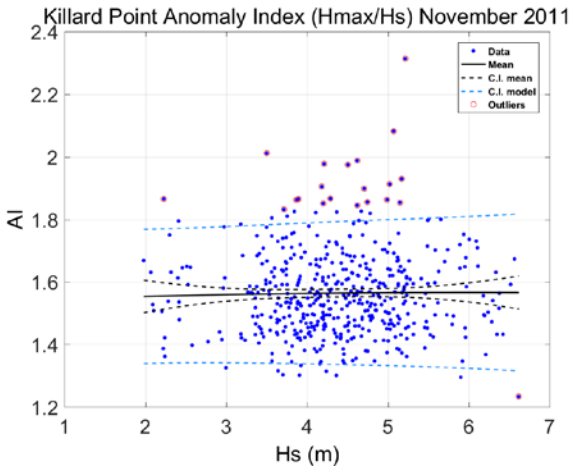


FIGURE 123: ANOMALY INDEX VS H_S DURING NOVEMBER 2011 KILLARD POINT BUOY DEPLOYMENT

Figure 123 displays the Anomaly Index value vs. H_s for the period November to January at the Killard Point site. Values are clustered around 1.4-1.8, with outliers as high as 2.3, though the presence of outliers diminishes with increasing waveheight, and the values tend to the median value of 1.55.

Based on the AI determined, the lower bound for the extreme H_{max} can be determined to be $1.366H_s$, and the upper bound $1.709H_s$. This gives 20-year return H_{max} values of 10.78*[1.366-1.709] at the nearshore site and 14.84*[1.366-1.709] at the offshore site.

5.4.3.4.1 Nearshore

TABLE 54: LOWER BOUND ESTIMATE H_{MAX} (M) AT KILLARD POINT NEARSHORE SITE

Curve Choice	Return Period	1 Year	5 Year	10 Year	20 Year	50 Year	100 Year
FT-1		12.05	13.60	14.12	14.61	15.26	15.75
Weibull .75		12.21	13.34	13.98	14.68	15.68	16.49
Weibull 1		12.09	13.51	14.12	14.73	15.54	16.15

TABLE 55: UPPER BOUND ESTIMATE H_{MAX} (M) AT KILLARD POINT NEARSHORE SITE

Curve Choice	Return Period	1 Year	5 Year	10 Year	20 Year	50 Year	100 Year
FT-1		15.07	17.02	17.66	18.28	19.09	19.70
Weibull .75		15.28	16.69	17.48	18.36	19.62	20.63
Weibull 1		15.13	16.90	17.67	18.43	19.44	20.20

TABLE 56: BEST ESTIMATE H_{MAX} (M) AT KILLARD POINT NEARSHORE SITE

Curve Choice	Return Period	1 Year	5 Year	10 Year	20 Year	50 Year	100 Year
FT-1		13.57	15.31	15.89	16.45	17.18	17.73
Weibull .75		13.75	15.02	15.74	16.52	17.65	18.57
Weibull 1		13.61	15.21	15.90	16.59	17.49	18.18

TABLE 57: SUMMARISED H_{MAX} (M) RESULTS FOR NEARSHORE OUTPUT OF HINDCAST MODEL

Site	Return Period	1 Year	5 Year	10 Year	20 Year	50 Year	100 Year
Lower Bound		12.09	13.51	14.12	14.73	15.54	16.15
Best Estimate		13.61	15.21	15.90	16.59	17.49	18.18
Upper Bound		15.13	16.90	17.67	18.43	19.44	20.20

Using the Anomaly Index figures derived through the linear regression analysis, H_{max} values at return periods of 1-100 years are derived for the Killard Point Nearshore location and shown above in Table 54, Table 55 and Table 56 above.

At a 20-year return period, the expected H_{max} based on the statistical analysis is 16.59m, with a range in the 95% confidence interval of [14.73-18.43m]. The H_{max} at the nearshore site is expected to fall towards the lower end of this range, given that

the upper H_{max} conditions predicted would be physically limited in maximum waveheight at the nearshore site.

5.4.3.4.2 Offshore

TABLE 58: LOWER BOUND ESTIMATE H_{MAX} (M) AT KILLARD POINT OFFSHORE SITE

Curve Choice	Return Period	1 Year	5 Year	10 Year	20 Year	50 Year	100 Year
FT-1		13.46	16.06	17.17	18.28	19.75	20.86
Weibull .75		14.03	18.45	20.52	22.67	25.63	27.96
Weibull 1		14.02	17.38	18.83	20.28	22.19	23.64

TABLE 59: UPPER BOUND ESTIMATE HMAX (M) AT KILLARD POINT OFFSHORE SITE

Curve Choice	Return Period	1 Year	5 Year	10 Year	20 Year	50 Year	100 Year
FT-1		16.84	20.09	21.48	22.87	24.71	26.10
Weibull .75		17.55	23.09	25.67	28.36	32.07	34.98
Weibull 1		17.54	21.75	23.56	25.37	27.76	29.58

TABLE 60: BEST ESTIMATE HMAX (M) AT KILLARD POINT OFFSHORE SITE

Curve Choice	Return Period	1 Year	5 Year	10 Year	20 Year	50 Year	100 Year
FT-1		15.16	18.08	19.33	20.59	22.24	23.49
Weibull .75		15.80	20.78	23.10	25.52	28.86	31.48
Weibull 1		15.78	19.57	21.20	22.83	24.99	26.62

TABLE 61: SUMMARISED HMAX RESULTS FOR OFFSHORE OUTPUT OF HINDCAST MODEL

Site	Return Period	1 Year	5 Year	10 Year	20 Year	50 Year	100 Year
Lower Bound		14.02	17.38	18.83	20.28	22.19	23.64
Best Estimate		15.78	19.57	21.20	22.83	24.99	26.62
Upper Bound		17.54	21.75	23.56	25.37	27.76	29.58

Using the Anomaly Index figures derived through the linear regression analysis, Hmax values at return periods of 1-100 years are derived for the Killard Point Offshore location and shown above in Table 59, Table 60 and Table 61.

At a 20-year return period, the expected Hmax is 22.83m, with a range in the 95% confidence interval of [20.28-25.37m].

5.4.3.5 Extreme wave summary

TABLE 62: BEST FIT EXTREME WAVE RESULTS SELECTED FOR NEARSHORE AND OFFSHORE SITES

Site	Return Period	1 Year	5 Year	10 Year	20 Year	50 Year	100 Year	R^2
Nearshore		8.82	9.96	10.33	10.70	11.17	11.53	0.978
Offshore		**10.26**	**12.72**	**13.78**	**14.84**	**16.25**	**17.31**	**0.997**

Peak values above the selected extreme threshold are detailed for each direction, as well as the associated extreme prediction for return periods of 1-100 years. These results are included in the appendix documents.

Given the directionally confined nature of the incident waves at the site, the directional analysis is of limited utility. In addition, it results in a lower prediction of extreme wave height. Thus, it is advised that the overall, non-directional analysis results be used. The largest extreme waves come from the 270 degree directional segment offshore, and the 300 degree segment at the nearshore site.

The Expected Offshore Extreme wave at a 20 Year Return Period of 14.84m is an extremely energetic wave condition, and will need to be considered in by device manufacturers in the design process. Preventative measures will need to be taken to ensure that premature wear or destruction of the device does not occur. The predicted extreme wave at the nearshore site of 10.7m is less likely to trouble a submerged device.

5.4.4 Spectral Analysis

Analysis was carried out to determine the level of variation in spectral shape for various sea-states at the Killard Point site. This analysis was completed using the Recorded Waverider RAW data from 2013-2015. The process for which is outline in Figure 124 below.

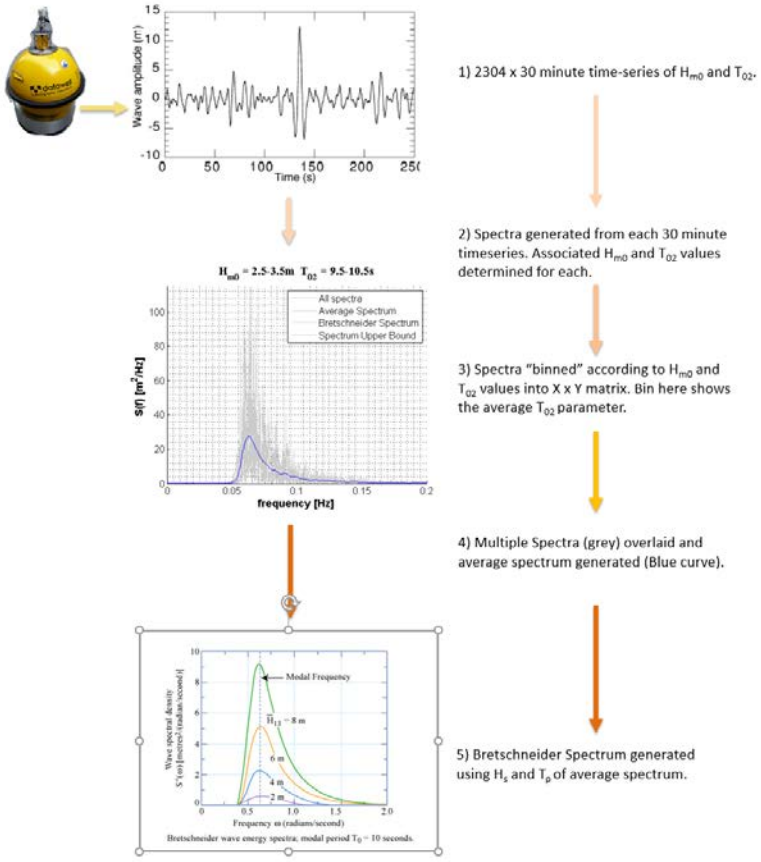


FIGURE 124: ANALYSIS OF TIMESERIES DATA FROM WAVERIDER BUOYS AT KILLARD POINT TO PRODUCE SPECTRAL SHAPE INFORMATION

These spectra represent the distribution of energy for an individual timeseries record which corresponds to a given sea-state. Some of the most commonly occurring of these are shown in Figure 125. The average of the spectral energy for each profile is displayed in blue, while the Bretschneider shape for the summary parameters associated with this spectrum (determined via spectral analysis of newly formed average spectral energy profile) are displayed in red. While these can be seen to be broadly similar, it is evident that the actual energy profile differs from that suggested

by the Bretschneider spectrum, containing more energy at the peak frequency, and with the peak frequency shifted left, toward lower frequency (higher period) waves.

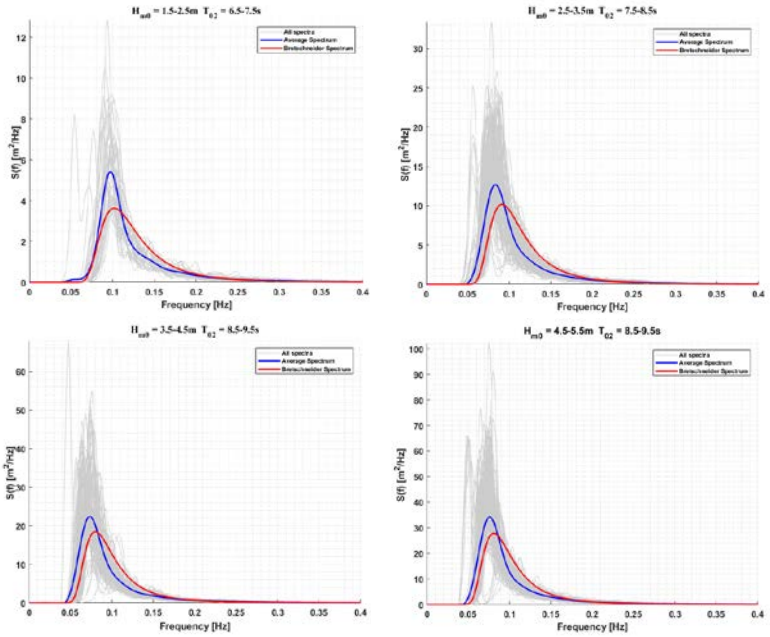


FIGURE 125: INDIVIDUAL (GREY), AVERAGE (BLUE) AND BRETSCHNEIDER REPRESENTATION (RED) FOR 4 OF THE MOST COMMONLY OCCURRING SEA-STATES AT KILLARD POINT

The spectral fit has been determined using the R^2 metric as follows:

$$R = \frac{\Sigma\left[S_{meas}(f_i) - \overline{S_{meas}(f_i)}\right]\left[S_{theory}(f_i) - \overline{S_{theory}(f_i)}\right]}{\sqrt{\Sigma\left[S_{meas}(f_i) - \overline{S_{meas}(f_i)}\right]^2 \Sigma\left[S_{theory}(f_i) - \overline{S_{theory}(f_i)}\right]^2}} \quad (5.1)$$

Where $S_{meas}(f_i)$ is the spectral ordinate for the recorded spectrum

and

$S_{theory}(f_i)$ is the spectral ordinate for the Bretschneider Spectrum.

To improve the utility of the calculation of the R^2 metric, its calculation was limited to consider only the spectral ordinate values in excess of 10% of the peak energy of the spectrum. This offered increased flexibility as it removed the need to determine an appropriate frequency range, and ensured that the long tail which did not contain a large amount of energy relative to the peak did not unduly influence the estimate of fit. This presents a significant advancement in flexibility and utility over the method of defining a limited frequency range, which is typically used.

For brevity, the R^2 values are given in a tabulated form rather than displaying the computed spectral plots for each sea-state. This is outlined in Figure 126 below.

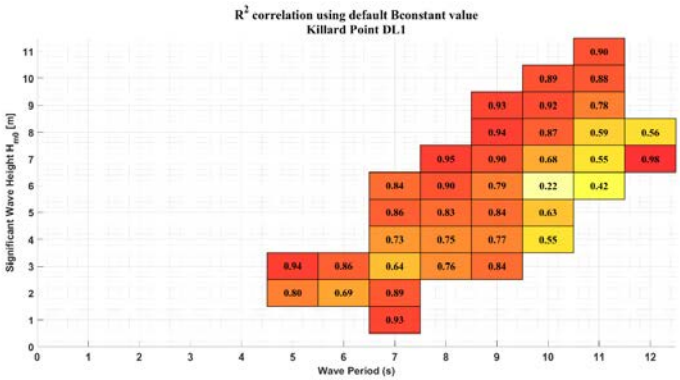


FIGURE 126: R^2 CORRELATION BETWEEN DEFAULT BRETSCHNEIDER SPECTRUM AND AVERAGE SPECTRUM FOR EACH SEA-STATE AT KILLARD POINT DURING BUOY DEPLOYMENT 1

This method of binning the correlation coefficient for the average real spectrum with Bretschneider Spectrum represents a novel way of assessing the degree to which the spectral energy profile at the site matches with a standard assumption commonly used in industry. This has significant implications as it represents a simple way of validating if the assumption of a Bretschneider Spectrum holds for the variety of conditions experienced at the site, allowing the dependability of its use for energy production prediction to be assessed.

It was found that improved correlation in wave spectral energy could be achieved by iteratively altering the parameters of the Bretschneider Spectrum, discussed in Section 6.5.1.1, and this work is further detailed at a later stage.

This analysis indicates the need to consider the spectral profile of this site as distinct from the Bretschneider Spectrum, with particular impact likely to occur on the assumed WPR. The existence of multi-modal spectral is evident here, and this has the potential for very large impact on device power production. This will be addressed in Chapter 6.

5.4.5 Wave Period Ratio

Given the variation in spectral shape at the Killard Point site from the standard theoretical shapes discovered in Section 5.4.4, the Wave Period Ratios at the site were examined, using the measured spectral data, to determine if significant variance existed across sea state conditions and between the recorded data. Where the work in Chapter 3 deals mainly with the conversion and correction of Wave Parameters between recorded and modelled data, this section intends to characterise the primary WPR relationship of interest at the Killard Point site, that of T_e/T_{01}, and to compare this to the ratio derived from the Bretschneider Spectrum.

The standard industry practice of assuming a constant relationship between Wave Periods (via the use of standardised spectra) has been shown to be questionable (Robertson *et al.*, 2016), and has further been shown to introduce some significant variations in the energy production that is estimated when using this constant factor conversion. The work below recaps the derivation of the T_e/T_{01} relationship based on an assumed Bretschneider spectrum, followed by a determination of the average T_e/T_{01} WPR from recorded data at Killard Point.

5.4.5.1 T_e/T_{01} derivation

The WPR between T_e and T_{01} was derived for the Bretschneider Spectrum by introducing a constant, αB to represent the relationship between the desired period parameter and the period parameter contained within the deployment records (Equation (**3**.**15**)), rewriting the equation in terms of spectral moments (Equation (**3**.**16**)) and expressing the spectral moments in terms of common parameters to allow the terms to be equated and expressed as a constant ratio (Equation (**3**.**8**) - (**3**.**10**)).

Resulting in a derived ratio of:

$$T_e = 1.1107 T_{01} \quad (5.2)$$

5.4.5.2 T_e/T_{01} empirical estimate

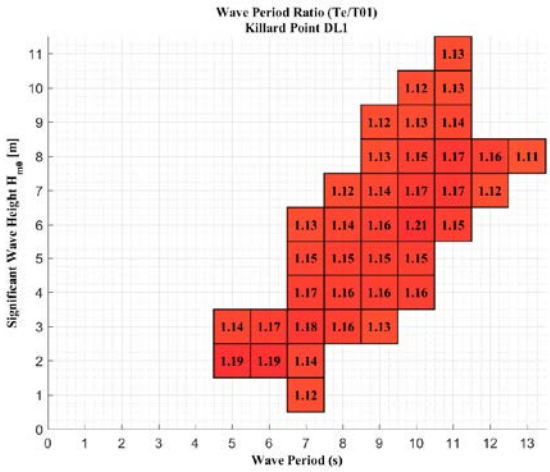


FIGURE 127: T_E/T_{01} WAVE PERIOD RATIOS BINNED BY WAVE HEIGHT AND PERIOD

The average WPR for T_e/T_{01} is 1.149, higher than the suggested Bretschneider WPR of T_e = 1.1107 T_{01}. The Bretschneider Spectrum assumption offers clear benefits in terms of expediency, and in formulating Wave Parameter Relationships during periods when detailed data is not available. This work makes clear, however, that there is potential for the spectral shapes at sites on the West Coast of Ireland to be significantly different than that suggested by the Bretschneider Spectrum, and thus it is important to be cognisant of the impact this can have on the analysis resulting from the characterisation of the site.

5.4.6 Weather Windows

A weather window can be defined as a successive period of time in which the parameter in question (typically H_{m0}) does not exceed a defined threshold. They are used to determine the best time for installation and O&M activities. A full weather window analysis of Significant Wave Height has been conducted using the 24 years of hindcast data. This has been computed to inform decisions for events ranging from minor repairs to device installation or overhaul.

Weather windows have been computed for H_{m0} values from 0.5-6m in 0.5m increments, T_{01} Wave period for values not exceeding 6, 7, 8, 9, 10, 11, 12 seconds; and for durations of 3, 6, 12, 18, 24, 36, 48 and 72 hours. Furthermore, a combined Weather Window analysis has been performed which takes into account each combination of Wave Height and Wave Period Threshold of non-exceedance.

Sample weather window plots are provided for nearshore and offshore sites at 1.5m & 2.0m H_{m0} Threshold and 12 & 24 hr duration. It is evident that the 1.5m H_{m0} threshold which is commonly used as a safety cut-off threshold for a wide-variety of service vessels is easily exceeded at the west coast Killard Point Site. Availability of weather windows at this threshold falls below 10% during November-February, rising to approximately 35% during summer months.

If this threshold is raised to 2m H_{m0} by the provision of a service vessel and crew that can operate in rougher conditions, this availability analysis becomes less onerous, with over 55% availability over a 24-hour period during May-August, and greater than 70% in the nearshore location.

672 combinations of Wave Height & Wave Period Threshold and duration are examined in the combined analysis, with 96 conditions and 56 conditions for Wave Height alone and Wave Period alone, respectively. This will enable full knowledge of the availability of the site during all sea-states in which work could be undertaken.

For comparison purposes, and to highlight the difference in conditions, the nearshore and offshore values are provided together in the following plots.

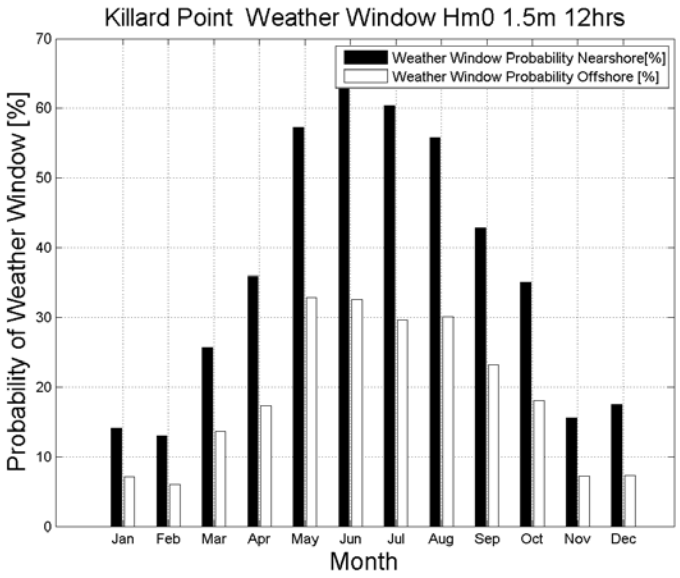


FIGURE 128: NEARSHORE AND OFFSHORE PERSISTENCE ANALYSIS AT 1.5M H_{M0} THRESHOLD FOR 12 HOUR WINDOW

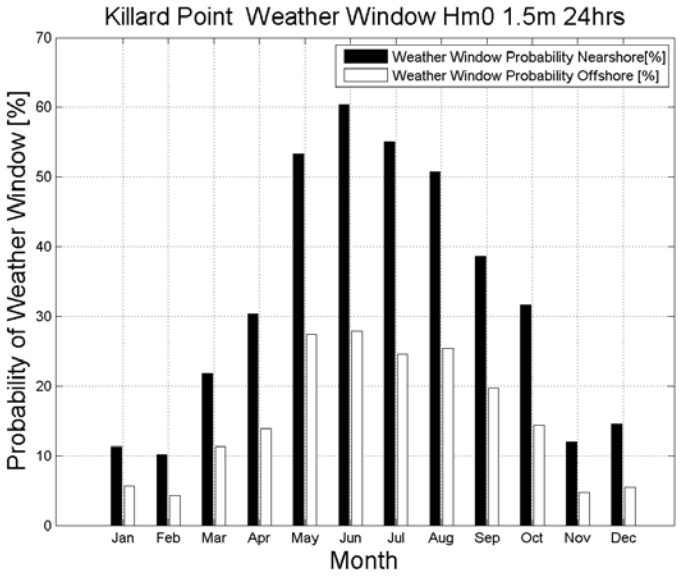


FIGURE 129: NEARSHORE AND OFFSHORE PERSISTENCE ANALYSIS AT 1.5M H_{M0} THRESHOLD FOR 24 HOUR WINDOW

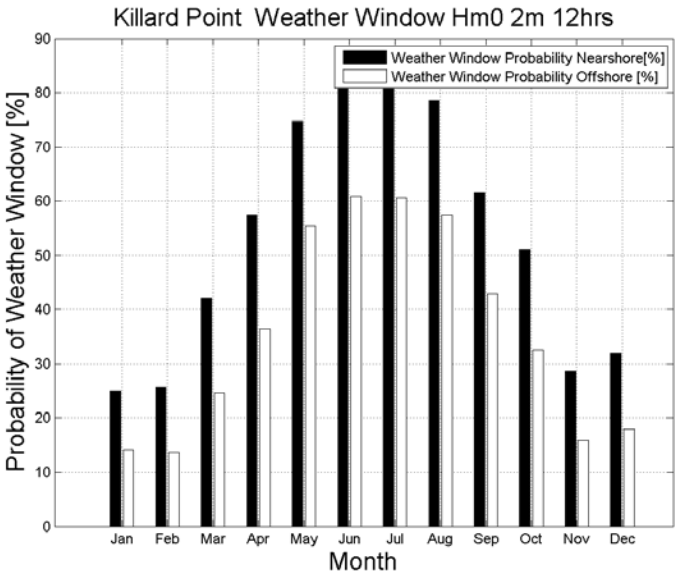


FIGURE 130: NEARSHORE AND OFFSHORE PERSISTENCE ANALYSIS AT 2M H_{M0} THRESHOLD FOR 12 HOUR WINDOW

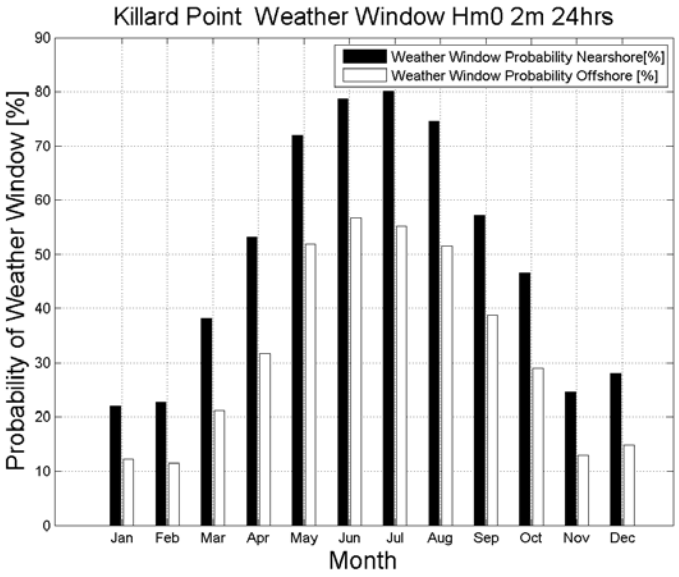


FIGURE 131: NEARSHORE AND OFFSHORE PERSISTENCE ANALYSIS AT 2M H_{M0} THRESHOLD FOR 24 HOUR WINDOW

The difference in nearshore and offshore availability is approximately 25-30% during summer months, dropping to ~5-10% during winter months.

Average availability of a 12-hour window for the Nearshore site during summer months is approximately 55-65% at a 1.5m H_{m0} threshold, and 75-85% at the 2.0m H_{m0} Threshold. For a 24-hour window, this decreases to 50-60% at a 1.5m H_{m0} threshold, and 70-80% at the 2.0m threshold.

Notably, the requirement of a 24-hour weather window is not appreciably more onerous than a 12 hour weather window; however, the requirement of a 1.5m H_{m0} threshold in place of a 2.0m threshold dramatically decreases the probability of attaining a weather window; approximately halving the probability of occurrence.

5.4.7 Forecasting Prediction Accuracy

Forecasting is an integral part of site assessment and characterisation in the development of sites for Marine Renewable Energy. The ability to predict future wave conditions forms part of a system-wide analysis of the impact of the conditions at a site on the economic outcomes of the project.

Forecasting wave conditions contributes to the determination of design decisions on planned developments and to assessing Operations & Maintenance strategy and the impact of unplanned repairs. In operation, forecasting is critical for projects considering energy (electricity) production scheduling and prediction of contribution to the energy grid/market.

This Section develops new methods that can provide more detailed, accurate, information for site assessment, and help to assess suitability of the available prediction models for informing design decisions and energy production.

The work:

- Develops a methodology for assessing forecast performance.
- Analyses accuracy of the Marine Institute forecast model for Irish wave sites.
- Identifies trends in model performance and behaviour.
- Analyses and quantifies the impact of forecast model on power production accuracy.

The correlation between data from the SWAN predictive numerical model provided by Marine Institute Ireland and the conditions which then occur at the wave buoys is examined. The study will compare the ability of the model to forecast the conditions at different time periods, ranging from 1-6 days forward. Provided the prediction accuracy proves to be good over this range, this would be instrumental in planning and scheduling for a wide variety of activities and outcomes both pre and post-deployment.

The Killard Point site provides a test case for analysing the impact of the forecast accuracy on the economic outcomes of Marine Renewable Energy projects.

5.4.7.1 Forecast Model Background

The numerical wave model, SWAN, simulates surface gravity waves for a domain covering Irish waters at a resolution of 0.025 degrees (approximately 1.5km). The model uses National Centers for Environmental Prediction (NCEP) Global Forecasting System (GFS) (NOAA, 2017) for wind forcing and the Fleet Numerical Meteorology and Oceanography Center (FNMOC) (The Fleet Numerical and Oceanography Centre, 2017) Wave Watch 3 data for the wave boundaries. A daily 6 day forecast is generated for parameters such as significant wave height, mean wave period and mean wave direction (Marine Institute, 2016). This data has been acquired via the THREDDS server, where it is supplied in Net CDF file format. This forecast covers a rolling duration of 36 days.

5.4.7.2 Forecast Model Behaviour

An explanation for the Forecast Model Behaviour has been provided following consultation with the Marine Institute, who provided detailed information on the data stored on the THREDDS server.

An explanation of model behaviour for data stored on THREDDS server (from email correspondence with Kieran Lyons of Marine Institute):

The wave forecast is set up to run a 13-day simulation from rest every day. It is broken up into a 7-day hindcast and 6-day forecast. It takes a number of days for the wave field to fully develop in the model domain, but it has done so by "day 7". Thus, the data is saved from each "day 7" and this corresponds to the day prior to the current

day. In this fashion, a hindcast dataset of wave data is built up. Each day's 6-day forecast is published and then, (the following day), trashed.

This explanation was necessary to accurately determine the structure of the data and to ensure that the correct time period was being considered for the analysis.

5.4.7.3 Forecast Model Methodology

Displaying and using this data requires accessing and downloading this data at daily intervals to create a composite dataset which expresses the forecast at 1-6 days forward. The data has been extracted by the author to plain-text format containing the date and parameters of interest, using a MATLAB script which has been created to allow extraction of data per site by longitude and latitude coordinates. A customised time-series synchronisation method was required to keep track of the day on which the forecast data was obtained, and the temporal distance from the date of extraction to the timestamp of the extracted data was used to determine the number of days "forward" the predicted data applied to. A major downside to this approach is that the duration of data available at a given point is limited, and a full realisation of forecast data requires continuous collection, processing, storage and analysis of data over a long period of time.

Fortunately, the Marine Institute have additionally made available a large dataset of 1 - 6 day forecasts which have been archived at the locations of the Marine Institute Buoys for use in this project. This has enabled a full view of the behaviour of the prediction model over a longer duration. This dataset covers the period 01-01-2015 to 31-07-2016, at 20 locations, including the M-Buoys (Weather Buoys) and a number of wave buoys including those at Belmullet, Galway Bay, Achill, Cork SmartBuoy and Killard Point. Four Sites were assessed; including Belmullet Berth A and Berth B, Galway Bay, and Westwave MK3. The location of these sites are as follows:

TABLE 63: FORECAST MODEL ANALYSIS LOCATIONS

Location	Coordinates
Belmullet Berth A	Lon: -10.27° Lat: 54.28°
Belmullet Berth B	Lon: -10.14° Lat: 54.23°
Galway Bay	Lon: -9.27° Lat: 53.23°
Westwave MK3 (Killard Point)	Lon: -9.70° Lat: 52.76°

These locations are highlighted in Figure 5. The predictions were compared at 1-6 days out, with assessment based on R^2 correlation, RMSE, Mean Error, Mean Average Error, Maximum error and Scatter Index metrics. The Marine Institute advised that the forecasting skill of the model performed very well up to a period of 24 hours, reasonably well from 24-36 hours, and began to deteriorate rapidly thereafter, owing predominantly to weakness in the ability of the wind forecast model to provide an accurate prediction. As part of this work, the aim was to test this assertion, and to display the impact on wave energy production of the inaccuracy in the wave forecast.

The assessment was performed using data obtained on the 28/07/2016. For the prediction data, this covered a span of 29-06-2016 – 02-08-2016, while the buoy data covered the period 29-06-2016 – 28/07/2016. Analysis of a longer duration dataset took place on the interval 01-01-2015 – 31-7-2016.

5.4.7.4 Forecast Model Performance Assessment

The performance of the Model for each site, for both H_{m0} and T_z parameters, is considered below. Using the R^2 correlation, RMSE, Mean Error, Mean Average Error, Maximum error and Scatter Index metrics; the accuracy and suitability of the forecast data is assessed.

5.4.7.4.1 Belmullet Berth A

An example of the timeseries comparison data for the Berth A site is provided in Figure 132 below. Each plot in descending order represents an incremental step forward in days of prediction, with the first plot being forecast data for 1 day ahead, and the final plot forecast data for 6 days ahead. Corrected buoy data is shown in blue, while the forecast data is shown in red. Forecast errors are most noticeable

around Q1 2016, with increasingly large storms predicted by the forecast model which deviate further and further from the actual conditions.

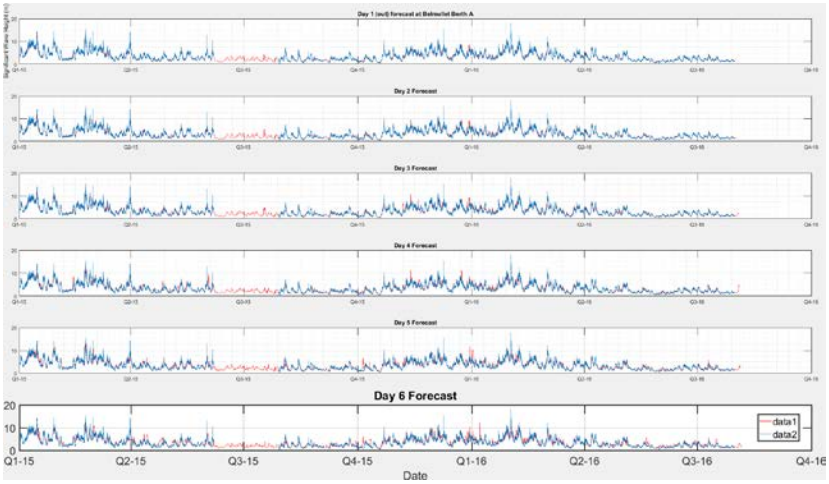


FIGURE 132: BELMULLET BERTH A SIGNIFICANT WAVE HEIGHT COMPARISON (DAY 1-6)

Tabulated results below provide an overview of additional error metrics.

TABLE 64: BELMULLET BERTH A FORECAST ACCURACY ANALYSIS (H_{M0})

Statistic	1 Day	2 Days	3 Days	4 Days	5 Days	6 Days
Mean Average Error	0.3838	0.4032	0.4727	0.5496	0.6303	0.7651
Mean Square Error	0.2999	0.3273	0.4535	0.6388	0.8385	1.2014
Max Error	7.1739	7.1005	7.8268	8.1101	8.9519	9.6174
Mean Error	-0.0116	-0.0657	-0.1092	-0.1349	-0.1180	-0.0687
R correlation	0.9626	0.9594	0.9439	0.9204	0.8944	0.8450
RMSE	0.5476	0.5721	0.6734	0.7992	0.9157	1.0961
Scatter Index	0.1575	0.1647	0.1942	0.2306	0.2641	0.3163

Examining the Mean Square Error for H_{m0} at the Belmullet Berth A site, it appears to be quite accurate up to 3 days forward, where the prediction accuracy begins to deteriorate rapidly. This is in line with the assertions of the Marine Institute. The R correlation value of 0.9626 to 0.9439 for 1-3 days out, respectively, is indicative of a very good fit between the forecast and buoy data; with little time-lag. Beyond this, the accuracy dis-improves, but the Mean Average Error at even 6 days forward of 0.7651 would still give rise to generally applicable and usable results in certain scenarios. The Mean Error shows that there is very little bias associated with the

forecast prediction data, although this site does carry a negative bias which increases to a maximum of -0.1349 at 4 days forward. The overall average of parameters is extremely similar between forecast and buoy data overall.

TABLE 65: BELMULLET BERTH A FORECAST ACCURACY ANALYSIS (T_z)

Statistic	1 Day	2 Days	3 Days	4 Days	5 Days	6 Days
Mean Average Error	0.6152	0.6069	0.6255	0.6999	0.7648	0.8629
Mean Square Error	0.6528	0.6611	0.6918	0.8481	1.0121	1.2969
Max Error	6.7361	6.6683	6.8502	7.0625	7.9707	8.4132
Mean Error	0.4303	0.3830	0.2990	0.2632	0.2858	0.3522
R correlation	0.9042	0.8968	0.8821	0.8486	0.8128	0.7599
RMSE	0.8080	0.8131	0.8318	0.9209	1.0060	1.1388
Scatter Index	0.1132	0.1139	0.1166	0.1291	0.1410	0.1596

The Forecast accuracy of T_z at Belmullet Berth A shows similar accuracy. The R correlation is reduced for T_z in comparison to H_{m0}. The scatter index, indicative of the RMSE relative to the mean value, is also lower, which is indicative of good accuracy, despite a minor increase in the time-scale based deviation which causes the reduced R correlation. The Mean Average and Mean Square Error begin to increase rapidly after Day 3, while R correlation coefficient diminishes significantly on Day 6 and RMSE sees the largest increase between forecast distance days between days 5-6. The Mean Error shows the presence of a positive bias in the predicted dataset of approximately 0.35 seconds.

5.4.7.4.2 Belmullet Berth B

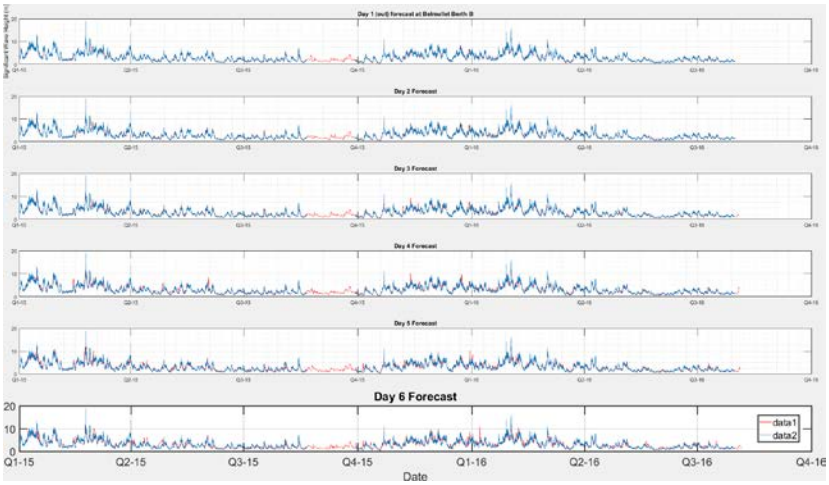


FIGURE 133: BELMULLET BERTH B H_S COMPARISON (DAY 1 - 6)

TABLE 66: BELMULLET BERTH B FORECAST ACCURACY ANALYSIS (H_{M0})

Statistic	1 Day	2 Days	3 Days	4 Days	5 Days	6 Days
Mean Average Error	0.3538	0.3628	0.4140	0.4828	0.5524	0.6779
Mean Square Error	0.2470	0.2576	0.3485	0.4954	0.6266	0.9421
Max Error	7.7076	8.7002	9.4088	9.1451	8.5777	10.568
Mean Error	0.0557	0.0001	-0.0385	-0.0542	-0.0413	-0.0076
R correlation	0.9642	0.9618	0.9481	0.9256	0.9057	0.8565
RMSE	0.4970	0.5075	0.5904	0.7039	0.7916	0.9706
Scatter Index	0.1614	0.1649	0.1921	0.2291	0.2576	0.3160

At the Berth B site the results mirror those of the Berth A site; with very little appreciable difference overall. RMSE and Mean Square Error are reduced marginally, but the Scatter Index result displays that this is in line with the change in the Mean Wave Height.

TABLE 67: BELMULLET BERTH B FORECAST ACCURACY ANALYSIS (T_z)

Statistic	1 Day	2 Days	3 Days	4 Days	5 Days	6 Days
Mean Average Error	0.6898	0.6708	0.6902	0.7650	0.8118	0.9098
Mean Square Error	0.7776	0.7759	0.8266	0.9890	1.1235	1.3986
Max Error	5.9453	5.8780	5.9400	6.4142	6.6822	6.9832
Mean Error	0.5326	0.4770	0.3899	0.3459	0.3750	0.4515
R correlation	0.9013	0.8945	0.8747	0.8393	0.8068	0.7566
RMSE	0.8818	0.8808	0.9092	0.9945	1.0600	1.1826
Scatter Index	0.1254	0.1253	0.1293	0.1415	0.1508	0.1683

Taking the forecast accuracy of T_z at the Belmullet Berth B site, the MI forecast behaviour is again similar to Berth A. Mean average and Mean Square Error begin to increase rapidly after Day 3. R correlation coefficient diminishes significantly on Day 6 and RMSE sees the largest increase between forecast distance days at this point. Similar to the Berth A site, there is a positive bias in the predicted data for T_z at the Berth B site.

5.4.7.4.3 Galway Bay ¼ Scale Test Site

TABLE 68: GALWAY BAY FORECAST ACCURACY ANALYSIS (H_{M0})

Statistic	1 Day	2 Days	3 Days	4 Days	5 Days	6 Days
Mean Average Error	0.1755	0.1813	0.2005	0.2316	0.2641	0.3045
Mean Square Error	0.0583	0.0638	0.0824	0.1167	0.1534	0.1952
Max Error	2.0673	1.8346	2.4461	2.9424	2.8330	2.8526
Mean Error	0.1010	0.0898	0.0837	0.0836	0.0912	0.1025
R correlation	0.9327	0.9194	0.8885	0.8327	0.7758	0.7108
RMSE	0.2414	0.2526	0.2871	0.3417	0.3917	0.4418
Scatter Index	0.2870	0.3010	0.3425	0.4075	0.4671	0.5269

Galway Bay has the most benign conditions of the sites studied, being a sheltered site that is generally considered to be reflective of a ¼ scale test-site. As a result of this, the overall error metrics look favourable for Mean Average, Mean Square, and Maximum Error. However, the relative metrics which are reflective of the error in relation to the conditions at the site such as Scatter Index and R Correlation suggest that the performance of the forecast model is certainly not as effective for the Galway Bay site. A Scatter Index of 0.287, rising to 0.5269 by Day 6 is a relatively poor result; and while the R correlation value of 0.9327 predicting 1 day forward is reasonable, this drops to 0.7108 at 6 days forward. The Mean Error displays a relatively constant positive bias of 0.1 m Hs.

TABLE 69: GALWAY BAY FORECAST ACCURACY ANALYSIS (T_z)

Statistic	1 Day	2 Days	3 Days	4 Days	5 Days	6 Days
Mean Average Error	0.7616	0.7680	0.7858	0.8497	0.8842	0.9604
Mean Square Error	1.0183	1.0735	1.1126	1.3023	1.4531	1.6099
Max Error	18.7619	18.4375	18.6261	18.6882	18.7817	18.6405
Mean Error	0.4703	0.4735	0.4130	0.3870	0.4270	0.4673
R correlation	0.6685	0.6449	0.6203	0.5432	0.4916	0.4263
RMSE	1.0091	1.0361	1.0548	1.1412	1.2054	1.2688
Scatter Index	0.2698	0.2771	0.2822	0.3053	0.3224	0.3393

At the Galway Bay site, the Marine Institute Forecast data again provides the worst accuracy of the sites studied, with low Mean Square Error and Maximum Error due to the low wave conditions present at the site; but high scatter index and low R correlation metrics. The best R correlation value of 0.6685 is reflective of poor fit between the forecast and buoy data, and is suggestive of a time-lag issue. The T_z parameter appears to be more sensitive to this than H_{m0}.

5.4.7.4.4 Westwave MK3 at Killard Point

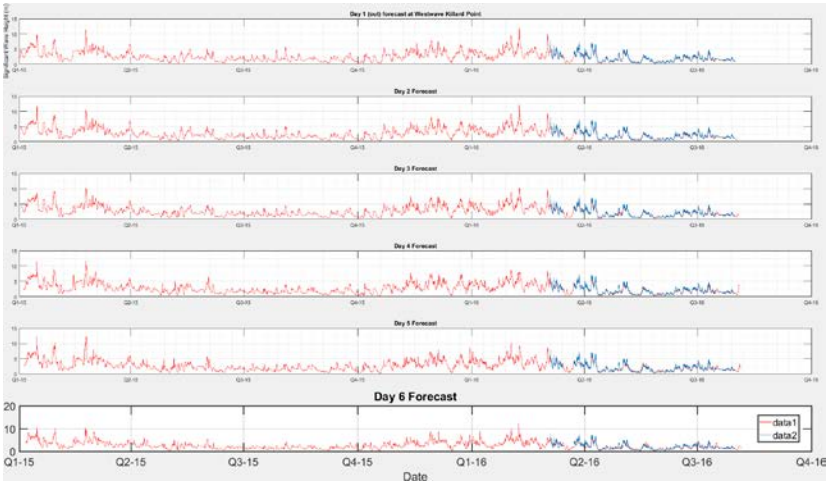


FIGURE 134: KILLARD POINT FORECAST ACCURACY ASSESSMENT (DAY 1 - 6)

TABLE 70: WESTWAVE (KILLARD POINT) MK3 BUOY FORECAST ACCURACY ANALYSIS (H_{M0})

Statistic	1 Day	2 Days	3 Days	4 Days	5 Days	6 Days
Mean Average Error	0.3091	0.3022	0.3246	0.3505	0.4243	0.4920
Mean Square Error	0.2039	0.1863	0.2178	0.2514	0.3641	0.4995
Max Error	3.4255	3.1889	3.2341	3.5400	3.9481	4.0574
Mean Error	0.2221	0.1778	0.1859	0.1527	0.1808	0.1855
R correlation	0.9544	0.9522	0.9446	0.9276	0.8933	0.8449
RMSE	0.4515	0.4316	0.4667	0.5014	0.6034	0.7067
Scatter Index	0.2199	0.2102	0.2273	0.2442	0.2939	0.3443

The Forecast Accuracy at the Killard Point site is very much in line with that at Belmullet Berths A & B. The most appreciable difference is that the Bias at the Killard Point site is the largest of all sites studied, while the scatter index is also larger than at the Belmullet Berth A or B sites. The Maximum Error is far lower than these at the Killard Point site.

TABLE 71: WESTWAVE (KILLARD POINT) MK3 BUOY FORECAST ACCURACY ANALYSIS (T_z)

Statistic	1 Day	2 Days	3 Days	4 Days	5 Days	6 Days
Mean Average Error	0.7285	0.7397	0.7859	0.8413	0.8597	0.9724
Mean Square Error	1.0273	1.0598	1.1859	1.2937	1.3273	1.7021
Max Error	6.5235	6.4978	6.5178	6.5307	6.5046	6.4336
Mean Error	0.5554	0.5300	0.4687	0.3905	0.4400	0.4858
R correlation	0.8728	0.8667	0.8459	0.8335	0.8168	0.7424
RMSE	1.0136	1.0295	1.0890	1.1374	1.1521	1.3047
Scatter Index	0.1692	0.1719	0.1818	0.1899	0.1924	0.2179

The T_z accuracy at the WestWave site is very consistent across the forecast duration of drops off noticeably at Day 5, with Mean Average Error, Mean Square Error and RMSE increasing rapidly, and R correlation decreasing to 0.8449 by Day 6. Interestingly, Day 2 forecast accuracy is marginally better than Day 1 for Mean Average Error, Mean Square Error, Max Error and RMSE.

5.4.7.5 Individual Error Statistic Comparison

To achieve a better understanding of the forecast error at each site, individual error metrics have been outlined for each of the four sites.

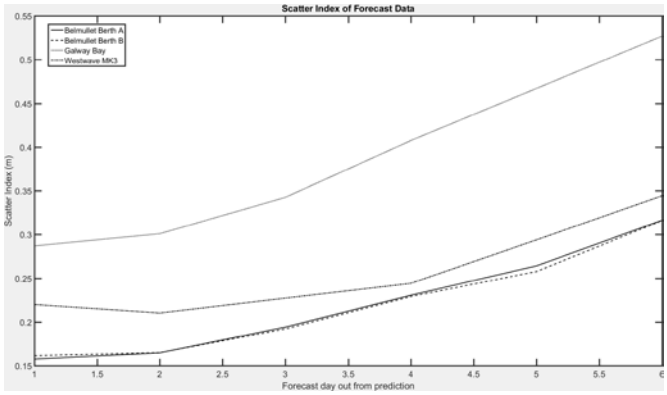


FIGURE 135: SCATTER INDEX FORECAST ACCURACY COMPARISON

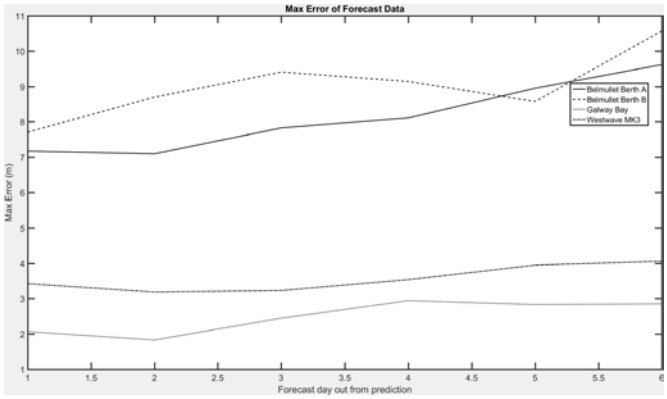


FIGURE 136: MAX ERROR FORECAST ACCURACY COMPARISON

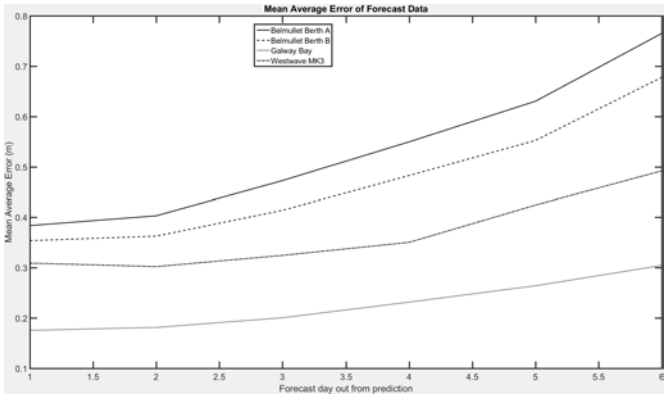


FIGURE 137: MEAN AVERAGE ERROR FORECAST ACCURACY COMPARISON

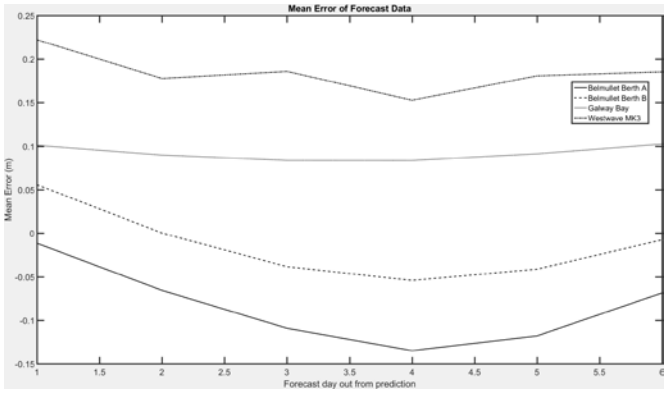


FIGURE 138: MEAN ERROR FORECAST ACCURACY COMPARISON

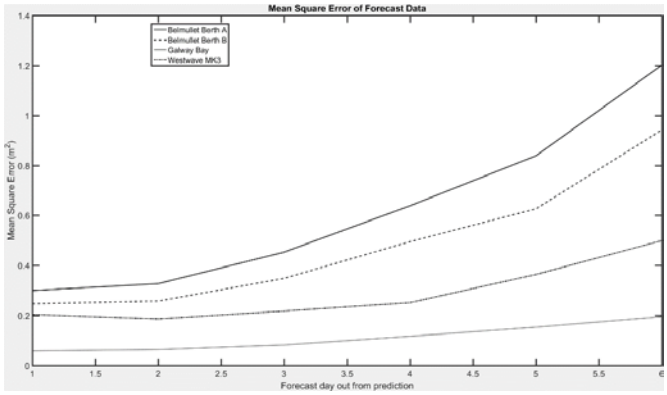


FIGURE 139: MEAN SQUARE ERROR FORECAST ACCURACY COMPARISON

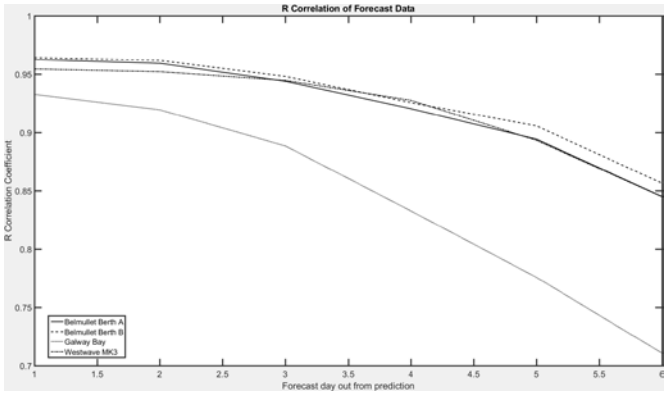


FIGURE 140: R^2 CORRELATION FORECAST ACCURACY COMPARISON

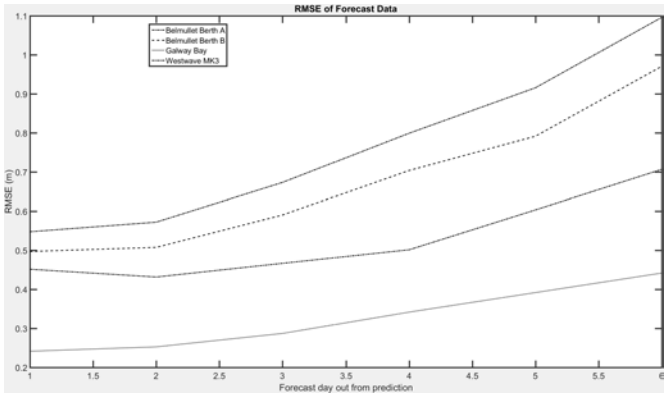


FIGURE 141: RMSE FORECAST ACCURACY COMPARISON

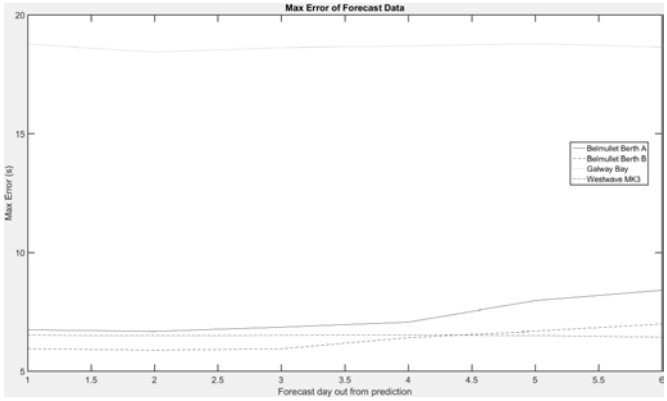


FIGURE 142: MAXIMUM ERROR FORECAST ACCURACY COMPARISON (T_Z)

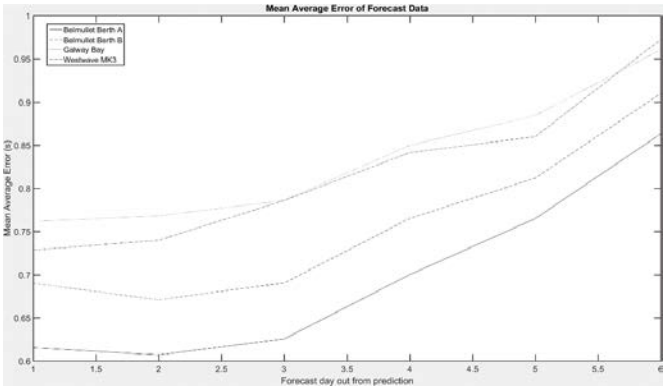


FIGURE 143: MEAN AVERAGE ERROR FORECAST ACCURACY COMPARISON (T_Z)

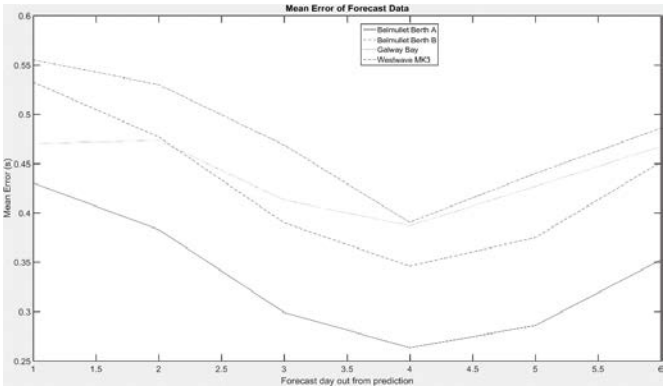


FIGURE 144: MEAN ERROR FORECAST ACCURACY COMPARISON (T_z)

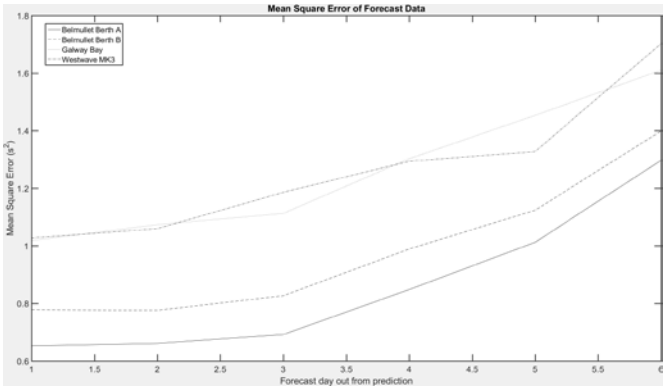


FIGURE 145: MEAN SQUARE ERROR FORECAST ACCURACY COMPARISON (T_z)

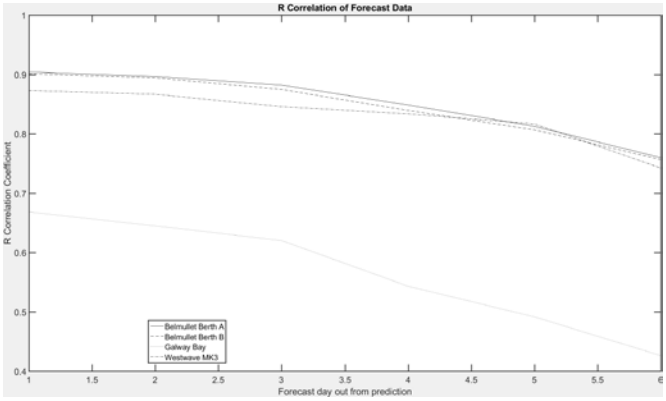


FIGURE 146: R^2 CORRELATION FORECAST ACCURACY COMPARISON (T_z)

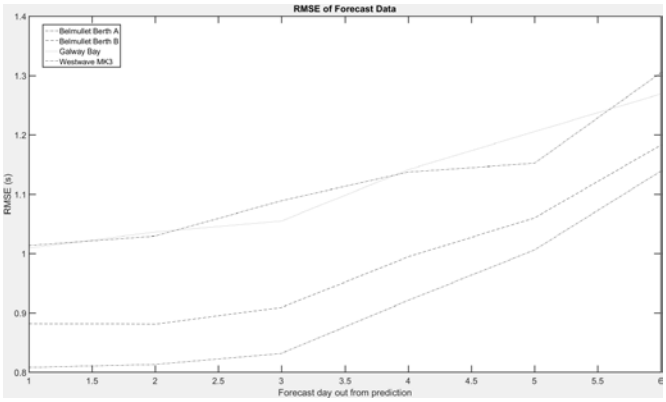


FIGURE 147: RMSE FORECAST ACCURACY COMPARISON (T_z)

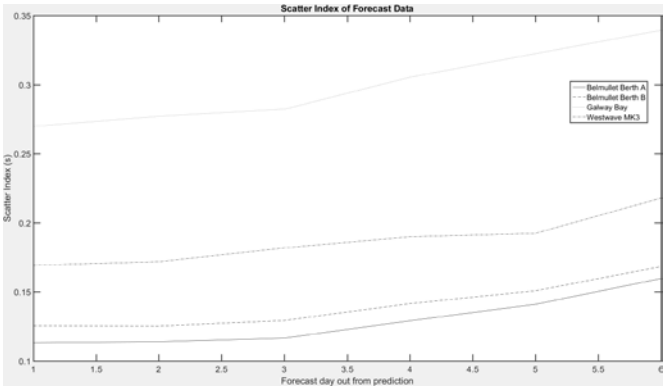


FIGURE 148: SCATTER INDEX FORECAST ACCURACY COMPARISON (T_z)

5.4.7.6 Power Production Comparison

Estimated power production was compared for both the buoy and prediction data over the forecast duration 1 - 6 days to examine the accuracy of the forecast data in prediction of energy production.

Buoy and prediction data was synchronised to ensure that there was no time-lag present in the comparison. As further quality control and pre-processing, NaN and zero values were removed to ensure that power production was done only where both datasets were sufficiently populated. In certain instances, this resulted in severely reduced number of data points present. This is particularly evident for both the Galway Bay and WestWave MK3 results, whose buoy data had many missing or corrupt values. This unfortunately prohibited a full analysis of variability (seasonal

and inter-annual). This lack of data also results in fluctuating energy production for the prediction data, given that the analysis is tied to data being present for each period of analysis for both buoy and prediction datasets.

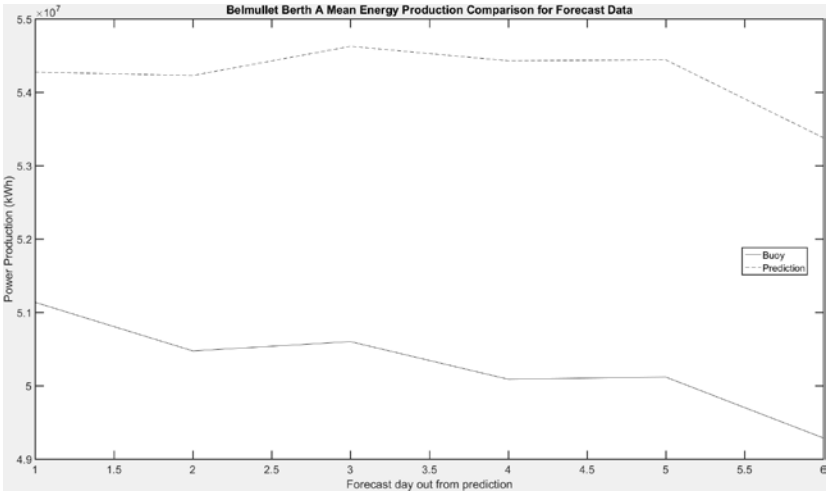


FIGURE 149: MEAN ENERGY PRODUCTION BUOY VS. PREDICTION AT BELMULLET BERTH A

The prediction data at Belmullet Berth A results in consistently higher Power Production estimates than those produced with the available buoy data. A power production bias of approximately 5% exists at one day out, which rises to 8.3% by Day 6. Given that there is a negative bias in the mean H_s value, it stands to reason that the power production error occurs during large over-predictions by the forecast model, which carry an outsized contribution to energy production given the square relationship of wave power with H_s.

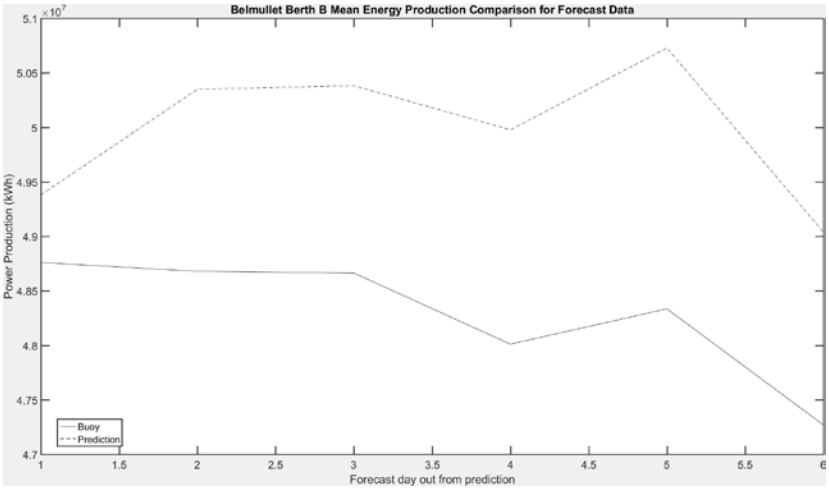


FIGURE 150: MEAN ENERGY PRODUCTION BUOY VS. PREDICTION AT BELMULLET BERTH B

Power production accuracy using the forecast model at Berth B is superior to that at Berth A, with a starting error of just 1% at 1 Day out, which increases to a maximum of 5% by Day 5.

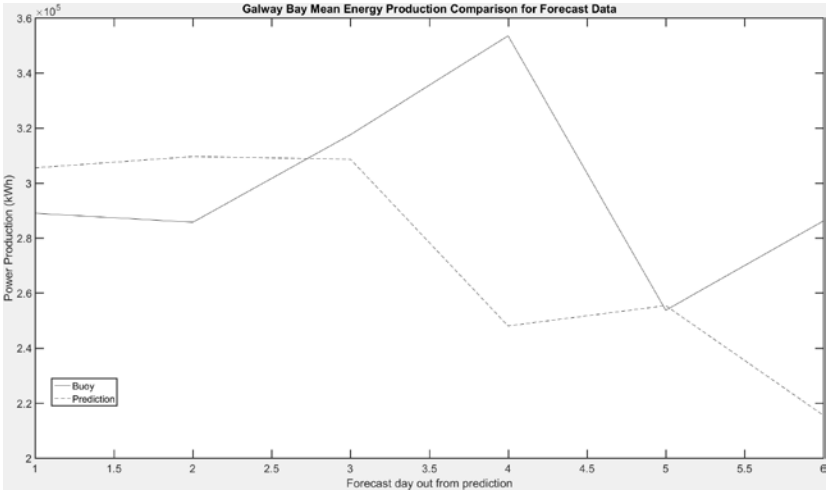


FIGURE 151: MEAN ENERGY PRODUCTION BUOY VS. PREDICTION AT GALWAY BAY

Power prediction accuracy using forecast data at the Galway Bay site is particularly poor, with a 5.7% over prediction of energy production at 1 Day forward, which then oscillates wildly over the remaining forecast durations; reaching a maximum under-

prediction against the buoy data of 30%. Given the poor R correlation of the T_z parameter at Galway Bay, coupled with the large relative errors in H_s, it does not appear feasible to achieve a reliable energy production forecast using the Marine Institute data for Galway Bay.

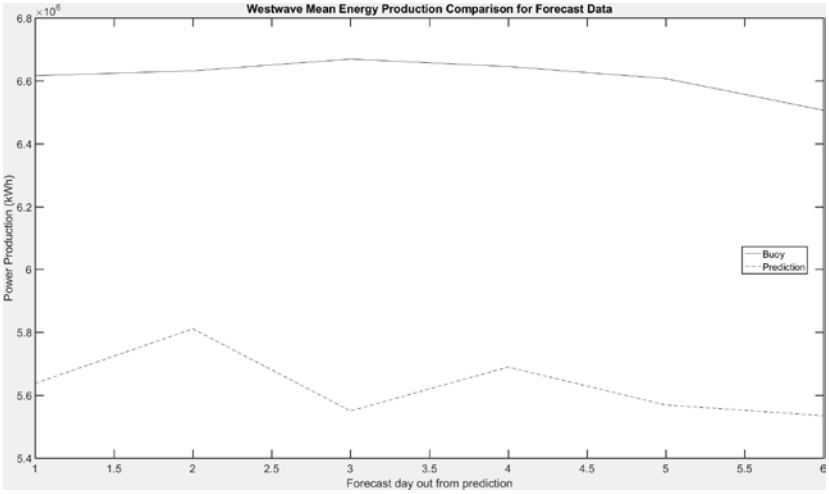


FIGURE 152: MEAN ENERGY PRODUCTION BUOY VS. PREDICTION AT KILLARD POINT

The prediction data at Killard Point results in a large under-prediction of energy production, at approximately 15% for all durations. The positive Bias in Hs and Te for the Prediction data does not appear to result in an over-prediction in power production, as might be expected.

5.5 Modelling & Characterisation Summary

5.5.1 Outcomes of Numerical Modelling

A Class 1 numerical model assessment was performed according to the IEC-TS for the Killard Point Site, using parametric wave data inputs (H_s, T_p, Peak Direction) and a 3rd generation spectral wave model. This model has been tuned to provide the best combination of accuracy and efficiency, and 24 years of high quality hindcast data has been produced, with output at multiple validation points indicative of likely locations of WEC deployment. The results of the calibration across three deployments show that the model very accurately represents the conditions recorded by the buoy; thus validating the input data and modelling methodology used.

5.5.2 Outcomes of Characterisation

A comprehensive metocean assessment has been performed which covers accessibility, extremes, directionality, monthly and annual variation of conditions, and power production. This hindcast data has been analyzed to determine summary statistics of key wave parameters according to the IEC-TS. This includes an assessment of the monthly and annual variation of the key parameters, H_s, T_e and wave power, giving a greater understanding of the characteristics of this energetic site. The ultimate energy production of wave farms is dependent upon, and highly sensitive to the estimates of wave conditions at deployment sites, and as a result, the analysis of wave power variability conducted in this Chapter is of very real value to potential developers and project owners. The WPR adjustment methods developed in Chapter 3 are used to provide more accurate estimates of Wave Period Parameters, and thus improve the resultant estimates of energy production.

The Marine Institute Forecast model

It is important to remember that the industry is still at a nascent stage, with many resource assessments so far proven (by failures of a number of deployed devices encountering “unexpected,” conditions) not to cover the wide range of design conditions required for the deployment of MRE projects.

The modelling and analysis in this project will directly feed the commercial model for the deployment of WECs at Killard Point. Given the current reticence in lending for

Marine Renewable Energy (MRE) projects, it is absolutely vital that the modelling results are as accurate and dependable as possible, and this is a good first step towards an analytical quantification of resource that is appropriate for MRE development.

As part of a system-wide analysis of the impact of the metocean conditions at site on the economic outcomes of the MRE projects, forecast model data was analysed to determine its suitability for informing design decisions on the planned deployment, Operations & Maintenance, emergency repair, and energy scheduling and prediction strategy. This Marine Institute model was found to be useful for forecasting H_s and T_z conditions up to three days forward, particularly at the more energetic and less sheltered sites studied.

5.5.3 Killard Point Site Specific Details

The Killard Point Site was found to be representative of the energetic wave climate on the West Coast of Ireland. When analysing wave height distribution, the nearshore and offshore sites feature a difference in magnitude of H_{m0} which could appreciably alter the availability of both sites, and make operations and maintenance activity challenging; especially when the additional travel distance to the offshore site is considered. Mean H_{m0} conditions at the Offshore and Nearshore sites are 2.75m and 2.56m respectively. The Offshore site features an average T_{01} period of 8.79s, while this is 8.71s at the Nearshore site. While there was a difference in magnitude of the parameters, the variability in conditions was not significantly different at both sites.

The Weather Window analysis conducted shows availability during summer months for a 2m H_{m0} threshold is relatively good, with a probability of weather window occurrence of in excess of 60%, whereas winter conditions will prove difficult for accessibility for crews with access limits of 1.5m threshold providing 30-35% availability during summer months, and only 5-10% during winter months.

The distribution of the wave parameters during the buoy deployments is heavily influenced by the seasonality of the conditions at the site, with the deployments covering mainly winter and spring months. This creates difficulty in validating the accuracy of availability using the buoy data, so it is strongly recommended that a

future deployment take place during summer months to better characterise the site for these conditions.

The prevailing wave direction is between 270-290 degrees, with these waves experiencing small reduction as they enter the nearshore, shallow water environment.

December, January and February feature the most onerous conditions, including the highest average H_{m0} and T_{01} values. An extreme wave of 15.88m was measured on the 27th of January 2014 during buoy deployment 3. The corresponding condition at this time in the modelled data is approximately 14.71m. The model tends to underpredict storm events, and thus the estimated extreme wave heights at the nearshore site of 15.45m (20 Year RP), 17.45m (50 Year RP) and 19.02m (100 Year RP) should be utilised with caution.

Power production at the site is a key concern for commercial interests. The mean annual wave power at the nearshore site was found to be approximately 45 kW/m, which is in line with other nearshore sites in 20m water depth on the West Coast of Ireland.

Power Production analysis at the nearshore site shows the annual power production estimated using a single WEC Device is 1034MWh, with an annual standard deviation of 88MWh.

An analysis of the variation in power over a monthly time-scale shows that there is significant seasonal variability in the power production, and this is a potential issue which will require careful consideration in terms of demand scheduling and cash-flow forecasting for the project.

Overall the Killard Point site has been shown to carry sufficient wave energy resource to justify the deployment of Wave Energy Converters, despite a potentially challenging operating environment.

5.6 IEC-TS Methodology Summary

5.6.1 Practicalities of Implementing IEC-TS

The modelling of the test site was conducted to Class 1 "Feasibility" standards as per the IEC-TS. Attempts were made to follow the guidelines for a Class 3 model assessment where possible, but a number of relaxations were made according to "Annex A" of the standards, which specify that model components found not to have greater than a 5% threshold difference can be omitted. This included the omission of a fully spectral formulation input approach, as the memory and computational requirements were deemed excessive.

A chief obstacle which presented itself was the difficulty in acquiring an extended buoy data record, which are commonly affected by loss or damage of deployed buoys, or simply cost and time implications involved in running an extensive measurement campaign. The acquisition of model data presents yet another barrier in achieving the standards outlined by the IEC-TS. Existing large scale wave models which cover large areas such as WW3, SWAN and W2C have been shown to be inaccurate in their estimation of extreme wave conditions, and to have a number of commonly occurring accuracy issues which affect their utility for conducting accurate metocean analysis (Mackay, Bahaj and Challenor, 2010a) (Mackay, Bahaj and Challenor, 2010b) (Ambühl, Kofoed and Sørensen, 2014).

This makes achieving the stringent requirements for validation accuracy of numerical modelling activities outlined by the IEC-TS difficult to attain; and the standards requirements were found not to mirror what is currently achievable by state of the art models (Section 5.3.3.3). The accuracy of the wave model produced in this work is in the region of 10 – 15% bias and 15 – 20% RMSE for H_s, and 10 – 26% bias and 13 – 56% RMSE for wave power, the primary accuracy requirements outlined by the IEC standards (Table 41). Despite displaying very encouraging statistical metrics and correlation with the buoy data at concurrent deployments, this falls outside the standards defined for even a Class 1 (Reconnaissance)—assessment. These standards, while presenting admirable targets, are particularly onerous, and are unlikely to be met by most existing models with the majority of available data sources. Only after calibration can results reach below a 10% bias or RMSE error. In

this case, the validity of MCP and calibration methods used become increasingly important, and these were found to be too lightly covered by the IEC-TS.

The input data used in this study was the best available model for the extraction locations which represented the boundary conditions of the Mike 21 SW model, yet the accuracy of the final model output was still found to be lacking, owing predominantly to inaccuracies in the input conditions used. With the modelling efforts in this study, a number of input boundary conditions were trialed, including the freely-available IOWAGA WW3 derived data, before determining the most accurate source, which was the MeteoGroup Metocean PRO model. The MIKE 21 model was found to be sensitive to this input wave data above all other factors. Having found that the model output is highly sensitive to the input wave data at the boundaries, the accuracy of this model data becomes paramount. However, a limited number of sources for this data exist, and fewer still which contain accurate hourly data for periods of 10 years or more.

Obtaining an accurate and well documented bathymetry study also proved problematic. No centralised repository exists to make this data easily obtainable in a convenient data format for wave modelling. Curiously, many of these studies also lack basic yet critical information such as the datum and projection used. This issue is likely to be particular to the accuracy of the available bathymetry information, and the degree to which an existing site has been characterized.

In terms of the numerical modelling, a thorough investigation of the inclusion and exclusion of a number of required parameters was made. A number of “Section A” omissions were required in the modelling process that greatly improved computation time and did not significantly impact the results produced. Most notably, utilizing a very fine mesh, with the 50m spatial resolution, specified in the IEC-TS for a Class 3 assessment, proved computationally costly to the extent that it was simply not feasible for the timeline involved in a commercial project. Investigating the ability to shorten the computation time, a model run which utilized a 315m mesh size revealed less than 1% difference in uncertainty at the locations studied. This relaxation in the mesh size additionally resulted in increased computation speed by a factor of ~36x. Thus, the refined mesh has the drawback of significantly increasing computational

time without appreciably improving accuracy. Memory limitations on the workstation prevented the running of a fully spectral formulation, despite a drastically reduced spatial domain to accommodate the increased complexity.

5.6.2 Suggestions for alterations to IEC-TS

While it is important to remember that an accurate wave modelling and analysis routine will shape the design decisions and commercial outcomes of MRE projects, it cannot be avoided that the IEC-TS imposed for validation of wave models are excessively stringent, given the current state of the art modelling techniques. These standards should be reformed so that they are both reflective of realistic expectations that can be placed on such modelling exercises, and better outline the procedures which will give accurate and dependable results.

The requirements of the IEC-TS were found to be inconsistent in a number of areas. The requirement for measurement instrument bias in determining H_{m0}, for example, was required to be less than 0.3m; yet the bias requirement for validating the model is typically lower than this except for extremely energetic seas. It is unclear how the stringent standards for model calibration are to be achieved if the same rigor is not present in the input wave data. Acquisition of all the required data from disparate sources, ensuring its integrity, and integrating it within a consistent project proved an onerous task.

IEC-TS provides a rather exhaustive list of analyses to be performed without a clear and concise methodology for achieving the output. Additionally, Weather windows, which are a useful and commonplace tool for informing deployment schedules and Operations & Maintenance actions, are a surprising omission from the IEC-TS. Treatment of extreme wave estimation is almost entirely absent in the IEC-TS. Given that this is one of the areas most susceptible to error in analysis and that the impact on the survival of wave energy devices is potentially a crucial issue, this is something that should be addressed in further detail in future iterations of the standards. Ultimately it is up to each project developer to define their acceptable level of risk, but a standardized methodology for doing so would be extremely beneficial for the industry as a whole.

There lies an opportunity to reform the IEC standards in line with the findings of this and other case studies. The standards should include a worked case study using the principles outlined, with specific instruction for each step, and highlight how best to obtain the specific accuracy requirements outlined. To extend the benefit of the standards, a concise approach to detailing estimation of energy production using device power matrix data could be added, further enhancing their real-world applicability.

In section 6.5, a methodology for addressing spectral shape deviation is outlined, and this process would greatly benefit the IEC-TS by its inclusion, given the level of impact that spectral shape deviation can have on power production as well as a multitude of other factors.

Accompanying these standards with an open source wave data analysis tool would be an ideal step in promoting the application of these standards, and in vastly improving the state of ocean wave data analysis for MRE projects.

It would behoove all in the industry to ensure that rigorous standards which result in real and tangible improvements to project outcomes are developed and maintained to ensure the healthy and sustainable growth of this industry. Performing a study to IEC-TS standards for a Class 1 assessment has been useful in highlighting information gaps which will be necessary to conduct further site analysis.

5.7 Conclusions

A first-of-kind numerical modelling and wave resource characterization study has been performed according to the IEC 62600-101 standards for Wave Energy Resource Assessment and Characterization, using Ireland's first commercial wave energy farm project as a test case for exploring the validity, cost and the practicality of implementing the IEC-TS. This work represents an important development for the future of Marine Resource assessment, and will serve to inform future use of, and improvements to, the IEC-TS.

This Chapter implemented novel methods and improved tools for resource characterisation, developed in Chapters 3 and 4, with a focus on improving energy production prediction via improved Wave Period Parameter estimations. This was achieved through the development of both a Machine Learning based methodology which improved the accuracy of T_e energy period prediction, and a characterization of the WPR through binning of values of these ratios across the most commonly occurring conditions at the site. The Extreme Wave determination methodology developed in Chapter 4 was used to obtain estimates of Extreme Wave conditions for wave height and period parameters at the Killard Point site, and to validate the utility of this approach in providing estimates which give increased information for the development of Marine Renewable Energy Projects.

These new methods have enabled an accurate characterization of the Killard Point site, generating a 24 year hindcast, numerical wave dataset; and demonstrable improvements to energy production estimates. The work in Section 5.3.3.2 has shown how the model output has been validated against in-situ buoy measurements at three separate locations for a total duration of approximately one year, and the accuracy of the results compare favorably to state of the art nearshore hindcast models for Ireland.

A methodology has been developed for assessing numerical model forecast performance for Irish Wave Energy sites. Section 5.4.7 analyses Marine Institute Forecast model data, identifying trends in model behaviour and performance. The impact of forecast model performance on power production accuracy has been analysed and quantified. This result indicates that the Marine Institute Forecast could

prove valuable in informing future design decisions for MRE projects, informing them of both the magnitude and expected variability of the resource.

Finally, a detailed characterisation of the test site, with a view toward Marine Renewable Energy project development; and potential opportunities for further work to improve upon best practice in terms of validity, cost and the practicality of implementing the IEC-TS have been discussed in Section 5.5 and 5.6. These improvements and novel applications are an instrumental development for the future of Marine Resource assessment.

6 Impact of Spectral Shape on Device Energy Production

6.1 Introduction

Following the work done in Chapter 5, the need for analysis of the impact of spectral shape is apparent. Section 5.4.2.1 - 5.4.2.3 utilised improved methods of determining the Wave Energy Period, T_e, to generate better estimates of wave power, and of WEC power production, and implementation of these methods showed that there is a significant benefit to be had in terms of the accuracy of energy prediction. The analysis of Spectral Shape at the test site, in Section 5.4.4, displayed the variation that can occur in the spectral shape across different sea-state conditions, while Section 5.4.5 examined WPRs at the site using measured and computed spectral wave data to determine if significant variance in WPR existed across sea-states. Given the impact that WPRs and Wave Period Parameters have on energy production, this Chapter will:

- Examine the impact of Spectral Shape on WEC power production:
    - Showing that the distribution of energy across the frequency domain can vary significantly from the standard theoretical assumptions.
    - Demonstrate how this can adversely impact energy production estimates.
    - Select the sea-states that are most commonly occurring and contribute most to energy production at the test site (Killard Point) and perform a theoretical assessment of the impact on energy production estimation of using the Bretschneider Spectrum in place of the actual spectrum via a Numerical model.
- Test the impact of this variation in a real-world environment, using custom designed prototype-scale WECs in a fully equipped testing facility.
- Develop and investigate a methodology for estimating optimal energy production for both testing and deployment.
    - Examining the variation in wave parameters and, specifically, the WPRs that occur across a range of conditions at the Killard Point test site, and how these may differ from the standard assumptions which are widely used.

The binning of WPRs performed in Chapter 5 is a valuable approach that can show us the variation of the WPR across sea-states, but we now seek to determine how we can best analyse the impact of this variation on the power produced by real WECs in a tank testing environment.

The work that follows will explain and quantify the impact the spectral shape can have on energy production versus the use of a theoretical spectrum, first in a theoretical approach, then by empirical testing of Oscillating Water Column (OWC) devices using real time-series conditions from the Killard Point site, and comparing these to Bretschneider estimates with equivalent summary statistics.

Looking towards the commercial application of Marine Renewable Energy devices, this work will provide an illustrative example of how the characteristics of sites on the West Coast of Ireland can vary from theoretical assumptions. It will demonstrate the value of improved spectral fitting, novel methods of resource binning and characterisation, and display a testing framework that should be used for future device testing to greatly enhance the accuracy of the energy estimates being produced.

6.2 Background

For many years it has been considered the standard of the Marine Renewable Energy industry to characterise sea states using a few synthetic parameters such as Significant Wave Height (H_s) and Mean Up-crossing Period (T_z), Mean Energy Period (T_e) or Peak Wave Period (T_p); with histograms and scatter tables of H_s and T_e to represent the distribution of sea-states at a site.

Many authors have suggested that H_s and T_e, used in both occurrence matrices and power matrices for devices, are insufficient to fully predict device output (Kerbiriou *et al.*, 2007; Robertson *et al.*, 2016). It has been proposed that other parameters, such as spectral bandwidth, mean direction coincident with peak frequency and direction should also be included alongside the power matrix. (Kerbiriou *et al.*, 2007) examined utilizing a 2D spectral representation of the sea-state against the standard 5-parameter assumptions that do not separate wind-seas and swell-seas, finding that the description of sea-states with a single set of parameters can lead to very large errors in the computation of available power. (Saulnier *et al.*, 2011) found, using

linear and non-linear systems to simulate the response of converters with realistic power take-off devices, that converters are not overly sensitive to wave directionality; but the addition of the bandwidth characteristic is an appropriate compliment to the set of overall parameters describing the sea-state for the purpose of estimating wave energy production. (Robertson *et al.*, 2016) found that using a partitioned spectral method to characterise the wave climate provided a higher fidelity and more accurate assessment of Wave Energy Converter (WEC) power production. This gives rise to the need to conduct a full spectral analysis of conditions at the site to ensure that the estimate of power production from H_s and T_e is reliable.

6.2.1 Current Methods

To date, by far the most common method for determining the energy production of a device in a given sea-state is the use of an occurrence matrix which defines the occurrence of conditions in "bins" of H_s and T_e, paired with a device power matrix, similarly defined by H_s and T_e. To then generate representative sea-states for numerical and physical testing of wave energy devices, random waves would be simulated based on a phase estimating/resolving model. These generate random waves based on some standard spectral density formula such as the Pierson Moskowitz or JONSWAP spectrum (for fully-developed and growing wind-seas respectively). The waves are generated in the time domain and run in numerical models or wave tanks for the purposes of model testing. The power value obtained at the scaled-size, from a test of 1 to 3 hours of stationary wave conditions, is then used to build a device power matrix, characterised by H_s and T_e.

It is easy to see why this method has been chosen; It provides an easy way to describe and characterise a device's energy production in the conditions it will be operating in. Unfortunately, such approaches neglect the fact that WECs are heavily sensitive to the overall distribution of energy in the entire sea-state. Given that these device power matrices are often produced with the assumption of a standard theoretical energy spectrum, such as the Bretschneider Spectrum, any deviation from this assumed spectrum can and does result in large shifts in the power produced.

Due to the widespread adoption of this approach, current methods of predicting device energy production can be highly inaccurate, and there can be significant variations in the energy production for a given H_s and T_e. This leads to two primary issues in the practical application of wave energy, the first of which is that the results achieved during tank testing and during small-scale testing are providing inaccurate results. This tends to become particularly apparent as projects move from tightly controlled environments, where the assumption of a theoretical energy distribution may seem valid and present a beneficial simplification, to larger scale, open-water test sites, where the simplification is not applicable, and results are often not replicable. The second issue caused by the adoption of this empirical spectra approach follows from the first; device developers and financial backers do not have the required level of detail to put faith in the testing procedures and thus have confidence in the ultimate project outcomes. This causes significant uncertainty surrounding project viability, which inevitably results in slow development of the technology through the TRLs, which is an unfortunate issue for both developers and financers.

While the recent IEC-TS standards exist for outlining best policy in the characterisation of wave energy resource, the focus on testing and estimating energy production has thus far seen insufficient guidance and input. One of the most glaring omissions is the lack of consideration given to the variation in energy distribution across sea-states that carry similar summary parameters. Neither has the industry pushed for enhanced understanding of the true energy content of a sea-state. Section 6.5 will discuss how the reservations in doing so need not persist, and will suggest intermediary solutions to allow the spectral shape distribution to be considered without being improbably restrictive or requiring exhaustive testing.

6.3 Theoretical Examination

6.3.1 Assessing Variation in Spectral Energy

As discussed in the previous section, variation in spectral shape can have significant ramifications for the characterisation, planning and design of wave energy developments. In this section, the variation in spectral energy that can occur for sea-states with outwardly similar summary parameters will be demonstrated, and the impact this can have on energy production characterised. This work will highlight the

need for a deeper examination of the entire energy profile of a sea, and support a move towards reduced reliance on the empirical spectra which are commonplace in the industry.

To illustrate the variation in spectral shape that occurs in real-world conditions, an analysis of the spectral shapes present in the recordings at the Killard Point site in Co. Clare has been performed. This forms a theoretical study that demonstrates the energy production impact of using an empirical spectrum. It will also serve to establish the motivation behind the real-world tank testing trials which are performed in Section 6.4.

6.3.2 Processing Data Records for Spectral Analysis

As part of the broader metocean analysis of the site undertaken in Chapter 5, spectral analysis was undertaken on the RAW data from the Killard Point buoy deployments. This was done to validate the output of spectral history parameters, to validate the selection of the Bretschneider Spectrum to represent the conditions at the site and, failing this, to determine a suitable open-ocean spectrum to represent the conditions at the site. Finally, in conjunction with the work undertaken in Chapter 3, it was necessary to determine and assess a methodology for accurate estimation and conversion of Wave Parameters crucial to further analysis of site characteristics.

In this process, the time-series data was analysed for each individual time-series record to produce a full spectral record. These time-series records were produced every 30 minutes by the Waverider Buoys at the Killard Point site (as described in Section 2.1.1.1.3). The spectral moments and wave parameters were generated using the RAW data of these time-series records, with H_{m0}, T_{01}, T_{02}, T_{p0}, T_e, Energy and Frequency output for each record. To provide meaningful information on the influence of the sea-state and prevailing weather conditions on the spectral shape, the H_{m0} and T_{02} (as well as T_{01}, T_e, T_p) records are then used to bin these spectra in 0.5m wave height and 1 second period increments. Figure 153 below examines the process of converting the time-series data to a spectra and generating an equivalent Bretschneider Spectrum for comparison.

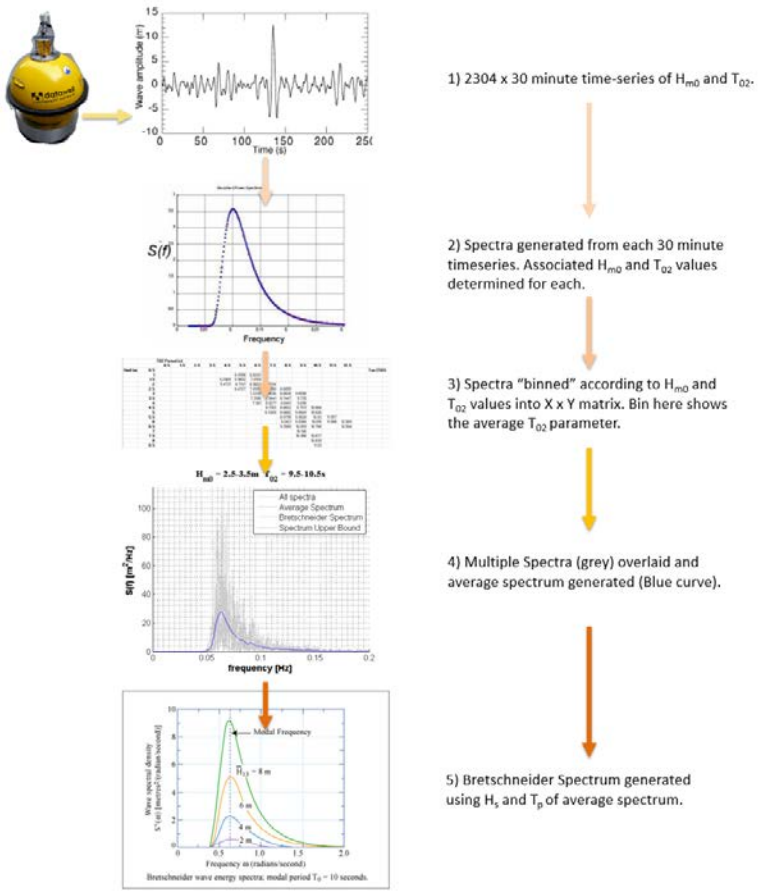


FIGURE 153: METHOD FOR PROCESSING TIMESERIES FILES TO SPECTRA, BINNING, AND GENERATING EQUIVALENT BRETSCHNEIDER FOR COMPARISON

This approach allows for an examination of the individual variation and the average trends within each sea-state, and presents the chance to retain superior detail than an approach where sea-states are simply characterised by a number of summary parameters.

The resulting spectral records in each bin are plotted, with the average spectral shape for that bin overlaid. The Savitzky-Golay filter (Savitzky and Golay, 1964), commonly used in the field of Digital Signal Processing (Schafer, 2011) was applied to the result of the average spectrum. This is a type of filter designed for performing noise

reduction on signal with a large frequency span; filters such as these perform better than standard averaging Finite Impulse Response (FIR) filters, which tend to remove a significant portion of the signal's high frequency content along with the noise. Savitzky-Golay filters are preferential, since they minimise the least-squares error in fitting a polynomial to frames of noisy data. With a comparatively low number of spectral records, this helps in determining what the average spectral shape will look like over a longer duration, with less influence from individual outliers.

The summary parameters are also averaged to give a characteristic average summary parameter for each bin. Using this characteristic average summary parameter, a Bretschneider Spectrum is generated. The correlation between the average wave spectrum for each bin and the Bretschneider Spectrum is determined. This allows the theoretical spectrum to be assessed for its suitability to represent the real conditions at the site.

The correlation between the Bretschneider Spectrum and recorded spectra was compared for each bin in which there was sufficient data. Given the data capture constraints and the limited number of data points captured overall, this was deemed to be three or more spectral records. Figure 154 shows an example of this spectral plot for an H_{m0} between 2.5 and 3m and a T_{02} between 7.5 and 8.5s. The average H_{m0} in this bin is 2.787m and the average T_{02} is 7.877s. These values were used to generate the idealised Bretschneider Spectrum, and this spectrum was compared to the values of the averaged spectra to validate the assumption that this spectrum accurately represents conditions for that sea-state.

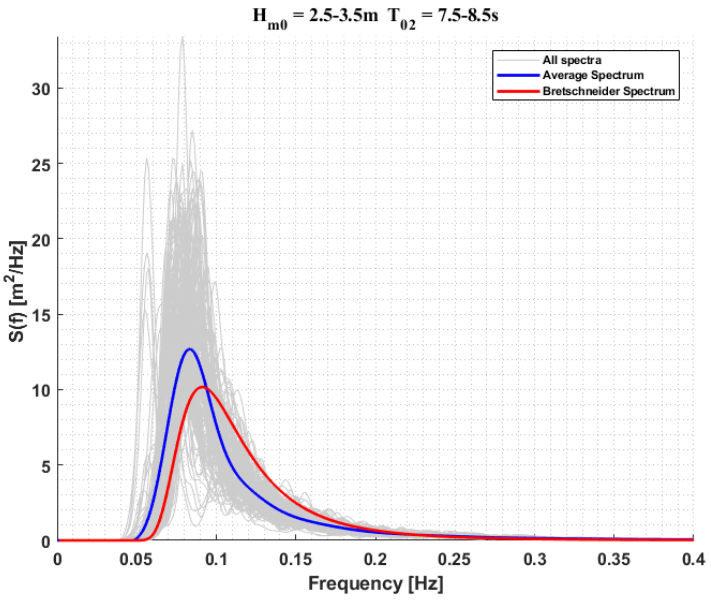


FIGURE 154: AVERAGE SPECTRA FROM TIME-SERIES RECORDS (BLUE) WITH BRETSCHNEIDER (RED) SPECTRA GENERATED FROM AVERAGE H_{MO} AND PERIOD RECORDS OVERLAID. ALL SPECTRAL RECORDS FOR EACH TIME-SERIES FILE ARE DEPICTED IN GREY.

Figure 154 shows each of the spectra for the timeseries record corresponding to the bin which encompasses sea-states with summary parameters in the range 2.5 - 3m H_{m0} and 7.5 - 8.5s T_{02}. The deviation in spectral shape shown in the individual spectral records (grey) for these short duration recordings is immediately apparent, with a large variety in shape, peaked-ness, maximum amplitude of spectral energy, and the presence of several multi-modal spectra which contain multiple, distinct, energy peaks. Looking at the average spectral shape (blue - Recorded data, red – Bretschneider Spectrum), there is a difference in peaked-ness, with the recorded data having a higher spectral amplitude at its peak frequency, while the Bretschneider Spectrum carries more energy in the higher frequency tail of the spectrum, between 0.10 and 0.15Hz. Clearly, then, it is not always the case that the Bretschneider Spectrum will provide an appropriate match for the prevailing conditions at a site on the West Coast of Ireland, and there is the potential for significant variation in the energy production estimated from both spectra. This will be outlined in a theoretical approach in the following Section 6.3, followed by an

examination of this variation in practice in small scale tank testing in Section 6.4 onwards.

6.3.3 Selection of Sea-States for Assessment

The process for the selection and testing of sea-states is an important component of determining the impact of spectral shape variation. These sea-state records were retrieved from the recorded data at the Killard Point site, and were selected based on the relative occurrence of these conditions, such that the analysis is truly reflective of the most commonly occurring conditions. These were additionally weighted to reflect the contribution to energy production at the site.

Occurrence and Power Production scatter diagrams were generated based on the buoy data records available at Killard Point, which provided approximately 75% coverage of annual conditions.

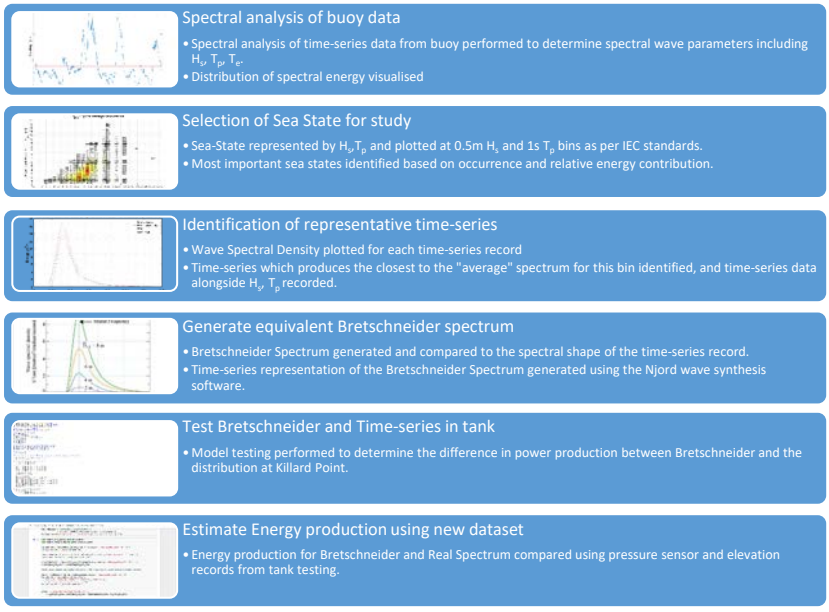


FIGURE 155: COMPARISON PROCESS FOR RECORDED VS THEORETICAL SPECTRAL SHAPE DATA

The hierarchy of testing is structured around the comparison of time-series wave recordings with the equivalent (H_s/T_p) Bretschneider wave conditions.

- The time-series values are obtained from buoy data records at Killard Point.

- Spectral analysis is then performed, and the resultant H_s and T_p are then used to separate the records according to pre-determined bin sizes of 0.5m H_s and 1s T_p – following IEC standards for the production of occurrence matrices.
- The spectral records are then averaged to achieve a representative spectral shape for each bin.
- The Bretschneider Spectrum corresponding to the time-series is then produced according to the form of the equations (**6.24**) - (**6.27**) with H_{m0} and T_{02} according to the equivalent summary parameters produced by the spectral analysis run on the time-series. The Bretschneider Spectrum and real spectrum are then overlaid to visually examine the difference in spectral energy distribution.

A visual for this process is displayed in Figure 153, which highlights the data flow from buoy, to spectral analysis, to the creation of the equivalent Bretschneider Spectrum.

An example of the conditions at Deployment Location 1 at the Killard Point can be seen in Figure 198

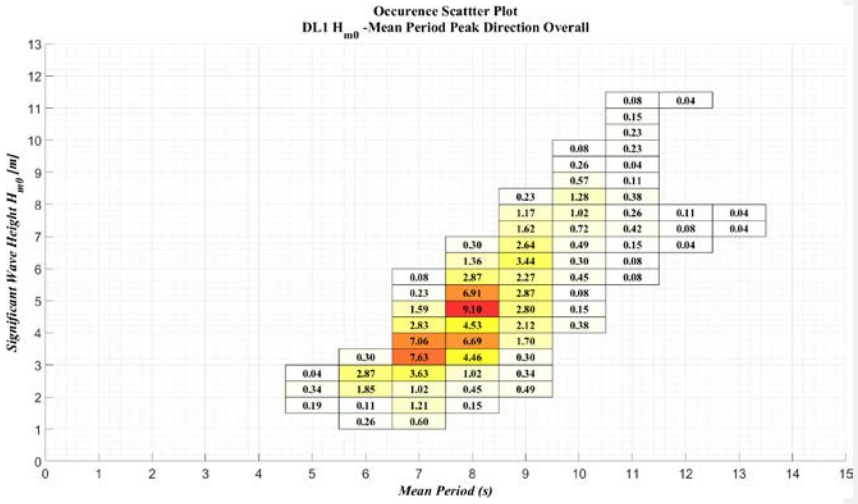


FIGURE 156: PERCENTAGE OCCURRENCE SCATTER PLOT FOR H_{M0} / T_{02} AT KILLARD POINT DL1

The prevailing climate during Deployment 1, which covered the period 19/11/2011 – 13/01/2012 with 2647 records, is shown in Figure 156. Metocean conditions during this period are visibly energetic, as heavy storms were experienced during this

period. A number a sea-states with an H_{m0} greater than 6m are encountered and typically have an accompanying period in the range 8-11s; while a number of outlier storm events are evident in the upper right quadrant of Figure 158. The most commonly occurring sea-state, with an occurrence percentage of 9.1%, is a significant wave height between 4.5 and 5.0m and a Wave Period between 7.5 and 8.0s.

The distribution of H_{m0} is shown for Deployment Location 1. The energetic conditions are evident, given that the most commonly occurring H_{m0} is 4m.

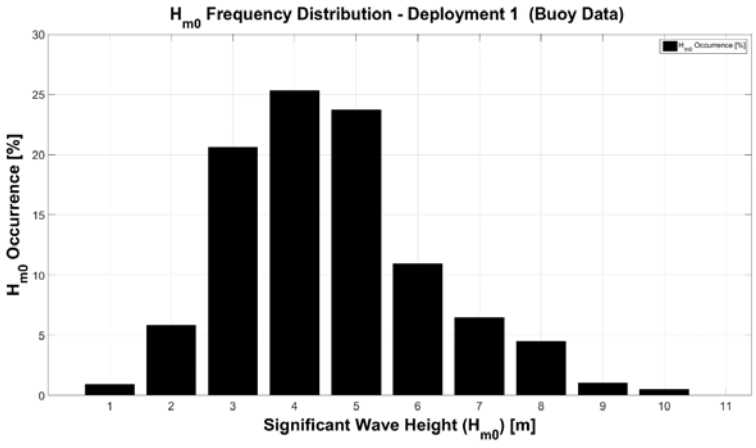


FIGURE 157: HISTOGRAM OF H_{M0} DISTRIBUTION FOR BUOY DATA AT DEPLOYMENT LOCATION 1.

Figure 157 displays the most commonly occurring wave condition at the site. A testing envelope was then established which bounded the most commonly occurring sea-states. A combined dataset encompassing the recordings from Deployment Locations 1 - 3 was used to identify the most commonly occurring sea-states, and those which contributed the most wave energy.

Conditions at the Killard point site were examined using both an occurrence matrix and a power contribution matrix, and the test sea-states were determined by selecting 16 bins, containing defined sea-states, which represented coverage of 90% of the events, as well as the most commonly occurring/most energy contributing conditions.

Bins were chosen based on:

- Covering a realistic operating area for WEC device.
- Giving a representative envelope of conditions occurring at the site.
- Power/Energy contribution of the bin. I.E. States which carried more energy were given preference.

To select the bins, H_s – T_e & H_s – T_p occurrence matrices were produced. Energy contribution matrices were also produced based on these occurrence values and using the formulas:

$$Power = 0.49\ {H_{m0}}^2\ T_e \tag{6.1}$$

$$Power = 0.42\ {H_{m0}}^2\ T_p \tag{6.2}$$

With the central value of H_s and T_e/T_p for each bin multiplied by the number of hours of occurrence:

$$P_{Contribution}(j,i) = 0.49\ {H_{avg}}^2 T_{avg} OccurrenceHours(j,i) \tag{6.3}$$

This served as a rough estimate for the power contribution of the sea-states.

NB: Three separate buoy deployments were used to obtain the occurrence data for the site. No coverage was available from April to August and thus there is a predominance of winter conditions. This is weighed out by the fact that the power contribution of larger sea states is much greater, and thus the impact of the absence of benign conditions is naturally diminished to an extent, given that we are primarily interested in conditions with a large energy contribution.

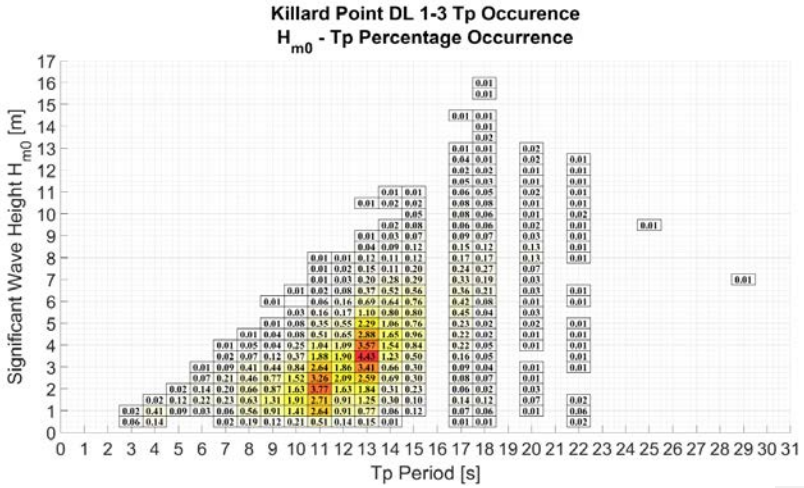


FIGURE 158: H_S-T_P OCCURRENCE MATRIX AT KILLARD POINT DEPLOYMENT LOCATION 1-3 (COMBINED)

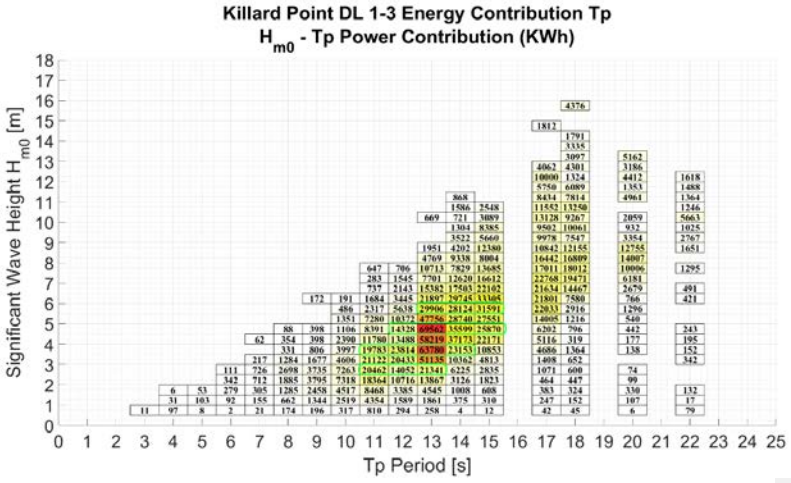


FIGURE 159: H_S-T_P POWER CONTRIBUTION MATRIX AT KILLARD POINT DEPLOYMENT LOCATION 1-3 (COMBINED)

These conditions were scaled to 1:50 scale based on the response of the device to initial testing. Additionally, a key characteristic of the Killard Point site was the existence of bi-modal sea-states, containing separate and distinct peaks in wave spectral density across the frequency range. It was important to identify the frequency of occurrence and impact of these sea-states to determine the impact on

the energy production of devices that these conditions are likely to have for sites on the West Coast of Ireland.

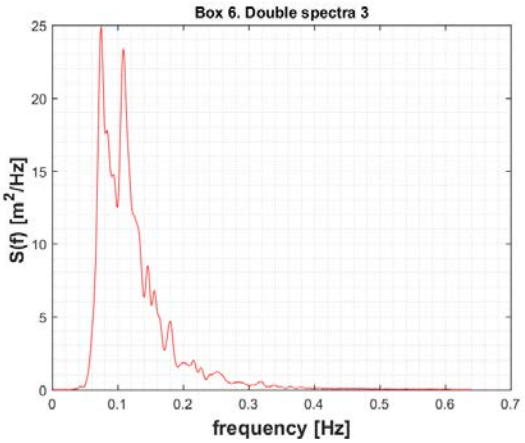


FIGURE 160: EXAMPLE OF DOUBLE PEAKED SPECTRA AT KILLARD POINT

Identification of bi-modal sea-states took place alongside the binning of sea-states into defined H_s and T_p bins. The criteria for determining double-peaked spectra have been outlined by a number of authors, notably (Guedes Soares, 1984). A methodology has been developed by (Barrett, Holmes and Lewis, 2007) which provides a simple and robust procedure, and has previously been used in the analysis of waves from Galway Bay. Following this methodology, a spectral ordinate can be considered to be a valid secondary peak if:

- The peak is a local maximum.
- It has a magnitude of at least 15% of S (f_{peak}).
- It is separated from the primary peak by a period of at least 2 seconds.

Similar to the work of (Cahill and Lewis, 2013), the methodology has been adapted to study different degrees of "multi-peakedness". That is; the degree of separation and magnitude of the secondary (or subsequent) peaks in relation to the primary peak. These adaptations to the methodology included the criteria that the magnitude of the secondary peak should be a defined percentage (e.g. 115%) greater than the lowest spectral ordinate separating it from the primary peak. Additionally, the

separation distance required to classify a sea-state as bi-modal was varied between 1 to 5 seconds.

Using a separation distance of 2 seconds, the following multi-modal sea-states were identified from the sea-states selected at Killard Point.

The occurrence of multi-modal sea-states was found to be only approximately 1.58% - likely due to the selection of sea-states with a minimum H_s of 2.8m – with multi-modal seas far more likely to occur below these conditions.

TABLE 72: IDENTIFICATION OF SEA-STATE OCCURRENCE AND QUANTIFICATION OF THE DISTRIBUTION OF BI-MODAL SEA STATES

H_s (m)	T_p (s)	Occurrence (Number of time-series records)	Number of Multi-Modal Sea-States
3-3.5	11.5-12.5	113	1
3-3.5	12.5-13.5	84	0
3.5-4	12.5-13.5	120	7
4-4.5	12.5-13.5	81	2
4.5-5	12.5-13.5	155	2
5-5.5	12.5-13.5	117	3
5.5-6	12.5-13.5	39	0
4-4.5	13.5-14.5	51	1
4.5-5	13.5-14.5	79	0
5-5.5	13.5-14.5	55	0
5.5-6	13.5-14.5	34	0
6-6.5	13.5-14.5	40	0
4.5-5	14.5-15.5	20	0
5-5.5	14.5-15.5	19	0
5.5-6	14.5-15.5	28	1
6-6.5	14.5-15.5	37	0

The bi-modal conditions are predominantly present between 3.0 - 4.5m H_s. The individual spectral records are selected as representatives of each of the 16 selected sea-states. There is large variation in the shape of spectra within each occurrence bin. Thus it is necessary to apply some element of control to ensure consistency between bins – allowing for some level of inter-comparability. The spectrum which most closely matches the “average” spectrum produced by all the time-series records within a given bin is chosen. This method is chosen over a re-constructed time-series based on the actual average spectrum for two main reasons.. Utilising a real time-

series and Froude-Scaling removed the need to generate a time-series by means of Inverse Fast Fourier Transform which utilises random phase information. This leads to the second advantage of using a spectrum matching the average spectral energy distribution. It is a real sea-state condition and the wave amplitudes and periods mirror those that would be seen in a real sea, thus giving a result that will be more in line with the real energy production of a device in such a sea-state.

This resulted in the selection of 16 individual time-series records by comparison of the spectral energy distribution to the average spectral energy distribution within the bin – which can be seen in Figure 161.

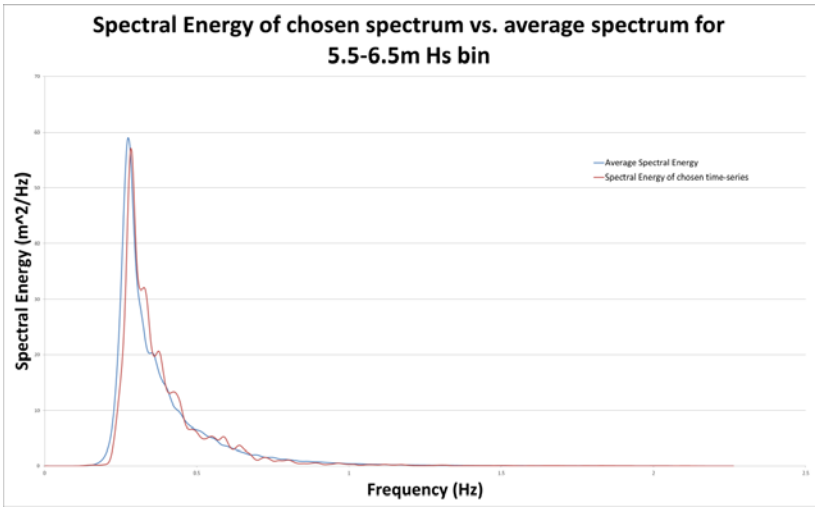


FIGURE 161: SELECTION OF TIME-SERIES RECORD MATCHING AVERAGE SPECTRAL ENERGY DISTRIBUTION IN CHOSEN BIN

While the average spectral energy provides the most useful information for estimating the relationship of the device energy production between the real sea-state and the theoretical spectral representation, it's also important to look at the maximum variation from the theoretical result that can happen. For this, a number of bi-modal/multi-modal spectra with two distinct peaks in spectral energy are selected. Additionally, an "outlier" spectrum is chosen for each bin studied, representing the time-series which showed the greatest deviation from the

theoretically suggested distribution of spectral energy. This was theorised to provide the largest change in device energy production over the theoretical assumption.

The data was segregated based on the peak period, T_p, and while the peak period for these sea-states fell within a defined 1 second range, there is significant variation in T_e energy period brought about by the change in distribution of energy. Given that T_e is a key element affecting the energy production for a device with given response and characteristics, this variation is likely to be noteworthy in that sea-states with corresponding energy period may not necessarily be located in the same sea-state bin.

6.3.4 Theoretical Device Power Study

The following comparison which outlines the practical difference that is made by the assumption of a Bretschneider (or other theoretical) Spectrum in place of using the real recorded spectrum. It will be demonstrated that the specific characteristics of devices can also have a large impact on the variation caused by this assumption. Given that devices often have defined resonant peak frequencies at which power production is optimised, any variation in the spectral shape profile can dramatically shift the resultant energy production estimated for a device.

To determine a useful power production estimate for each spectral shape, it was elected to utilise a simple theoretical model that is representative of a basic Oscillating Water Column WEC shape. A generic cylinder of radius 0.75m and submerged depth 5.0m was modelled in WAMIT (Wamit, 2012), a Boundary Element Method (BEM) solver using linear wave theory, to determine its response characteristics. Of primary interest was the device's heave Response Amplitude Operator (RAO) – the primary determinant of extractable energy.

This was determined using the following formula:

$$RAO(iz) = \left(\frac{fe(iz)}{\sqrt{(k-\omega(iz+1))^2 \times \left(m+m\omega(iz+1)\right)^2 + \left((Rr(iz+1)+bext)\times\omega(iz+1)\right)^2}}\right) \quad (6.4)$$

Where:

iz iterates along the length of the frequency vector
fe is the excitation force – the Froude-Krylov forces of the incoming waves.
m is the mass, and $m\omega$ the added mass at rotational frequency iz
k is the hydrostatic stiffness
$bext$ is the external damping
Rr the restoring force component

This RAO was then used alongside the spectral shape to determine the energy production of the device in each scenario. The spectral energy profile was collected for recorded and Bretschneider Spectra. The power production RAO of the device was developed using the output of the WAMIT model characteristics, and the heave power determined by multiplying the Spectral Amplitude by the calculated RAO as follows:

$$Power(iz) = SJ(iz + 1) \times RAO_{calc}(iz)^2 \tag{6.5}$$

This resulted in a power figure which allowed for a direct comparison between the estimated energy production for each spectrum.

In transitioning from the spectral density to the power spectral density, it was necessary to include the power per unit crest length developed by a sea-state, which is defined as:

$$P0_0 = \frac{\rho g^2}{4\pi} m - 1 \tag{6.6}$$

$$m - 1 = \int \frac{S_u(f)}{f} df \tag{6.7}$$

$$P0 = \sum_{i=1:n} P0_i \tag{6.8}$$

$$P0_i = \frac{\rho g^2}{4\pi} \int \frac{S_u(f)}{f} df \tag{6.9}$$

The power varies with the square of H_s, and with the inverse of the energy frequency. $f_e = \frac{m_0}{m_{-1}}$, The latter being affected by the bandwidth of the spectrum. For single systems, swells carry more power than wind-seas of the same H_s.

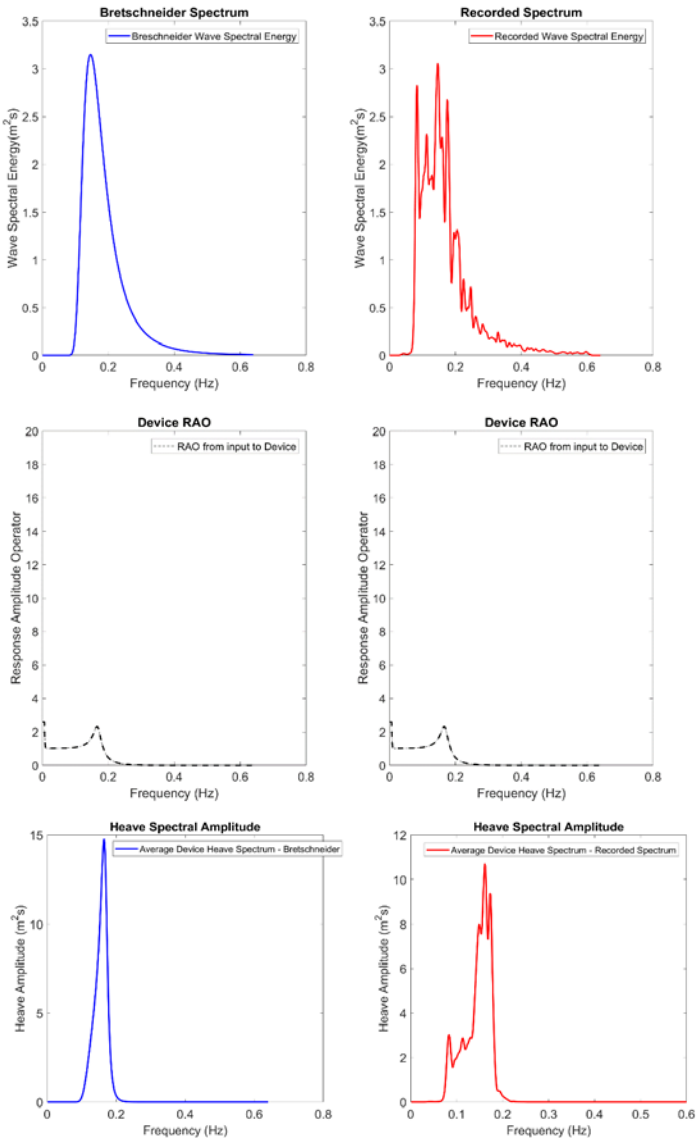


FIGURE 162: COMPARISON OF HEAVE SPECTRAL AMPLITUDE FOR RECORDED SPECTRUM VS. AN ASSUMED BRETSCHNEIDER SPECTRUM FOR A SEA-STATE WITH PARAMETERS: 2.268 M H_S AND 6.838 S T_P.

The impact of the assumed spectral shape is clearly visible in Figure 162. The Bretschneider estimate for the parameters of H_s and T_p has a single, defined, spectral energy peak. In the recorded data, the true spectral energy profile is more diffuse, of

lower maximum amplitude, and has multiple defined peaks within the energy profile. In this case, the (normalised) power produced for the Bretschneider Spectrum is $1.6799x10^2$ kw, while the power produced for the Recorded spectrum was $1.379x10^2$ kw – a 21.8% overestimation of the power production introduced by the use of the Bretschneider Spectrum.

The same comparison was next made for some of the most commonly occurring conditions (as selected in Section 6.3.3), and those which contributed most to energy production. This analysis is conducted by averaging all of the spectra in each sea-state, and producing an equivalent average Bretschneider based on the combination of all Bretschneider Spectra with the equivalent average summary spectral parameters.

The top panel of Figure 163 – Figure 167 displays all spectra within the bin, the resultant average spectrum, and the Bretschneider Spectrum. The middle panel shows the numerically derived RAO for the modelled cylinder. The bottom panel shows the resultant Heave Spectral Amplitude, while the annotation on the lower-right summarises the total power production and variance for both the actual and empirical spectra.

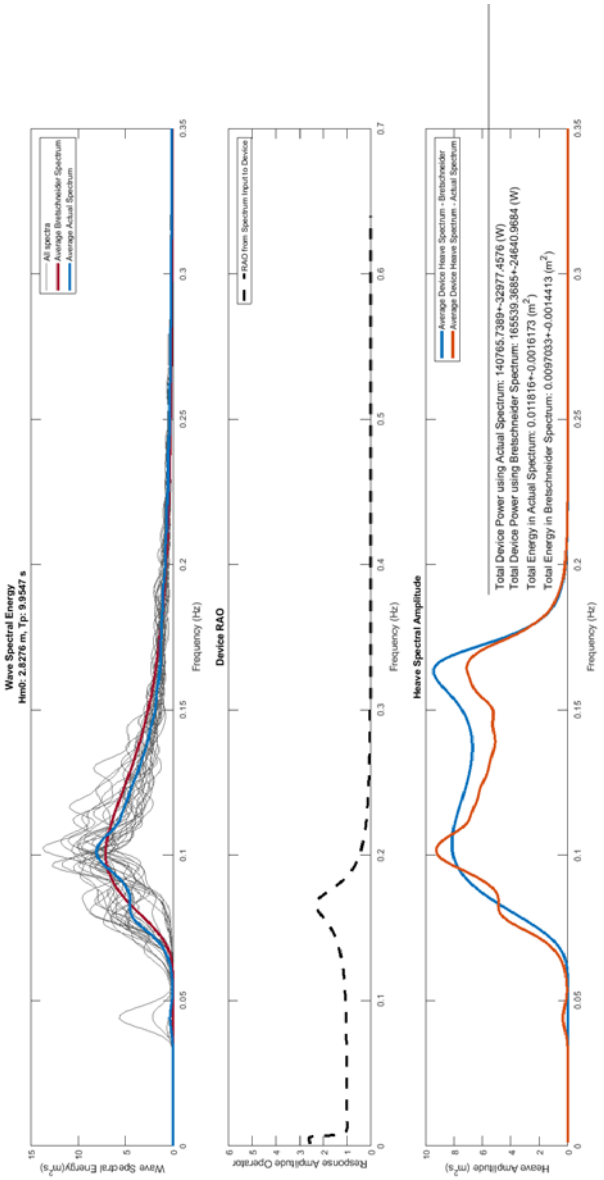


FIGURE 163: COMPARISON OF SPECTRAL SHAPE AND ENERGY PRODUCTION FOR SEA-STATES WITH H_S 2.5-3M AND T_P 9.5-10.5S

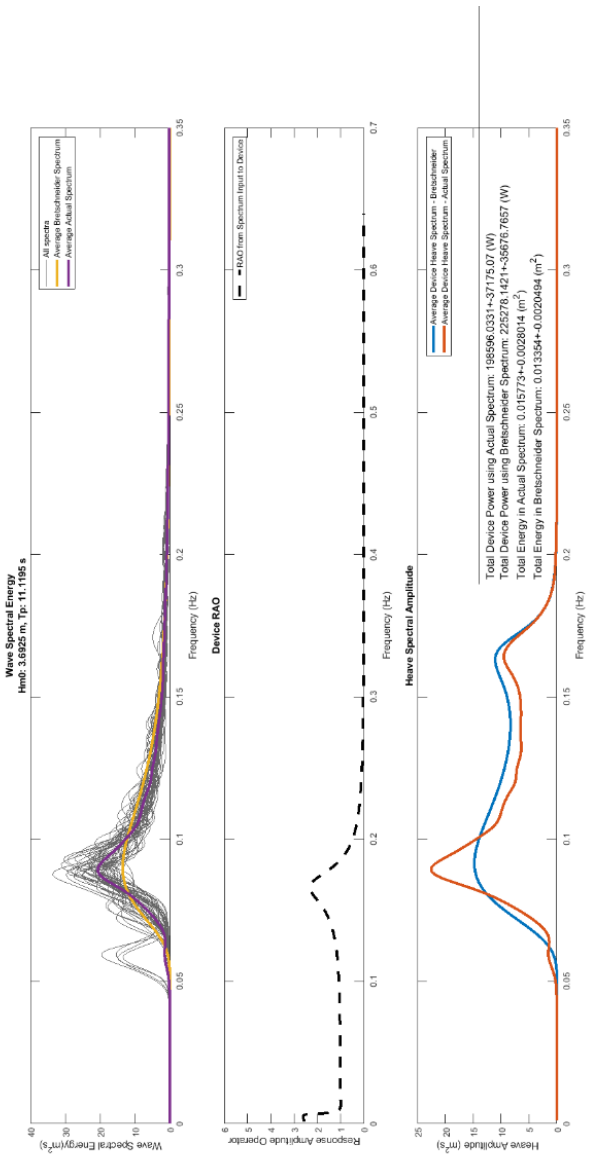


FIGURE 164: COMPARISON OF SPECTRAL SHAPE AND ENERGY PRODUCTION FOR SEA-STATES WITH H_S 3.5-4M AND T_P 10.5-11.5S

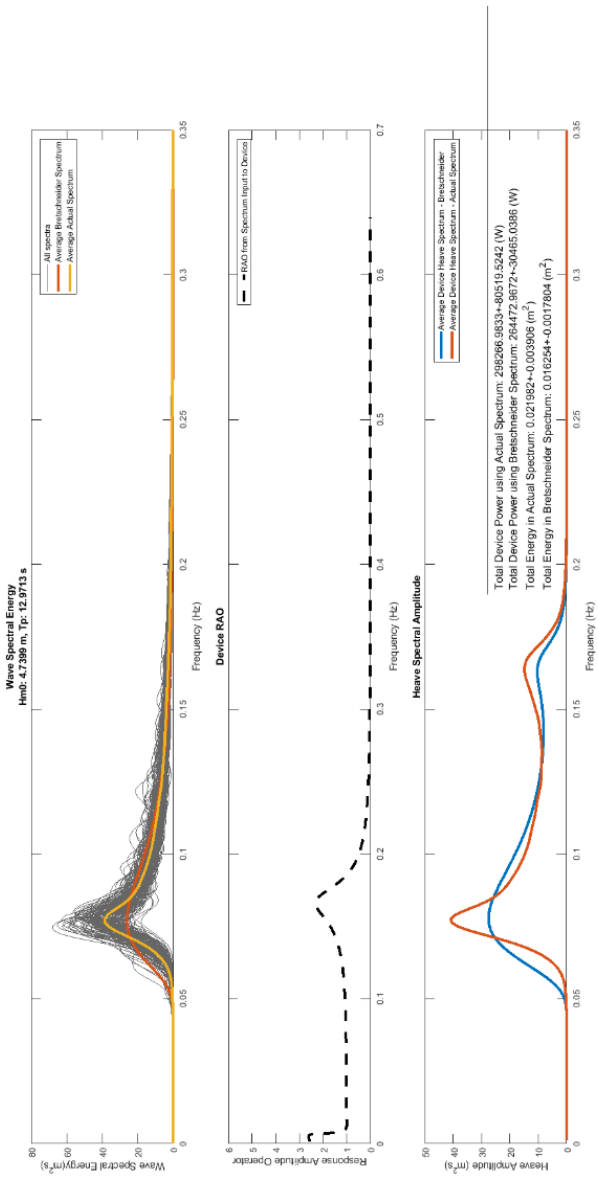


FIGURE 165: COMPARISON OF SPECTRAL SHAPE AND ENERGY PRODUCTION FOR SEA-STATES WITH H_S 4.5-5M AND T_P 12.5-13.5S

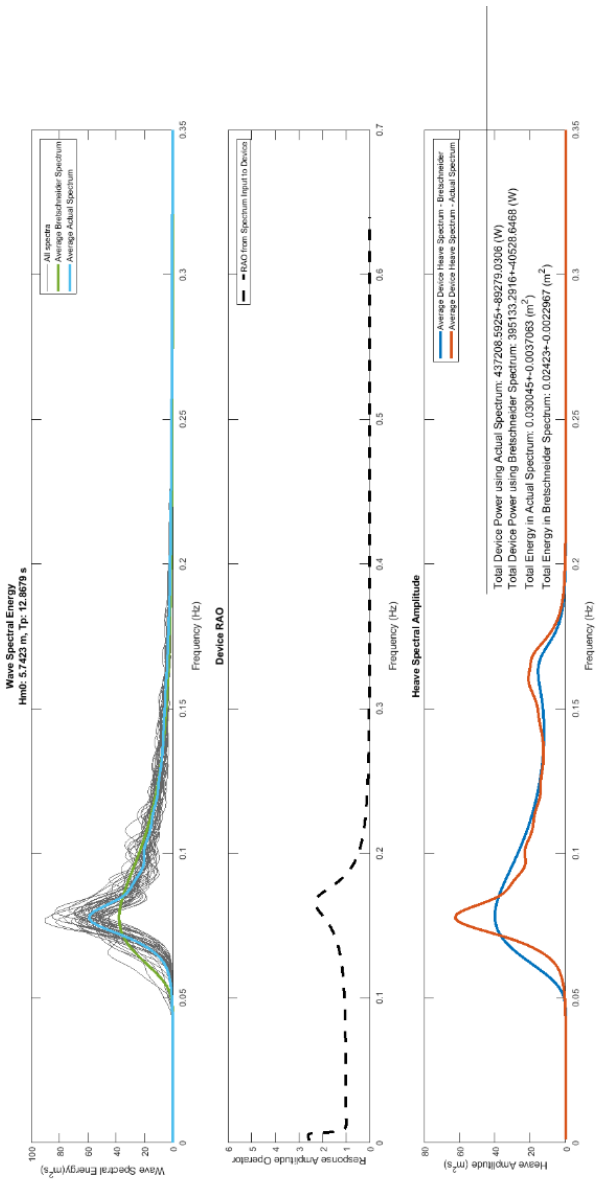


FIGURE 166:COMPARISON OF SPECTRAL SHAPE AND ENERGY PRODUCTION FOR SEA-STATES WITH HS 5.5-6M AND TP 12.5-13.5S

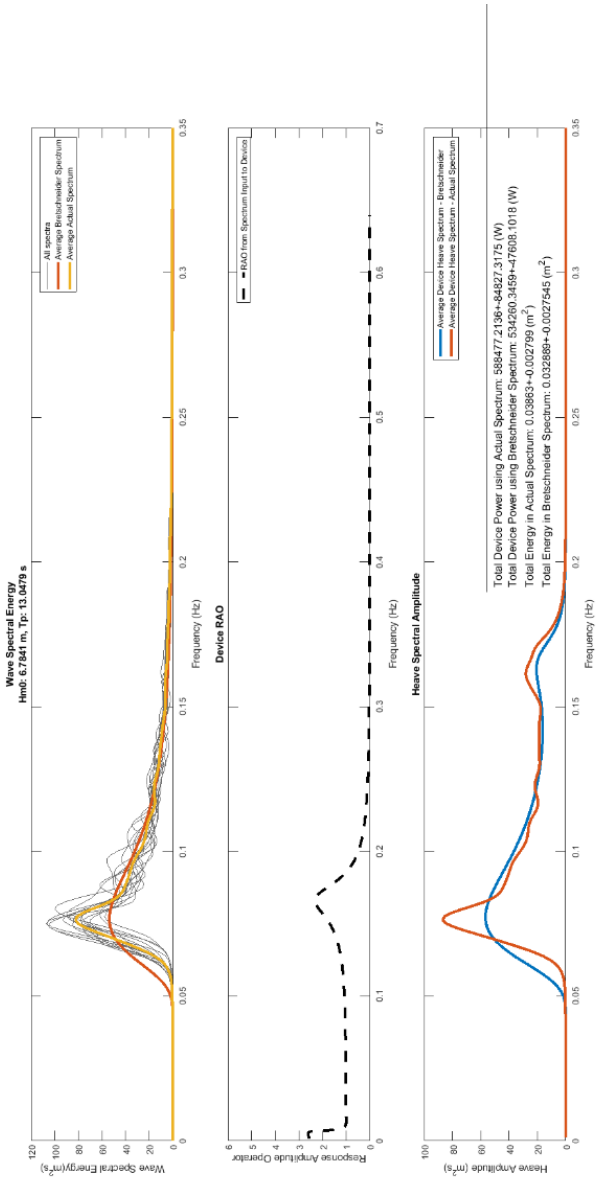


FIGURE 167: COMPARISON OF SPECTRAL SHAPE AND ENERGY PRODUCTION FOR SEA-STATES WITH HS 6.5-7M AND TP 12.5-13.5S

This analysis demonstrates the large impact that the change in spectral shape can have. The average spectrum at the Killard Point site is more peaked than the Bretschneider Spectrum, exhibiting a more concentrated energy distribution. As a result, there are significant Heave Spectral Amplitude differences between the two; with the estimate of total device power varying in excess of 10% for each of the Sea-States selected. For Sea-States with lower wave period, the Bretschneider Spectrum tended to estimate higher energy production, while larger wave periods in the 12.5s T_p range, which match well with the resonant period of the device, resulted in the real spectrum at the Killard Point test site producing a greater estimate for Heave Spectral Amplitude.

Given the frequency with which the Bretschneider Spectrum is used for such analyses, and the magnitude of the variation in power has been demonstrated to be possible, this is a potentially significant issue which must be addressed in the course of legitimising the development of wave energy. The variation in the energy estimates seen here is by no means the largest deviation seen in the testing data from Killard Point, furthermore multi-modal seas can introduce significantly higher deviations from the expected power production value. In Section 6.4.5.5, the difference in power production in a small-scale tank test environment is shown the same sea-states, furthering demonstrating the impact that spectral shape variation can have.

6.4 Small Scale Tank Testing of OWC Devices

6.4.1 Tank Testing Necessity & Requirements

The work done in both Chapter 3 and 5, as well as Section 6.3 has shown that the distribution of energy in the frequency domain for a given sea-state can vary significantly from the standard theoretical assumptions. It is proposed to test the impact of this variation in a real-world environment, using prototype scale wave energy device models in a fully equipped testing facility. The purpose of these tests is to verify the power production difference that exists between recorded time-series data and theoretical spectra.

Theoretical spectra, such as the Bretschneider Spectrum, are commonly used in all facets of the ORE industry - from device design and testing to energy production and

wave parameter relationship estimates. Looking towards the commercial application of Marine Renewable Energy devices, it is important to quantify the variation in energy production that can occur if these theoretical spectra are used.

Having demonstrated the potential impact of spectral shape variation, and the caveats to the use of standard empirical spectral, the logical progression is to examine the impact in a real-world environment which represents an immediately identifiable and applicable situation for wave energy developers and their associated contractors. Given the huge deviations in the expected device performance experienced by developers in moving from numerical modelling to even small-scale testing, a greater understanding of the method is required. The tank testing that takes place will detail the identification of sea-states for study, followed by the construction of multiple OWC devices to examine the variation between the idealised (Bretschneider) and real-world energy production of devices in small scale testing.

A primary aim will be to identify pitfalls and areas for improvement that exist with the current best practices, and work towards forming a cogent methodology for this stage of testing. This will pull together all of the current best practices and align them with the improvements possible by taking a more holistic approach of examining the entire spectrum of energy in a sea-state in a tailored, empirical fashion, hence building on the approach detailed in Section 6.5.2 to provide an enhanced methodology when greater accuracy is desired; rather than relying on theoretical methods which may not provide a useful fit for the conditions and device being tested. This testing should serve as a basis for how early prototype tank testing could be conducted in an optimal fashion; ensuring quick, concise and accurate testing that translates to real experience.

Tank testing took place at the LIR National Ocean Test Facility, which is part of the Marine and Renewable Energy Institute (MaREI) centre, housed at the Beaufort building in Cork, Ireland. The testing examined the differences that variations in spectral shape creates in the resultant energy production, even when the spectral average parameters such as H_s and T_e/T_p are identical.

This work documents the methodology of designing devices, identifying appropriate sea-states, and testing the impact of the variation in wave spectral density

distribution on the energy produced by these devices. It is also hoped that the simple design of these devices and the outlined methodology for testing and presentation of the results, which will be made freely available, can be easily replicated at other facilities as a means of testing the impact of the variation in spectral shape between standardised spectra and the candidate sites that are being examined. Further, this is an exercise in demonstrating the real-world impact of statistical simplifications on the developing wave energy industry.

6.4.2 Preliminary Actions

The brief for this testing is to examine the impact of spectral shape on real device energy production. It is imperative that the chosen wave energy device design clearly demonstrate any difference in the distribution of energy, while balancing this with both the ease and speed of construction. The idea is to create a device that is cheap and easily replicable such that a number of models with various alterations can be created and tailored to the specific sea-state conditions which are to be tested.

In addition, to remove a large amount of the variability in testing, the device movement is constrained in all 6 degrees of freedom, allowing a simple examination of the heave motion of the water column of the Oscillating Water Column in determining the device power production, thus simplifying the testing procedure and concurrently improving the dependability of the results.

6.4.3 Experiment Setup

6.4.3.1 Deep Ocean Basin

The device testing took place in the Deep Water Ocean Basin at the LiR National Ocean Test Facility (NOTF), a custom designed test facility which operates within the MaREI Centre. It houses Ireland's only infrastructure for small to medium scale laboratory testing of ocean and maritime systems. The NOTF houses four tanks at various scales and depths for emulation of ocean waves and currents. They are equipped with measurement capabilities including laser PIV, acoustic probes, above and sub-surface motion and real-time video. There are a variety of bench test rigs for electrical, power take off and mooring system tests along with a microgrid/on grid infrastructure for test of generation, control, power take off, storage, grid integration, power quality, subsea transmission and fault synthesis. The tank and

institution are reputed for contributions to wave, tidal and offshore wind energy development including towing, installation, performance and survival testing, work with floating structures, offshore structures, coastal engineering including breakwaters and harbours, hydrodynamics, scour, vessels and offshore logistics.

The Deep Ocean basin has a moveable floor plate, allowing water depth to be adjusted, and making it suitable for circa. 1/15 scale operational conditions and 1/30 scale Atlantic survival states. The basin is equipped with 16 hinged force-feedback paddles, making it capable of peak wave generation conditions of H_s = 0.6m, T_p = 2.7s and H_{max} = 1.1m. It is 35m x 12m x 3m deep, with the hydraulic, movable, floor (Figure 168 & Figure 169) allowing depths from 0 to 3m.

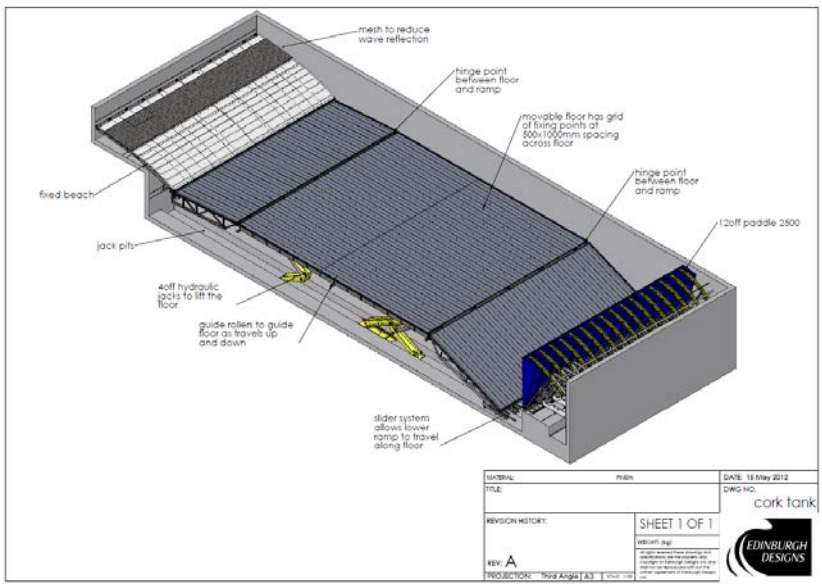


FIGURE 168: DEEP WATER OCEAN BASIN OVERVIEW

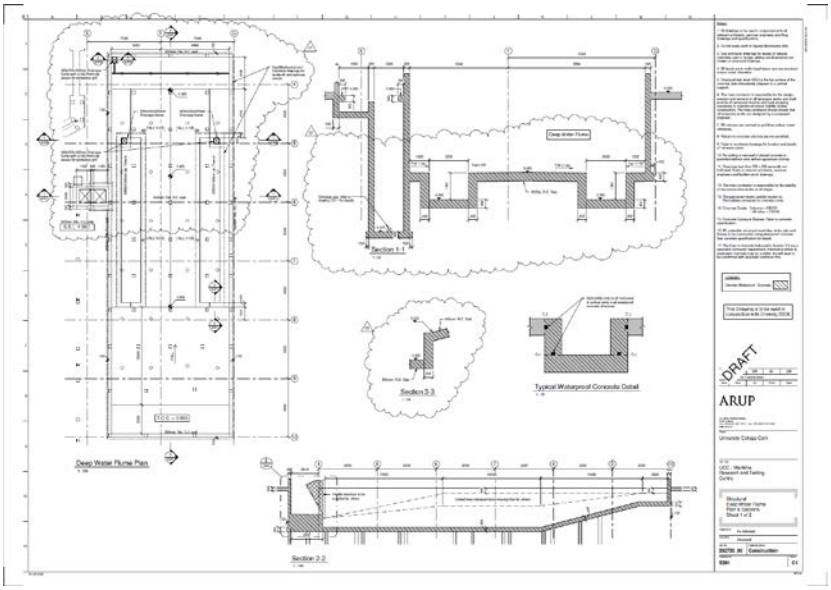


FIGURE 169: DEEP WATER OCEAN BASIN SCHEMATIC

6.4.3.2 Device Design

The design of the OWC devices for this testing exercise will be outlined in this Section. The guiding principles are simplicity, the ability to directly demonstrate issues caused by spectral shape variation on device energy production, and replicability of the device construction and testing procedure. In addition to this testing, this methodology could be used as a template to examine real-world impact of spectral shape in tank testing with cheap materials which are available worldwide.

6.4.3.2.1 Fabricated OWC Description

Three devices were constructed for the testing. These were OWC devices consisting of a long cylindrical pipe, with one open end submerged in water and the other end open to the atmosphere. A closed cap featuring a 16mm orifice allowed for air to exit the device. The top featured a further 8mm tapping to affix a pressure transducer, to perform continuous pressure measurements fed back via LabVIEW throughout testing.

The OWCs were constructed of 160mm diameter Wavin Pipe with a wall thickness of 3.9mm, a tapered end and an end cap. The endcap features a 16mm unchamfered orifice in a plate of 4.2mm thickness. There is an 8mm pressure transducer tapping which has been offset to the side of the endcap to minimize its influence on the flow through the orifice.

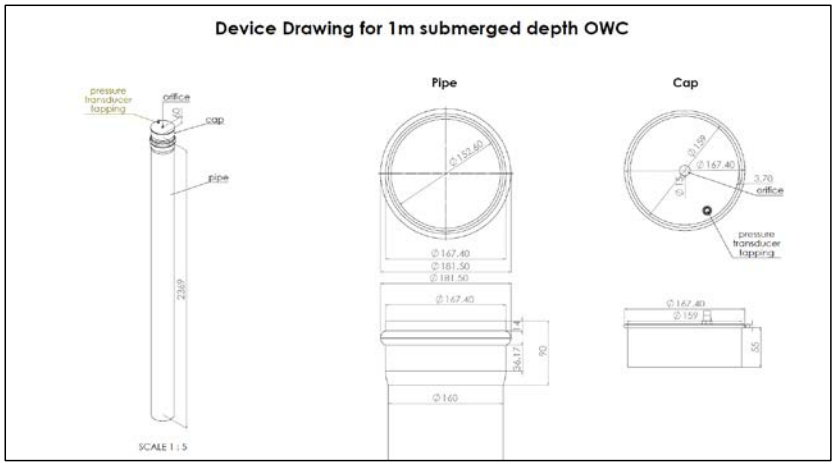


FIGURE 170: OWC DEVICE SOLIDWORKS ASSEMBLY DIAGRAM

The devices were cut to their determined lengths for the desired frequency response, and individually tested to determine damping and the orifice values required for maximum power production. This resulted in the selection of a uniform 16mm orifice for the three devices, as it proved the best compromise for power production, ease of testing, and reduction in confounding variables during testing.

The OWC devices were attached to the tank instrumentation bridge by means of steel angle section fitted to the device at positions corresponding to the top and bottom flat surfaces of the bridge. The steel angle section rests with one face flat to the bridge, and is affixed to the device by means of a single M8 bolt.

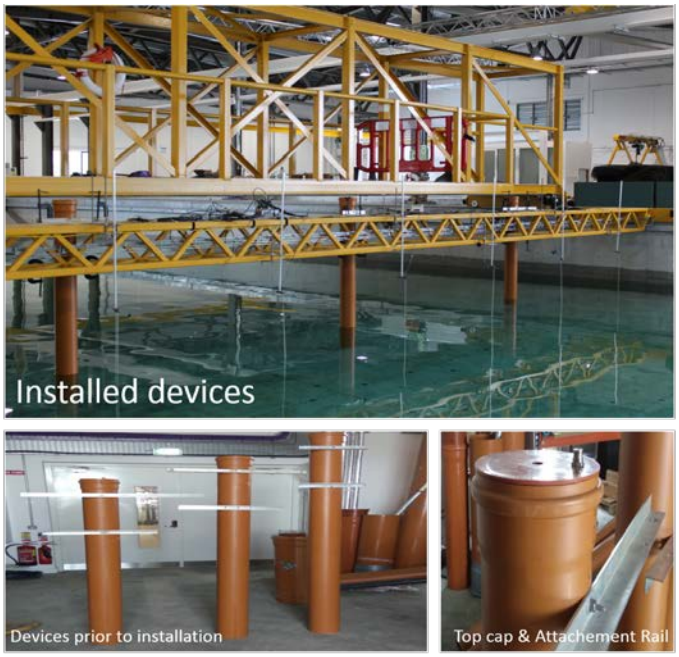


FIGURE 171: DEVICES, ATTACHMENT MECHANISM AND INSTRUMENT BRIDGE

6.4.3.2.2 Selection of Device Scale

The scale of the devices is selected according to a number of constraints. These chiefly include the minimum and maximum wave conditions which can be reliably reproduced in the Deep Ocean Basin. Another consideration is to fit the envelope of sea-states chosen to the resonant period of the device, while maintaining a device length less of than 1.0m to prevent difficulties with mounting and manoeuvring the device in the tank. The study would be conducted with T_p, but the selection criteria also takes account of the energy production using the T_e record.

Both occurrence and power production are considered in selecting the test conditions for the devices, and this extends to the selection of Wave Period at scale. Selection of Froude Scale for testing are based on the maximum Wave Period the devices will respond to.

e.g. the Froude-Scaled ratio of T_p at 1:30 and 1:50 scale are as follows:

$$1{:}30 \text{ scale} : \frac{1}{\sqrt{30}} \text{ x } T_p = 0.1826\ T_p \qquad (6.10)$$

$$1{:}50 \text{ scale} : \frac{1}{\sqrt{50}} \text{ x } T_p = 0.1414\ T_p \quad (6.11)$$

A maximum of a 2.7s T_p is attainable when generating the maximum wave height achievable with the current Deep Ocean Basin configuration. This is the maximum non-breaking height, whereupon the amplitude is necessarily lowered after exceeding this period value. This means that the upper Wave Periods, which contributed a large amount to the overall energy contribution of the sea-states, could not feasibly be tested at 1:30 scale. Taking these factors and constraints into consideration, a device scale of 1:50 was selected. The maximum resonant period of the devices built is 2.07s, thus the maximum wave condition to test carries a full scale Wave Period of approximately 11.34 – 14.64s. Likewise, the minimum period selectable will be determined by the lowest resonant period of the devices constructed. This process ultimately resulted in the selection of a 1:50 scale for testing, and device submerged lengths of 0.5 – 1.0m, as indicated in Table 74.

The device scale selected informs the tank testing duration, which is determined based on the Froude-Scaled duration of each buoy data record from the Killard Point data:

Original buoy record duration = 30 minutes

Froude Scaled record duration at 1:50 scale = $\frac{30\ minutes}{\sqrt{50}}$ = 4m15s

6.4.3.2.3 Selection of Device Characteristics

The OWC design is tailored to the expected sea-states that are to be analysed. Testing is performed at 1:50 scale with a range of wave conditions varying from 2.5 - 7m H_s and 9.5 - 15.5s T_p, corresponding to 0.05 - 0.14m H_s and 1.34 - 2.19s T_p at prototype scale. To determine the device characteristics required to achieve resonance at this scale, a preliminary theoretical analysis was performed using the Evans et Al., McCormick Equation and Veer et Al. approaches. These have been shown to give results which are quite similar to a Boundary Element Method approach (Sheng, Alcorn and Lewis, 2014). These approaches are based on the notion of an imaginary

"piston" or slug of water moving within the OWC and effecting a movement of the air in the device at the boundary with the water surface (Figure 172).

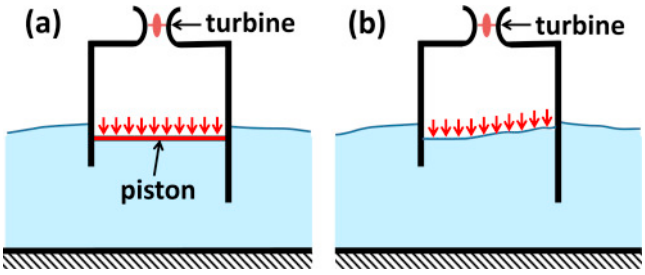


FIGURE 172: OWC WATER SURFACE PISTON REPRESENTATION

The formula given by (Evans and Porter, 1995) relates the natural period of the device to the water depth, in the case where the draft, D, is far greater than the diameter, as follows:

$$T_0 = 2\pi\sqrt{\frac{D}{g}} \tag{6.12}$$

Where:

T_0 is the natural period (in seconds)

D is the Draft to mouth of device (in metres)

g is acceleration due to gravity

(Michael E. McCormick, 1981), considering the imaginary water piston as an isolated cylinder, and again assuming that D is far larger than the diameter, gives a corresponding natural period for heave motion of:

$$T_0 = 2\pi\sqrt{\frac{D + 0.848R}{g}} \tag{6.13}$$

Where R is the radius of the cylinder.

(van 't Veer and Tholen, 2008) give the natural period of the internal water surface motion for a large water column or moonpool (the underwater opening in the vessel):

$$T_0 = 2\pi \sqrt{\frac{D + 0.41 \times So^{0.5}}{g}} \tag{6.14}$$

Where S_o is the Sectional area of the moonpool/water column.

These approximations for the natural period allowed an estimation of the likely resonant period ranges which can be captured by a given device diameter and draft, and thus enabled the selection of a range of device characteristics to examine a broad range of sea states.

These three approaches are used to determine the resonance period of the OWC devices based on their chosen design characteristics (D, S) and by varying the submerged depth to alter the devices' resonant period to capture the power response across a broad range of sea-states.

The results of these formula for submerged depths ranging from 0.1 – 1.0m are tabulated below.

TABLE 73: RESONANCE PERIOD OF PARTIALLY SUBMERGED OWC DEVICE AS A FUNCTION OF DEVICE DRAFT/SUBMERGED DEPTH

D (m)	Resonance period. T_o (s)		
	Evans et al	McCormick Equation	Veer et Al
1	2.01	2.07	2.17
0.9	1.90	1.97	2.08
0.8	1.79	1.86	1.98
0.7	1.68	1.75	1.87
0.6	1.55	1.63	1.76
0.5	1.42	1.51	1.64
0.4	1.27	1.37	1.52
0.3	1.10	1.21	1.38
0.2	0.90	1.03	1.22
0.1	0.63	0.81	1.04

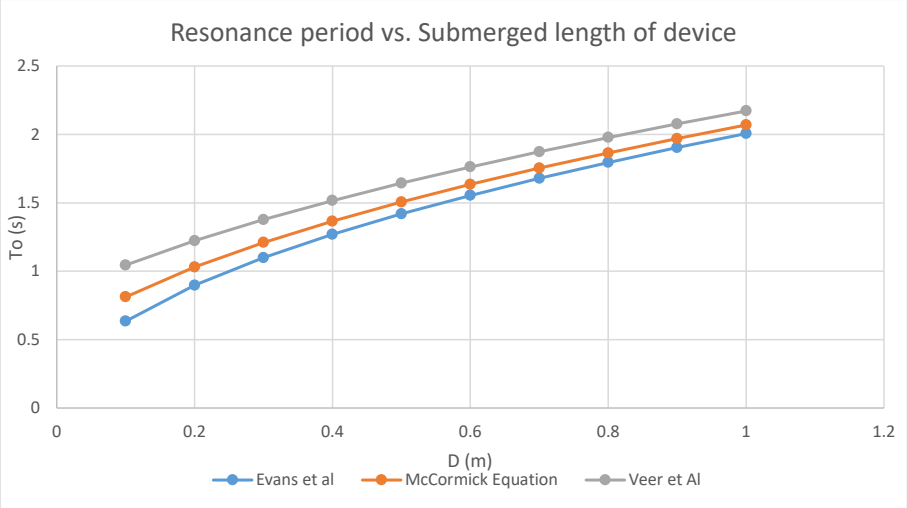


FIGURE 173: RESONANCE PERIOD OF DEVICE VS. SUBMERGED DEPTH

The three equations provided relatively consistent results, with a spread of approximately 10% between the lowest and highest estimates for all but the shortest submerged depths, where the deviation between formulae increases.

The McCormick Equation was chosen to calculate the natural period of the device, being the simplest equation to include the radius of the device and model the internal water surface, and representing the midpoint of the three equations. It was used to determine the device lengths for the range of Wave Period occurrences

To verify the results of the numerical estimates of resonant period, the device was physically tested in the tank at varying submerged depths. To do this, the device was placed in the Deep Ocean Basin as a large uncut length of pipe to facilitate investigation of a full range of submerged depths and their effect on device response, performance, pressure/power production. Alongside this testing, other factors such as the stability of the instrumentation bridge truss structure to which the devices would be attached were tested.

The submerged depth was initially set at 1m, and progressively altered from the initial value with the aim of discovering which submerged depths were capable of

eliciting sufficient device performance and optimal response to the proposed testing sea-states. Thus, a series of acceptable depths were determined in which the device performance was sufficient. The final device selection must also be suited to the scaled operational spread of the test wave conditions. Additionally, the practicalities of working in the tank must be taken into account, chiefly how the moveable floor in the Deep Ocean Basin can restrict device length where it reaches its lowest serviceable level.

The chosen OWC lengths, optimised to the coverage of sea-states, are as follows:

TABLE 74: CHARACTERISTICS OF CHOSEN DEVICE DESIGNS

Device ID	Draft (m)	T_0 McCormick (s)	Pipe Length Required (mm)	Pipe Length Below Taper Required (mm)
OWC_1	1	2.073	2369	2269
OWC_2	0.75	1.814	2119	2019
OWC_3	0.5	1.512	1869	1769

6.4.3.3 Selection of Wave Probe Locations

Wave probe locations were placed at evenly spaced intervals of 1.5m across the tank. A 3m gap was left on the nearside of the tank (bottom of Figure 174) and a 1.5m gap on the offside of the tank. These wave probe locations corresponded to the intended location of the OWC devices, and the centre position between the devices.

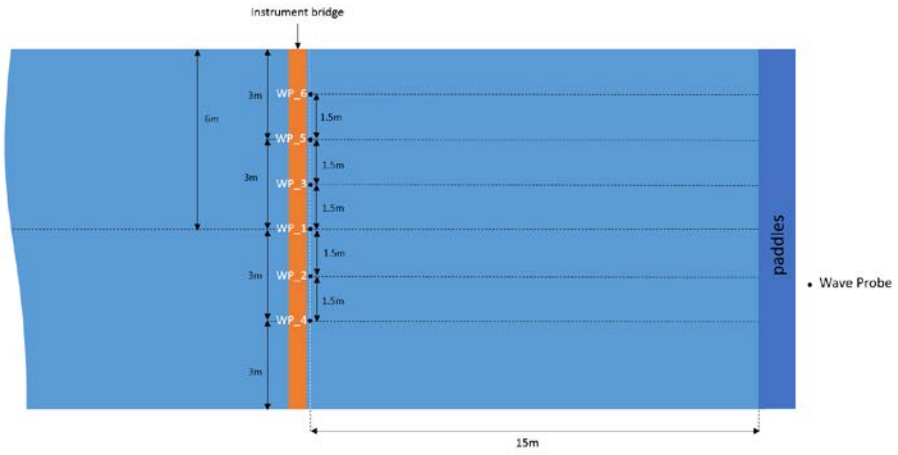


FIGURE 174: TANK ARRANGEMENT FOR WAVE CALIBRATION

Figure 175 & Figure 176 display the wave probe arrangement in situ for the calibration configuration.

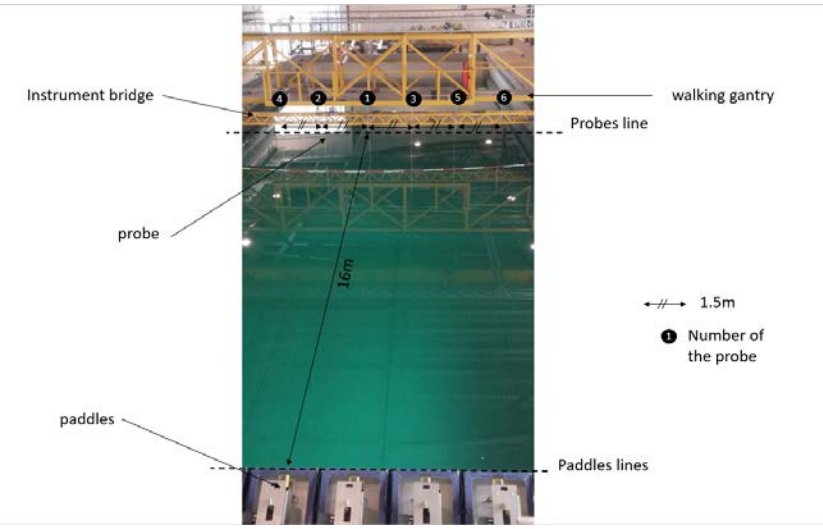


FIGURE 175: WAVE PROBE ARRANGEMENT IN TANK

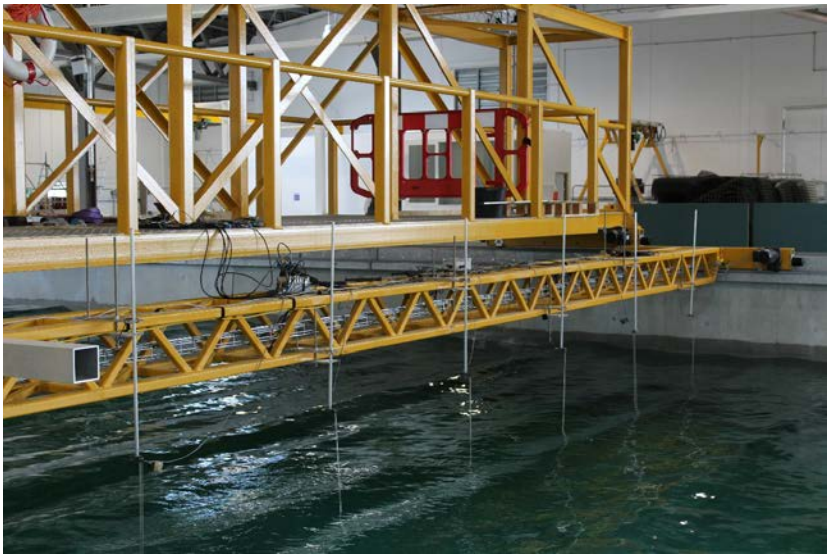


FIGURE 176: WAVE PROBE INSTALLATION ON INSTRUMENTATION BRIDGE

The probes were calibrated by progressively moving them by defined 100mm distances to ensure that the water elevation change was proportional to the output voltage of the sensors. This provided a reliable and consistent measurement of water surface elevation during calibration and testing.

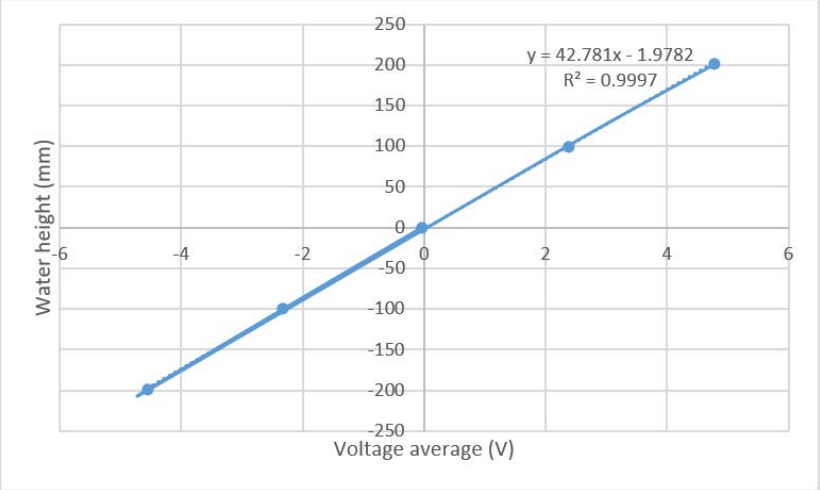


FIGURE 177: WAVE PROBE SENSOR VOLTAGE AS A FUNCTION OF WATER SURFACE ELEVATION

For testing, the devices were attached as outlined in Figure 178 & Figure 179. This involved the attachment of OWC devices at the positions of Wave Probe 1, 4 and 5.

The instrumentation bridge was moved towards the paddles to place the devices at the former probe locations (of probes 1, 4 and 5). There was 0.7m between the device centres and the wave probe locations to the paddle side of the bridge, thus necessitating a 0.7m movement of the bridge towards paddles.

Probes 2 and 3 (the probes placed between the devices) were moved to the opposite side of the instrumentation bridge to give confirmation of wave readings at precisely the same location and to give an indication of the replicability of the wave conditions between calibration and device testing.

The position of Wave Probe 6 (between Device 3 and wall) was maintained to give a reference point for determining the existence of a potential wall effect, which would alter the wave heights in proximity to the tank walls. The readings of Wave Probe 6 will later be compared to those of Wave Probes 1 & 2 to look at any potential wall effect.

Pressure sensors were then attached to the three OWC devices by means of the 8mm pressure tapping. This was connected via a National Instruments EtherCat system to

the computer in the tank control room which monitored the pressure readings via a custom configured LabVIEW setup.

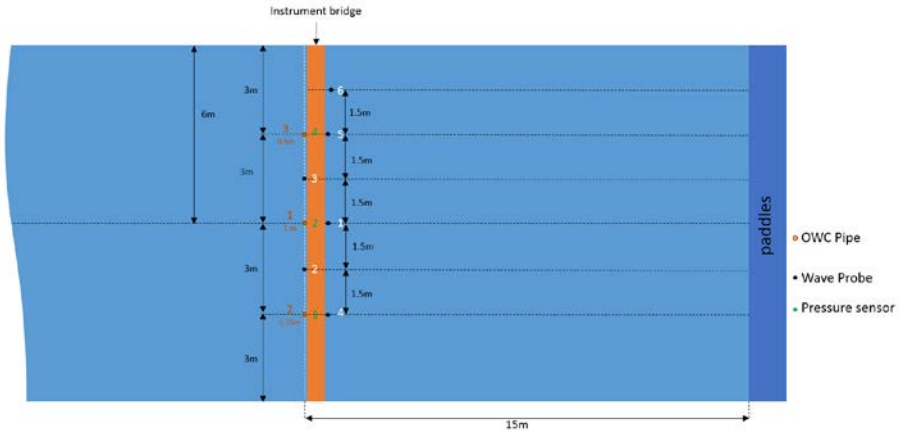


FIGURE 178: TANK ARRANGEMENT FOR TESTING

TABLE 75: LABELLING OF DEVICE, WAVE PROBE AND PRESSURE SENSORS

Device Number	Device Draft (m)	Wave Probe Number	Pressure Sensor
OWC_1	1	1	2
OWC_2	0.75	5	1
OWC_3	0.5	4	4

Figure 178 and Table 75 give an overview of the arrangement of the devices, probes, and the pressure sensors attached to the devices. Pressure sensors 1, 2 and 4 have been attached from nearside to offside respectively.



FIGURE 179: WAVE PROBES AND DEVICES INSTALLED ON INSTRUMENTATION BRIDGE

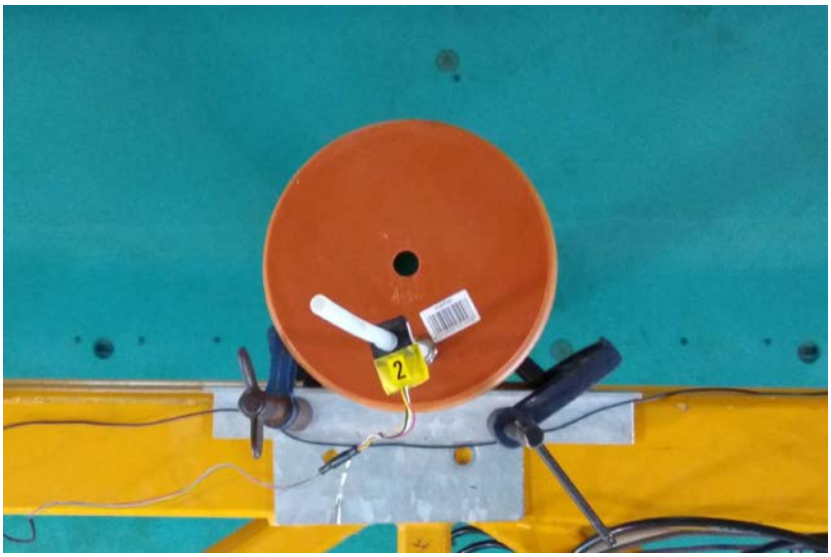


FIGURE 180: TOP VIEW OF OWC DEVICE SHOWING PRESSURE SENSOR AND ATTACHMENT CONFIGURATION

Figure 180 displays the attachment of the OWC device to the instrumentation bridge by means of the steel angle section, which overlaps the bridge and is mounted by four G-Clamps (two top, two bottom). This mounting mechanism allowed for rapid

attachment and detachment of the devices, accurate positioning, and secure hold. (A H_{max} of 1m was trialled to ensure the device did not experience any slip during testing conditions).

6.4.4 Tank Testing

6.4.4.1 Tank Testing Overview

Tank testing commenced with calibration to ensure the correct wave conditions were being produced in the tank at the desired location, and to provide a reference wave condition at the intended position of the OWC devices. In total 93 tests were performed, comprising of 47 calibration runs and 46 device tests. These are itemised in Table 76.

Data capture for tank testing comprised a two computer system located in the Deep Ocean Basin control cabin. These received the central pressure sensor pass-through feed from the National Instruments EtherCat device, as well as receiving and displaying the water surface elevation readings from the wave probes. A core component in the operation of the Deep Ocean Basin is the Edinburgh Designs wavemaker software suite, which consists of two main software applications and a collection of software tools for diagnostic and configuration purposes. The two main components are:

• **Wave Runtime** – this is the runtime software used to operate the wavemaker hardware. It provides the main human-machine interface, allowing the user to control the power state of the machine, generate or play back waves, capture operational data from the machine and monitor the state of the machine for maintenance or troubleshooting. It consists of two programs: the Engine, which performs the real time data processing, and the Client, which provides a graphical front end. The Client can communicate with the Engine via TCP/IP allowing it to be run remotely over a network if required.

• **Wave Synthesiser** – this is a graphical application for creating wave designs to be run by a wavemaker. Waves are built by adding components, such as sine waves, spectra or angle spreading functions, to a tree structure. Components can be specified using mathematical expressions or data input allowing a large amount of flexibility. The software provides the ability to visualise the wave to aid in the design

process. Wave files generated by the program are loaded by Wave Runtime to be played back by the wavemaker. (Greig, Jason and Edinburgh Designs, 2012)

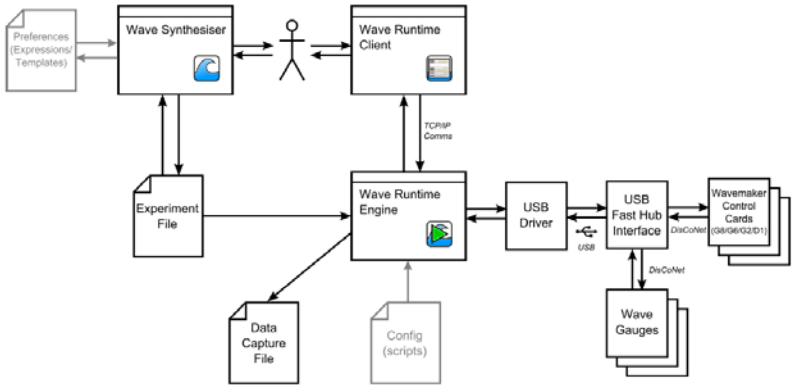


FIGURE 181: EDINBURGH DESIGNS WAVE GENERATION SOFTWARE OVERVIEW

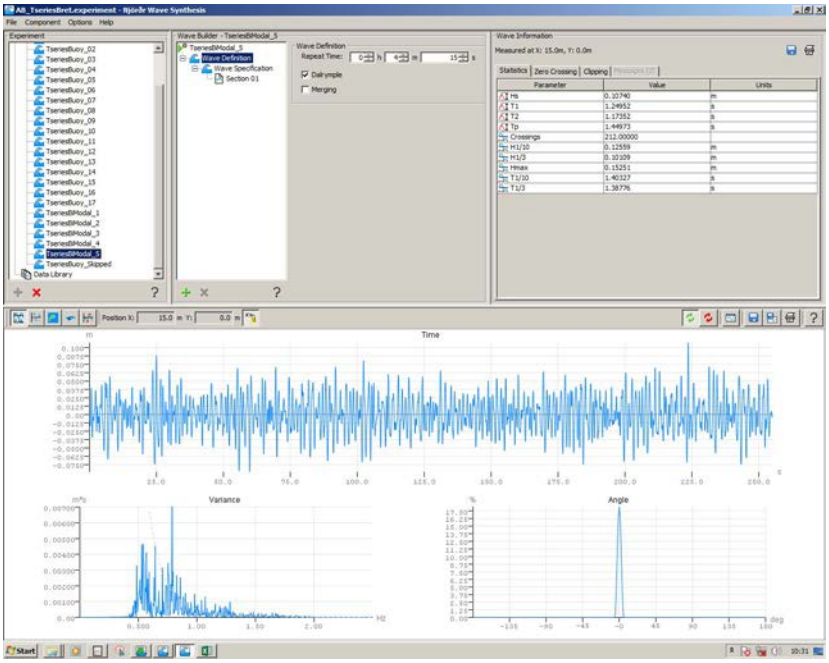


FIGURE 182: NJORD WAVE SYNTHESIS INPUT INTERFACE: GENERATION OF BI-MODAL TIME-SERIES WITH H_S 0.1074M AND T_P 1.4497S (AT SCALE)

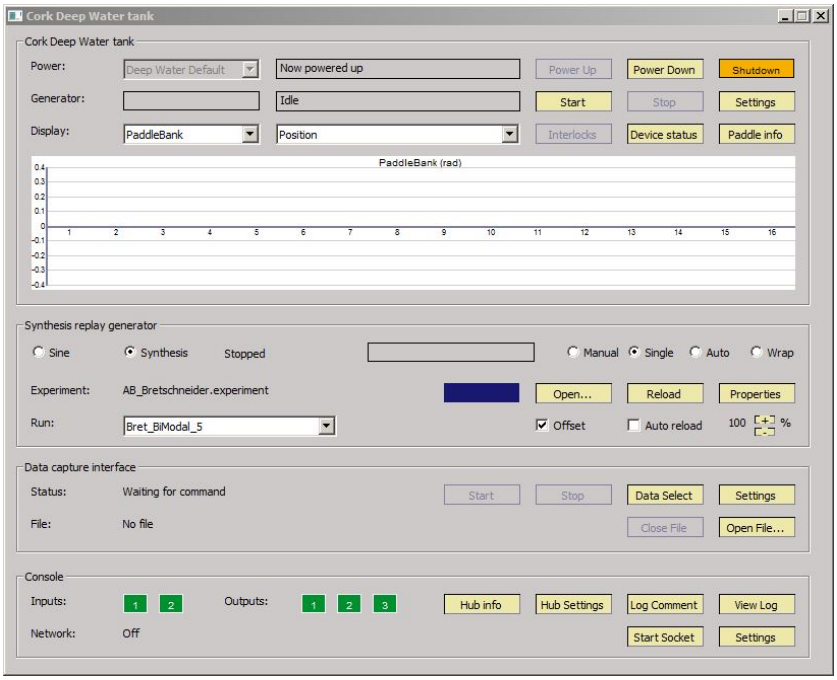


FIGURE 183: TANK CONTROL INTERFACE: SHOWING TANK CONTROLS AND ABILITY TO SELECT GENERATED TIME-SERIES FILES TO BE CREATED BY WAVEMAKER

The secondary PC ran LabVIEW (National Instruments, 2017) which took continuous readings of wave elevation from the six wave probes and three pressure sensors attached to the devices.

Lab View Test logs; comprising the wave probe measurements and pressure sensor readings, were stored to files named AB_0XX.txt and stored on the National Instruments CompactRIO (cRIO) device.

6.4.4.2 Wave Calibration

Tests 001 - 041 and 088 - 093 (Table 76 and Table 81) were performed to calibrate the wave conditions in the tank, ensuring that the required wave conditions were being properly re-created in the tank, and that the conditions at the six wave probes are consistent with those of the input time-series files. These tests comprised of 18 unique Bretschneider derived time-series with equivalent H_s, T_p to the time-series files chosen from the Killard Point data. Additionally, 5 bi-modal sea states were

chosen from the Killard Point time-series data, and 5 corresponding Bretschneider time-series files with equivalent H_s, T_p then generated to match these.

6.4.4.3 Calibration of device orifice

It was necessary to calibrate the Pressure to Flow relationship of the orifice installed on the device to achieve an accurate estimate of the power production of the device from the pressure readings recorded during testing. This process was conducted using a custom-built rig for orifice calibration (Figure 184: Rig for Orifice

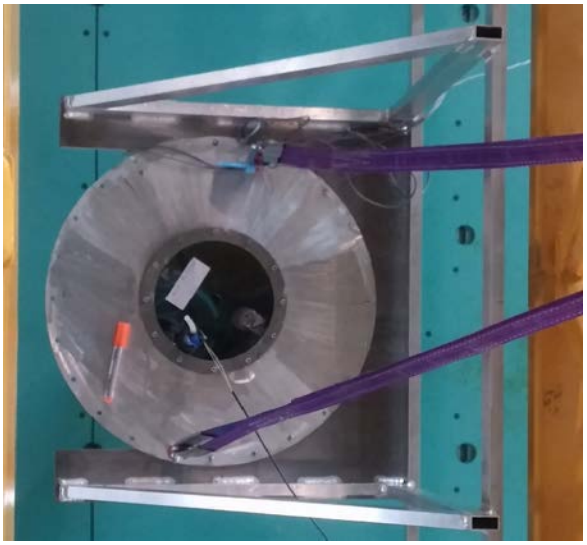


FIGURE 184: RIG FOR ORIFICE CALIBRATION

The top cap of the OWC device was attached to a Perspex sheet cut to fit the top mounting position to ensure an air-tight seal between the device and orifice. Two wave probes were installed in the testing rig, alongside pressure sensors attached to the pressure tapping of the OWC cap with orifice to be tested.

The wave probes were calibrated in the same fashion as described in Section 6.4.3.3. With LabVIEW recording pressure and water surface elevation within the device, the device was slowly raised and lowered by means of a gantry mounted crane. This was followed by rapid oscillations produced through manual perturbation of the device using a long metal rod. This process gave a time-series of pressure and water surface

elevation readings which could be used to determine the flow rate of air within the device at a given pressure.

Flow Velocity in the chamber was determined assuming the air moved completely and incompressibly with the movement of the internal water surface of the device (as measured by the wave probes).

$$V = {}^{\Delta H}/_{\Delta T} \tag{6.15}$$

Where:

V = Flow Velocity (m/s)

H = Water Surface Elevation (m)

T = Time (s)

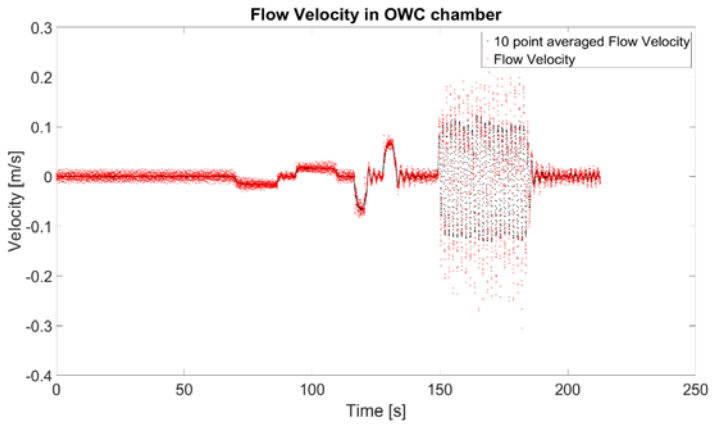


FIGURE 185: FLOW VELOCITY IN OWC CHAMBER DURING ORIFICE CALIBRATION

This was converted to flow rate by multiplying by the sectional area of the internal chamber of the device:

$$Q = {}^{\Delta H}/_{\Delta T} \times \pi \times r^2 \tag{6.16}$$

Where:

Q = Flow Rate (m^3/s)

H = Height of water surface (m)

r = Internal radius of device (m)

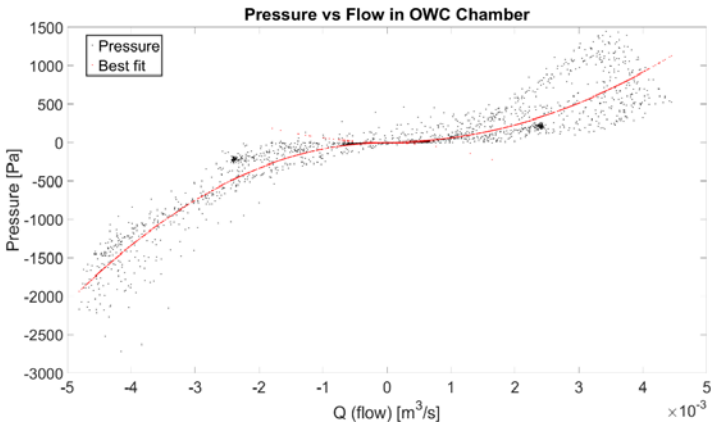


FIGURE 186: PRESSURE VS FLOW DURING ORIFICE CALIBRATION. POSITIVE AND NEGATIVE BEST FIT SHOWN

The relationship between Flow and Pressure was then determined using a 2nd order polynomial fit for both positive and negative flows. The constant, K_p relating pressure and flow was determined to be:

$$K_{p_pos} = 5.708 \times 10^7$$

$$K_{p_neg} = -8.37 \times 10^7$$

And device instantaneous power production was determined by:

$$Power_{device} = Q \times P \quad (6.17)$$

$$Power_{device} = K_p \times P \times P \quad (6.18)$$

Where:

P = Pressure (Pa)

6.4.4.3.1 Alternative Method for Power Production Determination

An alternative method was also used to determine the power production of the OWC device; making the assumption that the water surface elevation within the devices mirrored the adjacent probe reading of water surface elevation. Given that the correlation coefficient between probe 3 and probes 1/4/5 is always more than 0.95,

a further assumption was made that the water surface elevation recorded by probe 3 was representative of the interval water surface elevation in the three OWC devices.

Device Power was then determined by:

$$Power_{device_{alt}} = |P| \times Q \tag{6.19}$$

Where:

With Q determined as by eqn (**6.16**).

6.4.5 Analysis of Tank Test Results

6.4.5.1 Observations

The following are some observations following the tank testing performed. These are wide-ranging observations which will be examined in more detail in subsequent sections. Tank testing was conducted successfully, with no failures of device mounting mechanisms, components or measuring equipment. Preliminary analysis of the wave probe measurements reveals consistent and reasonably accurate output. Likewise, the pressure sensors functioned correctly across all devices. These are the key facets of testing which will enable a number of important conclusions to be drawn regarding the power production of the device, its influencing factors, and, as is the overarching goal; to determine the impact the variation in spectral shape from the commonly used empirical spectra can have on the resultant power production.

There are some findings which necessitated further analysis to determine the accuracy and validity of the testing carried out. Chiefly, there were some notable differences between the requested time-series and the time-series produced by the tank. While the reproduction of simple Bretschneider sea-states was good throughout testing, there were issues with the generation of real sea-states, which were exacerbated in the generation of bi-modal sea-states.

The test conditions are listed below in Table 76 to Table 81 and are primarily characterised by H_s and T_p. These time-series are selected based on matching the average spectral shape within a given H_s, T_p bin. The time-series are then scaled to

match the 1:50 scale of the device by altering both the timestep and elevation record according to Froude Scaling similarity.

TABLE 76: LIST OF OWC BRETSCHNEIDER CALIBRATION TESTS

LabVIEW Test Number	Wave File Name	Sea-State No.	H_s	T_p	Scale H_s	Scale T_p
001	Bret_01	1	2.81	10.00	0.056	1.41
002	Bret_02	2	2.84	10.53	0.057	1.49
003	Bret_03	3	2.82	12.12	0.056	1.71
004	Bret_04	4	2.96	12.70	0.059	1.80
005	Bret_05	5	3.50	10.67	0.070	1.51
006	Bret_06	6	3.97	12.31	0.079	1.74
007	Bret_07	7	3.84	13.33	0.077	1.89
008	Bret_08	8	3.54	14.29	0.071	2.02
009	Bret_09	9	4.66	13.33	0.093	1.89
010	Bret_10	10	4.87	14.29	0.097	2.02
011	Bret_10 (repeat)	10	4.87	14.29	0.097	2.02
012	Bret_11	11	4.83	14.82	0.097	2.10
013	Bret_12	12	4.73	16.00	0.095	2.26
014	Bret_13	13	5.58	12.50	0.112	1.77
015	Bret_14	14	5.97	14.29	0.119	2.02
016	Bret_15	15	5.76	15.09	0.115	2.13
017	Bret_16	16	6.88	13.12	0.138	1.85
018	Bret_17	17	6.77	13.56	0.135	1.92
019	Bret_18	18	6.75	14.55	0.135	2.06

TABLE 77: LIST OF OWC TIMESERIES CALIBRATION TESTS

LabVIEW Test Number	Wave File Name	Sea-State No.	H_s	T_p	Scale H_s	Scale T_p
020	TSeriesBuoy_01	1	2.81	10.00	0.056	1.41
021	TSeriesBuoy_02	2	2.84	10.53	0.057	1.49
022	TSeriesBuoy_03	3	2.82	12.12	0.056	1.71
023	TSeriesBuoy_04	4	2.96	12.70	0.059	1.80
024	TSeriesBuoy_05	5	3.50	10.67	0.070	1.51
025	TSeriesBuoy_06	6	3.97	12.31	0.079	1.74
026	TSeriesBuoy_07	7	3.84	13.33	0.077	1.89
027	TSeriesBuoy_08	8	3.54	14.29	0.071	2.02
028	TSeriesBuoy_09	9	4.66	13.33	0.093	1.89
029	TSeriesBuoy_10	10	4.87	14.29	0.097	2.02
030	TSeriesBuoy_11	11	4.83	14.82	0.097	2.10
	XX -file not created	12	4.73	16.00	0.095	2.26
031	TSeriesBuoy_12	13	5.58	12.50	0.112	1.77
032	TSeriesBuoy_13	14	5.97	14.29	0.119	2.02
033	TSeriesBuoy_14	15	5.76	15.09	0.115	2.13
034	TSeriesBuoy_15	16	6.88	13.12	0.138	1.85
035	TSeriesBuoy_16	17	6.77	13.56	0.135	1.92
036	TSeriesBuoy_17	18	6.75	14.55	0.135	2.06
037	TseriesBiModal_1	B_1	3.70	12.50	0.074	1.77
038	TseriesBiModal_2	B_2	3.68	13.11	0.074	1.85
039	TseriesBiModal_3	B_3	4.33	12.70	0.087	1.80
040	TseriesBiModal_4	B_4	5.03	12.90	0.101	1.82
041	TseriesBiModal_5	B_5	5.44	13.33	0.109	1.89
End of calibration runs	-		-	-	-	-

TABLE 78: LIST OF OWC BRETSCHNEIDER TESTS

LabVIEW Test Number	Wave File Name	Sea-State No.	H_s	T_p	Scale H_s	Scale T_p
042	Bret_01	1	2.81	10.00	0.056	1.41
043	Bret_02	2	2.84	10.53	0.057	1.49
044	Bret_03	3	2.82	12.12	0.056	1.71
045	Bret_04	4	2.96	12.70	0.059	1.80
046	Bret_05	5	3.50	10.67	0.070	1.51
047	Bret_06	6	3.97	12.31	0.079	1.74
048	Bret_07	7	3.84	13.33	0.077	1.89
049	Bret_08	8	3.54	14.29	0.071	2.02
050	Bret_09	9	4.66	13.33	0.093	1.89
051	Bret_10	10	4.87	14.29	0.097	2.02
052	Bret_11	11	4.83	14.82	0.097	2.10
053	Bret_12	12	4.73	16.00	0.095	2.26
054	Bret_13	13	5.58	12.50	0.112	1.77
055	Bret_14	14	5.97	14.29	0.119	2.02
056	Bret_15	15	5.76	15.09	0.115	2.13
057	Bret_16	16	6.88	13.12	0.138	1.85
058	Bret_17	17	6.77	13.56	0.135	1.92
059	Bret_18	18	6.75	14.55	0.135	2.06

TABLE 79: LIST OF OWC TIMESERIES TESTS

LabVIEW Test Number	Wave File Name	Sea-State No.	H_s	T_p	Scale H_s	Scale T_p
060	TSeriesBuoy_01	1	2.81	10.00	0.056	1.41
061	TSeriesBuoy_02	2	2.84	10.53	0.057	1.49
062	TSeriesBuoy_03	3	2.82	12.12	0.056	1.71
063	TSeriesBuoy_04	4	2.96	12.70	0.059	1.80
064	TSeriesBuoy_05	5	3.50	10.67	0.070	1.51
065	TSeriesBuoy_06	6	3.97	12.31	0.079	1.74
066	TSeriesBuoy_07	7	3.84	13.33	0.077	1.89
067	TSeriesBuoy_08	8	3.54	14.29	0.071	2.02
068	TSeriesBuoy_09	9	4.66	13.33	0.093	1.89
069	TSeriesBuoy_10	10	4.87	14.29	0.097	2.02
070	TSeriesBuoy_11	11	4.83	14.82	0.097	2.10
-	XX -file not created	12	4.73	16.00	0.095	2.26
071	TSeriesBuoy_12 (Bret_13 equivalent)	13	5.58	12.50	0.112	1.77
072	TSeriesBuoy_13	14	5.97	14.29	0.119	2.02
073	TSeriesBuoy_14	15	5.76	15.09	0.115	2.13
074	TSeriesBuoy_15	16	6.88	13.12	0.138	1.85
075	TSeriesBuoy_16	17	6.77	13.56	0.135	1.92
076	TSeriesBuoy_17	18	6.75	14.55	0.135	2.06

TABLE 80: LIST OF OWC BIMODAL TESTS

LabVIEW Test Number	Wave File Name	Sea-State No.	H_s	T_p	Scale H_s	Scale T_p
077	TseriesBiModal_1	B_1	3.70	12.50	0.074	1.77
078	TseriesBiModal_2	B_2	3.68	13.11	0.074	1.85
079	TseriesBiModal_3	B_3	4.33	12.70	0.087	1.80
080	TseriesBiModal_4	B_4	5.03	12.90	0.101	1.82
081	TseriesBiModal_5	B_5	5.44	13.33	0.109	1.89
082	TseriesBuoy_Skipped	12	4.73	16.00	0.095	2.26
083	BretBiModal_1	B_1	3.70	12.50	0.074	1.77
084	BretBiModal_2	B_2	3.68	13.11	0.074	1.85
085	BretBiModal_3	B_3	4.33	12.70	0.087	1.80
086	BretBiModal_4	B_4	5.03	12.90	0.101	1.82
087	BretBiModal_5	B_5	5.44	13.33	0.109	1.89

TABLE 81: LIST OF OWC ADDITIONAL CALIBRATION TESTS

LabVIEW Test Number	Wave File Name	Sea-State No.	H_s	T_p	Scale H_s	Scale T_p
088	TseriesBuoy_Skipped	12	4.73	16.00	0.095	2.26
089	BretBiModal_1	B_1	3.70	12.50	0.074	1.77
090	BretBiModal_2	B_2	3.68	13.11	0.074	1.85
091	BretBiModal_3	B_3	4.33	12.70	0.087	1.80
092	BretBiModal_4	B_4	5.03	12.90	0.101	1.82
093	BretBiModal_5	B_5	5.44	13.33	0.109	1.89

6.4.5.2 Plots and summaries

6.4.5.2.1 Information on Test Data

The LabVIEW data obtained from the tank testing was in .csv format and featured the 6 wave-probe water surface elevation readings and 3 pressure sensor readings.

The data was sampled at a frequency of 32Hz, resulting in 11072 data-points recorded over the sampling duration. This corresponded to approximately 5 minutes 46 seconds of recording; with a repeat time of 4 minutes 15 seconds determined in the wave generation software (Equivalent to the scale duration of the time-series data from the Killard Point Buoy Recordings), after which the program would repeat the time-series data.



FIGURE 187: SAMPLE RECORDED DATA FROM LABVIEW FOR TEST 001

The requested data file, generated by the Njord Wave Synthesis program consisted of 2304 data points sampled at approximately 9Hz (due to the scaling of the waves to 1:50 scale).

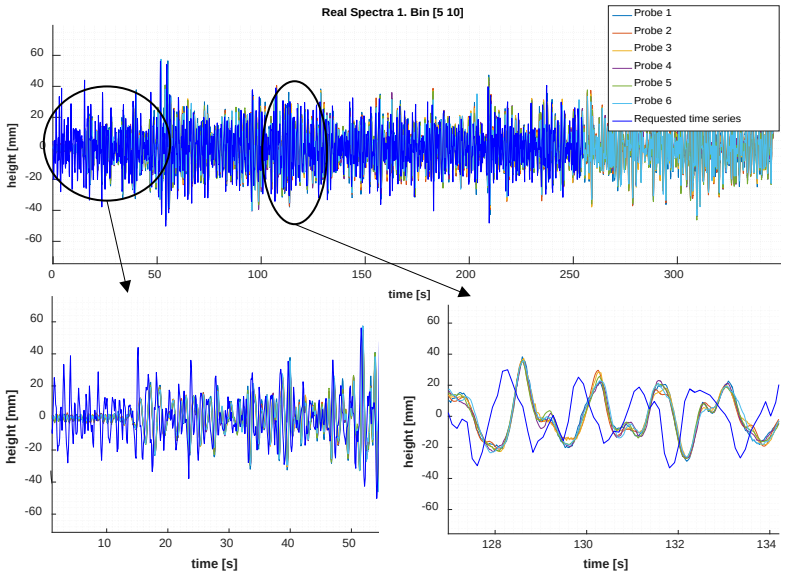


FIGURE 188: REQUESTED TIME-SERIES VS PROBE READINGS FOR TEST 042.

A sample of the probe readings and the requested time-series is shown in Figure 188. The transition period between the start of the test and the time at which the waves reach the probes can be seen in the lower left of this image. There was a delay of approximately 10 - 15 seconds between the start of the test and the waves reaching the probes, dependant on the wave period of the sea state being tested. There is a

time-lag evident in the figure on the lower right, which was corrected for in subsequent stages of the analysis.

6.4.5.2.2 Data Processing Steps

The LabVIEW data files from the tank testing were first imported from the .csv format, creating a Matlab organisational structure that allowed each probe and pressure sensor value to be easily obtained for each test. The time-series data from the tank was then de-meaned as a first step toward preparing it for comparison with the requested time-series data. This was accomplished by subtracting the overall mean of the time-series from each entry as in the equation below:

$$X_t = \sum_{i=1}^{t} (x_i - \overline{x}) \tag{6.20}$$

The data was then ready for visual inspection and analysis. The 6 wave probes were plotted against the requested time-series for each of the 93 tests that were run, encompassing the Bretschneider, Recorded Killard Point time-series and Bi-Modal sea states.

To enable proper comparison of the recorded and requested data, it was necessary to transform the data to a uniform timescale. This was accomplished using a linear interpolation routine in MATLAB. The Requested time-series data, which was sampled at a lower frequency, was up-sampled to match the LabVIEW recordings taken.

Given that there existed a transitional period during which the waves had not yet reached the wave probes/devices, it was necessary to apply a time window with lower and upper bounds to enable study of the useful area of testing in which the tank had established stable wave generation for the area of interest.

The time-series were aligned using the MATLAB “finddelay” function, which finds the correlation and the lag between two time-series using the cross-correlation between the two signals. The normalized cross-correlation is then calculated, and this allows for the removal of the time lag that is inherent between the requested and recorded values.

This process removed the phase delay which is visible in the Figure 188. As is evident in the wave probe signal, the waves are repeated after the 4 minute and 15 second input time-series. For the determination of power from the time-series, a composite dataset was constructed from the portion of the test beginning after the waves had reached the probes, and the equivalent repeated portion after the 4 minutes and 15 seconds.

Plotting the data alongside the deviation values between the requested and recorded data reveals that, after correction is performed to remove the phased delay and the transitional phase for each sea-state, the signals requested and recorded are very similar. This can be seen in Figure 189 below.

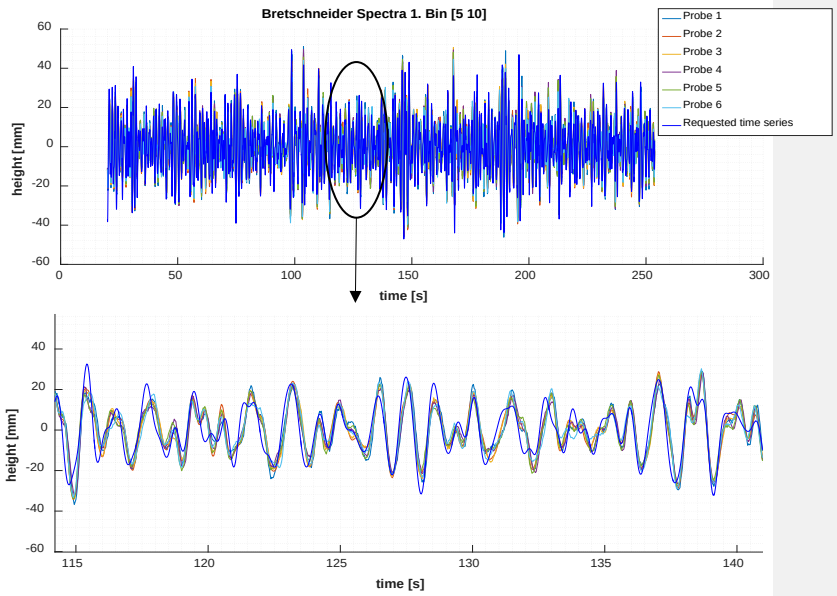


FIGURE 189: DATA FROM TEST 001 SHOWING PROBE READINGS AND REQUESTED TIME-SERIES AFTER THE TIME-SERIES HAVE BEEN ALIGNED

6.4.5.3 Statistical Analysis of Reproduction Error

Reproduction of the waves was a key element of this study. Prior to performing any detailed statistical analysis, it was necessary to ensure that the conditions which were requested were properly reproduced by the tank. The first step in analysing this was to visualise the probe readings alongside the requested time-series.

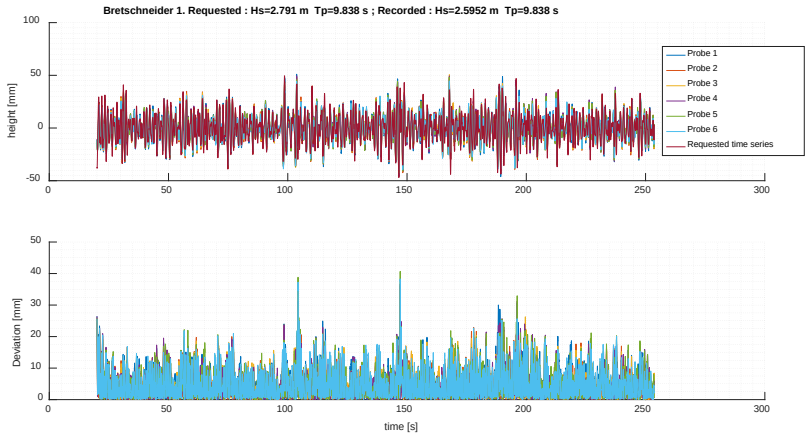


FIGURE 190: REQUESTED AND RECORDED TIME-SERIES MEASUREMENTS FOR TEST 001 / BRETSCHNEIDER SEA-STATE 1

This allowed for a visualisation of the reproduction of the waves, as well as the associated deviation from the requested condition. Visible in Figure 190 are the readings for Test 001. There are some noticeable spikes in the deviation of the recordings from the requested time-series, which tend to occur during larger, rapid, changes in wave amplitude. The average deviation is in the region of 6.0 – 7.0mm (model scale), with an overall bias of 5.9mm, indicating that the conditions produced in the tank are consistently lower than the requested conditions.

A detailed statistical analysis of the waves requested and recorded at the probes was performed to determine the precision of the tank transfer function in reproducing the required sea-state, and to determine the level of consistency, and thus interoperability between tests with equivalent conditions. A tabulated statistical error summary across all probes between requested and recorded H_s and T_p was then generated as detailed below.

6.4.5.3.1 Significant Wave Height (H_s) Comparison

Tabulated results of H_s and T_p vs requested H_s and T_p for each probe are shown below:

TABLE 82: REQUESTED HS VS. RECORDED HS - BRETSCHNEIDER WAVES

Wave Probe		1	2	3	4	5	6
Sea-State Number	*H_s Requested (m)*	***H_s Recorded (m)***					
1	2.78	2.60	2.58	2.50	2.46	2.44	2.42
2	2.82	2.63	2.59	2.54	2.48	2.49	2.45
3	2.81	2.62	2.60	2.55	2.47	2.52	2.49
4	2.95	2.75	2.72	2.67	2.58	2.65	2.64
5	3.48	3.26	3.25	3.16	3.07	3.06	3.04
6	3.95	3.74	3.69	3.62	3.51	3.54	3.51
7	3.83	3.61	3.55	3.51	3.39	3.46	3.43
8	3.54	3.32	3.28	3.25	3.16	3.22	3.21
9	4.64	4.40	4.34	4.29	4.15	4.19	4.18
10	4.86	4.61	4.57	4.50	4.39	4.44	4.43
11	4.82	4.53	4.47	4.43	4.35	4.43	4.47
12	4.72	4.45	4.39	4.35	4.28	4.37	4.43
13	5.56	5.29	5.22	5.11	4.95	4.97	5.04
14	5.95	5.66	5.61	5.52	5.38	5.45	5.51
15	5.75	5.49	5.43	5.34	5.24	5.33	5.37
16	6.86	6.47	6.44	6.32	6.13	6.18	6.25
17	6.75	6.43	6.37	6.24	6.07	6.14	6.17
18	6.74	6.47	6.39	6.29	6.10	6.18	6.23

TABLE 83: PERCENTAGE DEVIATION FROM REQUESTED H_S - BRETSCHNEIDER WAVES

Wave Probe		1	2	3	4	5	6
Sea-State Number	*H_s Requested (m)*	***% Deviation H_s Recorded from Requested***					
1	2.78	5.05%	6.01%	8.79%	10.17%	11.08%	11.57%
2	2.82	5.24%	6.40%	8.26%	10.28%	10.16%	11.58%
3	2.81	5.43%	6.16%	7.95%	10.89%	9.14%	10.00%
4	2.95	5.18%	6.36%	7.99%	11.01%	8.93%	9.15%
5	3.48	4.67%	5.13%	7.55%	10.15%	10.44%	11.16%
6	3.95	3.88%	5.19%	6.90%	9.81%	9.02%	9.96%
7	3.83	4.21%	5.71%	6.78%	9.87%	8.35%	8.88%
8	3.54	4.62%	5.71%	6.54%	9.57%	7.75%	8.01%
9	4.64	3.71%	4.94%	6.13%	9.16%	8.29%	8.67%
10	4.86	3.74%	4.71%	6.11%	8.60%	7.46%	7.78%
11	4.82	4.64%	5.85%	6.73%	8.49%	6.93%	5.94%
12	4.72	4.44%	5.68%	6.40%	8.17%	6.20%	4.99%
13	5.56	3.19%	4.64%	6.62%	9.45%	9.19%	7.83%
14	5.95	3.59%	4.60%	5.99%	8.48%	7.37%	6.26%
15	5.75	3.33%	4.32%	5.76%	7.82%	6.17%	5.43%
16	6.86	4.14%	4.81%	6.65%	9.45%	8.67%	7.56%
17	6.75	3.36%	4.37%	6.29%	8.88%	7.85%	7.32%
18	6.74	2.77%	4.02%	5.55%	8.37%	7.25%	6.42%

TABLE 84: REQUESTED HS VS. RECORDED H_S – TIME-SERIES WAVES

Wave Probe		1	2	3	4	5	6
Sea-State Number	*H_S Requested (m)*	***H_S Recorded (m)***					
1	2.78	2.59	2.54	2.46	2.43	2.46	2.43
2	2.82	2.49	2.49	2.43	2.38	2.41	2.37
3	2.81	2.69	2.66	2.59	2.56	2.61	2.56
4	2.95	2.78	2.72	2.65	2.63	2.65	2.62
5	3.48	3.26	3.25	3.15	3.11	3.12	3.10
6	3.95	3.76	3.76	3.71	3.60	3.64	3.64
7	3.83	3.55	3.46	3.44	3.32	3.40	3.36
8	3.54	3.33	3.29	3.25	3.16	3.23	3.19
9	4.64	4.38	4.24	4.20	4.02	4.13	4.05
10	4.86	4.73	4.71	4.65	4.47	4.55	4.51
11	4.82	4.80	4.66	4.60	4.47	4.53	4.55
12	4.72	4.50	4.39	4.35	4.35	4.37	4.52
13	5.56	5.12	5.03	5.01	4.80	4.84	4.85
14	5.95	5.83	5.69	5.67	5.49	5.62	5.56
15	5.75	5.74	5.65	5.58	5.46	5.51	5.53
16	6.86	6.47	6.44	6.32	6.13	6.18	6.25
17	6.75	6.43	6.37	6.24	6.07	6.14	6.17
18	6.74	6.47	6.39	6.29	6.10	6.18	6.23

TABLE 85: PERCENTAGE DEVIATION FROM REQUESTED H_s – TIME-SERIES WAVES

Wave Probe		1	2	3	4	5	6
Sea-State Number	*H_s Requested (m)*	***% Deviation H_s Recorded from Requested***					
1	2.78	7.58%	9.29%	12.45%	13.21%	12.29%	13.50%
2	2.82	12.30%	12.32%	14.30%	16.29%	15.03%	16.31%
3	2.81	4.61%	5.74%	8.43%	9.49%	7.48%	9.33%
4	2.95	6.20%	8.18%	10.59%	11.16%	10.46%	11.51%
5	3.48	6.87%	7.12%	9.92%	11.19%	10.95%	11.48%
6	3.95	5.13%	5.14%	6.42%	9.36%	8.34%	8.18%
7	3.83	7.54%	9.87%	10.35%	13.54%	11.58%	12.62%
8	3.54	6.01%	7.29%	8.19%	10.84%	8.80%	9.92%
9	4.64	6.04%	8.87%	9.74%	13.63%	11.37%	13.08%
10	4.86	2.84%	3.38%	4.65%	8.21%	6.66%	7.35%
11	4.82	0.56%	3.35%	4.75%	7.32%	6.10%	5.75%
12	4.72	4.95%	7.14%	7.98%	8.08%	7.57%	4.40%
13	5.56	8.13%	9.74%	10.14%	13.91%	13.16%	12.97%
14	5.95	2.36%	4.73%	4.91%	7.96%	5.91%	6.88%
15	5.75	0.36%	1.92%	3.16%	5.20%	4.39%	3.95%
16	6.86	8.47%	10.07%	10.75%	13.47%	12.31%	11.06%
17	6.75	3.96%	6.40%	7.47%	9.96%	7.55%	7.20%
18	6.74	9.04%	11.19%	11.44%	13.82%	11.74%	10.72%

Time-series input waves display a greater disparity in the requested vs. recorded value than for the Bretschneider wave conditions, echoing the results of the RMSE, Bias and Scatter Index error metrics.

From the above tables, it is evident that wave heights are under produced in the tank – with 5-10% deviation from the requested H_s being common across all sea-states. There is a noticeable difference in the H_s across the wave probes, with a definite trend of decreasing H_s in moving from probe 1 - 6.

With reference to the locations of the wave probes, best seen in Figure 175, this data is suggestive of a "wall effect," whereby the heights of the waves are diminished in proximity to the tank wall.

Fortunately, the probes which show the least deviation from the requested condition are probes 1, 2 and 3; which are the centre-most probes placed at the locations of the OWC devices.

Examining the replication of bi-modal sea-states, it is again evident that the tank has difficulty in correctly emulating these conditions; with the primary effect here being a dramatic lowering of the H_s in the recorded time-series.

6.4.5.3.2 Period (T_p) Comparison

TABLE 86: REQUESTED T_P VS. RECORDED T_P - BRETSCHNEIDER WAVES

Wave Probe		1	2	3	4	5	6
Sea-State Number	*T_p Requested (s)*	***T_p Recorded (s)***					
1	9.43	9.43	9.43	9.43	9.84	9.84	9.84
2	10.29	9.84	9.84	10.29	10.29	10.29	10.29
3	11.91	11.91	11.31	11.91	11.91	11.91	11.91
4	12.57	11.91	11.91	12.57	11.91	12.57	12.57
5	10.29	9.84	10.29	10.29	10.29	10.29	10.29
6	11.91	11.91	11.91	11.91	11.91	11.91	11.91
7	12.57	12.57	12.57	12.57	12.57	12.57	12.57
8	13.31	13.31	13.31	13.31	13.31	13.31	14.14
9	12.57	12.57	12.57	12.57	12.57	12.57	12.57
10	13.31	13.31	13.31	13.31	13.31	13.31	14.14
11	14.14	14.14	14.14	14.14	14.14	14.14	14.14
12	15.08	15.08	15.08	15.08	15.08	15.08	15.08
13	11.91	11.91	11.91	11.91	11.91	11.91	11.91
14	13.31	13.31	13.31	13.31	13.31	13.31	14.14
15	14.14	14.14	14.14	14.14	14.14	14.14	14.14
16	12.57	12.57	12.57	12.57	12.57	12.57	12.57
17	13.31	13.31	12.57	13.31	13.31	13.31	13.31
18	14.14	13.31	14.14	13.31	14.14	14.14	14.14

TABLE 87: PERCENTAGE DEVIATION FROM REQUESTED T_P - BRETSCHNEIDER WAVES

Wave Probe		1	2	3	4	5	6
Sea-State Number	*T_p Requested (s)*	***% Deviation T_p Recorded from Requested***					
1	9.43	0.00%	0.00%	0.00%	4.35%	4.35%	4.35%
2	10.29	4.35%	4.35%	0.00%	0.00%	0.00%	0.00%
3	11.91	0.00%	5.00%	0.00%	0.00%	0.00%	0.00%
4	12.57	5.26%	5.26%	0.00%	5.26%	0.00%	0.00%
5	10.29	4.35%	0.00%	0.00%	0.00%	0.00%	0.00%
6	11.91	0.00%	0.00%	0.00%	0.00%	0.00%	0.00%
7	12.57	0.00%	0.00%	0.00%	0.00%	0.00%	0.00%
8	13.31	0.00%	0.00%	0.00%	0.00%	0.00%	6.25%
9	12.57	0.00%	0.00%	0.00%	0.00%	0.00%	0.00%
10	13.31	0.00%	0.00%	0.00%	0.00%	0.00%	6.25%
11	14.14	0.00%	0.00%	0.00%	0.00%	0.00%	0.00%
12	15.08	0.00%	0.00%	0.00%	0.00%	0.00%	0.00%
13	11.91	0.00%	0.00%	0.00%	0.00%	0.00%	0.00%
14	13.31	0.00%	0.00%	0.00%	0.00%	0.00%	6.25%
15	14.14	0.00%	0.00%	0.00%	0.00%	0.00%	0.00%
16	12.57	0.00%	0.00%	0.00%	0.00%	0.00%	0.00%
17	13.31	0.00%	5.56%	0.00%	0.00%	0.00%	0.00%
18	14.14	5.88%	0.00%	5.88%	0.00%	0.00%	0.00%

TABLE 88: REQUESTED T_P VS. RECORDED T_P – TIME-SERIES WAVES

Wave Probe		1	2	3	4	5	6
Sea-State Number	*T_p Requested (s)*	***T_p Recorded (s)***					
1	10.00	10.77	10.77	10.77	10.77	11.31	10.77
2	10.53	10.77	10.77	10.77	10.77	10.77	10.77
3	12.12	11.31	11.31	11.31	11.31	11.91	11.31
4	12.70	11.91	11.91	11.91	11.91	11.91	11.91
5	10.67	10.77	10.77	11.31	11.31	11.31	11.31
6	12.31	12.57	11.91	12.57	12.57	12.57	12.57
7	13.33	12.57	12.57	12.57	12.57	12.57	12.57
8	14.29	12.57	12.57	12.57	12.57	12.57	12.57
9	13.33	12.57	11.91	12.57	11.91	12.57	12.57
10	14.29	14.14	14.14	14.14	14.14	14.14	14.14
11	14.81	14.14	14.14	14.14	14.14	14.14	14.14
12	16.00	15.08	15.08	15.08	15.08	15.08	15.08
13	12.50	11.91	11.91	11.91	11.91	11.91	11.91
14	14.29	13.31	13.31	13.31	13.31	13.31	13.31
15	15.09	14.14	14.14	14.14	14.14	14.14	14.14
16	13.11	12.57	12.57	12.57	12.57	12.57	12.57
17	13.56	13.31	13.31	13.31	13.31	13.31	13.31
18	14.55	13.31	13.31	13.31	13.31	13.31	13.31

TABLE 89: PERCENTAGE DEVIATION FROM REQUESTED T_P – TIME-SERIES WAVES

Wave Probe		1	2	3	4	5	6
Sea-State Number	*T_p Requested (s)*	***% Deviation T_p Recorded from Requested***					
1	10.00	7.75%	7.75%	7.75%	7.75%	13.14%	7.75%
2	10.53	2.36%	2.36%	2.36%	2.36%	2.36%	2.36%
3	12.12	6.66%	6.66%	6.66%	6.66%	1.75%	6.66%
4	12.70	6.22%	6.22%	6.22%	6.22%	6.22%	6.22%
5	10.67	1.02%	1.02%	6.07%	6.07%	6.07%	6.07%
6	12.31	2.14%	3.24%	2.14%	2.14%	2.14%	2.14%
7	13.33	5.72%	5.72%	5.72%	5.72%	5.72%	5.72%
8	14.29	12.00%	12.00%	12.00%	12.00%	12.00%	12.00%
9	13.33	5.72%	10.68%	5.72%	10.68%	5.72%	5.72%
10	14.29	1.01%	1.01%	1.01%	1.01%	1.01%	1.01%
11	14.81	4.54%	4.54%	4.54%	4.54%	4.54%	4.54%
12	16.00	5.72%	5.72%	5.72%	5.72%	5.72%	5.72%
13	12.50	4.73%	4.73%	4.73%	4.73%	4.73%	4.73%
14	14.29	6.83%	6.83%	6.83%	6.83%	6.83%	6.83%
15	15.09	6.31%	6.31%	6.31%	6.31%	6.31%	6.31%
16	13.11	4.15%	4.15%	4.15%	4.15%	4.15%	4.15%
17	13.56	1.84%	1.84%	1.84%	1.84%	1.84%	1.84%
18	14.55	8.49%	8.49%	8.49%	8.49%	8.49%	8.49%

Time-series input waves display a greater disparity in the requested vs. recorded value than for the Bretschneider wave conditions, echoing the results of the H_s analysis. For Bretschneider sea-states, the error in T_p is typically 0%, with a small number of results showing a disparity between requested and recorded T_p of up to 6%, these being predominantly at lower T_p values.

6.4.5.3.3 RMSE Error

The Root Mean Square Error (RMSE) between requested and recorded time-series was determined for each probe, during each sea-state, as follows:

$$RMSE = \sqrt{\sum_{i}^{n} \frac{1}{n}(x_i - y_i)^2} \qquad (6.21)$$

TABLE 90: RMSE H_s REQUESTED VS. RECORDED - BRETSCHNEIDER SEA-STATES

Sea-State Number	*Metric: Root Mean Square Error (mm)*					
Wave Probe	1	2	3	4	5	6
1	7.53	7.12	7.29	7.40	7.79	7.57
2	6.35	6.77	6.34	6.43	7.25	6.64
3	4.27	4.84	4.33	4.43	5.26	4.74
4	3.76	4.20	3.71	4.04	4.65	4.82
5	8.11	7.60	8.00	7.95	8.35	8.18
6	7.30	7.67	8.26	8.15	8.58	8.74
7	6.18	6.68	6.06	6.26	6.61	6.67
8	4.35	4.90	4.25	4.58	5.20	5.44
9	8.08	8.61	9.21	9.33	9.54	9.50
10	7.84	8.47	7.77	8.08	9.23	8.40
11	8.70	9.42	8.60	9.40	9.08	8.98
12	6.48	7.34	6.48	6.96	7.59	6.78
13	13.24	13.82	13.19	13.39	13.52	13.47
14	10.96	10.55	10.92	11.36	11.20	11.21
15	8.76	9.45	8.52	8.87	8.37	8.49
16	17.09	18.30	17.73	17.70	17.39	17.44
17	16.49	17.35	16.87	17.28	17.00	17.04
18	13.36	14.15	13.56	14.43	13.92	13.95

The RMSE values for requested vs. recorded data across all Bretschneider representations of the sea-states are low, and are reflective of accurate reproduction of the wave conditions. The RMSE values tend to increase with increasing wave height, while sea-states with larger T_p values tend to have lower RMSE values. RMSE values are consistent across the 6 wave probes, indicating a high degree of consistency in the accuracy of wave reproduction across the spatial domain.

TABLE 91: RMSE REQUESTED VS. RECORDED - REAL WAVES

Sea-State Number	*Metric: Root Mean Square Error (mm)*					
Wave Probe	*1*	*2*	*3*	*4*	*5*	*6*
1	9.61	9.39	9.23	9.99	10.28	9.43
2	7.56	7.97	7.72	7.21	7.74	7.44
3	8.02	8.31	8.13	7.74	8.95	8.00
4	7.68	7.66	7.65	7.41	8.51	7.76
5	8.94	8.92	8.74	8.57	9.95	9.59
6	10.68	10.23	10.32	10.57	11.17	10.48
7	7.86	8.24	7.98	8.74	9.01	8.10
8	9.16	9.02	8.98	9.34	9.33	8.53
9	12.69	12.72	12.39	13.20	13.55	12.65
10	13.68	14.23	13.52	13.66	13.60	13.54
11	10.37	10.83	10.28	10.35	10.49	10.17
12	9.72	8.54	9.27	10.45	8.60	9.38
13	14.19	14.96	14.72	14.34	14.52	14.50
14	16.63	17.43	17.43	17.60	17.41	16.71
15	14.62	15.40	14.67	14.96	14.59	14.86
16	20.21	20.83	20.87	20.93	20.13	20.43
17	19.87	20.80	20.34	20.69	20.12	20.83
18	20.72	21.77	21.09	21.38	20.73	20.80

The RMSE values when reproducing real time-series data were higher, but remained indicative of reasonable accuracy. Again, the RMSE values for H_s increased with increasing wave amplitudes and showed a slight decrease for larger values of T_p.

6.4.5.3.4 R Correlation Error

Next, the R correlation (R Corr) between requested and recorded time-series was determined for each probe, during each sea-state, as follows:

$$R = \frac{n\sum xy - (\sum x)(\sum y)}{\sqrt{n(\sum x^2) - (\sum x)^2}\sqrt{n(\sum y^2) - (\sum y)^2}} \qquad (6.22)$$

With x being the recorded data point and y the requested data.

This measures the strength and direction of the linear relationship between the two variables, with a value of 1 representing a perfect positive fit, and a value of 0 representing no correlation.

TABLE 92: R^2 CORRELATION COEFFICIENT FOR REQUESTED VS RECORDED TIME-SERIES - BRETSCHNEIDER SEA-STATES

Sea-State Number	***Metric: R^2Correlation***					
Wave Probe	1	2	3	4	5	6
1	0.85	0.86	0.85	0.85	0.83	0.84
2	0.89	0.88	0.89	0.89	0.86	0.88
3	0.95	0.94	0.95	0.95	0.93	0.94
4	0.97	0.96	0.97	0.96	0.95	0.95
5	0.89	0.90	0.89	0.89	0.88	0.88
6	0.93	0.92	0.91	0.91	0.90	0.90
7	0.95	0.94	0.95	0.95	0.94	0.94
8	0.97	0.96	0.97	0.97	0.96	0.95
9	0.94	0.93	0.92	0.92	0.91	0.91
10	0.95	0.94	0.95	0.94	0.93	0.94
11	0.89	0.87	0.88	0.88	0.88	0.88
12	0.96	0.95	0.96	0.95	0.95	0.96
13	0.89	0.87	0.88	0.88	0.88	0.88
14	0.93	0.94	0.93	0.92	0.93	0.93
15	0.95	0.94	0.95	0.95	0.96	0.96
16	0.87	0.85	0.86	0.86	0.86	0.86
17	0.88	0.86	0.87	0.86	0.87	0.87
18	0.92	0.91	0.92	0.90	0.91	0.91

The tank is capable of accurately producing the required wave conditions when generating Bretschneider waves. The R^2 correlation tends to increase with increasing T_p, while the values tend to be very consistent across wave-probes – indicative of the high degree of correlation in the measurements taken across wave-probes. This can also be seen in the RMSE results given in Table 90.

TABLE 93: R^2 CORRELATION COEFFICIENT FOR REQUESTED VS RECORDED TIME-SERIES - REAL WAVES

Sea-State Number	***Metric: R^2Correlation***					
Wave Probe	1	2	3	4	5	6
1	0.74	0.75	0.75	0.71	0.69	0.74
2	0.84	0.82	0.83	0.85	0.83	0.84
3	0.82	0.81	0.82	0.83	0.78	0.82
4	0.86	0.86	0.86	0.87	0.83	0.85
5	0.86	0.86	0.86	0.87	0.82	0.84
6	0.85	0.86	0.86	0.85	0.83	0.85
7	0.91	0.90	0.91	0.88	0.88	0.90
8	0.86	0.86	0.86	0.85	0.85	0.88
9	0.85	0.84	0.85	0.83	0.82	0.84
10	0.84	0.83	0.84	0.84	0.84	0.84
11	0.90	0.89	0.90	0.90	0.90	0.90
12	0.92	0.93	0.92	0.90	0.93	0.92
13	0.86	0.84	0.85	0.85	0.85	0.85
14	0.85	0.83	0.83	0.82	0.83	0.84
15	0.87	0.86	0.87	0.86	0.87	0.86
16	0.81	0.80	0.80	0.79	0.81	0.80
17	0.83	0.81	0.81	0.80	0.82	0.80
18	0.81	0.78	0.79	0.79	0.80	0.80

6.4.5.3.5 Bias Error

TABLE 94: H_S BIAS REQUESTED VS. RECORDED – BRETSCHNEIDER SEA-STATES

Sea-State Number	***Metric: Bias (mm)***					
Wave Probe	1	2	3	4	5	6
1	5.90	5.60	5.75	5.79	6.12	5.98
2	4.90	5.34	4.96	4.98	5.65	5.21
3	3.35	3.87	3.43	3.48	4.18	3.73
4	2.97	3.32	2.92	3.20	3.70	3.83
5	6.33	5.87	6.21	6.16	6.43	6.32
6	5.61	6.02	6.51	6.35	6.69	6.89
7	4.88	5.30	4.73	4.92	5.12	5.19
8	3.50	3.90	3.37	3.63	4.16	4.33
9	6.26	6.71	7.17	7.33	7.44	7.42
10	6.17	6.62	6.04	6.28	7.33	6.57
11	6.93	7.57	6.88	7.50	7.22	7.16
12	5.16	5.75	5.07	5.49	6.07	5.36
13	10.31	10.85	10.19	10.39	10.47	10.41
14	8.65	8.14	8.55	8.85	8.77	8.72
15	6.91	7.41	6.67	6.91	6.51	6.69
16	13.39	14.36	13.80	13.75	13.58	13.59
17	13.05	13.69	13.19	13.62	13.40	13.46
18	10.58	11.22	10.66	11.32	10.95	10.91

TABLE 95:H_s BIAS REQUESTED VS. RECORDED - TIME-SERIES SEA-STATES

Sea-State Number	*Metric: Bias (mm)*					
Wave Probe	1	2	3	4	5	6
1	7.56	7.43	7.29	7.91	8.16	7.43
2	5.90	6.20	5.98	5.63	5.95	5.78
3	6.34	6.59	6.42	6.15	7.12	6.31
4	5.98	6.01	6.00	5.76	6.71	6.09
5	7.05	7.05	6.94	6.72	7.94	7.60
6	8.50	8.10	8.20	8.41	8.89	8.29
7	6.19	6.56	6.30	6.92	7.15	6.39
8	7.20	7.07	7.04	7.38	7.38	6.68
9	10.08	10.10	9.84	10.54	10.84	10.12
10	10.88	11.30	10.71	10.76	10.79	10.76
11	8.17	8.61	8.12	8.15	8.27	8.10
12	7.74	6.80	7.40	8.31	6.88	7.51
13	10.81	11.42	11.12	10.84	10.97	10.98
14	13.04	13.69	13.80	13.92	13.85	13.14
15	11.67	12.28	11.63	11.90	11.64	11.80
16	15.96	16.27	16.31	16.27	15.62	15.84
17	15.76	16.57	16.18	16.43	15.96	16.49
18	16.14	16.80	16.26	16.52	16.15	16.13

Overall, the bias error for H_s mimics the results displayed by the Root Mean Square error examination, with Bretschneider waves being reproduced most accurately, and Bi-Modal sea-states being reproduced poorly.

6.4.5.3.6 Scatter Index Error

Scatter Index was used as a means of giving a normalised metric of the RMSE error relative to the range of the values.

$$SI = \frac{RMSE}{(X_{max} - X_{min})} \tag{6.23}$$

TABLE 96: H_S SCATTER INDEX REQUESTED VS. RECORDED – BRETSCHNEIDER SEA-STATES

Sea-State Number	***Metric: Scatter Index***					
Wave Probe	1	2	3	4	5	6
1	0.08	0.08	0.08	0.08	0.09	0.09
2	0.06	0.07	0.07	0.07	0.08	0.07
3	0.04	0.05	0.05	0.05	0.06	0.05
4	0.04	0.04	0.04	0.04	0.05	0.05
5	0.06	0.06	0.07	0.07	0.07	0.07
6	0.05	0.05	0.06	0.06	0.06	0.07
7	0.04	0.05	0.05	0.05	0.05	0.06
8	0.04	0.04	0.04	0.04	0.05	0.05
9	0.05	0.05	0.06	0.06	0.06	0.07
10	0.05	0.05	0.05	0.05	0.06	0.05
11	0.05	0.06	0.05	0.06	0.06	0.06
12	0.04	0.05	0.04	0.05	0.05	0.04
13	0.06	0.07	0.07	0.07	0.07	0.07
14	0.05	0.05	0.06	0.06	0.06	0.06
15	0.04	0.05	0.04	0.05	0.04	0.05
16	0.07	0.08	0.08	0.08	0.08	0.08
17	0.07	0.07	0.07	0.08	0.08	0.08
18	0.06	0.06	0.05	0.06	0.06	0.06

TABLE 97:H_s SCATTER INDEX REQUESTED VS. RECORDED - TIME-SERIES SEA-STATES

Sea-State Number	*Metric: Scatter Index*					
Wave Probe	1	2	3	4	5	6
1	0.10	0.09	0.10	0.10	0.11	0.09
2	0.09	0.09	0.09	0.09	0.10	0.09
3	0.08	0.09	0.09	0.09	0.10	0.08
4	0.07	0.07	0.08	0.07	0.09	0.07
5	0.08	0.08	0.08	0.08	0.09	0.09
6	0.08	0.08	0.08	0.08	0.09	0.08
7	0.06	0.06	0.06	0.07	0.07	0.07
8	0.08	0.08	0.07	0.08	0.08	0.07
9	0.08	0.08	0.08	0.09	0.09	0.08
10	0.10	0.10	0.09	0.10	0.10	0.10
11	0.05	0.06	0.06	0.06	0.06	0.06
12	0.06	0.05	0.06	0.07	0.06	0.06
13	0.07	0.07	0.07	0.07	0.07	0.07
14	0.08	0.08	0.08	0.09	0.09	0.08
15	0.07	0.08	0.07	0.08	0.08	0.08
16	0.09	0.09	0.09	0.10	0.09	0.09
17	0.10	0.10	0.10	0.10	0.10	0.10
18	0.08	0.09	0.09	0.09	0.08	0.08

6.4.5.3.7 Spectral Shape Reproduction

The overall spectral shape reproduction was also examined in addition to the summary spectral parameters to provide a more nuanced look at the ability of the Deep Ocean Basin to produce the requested conditions.

Shown below is a sample of the spectral shape and energy distribution for the requested vs recorded time-series. The plot shows the spectral energy density for the time-series wave, the time-series wave as it was reproduced in the tank, the Bretschneider representation of the time-series (equivalent H_s and T_p) and the Bretschneider representation as it was produced in the tank.

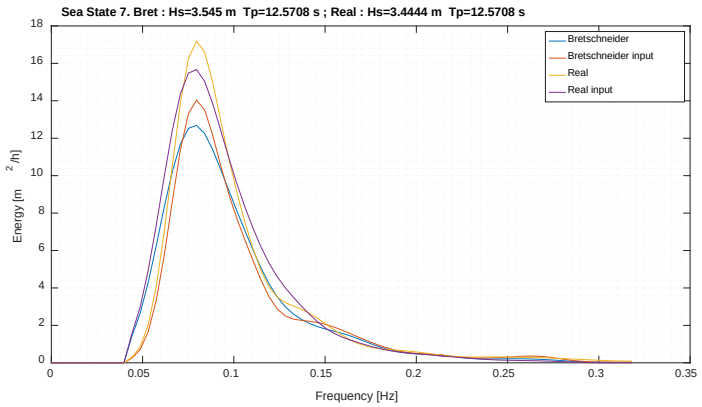


FIGURE 191: WAVE SPECTRAL DENSITY DISTRIBUTION COMPARISON FOR REQUESTED AND RECORDED BRETSCHNEIDER AND TIME-SERIES CONDITIONS

The Bretschneider waves produced by the Deep Ocean Basin carry more energy in the lower portion of the frequency domain, while the peak of spectral energy is "rounded," producing a lower peak amplitude across a marginally wider frequency domain.

The opposite is seen to occur for the real time-series. The spectral energy distribution shows a reduction in the energy at lower frequencies, while the peak is enhanced and carries more energy than the input file.

6.4.5.4 Spectral Analysis of Requested vs. Recorded Data

A theoretical examination of the impact of spectral shape was conducted in Section 6.3.4, and here an equivalent study has been conducted for the same sea-state conditions as produced during tank testing. Figure 192 - Figure 196 display five distinct sea-states, representing the most commonly occurring and energy contributing sea-states at the test site. The Real and Bretschneider Record and Input value spectra are given for each Figure.

(N.B.) the conditions given for the tank testing have been converted back to full scale figures prior to analysis to simplify the comparison between the requested time-series and the values.

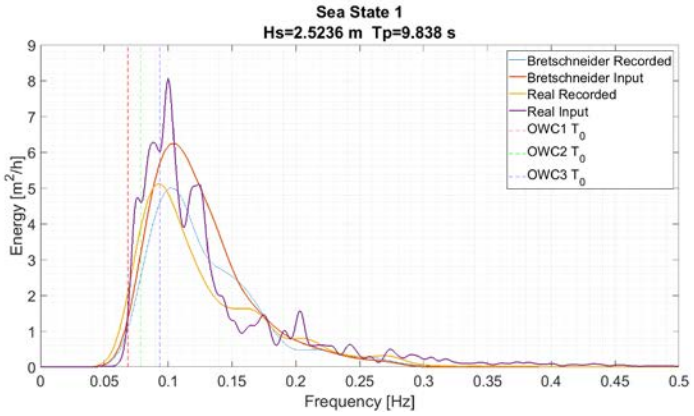


FIGURE 192: COMPARISON OF INPUT AND RECORDED SPECTRA FOR BRETSCHNEIDER AND REAL SPECTRA – SEA STATE 1: 2.5-3M HS, 9.5-10.5S TP (REQUESTED)

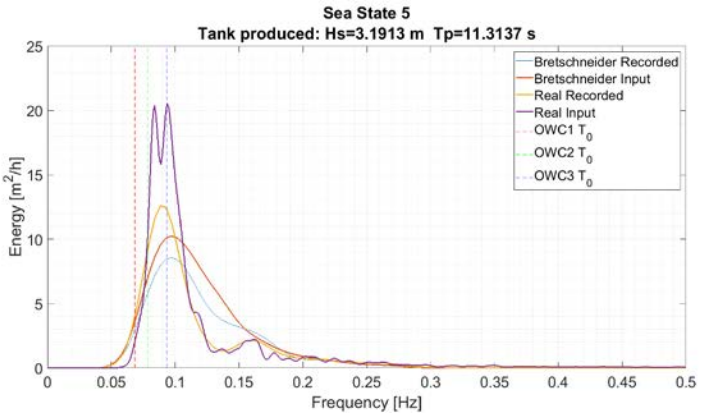


FIGURE 193: COMPARISON OF INPUT AND RECORDED SPECTRA FOR BRETSCHNEIDER AND REAL SPECTRA – SEA STATE 5: 3.5-4M HS, 10.5-11.5S TP (REQUESTED)

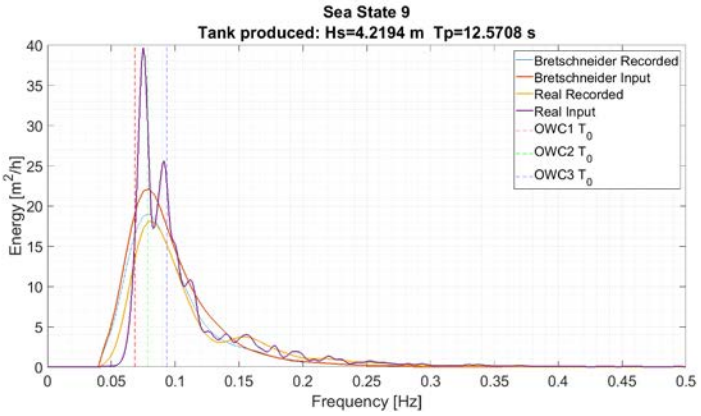


FIGURE 194: COMPARISON OF INPUT AND RECORDED SPECTRA FOR BRETSCHNEIDER AND REAL SPECTRA – SEA STATE 9: 4.5-5M HS, 12.5-13.5S TP (REQUESTED)

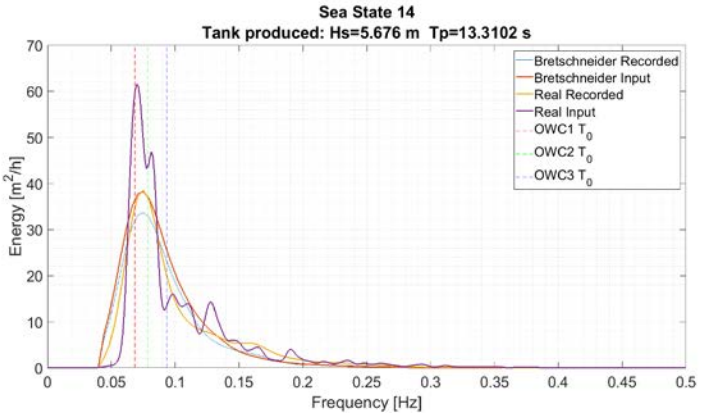


FIGURE 195: COMPARISON OF INPUT AND RECORDED SPECTRA FOR BRETSCHNEIDER AND REAL SPECTRA – SEA STATE 14: 5.5-6M HS, 12.5-13.5S TP (REQUESTED)

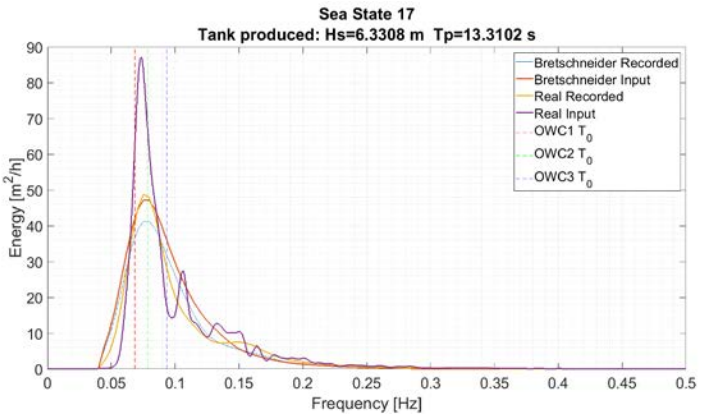


FIGURE 196: COMPARISON OF INPUT AND RECORDED SPECTRA FOR BRETSCHNEIDER AND REAL SPECTRA – SEA STATE 17: 6.5-7M HS, 12.5-13.5S TP (REQUESTED)

It was found that the test site spectral conditions had a more pronounced peak than the Bretschneider Spectrum, with spectral energy skewed toward lower frequencies, resulting in characteristically different device response and resultant energy production during tank testing. These power production results are summarised in Table 98.

6.4.5.5 Power Production

The power production from the devices was determined for each sea-state, enabling the comparison of both Bretschneider conditions and the real time-series data. The two wave conditions are directly compared by generating the scaled time-series equivalents in the deep ocean basin.

Using the Njord Wave Synthesis program, a random-seeded time-domain representation of the Bretschneider Spectrum is generated (Figure 197), and it a test is carried out using both Bretschneider and time-series records. For all tests, the wave probe and pressure readings have been recorded, and these are subsequently used to generate a power production estimate based on each sea-state.

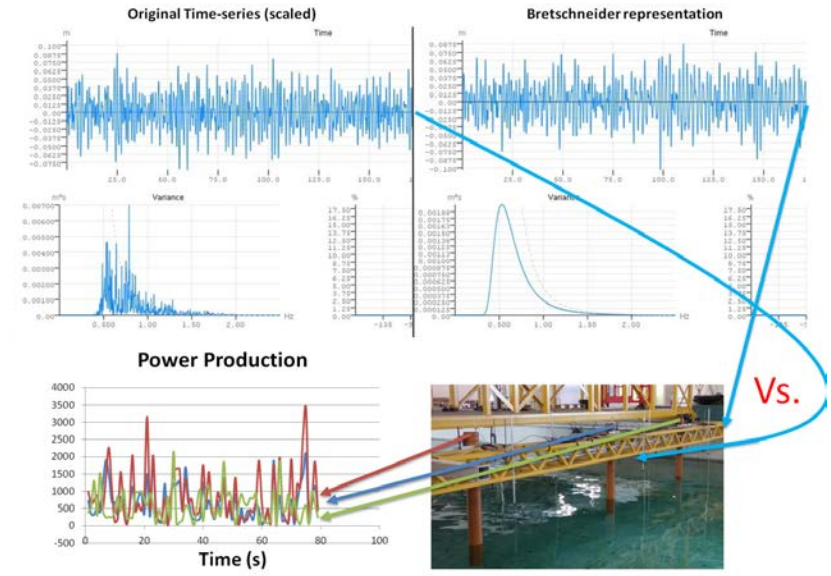


FIGURE 197: COMPARATIVE TESTING OF BRETSCHNEIDER AND RECORDED TIME-SERIES RECORDS TO DETERMINE POWER PRODUCTION VARIATION

The power production information for each of the three devices enables an analysis of the effect the change in distribution has for the case where the device's resonant period is close to the peak period of the spectral energy distribution, and the alternate case where the peak energy production happens at a frequency outside the natural response frequency of the device.

6.4.5.5.1 Methods of Power Production Determination.

Two methods were used to determine power production for each sea-state that was assessed. The primary method used was to determine the pressure-flow relationship for the orifice installed on the devices, and use this relationship to determine the power output using equation (**6.18**) in Section 6.4.4.3. Using the determination for volume flow equation (**6.16**), the power output of each device was determined.

A second method of power production estimation was also used. Using the same equation for the determination of volume flow as in (**6.16**):

Making the simplifying assumption that the water surface elevation inside the devices mirrored that of the water level outside the pipes, and observing from the

wave calibration results that the coefficient of correlation between probe 3 and probes 1/5/4 is always greater than 0.95, it was reckoned that the water surface elevation recorded at probe 3 was representative of the water surface elevation at each device. This allowed for a simplified determination of the power captured by the devices. Below is the tabulated result of the total power production in MWh, corresponding to each sea-state.

TABLE 98: DEVICE POWER PRODUCTION (MEGAWATTHRS) FOR REAL AND BRETSCHNEIDER WAVES (CALCULATED AT FULL-SCALE)

	Req. Waves		Bretschneider Waves					Real Waves					Difference (%)				
	H_s (m)	T_p (s)	H_s (m)	T_p (s)	1m	.75 m	.5m	H_s (m)	T_p (s)	1m	.75 m	.5m	H_s (m)	T_p (s)	1m	.75m	.5m
1	2.78	9.43	2.52	9.84	38	86	176	2.53	10.77	63	122	197	0.13 %	8.70%	40.67%	29.47%	10.49%
2	2.82	10.29	2.62	10.29	58	110	199	2.48	10.77	59	115	205	5.66 %	4.55%	1.98%	3.95%	2.79%
3	2.81	11.91	2.59	11.91	108	136	205	2.64	11.31	77	148	231	1.74 %	5.26%	-41.06%	8.30%	11.22%
4	2.95	12.57	2.72	12.57	138	164	230	2.68	11.91	105	175	257	1.13 %	5.56%	-30.95%	6.60%	10.51%
5	3.48	10.29	3.19	10.29	102	179	316	3.19	11.31	109	231	393	0.07 %	9.09%	6.49%	22.57%	19.70%
6	3.95	11.91	3.65	11.91	252	319	472	3.74	12.57	299	414	563	2.26 %	5.26%	15.60%	22.95%	16.23%
7	3.83	12.57	3.55	12.57	278	315	442	3.44	12.57	241	335	439	2.92 %	0.00%	-15.48%	6.03%	-0.69%
8	3.54	13.31	3.26	13.31	227	251	337	3.27	12.57	246	300	404	0.50 %	5.88%	7.82%	16.54%	16.37%
9	4.64	12.57	4.31	12.57	459	540	753	4.22	12.57	375	524	737	2.08 %	0.00%	-22.44%	-3.07%	-2.15%
10	4.86	13.31	4.53	13.31	527	610	813	4.66	14.14	672	781	906	2.79 %	5.88%	21.52%	21.80%	10.24%
11	4.82	14.14	4.46	14.14	529	595	769	4.62	14.14	653	783	942	3.56 %	0.00%	19.09%	23.97%	18.39%
12	4.72	15.08	4.35	15.09	493	535	674	4.40	15.08	600	632	763	1.23 %	0.00%	17.89%	15.36%	11.64%
13	5.56	11.91	5.24	11.91	577	705	1038	5.03	11.91	477	789	1159	4.17 %	0.00%	-20.92%	10.67%	10.44%
14	5.95	13.31	5.60	13.31	884	1019	1351	5.68	13.31	930	1157	1483	1.37 %	0.00%	4.93%	11.97%	8.92%
15	5.75	14.14	5.39	14.14	838	951	1240	5.55	14.14	1038	1209	1450	2.87 %	0.00%	19.30%	21.33%	14.46%
16	6.86	12.57	6.45	12.57	1226	1443	2029	6.16	12.57	988	1342	1792	4.73 %	0.00%	-24.05%	-7.46%	-13.22%
17	6.75	13.31	6.33	12.57	1304	1519	2023	6.33	13.31	1213	1555	2062	0.04 %	5.56%	-7.43%	2.30%	1.86%
18	6.74	14.14	6.27	13.31	1346	1552	2008	6.01	13.31	1224	1472	1906	4.48 %	0.00%	-9.95%	-5.41%	-5.32%

Table 98 contains a large amount of information on the power production of each device for a multitude of different sea-states. A number of findings are immediately obvious:

- The submerged depth has a large effect on the power production of devices.
- The 0.5m device produces the most power across all sea-states.
- There is a significant power production difference between the Bretschneider and real waves.

- The average power production difference is 18.2% for the 1m device, 13.32% for 0.75m device and 10.26% for the 0.5m device (uni-modal sea-states).
- This indicates that the difference in power production between the theoretical and real sea-state representations is enhanced when the device is operating further from its point of optimal power production (and resonant frequency).
- For the bi-modal sea-states, there was a large difference in the H_s and T_p of the waves produced versus the waves requested, and this invalidates the applicability of the results to a large extent. These results are further addressed in Appendix A

6.5 Addressing Spectral Shape Variation

This section will examine how spectral shape variation can be assessed and addressed in practical terms. It will first detail a proposed methodology for the modification of standard spectral shapes in a fashion that offers the consistency and familiarity of these established shapes, while enhancing the statistical fit that these spectra have with the prevailing conditions at the site. Given the widespread, and often inaccurate, use of WPRs it is useful to move toward taking a spectral approach which retains a far greater amount of information on the characteristics of the sea-state in question.

6.5.1 Modification of Standard Spectral Shapes

This section deals with the modification of standard spectral shapes to provide a more accurate reflection of the available resource, with beneficial effects on both resource assessment and device testing. This approach to modifying standard spectral shapes will offer a method for improving accuracy; while recognising that there is clear value in adopting a methodology that closely follows the industry standard approach, which is widely accepted and reasonably applicable to a wide variety of sea-states, particularly with the outlined modifications.

6.5.1.1 Bretschneider Spectrum

At the Killard Point site, the Bretschneider Spectrum does not accurately fit the occurring conditions. It was found that the wave energy period T_e, on average, was overestimated when using the Bretschneider Spectrum. Therefore, the following

experiment was devised to create a spectrum which better represents the conditions at the site. As well as informing an accurate measure of the extractable energy available at the site, this work will later drive the generation of waves for testing the power take-off system of the device to be deployed at the site, and thus it is crucial that it accurately represents the conditions and the achievable power production.

The Bretschneider Equation was used as the basis function, with its parameters adjusted iteratively to achieve an improved fit to the real conditions at the physical location. The difference was first qualitatively assessed, to determine the likely impact that manipulation of each parameter would have, and the difference this would make to power production, Wave Period, and estimation of H_{m0}. The modified Bretschneider Spectra were then iteratively generated and the difference between these and the average spectra from time-series records assessed by evaluation the R_{corr} (a measure of the linear dependence of two random variables) and R^2 values between the respective spectra.

The spectra had long tails, mostly devoid of significant energy that would not be sufficient to elicit a major device response, and that these caused erroneously high (optimistic) values of $R^2$and Root Mean Square (RMSE). As a result, a methodology was devised to consider these Rcorr and R^2 values only in the energetic portion of the spectra. As an initial filter, the correlation was not considered in areas of the spectrum containing less than 10% of the peak energy in the spectrum. This gives results that are consistent with the method used by (Sakhare and Deo, 2009), but give greater flexibility than defining a stricter frequency limit. This approach proved sufficient to eliminate the undue influence of the tail on accuracy statistics, while maintaining the ability of the search routine to determine the best fitting spectrum.

The Bretschneider Spectrum, a generalised Pierson-Moskowitz Spectrum, is defined as follows:

$$S(\omega) = \frac{5}{16}\frac{\omega_m^4}{\omega^5}H_{\frac{1}{3}}^2 e^{-\frac{M\omega_m^4}{N\omega^4}} \tag{6.24}$$

$$S(f) = Af^{-5}\exp(-Bf^{-4}) \tag{6.25}$$

$$B = \left(\frac{0.751}{T_{av}}\right)^4 \tag{6.26}$$

$$A = B\frac{{H_{m0}}^2}{4} \tag{6.27}$$

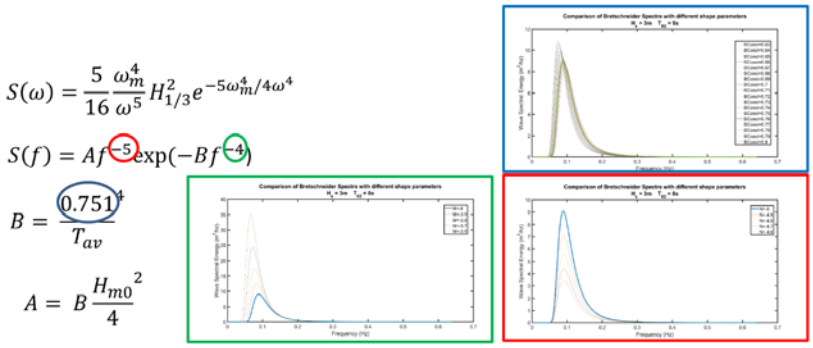


FIGURE 198: BRETSCHNEIDER SPECTRUM EQUATION NOTATION AND SHAPE AFFECTING PARAMETERS HIGHLIGHTED

The standard spectral shapes using the default parameters, as well as with a set of modified B constant, M and N parameters are shown below, with the standard shape highlighted by the lines of increased thickness.

The modified spectral shapes are generated first based on a selected H_{m0} and T_{02} value, which is then altered by modifying the exponents and constant values in the Bretschneider equation.

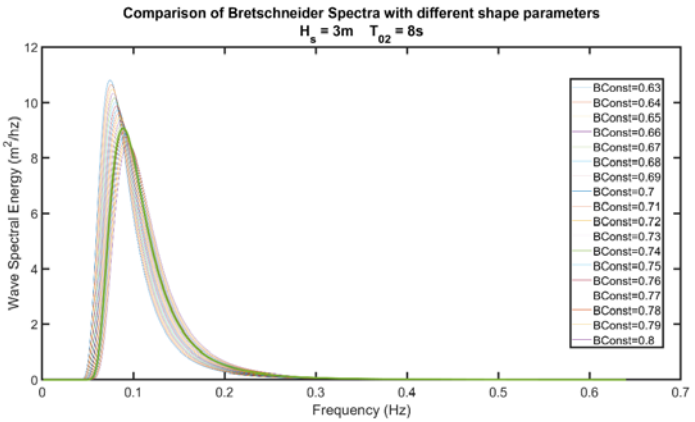


FIGURE 199: BRETSCHNEIDER SPECTRA WITH CONSTANT VALUES IN B PARAMETER FROM 0.63 TO 0.8 (STANDARD VALUE 0.751)

Altering the constant value in the "B" term of the Bretschneider Spectrum is seen to have a significant impact on the shape and distribution of the spectrum. Decreasing the value of the constant in the B equation ($B = \left(\frac{\mathbf{0.751}}{\boldsymbol{T_{av}}}\right)^4$) shifts the peak of the spectral amplitude toward the lower frequencies, and increases the maximum amplitude, while the energy contained in the high frequency tail is reduced. Increasing the value of the constant from the default value was found to reduce the maximum amplitude, shifting the energy in the spectra toward the higher frequency components.

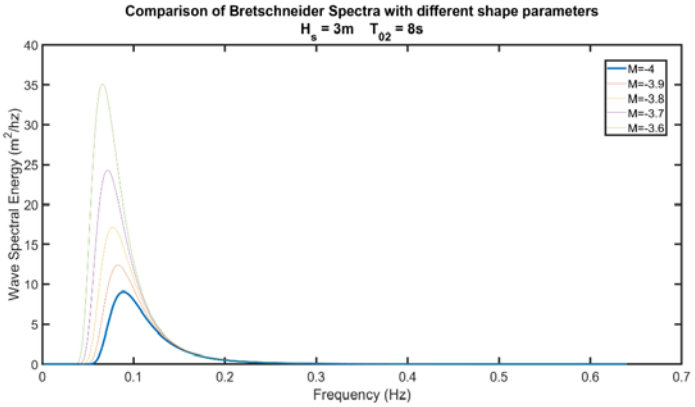


FIGURE 200: BRETSCHNEIDER SPECTRA WITH M VALUES -3.6 TO -4 (STANDARD VALUE -4)

Altering the first exponent on the frequency component in the Bretschneider Spectrum has a pronounced effect on the overall energy, maximum amplitude, shape and peak period. Decreasing the value of M, even fractionally, markedly increases the maximum Wave Spectral Energy, with the spectrum becoming increasingly peaked, and predominantly enhancing the energy contained in the lower frequency components.

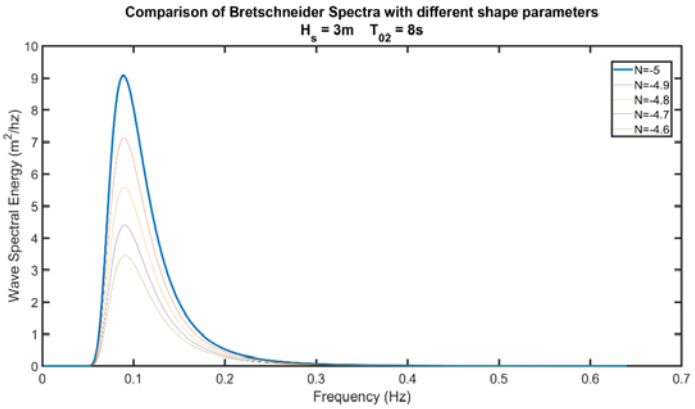


FIGURE 201: BRETSCHNEIDER SPECTRA WITH N VALUES -4.6 TO -5 (STANDARD VALUE -5)

Altering the second frequency exponent, N, has the reverse effect to the M exponent on the overall energy in the spectrum. Decreasing N rapidly decreases the energy and peaked-ness of the spectrum. With alteration of the N exponent, however, the peak frequency of the spectrum is not affected.

TABLE 99: SUMMARISED EFFECT OF ALTERING BRETSCHNEIDER PARAMETERS

Parameter Altered	Description	Direction (+/-)	Effect
B Constant (Also alters A)	Constant modifying period component – and H_{av} component by association	-	Peak Spectral energy increases and moves toward lower frequency component (shifted left)
M (First Frequency Exponent)	Generalised order applied to first frequency term in equation	+	Peak Spectral energy increases and moves toward lower frequency component (shifted left)
N (Second Frequency Exponent)	Generalised order applied to second frequency term in equation	+	Peak spectral energy decreases, but frequency is maintained.

There are a number of alterable parameters in the Bretschneider spectrum, all of which offer a unique effect on the magnitude, shape, and distribution of the spectrum.

Decreasing the value of the constant in the equation for B will allow us to simultaneously shift the spectrum towards the lower frequency components and increase the amplitude. Conversely, increasing the value will decrease the amplitude and shift the distribution towards the higher frequency components. This is useful in simplifying the modification of the spectrum by considering the alteration of only a single parameter in the pursuit of a better fit. Indeed, this is the approach that will be pursued in seeking the optimal R_{corr} in the following work.

Increasing the N parameter, the second frequency exponent in the formulation of the Bretschneider Equation, decreases the overall spectral energy and the magnitude of the peak spectral energy, but the peak frequency is unaltered. This parameter will be useful, then, where the Bretschneider Spectrum accurately reflects the peak

period of the sea-state in question, but the magnitude of the peak energy needs to be altered for a better fit.

The following section explores the practical application of these modifications in enhancing the level of fit with the recorded conditions for each sea-state.

6.5.1.2 Improving Spectral Fit for a Sea-State using Modified Bretschneider Formulation

Figure 202 gives the R^2 correlation between the default formulation of the Bretschneider Spectrum, and the average spectral shape at the Killard Point site.

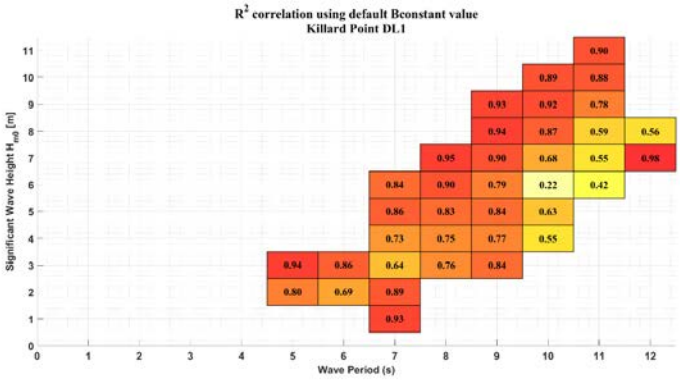


FIGURE 202: R^2 CORRELATION BETWEEN DEFAULT BRETSCHNEIDER SPECTRUM AND AVERAGE SPECTRA FOR EACH SEA-STATE.

It was found that improved correlation in wave spectral energy could be achieved by iteratively altering the parameters of the Bretschneider Spectrum discussed in Section 6.5.1.1 above, and selecting the value which gives the best representation of the spectrum. The correlation metric selected was the R^2 correlation coefficient, applied to the spectrum where the average spectrum's energy exceeded 10% of the peak spectral energy. This was to prevent erroneously high correlation results caused by attempting to fit the curve to the tail values, which contain a relatively negligible amount of energy.

For this analysis, the standard Bretschneider Spectrum has been modified to better represent the conditions at the site by iteratively changing the empirical parameter in "B" below, from an initial value of 0.751, to the best fit that could be determined

across all spectral records. On average, this returned a result for the empirical value in the Bconstant equation of 0.686, with the resulting equation being:

$$B = \frac{0.686^4}{T_{av}} \tag{6.28}$$

An analysis of the optimal B constant value for each sea-state at Killard Point is shown below.

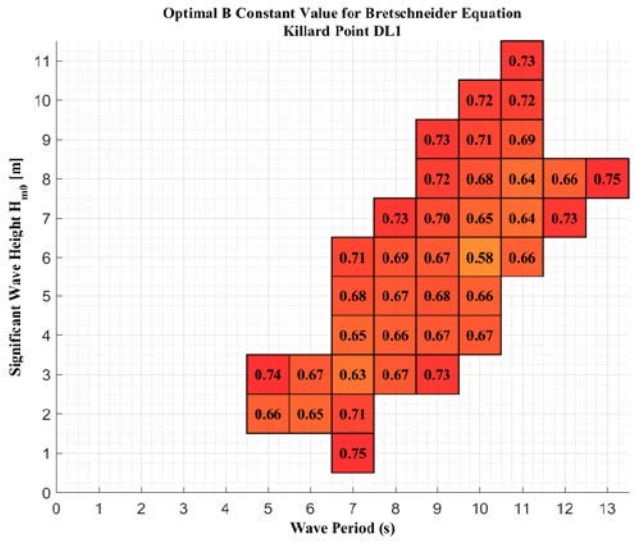


FIGURE 203: OPTIMAL "B CONSTANT" VALUES FOR BRETSCHNEIDER SPECTRUM AT KILLARD POINT

By implementing these B constant values, it can be seen that the Bretschneider Spectrum represents the conditions well for Wave Periods from 4.5 seconds to 8.5 seconds, with average R^2 Correlation values from 0.938 to 0.985, while the conditions are generally well represented across all wave heights, with average R^2 Correlation values from 0.88 to 0.996. It is worth noting that the number of spectra used in each case varies according to the occurrence of each sea-state.

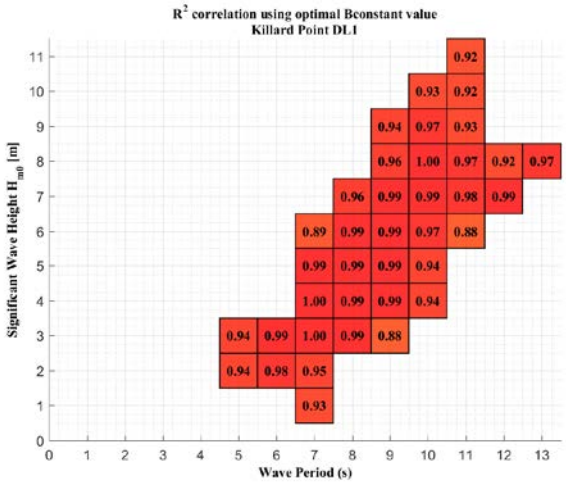


FIGURE 204: R^2 CORRELATION BETWEEN IDEALISED BRETSCHNEIDER SPECTRUM AND AVERAGE SPECTRA FOR EACH SEA-STATE

Figure 204 displays the R^2 correlation values between the average spectrum for each sea-state and the idealised Bretschneider Spectrum based on the average conditions of H_{m0} and T_{02} for that sea-state.

In general the sea-states that show the poorest correlation are those which contain the fewest occurrences. Given the short duration of the recording, this has a noticeable impact on the predicted accuracy of the spectral fits, with the spectra generally exhibiting greater divergence from the Bretschneider Spectrum at the more extreme conditions of wave height and period. For reference, the number of spectra records representing the reconstruction of each sea-state are provided below.

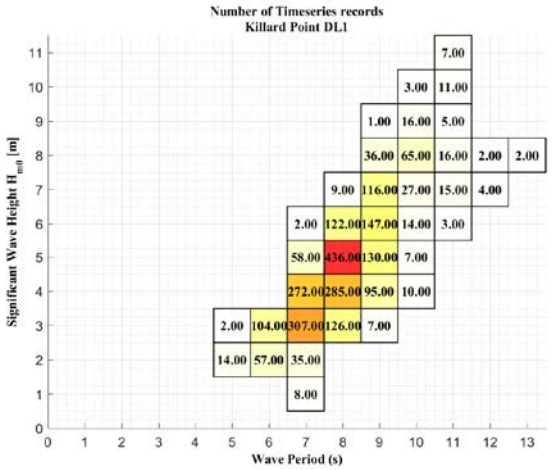


FIGURE 205: OCCURRENCE OF EACH SEA-STATE WITHIN DL1 TIME-SERIES RECORDS – EACH TIME-SERIES RECORD REPRESENTS A 28MINUTE RECORDING.

There are several sea-states represented by less than three spectra, which is certainly not sufficient to consider the correlation with an idealised spectrum, and these should be discounted when considering the spectral fit. A trend becomes evident when comparing the average spectra to the Bretschneider fit. The spectral energy at Killard Point is more peaked, particularly when there are a low number of time-series records which make up the spectral analysis. The peak spectral energy occurs in some instances at a lower period than the Bretschneider Spectrum would suggest. However, the Bretschneider Spectrum can be said to be a reasonable estimation of the conditions at the site, and is suitable for future use in determining wave parameter relationships, provided it is used for the more commonly occurring conditions.

6.5.1.3 JONSWAP Spectrum

The Joint North Sea Wave Project (JONSWAP) spectrum was found not to fit the spectral records well. For comparison, the R^2 correlation values for each sea-state are shown below:

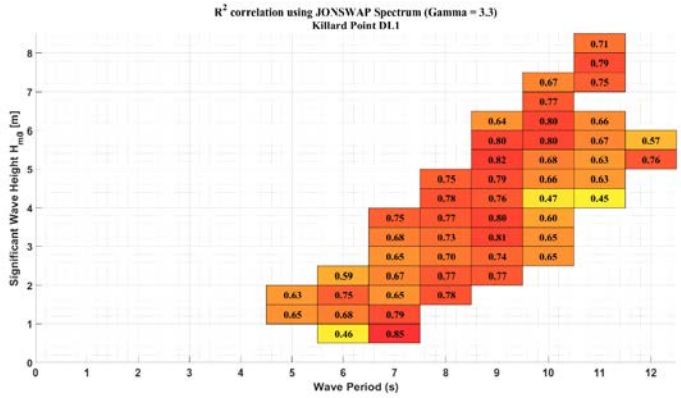


FIGURE 206: R CORRELATION BETWEEN IDEALISED JONSWAP SPECTRUM AND AVERAGE SPECTRA FOR EACH SEA STATE

The JONSWAP Spectrum does not accurately represent the conditions at the site, with an average R^2 correlation value of 0.70.

6.5.2 Wave Period Ratios (WPRs)

The characterisation of wave energy resource where there is a paucity of wave measurements necessitates the use of a theoretical approach to generate the required parameters. Taking the work done in Chapter 5 on the metocean assessment to IEC standards, for example, the Mike 21 SW wave model provides values for T_{01}. However, wave energy resource assessment parameters such as T_e are far more commonly used for the determination of power production in WECs, and are a staple parameter used in Power Matrices provided by developers (although there is a noticeably increasing trend in the T_p parameter being utilised for this). Similarly, the buoy data often suffers from missing or corrupted data due to technical, transmission and logistical issues.

WPRs have necessarily become employed as fixed conversion factors to allow for interoperability between Wave Parameters. These WPRs are commonly used as fixed conversion factors based on a theoretical spectral shape such as Bretschneider or JONSWAP, which are taken to be representative of the dominant wave conditions for fully developed and predominantly wind-driven seas, respectively. Given the importance of correctly determining the Wave Period, and the sensitivity of WECs to the energy period, wave energy resource assessments are highly sensitive to

inaccuracies in this assumed relationship. This is particularly the case where the spectral shape used to generate this assumption does not match the true spectral shape at the location under assessment. There has been significant work done in this area by (Cahill, 2014) illustrating how unsuitable assumptions for the WPR can result in substantial inaccuracies.

Although there have been significant advances in the availability of spectral measurements, coupled with the development of standards which aim to aid in the interpretation of how this data should be utilised (notably EquiMar (EquiMar, 2010b) standards and IEC TS 626-101), cases where data availability is limited will still necessitate the use of a user-defined WPR. Thus, the following work will focus on improving the level of accuracy and dependability of the use of this method through better characterisation of its variability.

The work which follows will build upon the derivation of the WPR for the most commonly used case (T_e/T_{01}) performed in Section 3.3.6.2.2, and will further show that the use of such a WPR is likely to present significant inaccuracies. Further, analysis of the buoy data at Killard Point will examine the variation that can exist in this relationship in practical applications, with this relationship being impacted by the prevailing wave conditions, as well as seasonal and intra-annual changes. The goal of this work is ultimately to derive better ratios that can be used functionally and are more reflective of real conditions.

6.5.2.1 WPR empirical estimates

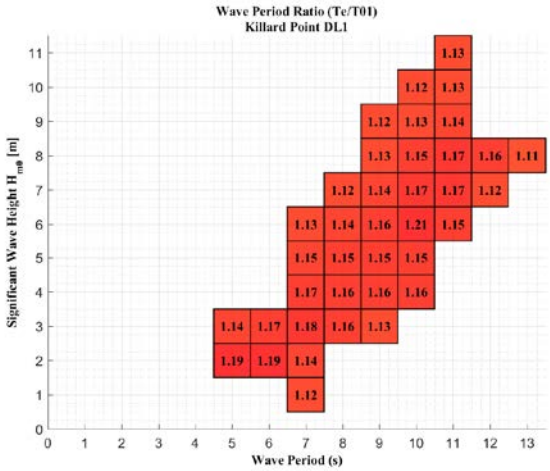


FIGURE 207: T_E/T_{01} WPRS BINNED BY WAVE HEIGHT AND PERIOD

The average WPR for T_e/T_{01} is 1.1490, compared to 1.1577 using the longer-in-time averaged history of spectral parameters using arithmetic division, and higher than the suggested Bretschneider WPR of T_e = 1.1107 T_{01}. However, the Bretschneider Spectrum assumption offers clear benefits in terms of expediency, and in formulating Wave Parameter relationships during periods when detailed data is not available. A noticeable trend is that the T_e/T_{01} ratio tends to a lower value for the extremes of both high and low wave steepness, and tends towards a larger value in intermediate wave steepness conditions.

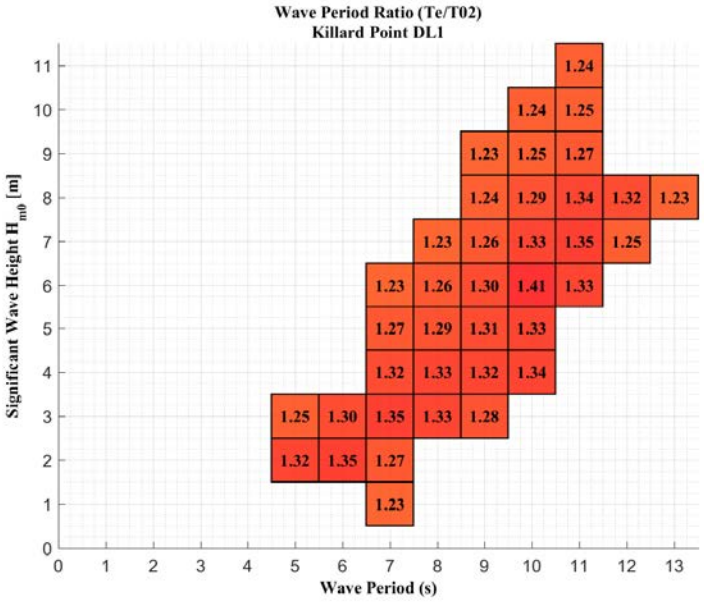


FIGURE 208: KILLARD POINT DL1 T_E/T_{02} WPRS BINNED BY WAVE HEIGHT AND PERIOD

The average T_e/T_{02} WPR for DL1 data used was found to be 1.29, with variation of approximately +-0.06 at the extremes. Steeper waves, i.e. those with large H_{m0} values in relation to the Wave Period value, were found to have a lower and less variable T_e/T_{02}. Conditions with the lowest value of wave steepness, i.e. those with lower H_{m0} values with respect to the Wave Period, were significantly more variable. Sea-states with intermediate wave steepness values were found to have the highest ratios of T_e/T_{02}, on average.

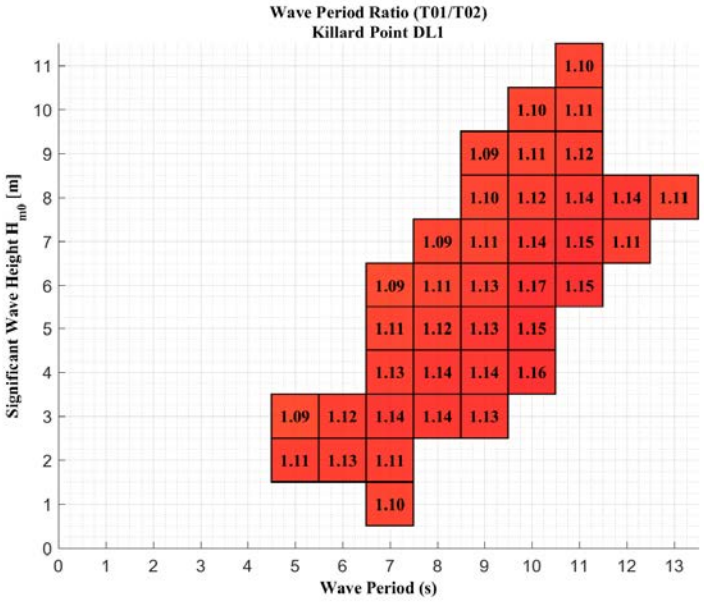


FIGURE 209: KILLARD POINT DL1 T_{01}/T_{02} WPRS BINNED BY WAVE HEIGHT AND PERIOD

The average T_{01}/T_{02} WPR for DL1 data used was found to be 1.126, which compares reasonable fairly with the direct division value of 1.124 (with minor deviation caused by the averaging of recorded data over a longer time period for the time-series records) and the Bretschneider derivation of 1.086. A variation of +-0.030 covered 95% of the variance in WPR, while – similarly to the T_e/T_{02} ratio, waves of intermediate steepness were seen to have the highest WPRs, while sea-states with lower values of steepness were found to be the highest and most variable, on average. The sea-states with the steepest waves had an almost uniform WPR of 1.090, highlighting the influence that the development of the sea and the spectral bandwidth have on the WPR; whereby the steeper waves which are typically accompanied by narrower spectral bandwidth and more concentrated spectral energy, and with a more defined spectral peak, had a more uniform WPR.

6.5.2.2 Use of WPRs

This has detailed the derivation of the T_e/T_{01} WPR, as well as providing empirical estimates of the T_e/T_{01}, T_e/T_{02} and T_{01}/T_{02} WPRs based on the data at Killard Point, finding that there is a significant difference between the theoretical WPR suggested

by the Bretschneider Spectrum and, thus, the following work will focus on improving the level of accuracy and dependability of the use of this method through better characterisation of its variability.

6.6 Framework for Implementation of Enhanced Spectral Shape Information in Wave Energy Projects

Following from the work in Sections 6.3- 6.4, this Section deals with the creation of a methodology for dealing with the impacts of spectral shape variation in both resource assessment and device testing. Given the current industry standard of assuming that sea conditions will fit neatly into an empirical spectrum, there needs to be an awareness of the impact of making this assumption and the steps that can be taken to mitigate the impact this, as well as a move toward reducing the reliance on these empirical spectra has when it comes to characterising device energy production.

When attempting to displace the use of any approach, it must be recognised that there is a clear value to adopting the standard industry approach. There are a multitude of benefits to maintaining the status quo with respect to the use of standard empirical spectra. Their use is widely accepted, well studied, reasonably applicable to a wide variety of sea-states; along with being relatively simple and quick to apply. Thus, any attempts to displace this method will need to be cognisant of the trade-off in practicality vs. accuracy that will exist. Given that the industry is currently struggling with the bankability of projects, and that financiers are demanding more accurate and dependable results, it seems logical that it would be desirable for the industry to move toward an approach which can improve accuracy.

The solution, then, may lie in producing a framework for assessment which allows the approach taken to be tailored to the level of accuracy required of the assessment in question. A detailed account of how this method can be implemented in practical application, and a discussion of proposed changes to the IEC TC114 standards to accommodate this, will be given. In keeping with this, the levels of assessment will be Class 1, 2, 3 – or respectively: “Reconnaissance,” “Feasibility,” and “Design,” - used by the IEC-TS to guide the implementation of resource modelling, and here representing incrementally more stringent and accurate standards for the approach

to determining device energy production following a detailed resource characterisation, and as appropriate to the importance of the analysis being conducted.

It's useful to first discuss some of the potential areas for improvement to the current methodologies, approach this from a cost : benefit standpoint. Starting from an idealised scenario with no time constraints, the idea is to move towards progressively more implementable solutions. The best possible results would, of course, be achieved by testing the wave energy devices with every conceivable time-series they might encounter at sea. Innumerable time and financial constraints prevent this from becoming a reality, and it is simply not feasible for any commercial project, nor does it take advantage of any particularly scientific approach in reducing the degree of testing required, thereby passing up significant cost : benefit gains.

Though it may not be possible to test every conceivable time-series, particularly in real sea-trials, the proliferation of facilities in Europe and further afield which now have the capability to generate custom time-series waves mean that it is certainly possible to test a device using real time-series data from its proposed deployment site. This is generally feasible only if there is an ongoing measurement campaign, of which several currently exist, but it is achievable, and has been shown to provide a more accurate result than the use of an assumed theoretical spectrum (Robertson *et al.*, 2016). This will be echoed by the results of the tank testing performed in Section 6.4 which involve the use of recorded sea conditions being replicated in the tank environment.

While using recorded data of limited duration, it's also possible to determine the average spectral shape at the site (for a given H_s, T_e if necessary). Then generate, or otherwise, appropriate time-series based on this average spectral shape, allowing the device to be tested with a number of variations of randomly generated time-series which closely match the true conditions at the site, offering an expansion to conditions which may not be seen at the site but can thus be estimated with appreciable improvements in accuracy. Using this approach, wave energy devices could be tested with a variety of spectral shapes for each wave condition which represent the extrema of the distributions of spectral energy. Using this as a 'map,'

it's possible to estimate far more accurately the energy production of devices without necessitating the testing of every conceivable sea-state.

This approach using real recorded data is undoubtedly the most feasible thus far, but certainly time consuming and likely to be unacceptably expensive for early stage projects. A more viable option in these cases, assuming a lack of recorded data is a key constraint, is to test the device and give its power output response to a number of modified spectra, using an approach similar to that detailed in Section 6.3.3. This will give a broader overview of device response, as well as populating a 'map,' of the device response to altered spectral shape characteristics, which can be utilised by selecting the closest condition when recorded data becomes available for a project.

The above approaches assume that the assessment of device performance is the primary goal, as this is currently a crucial issue preventing the further advancement of wave energy. In general, projects tend to be focused on a single device type, either being device-developer driven or through lack of alternative options. However, in the case that a site has the potential for deployment of various types of devices, and the performance characteristics of these devices have already been mapped in the typical power matrix fashion, a WPR assessment approach that follows the methodology of Section 6.5.2 could be implemented to enhance the accuracy of the resource data used to determine power production.

To categorise these in terms of IEC-TS Class 1, 2, 3 assessments:

6.6.1 Class 1 – Reconnaissance:

For a Class 1 assessment, it is assumed that there may be significant variations in the level of data available to the analysts and developers. Therefore, the approach is multi-faceted depending on the individual constraints of the project at this early stage.

Assuming the project has information on the device power production which is characterised by a standard H_s, T_e power matrix, assessment should begin with a parameterised approach, rather than using an assumed WPR (e.g. the T_e/T_{01} ratio). The available data may be taken from the site, and following spectral analysis, the WPR characterised over the full range of sea-states. This will already allow for more accurate WPR estimation that is reflective of both the real site conditions, and the

variation in WPR that can occur across sea-states. An example of this approach is detailed in Section 6.5.2.

If the project is device-led and has insufficient resource information for the likely site of deployment, the device should be tested and its power output response to a number of modified spectra given, using an approach similar to that detailed in Section 6.5.1. The number of spectral shapes to be considered is flexible based on the constraints of the project, but a suggested minimum would be 3 spectral shape alterations per H_s/T_e bin.

6.6.2 Class 2 – Feasibility:

At this stage of assessment, the approach should become fully spectral in nature. It is possible to retain the assumption of a Bretschneider Spectrum, but additionally tune a number of parameters related to the generation of the spectrum to achieve a superior fit to the real site conditions. At this stage, it is assumed that there has been sufficient site information collected to characterise the spectral shape of individual sea-states as determined by a 0.5m H_s and 1s T_e binning.

Caution should be exercised in attempting to analyse bins for which less than 10 spectral records exist, and depending on the variation within such bins, it may be preferable to utilise a hybrid approach whereby the Bretschneider spectrum is implemented in this scenario to reduce the impact of outliers. This approach maintains the dependability of using a recognised spectrum, while offering greatly increased accuracy. An example implementation and further background to this approach can be found in 6.5.1.

6.6.3 Class 3 – Design:

At Class 3, more advanced methods could be incorporated, such as a weighted-spectral basis approach which learns the spectral shape's relationship with Hs, and Wave Period, and is able to recreate this spectrum when a new H_s, T_p parameter is given. This approach is discussed in Chapter 3, and offers the potential for vastly improving accuracy and results which are entirely tailored to the conditions at a given site. When using this approach, the statistical model by which spectral shape is generated should be thoroughly analysed to ensure the results are applicable to the conditions, and that it is scalable to the conditions which need to be analysed. Being

a fully spectral rather than parameterised approach, far more information is retained, allowing for a more detailed analysis. Additionally, once the model has "learned" the characteristics of the site based on the information it receives, it can be paired with modelled data to recreate the spectral records for a much longer duration than those provided by recorded data alone, hence offering the benefits of both increased duration and improved characterisation accuracy.

6.6.4 Additional requirements and summation.

In each of these cases, the performance characteristics of the device should be displayed across a spectrum rather than averaging device performance based on H_s and T_e. This would necessitate slightly more complex computation to determine the energy production for a given device and resource, but the improvement in accuracy would be substantial and it is certainly achievable.

It is hoped that the framework outlined in this section provides a guide for developers and device manufacturers for achieving the level of accuracy necessary to satisfy project funding requirements, while maintaining a realistic project schedule.

6.7 Conclusions

6.7.1 Spectral Shape analysis

The work in this Chapter has examined the impact of Spectral Shape on WEC Energy Production, showing that the distribution of energy across the frequency domain varies significantly from the standard theoretical assumptions for the Killard Point Test Site, and has demonstrated how this adversely impacts energy production estimates.

Spectral Shape has been determined across a large range of sea-states at the Killard Point test site. The Bretschneider Spectrum has been shown to vary significantly from the Killard Point Characteristic Spectrum, and the resultant impact of spectral shape on device energy production has been demonstrated; both through a numerical model demonstrated in WAMIT for a cylinder-type device, and through tank testing of a 1:50 scale OWC device. A significant difference was found in the energy production estimates when using the actual recorded conditions versus empirical estimates, which is a important finding that has large impact for the development of Marine Renewable Energy Devices and Projects. Neglecting the bi-modal sea-states,

which could not be accurately re-created in the tank within the testing timeframe, power production differences as large as 41% were found between the recorded data and a Bretschneider Spectrum generated with equivalent parameters.

The resource at Killard Point has been accurately characterised and segregated according to sea-states at a division of 0.5m H_s and 1s T_p. The average WPR for each bin was produced. A clear variation between sea-states was determined, with significant deviation from the assumed average WPR based on the Bretschneider Spectrum which is in widespread use. This WPR analysis can be used as a simple mask to apply to the T_{01} wave period parameter to produce the T_{02} and T_e periods in an accurate representation of the conditions at Killard Point. Using these methods, a modified Bretschneider Spectrum has been shown to reasonably represent the conditions at Killard Point, and there is clear value to be found in modifying the parameters of the spectrum to achieve a better representation of the recorded data, with this achieving very accurate replication of the wave spectral energy profile.

A framework for implementing enhanced spectral analysis has been outlined; with a number of suggestions regarding the treatment of ocean wave analysis for 3 stages of project life-cycle, from “Reconnaissance”, to “Feasibility”, to “Design”. Suggestions are made for a multi-faceted approach depending on the individual constraints of the project at early stages, while the later stages suggest the benefits to be obtained by implementing approaches which have the potential to greatly improve the correlation of wave spectral energy estimates, and the resulting performance estimates for devices. These suggestions are further reinforced by in-tank testing which shows the impact of spectral shape on the power production of the device in a real-world scenario.

6.7.2 Ability of Tank to Generate Waves

The ability of the tank to faithfully replicate the input time-series was examined with respect to standard error metrics such as Bias, RMSE and Scatter Index. Additionally, the time-series was then subject to spectral analysis to determine the actual H_s and T_p values produced during testing. Finally, the distribution of spectral energy across the frequency domain and the shape of the spectral energy distribution were analysed. There were some distinct findings in terms of the ability of the Deep Ocean

Basin to produce the required wave conditions. Chiefly, it appears that the production of Bretschneider waves is more accurate than that of "real" time-series data. For Bretschneider conditions, H_s values were routinely within 5-10% of the requested value, and T_p values showed no variation from the requested condition. Conversely, "real" data resulted in 6-13% variation in H_s and up to 3-6% variation in T_p. For conditions that could be classified as multi-modal, this variation increased greatly. Variation in H_s from that requested was as high as 47%, with this pointing to a definite issue with the reproduction of multi-modal seas using the Deep Ocean Basin facility. The tank transfer function was not set up correctly for producing such waves, and the calibration process to correct this would have been overly time consuming. This greatly diminished the ability of this study to give an accurate reflection of the difference in energy production based on a bi-modal versus Bretschneider Spectrum. As a result, the outputs from the bi-modal study are not truly applicable, but these are available in APPENDIX A.

6.7.3 Power Production Estimation

There was a significant variation in the power production of the devices using a real spectrum (as found at Killard Point), versus using the idealised Bretschneider Spectrum. Table 98 displays the power production statistics of each spectral shape. There is a significant difference shown here in the power production for the idealised vs. real spectrum, with the real wave conditions routinely resulting in greater power production across all three devices. The shortest, 0.5m, device produced the most power in each case, whilst also typically showing the least deviation in energy production between the real and theoretical spectra tested. The devices suffered particularly as the distance between the resonant period and peak period of the spectrum grew. This was exacerbated in the case where the peak of the spectral energy was particularly defined (as was the case in the majority of recorded conditions at the site), rather than spread out over a greater frequency range.

Thus, a key take-away from this work is that variation in the spectral shape will significantly affect the power production of a device, and it is imperative to measure the impact of this with reference to the site being studied.

6.7.4 Determining Power Production from Sea-states.

This work has shown that the energy produced in a given sea-state can vary a large amount from the standardised spectral shape assumptions (Bretschneider) that are commonly in use today. This occurs across all H_s and T_p combinations, with outliers particularly producing large variations in power production. Where the peak of wave spectral density falls outside the resonant period the device, the power produced can drop off quite rapidly. For this reason, bi-modal sea states can be seen to have the same H_s and T_p, with wildly varying power production occurring where the peaks of spectral energy fall outside the response range of the device.

The degree of variation in spectral shape within the same bin is often large, and should give pause to researchers intending to give average "power matrix" figures which distil the power production of a device over a range of a 0.5 meter and 1.0 second division. This work has shown that, with an average of 10-18% deviation in power production from the idealised spectrum, further distilling the energy production of a device into an average figure is unwise. The power matrix format itself does not lend itself to great accuracy in determining energy production. Device developers and resource analysts should be encouraged to make their information available in full spectral format, to avoid any unnecessary mis-steps and introduction of inaccuracy in the determination of device power production.

In the case where the full complement of spectral sea-state information is not available, the optimal strategy in determining the power output that we get from a given sea-state should follow the conclusions of section 6.5 on determining spectra shape from the summary spectral parameters. Building an accurate picture of the spectral shape based on the summary parameters, the site location, the season; and taking account of unique characteristics of the site will allow us to optimise the estimation of power production for a given location and device. Further, this highlights the need to expand our efforts in obtaining high quality, high temporal resolution information at the site that is being studied for as long as possible. These measures, taken together, represent what should be taken as best practice when attempting to determine the energy production potential of a site.

7 Conclusions

Increasing interest in Marine Renewable Energy technologies has driven the field to a crucial juncture where it now rests on the cusp of commercialisation, and recent developments have created a greater need for metocean analysis which accurately characterizes the sea-states in which future projects will operate. The research contained in this thesis has aggregated available data sources for sites on the West Coast of Ireland, and utilised these to study methods for the enhancement of our knowledge of the available wave energy resource.

This work has:

- Performed a review of the existing literature and methods for wave data analysis, metocean analysis and standards governing the analysis.
- Given an overview of Machine Learning methods and the utility they can bring to the Marine Renewable Energy field.
- Identified areas of metocean analysis that are currently lacking and would benefit most from a data-driven approach.
- Utilised data available at the Belmullet test-site to examine the relationship between wave height and wave period at extreme conditions, with the aim of improving the understanding of the distribution of these parameters, as well as obtaining a value of Abnormality Index/Anomaly Index for this West-Coast site.
- Investigated the relationship between Wave Parameters, and subsequently created a Machine Learning model which learns the relationship between Wave Parameters, enabling the prediction of absent wave parameters in modelled data.
- Validated this Machine Learning Model using data available at West Coast sites in Ireland (Belmullet and Killard Point).
- Established a Nearshore domain model for the Killard Point Site in Co. Clare in MIKE21 SW to provide long term hindcast data for energy production prediction and operational decision-making processes; subsequently performing a metocean analysis to the newly formed IEC TS 626-101 standards, as well as a first-of-kind examination of the efficacy of these new

standards in relation to wave modelling and characterisation for Marine Renewable Energy Projects.

- Characterised ocean sites using modelled data, and determined the effect which over-reliance on modelled data can have on the ultimate production of energy at the site, as well as the impact on operation and maintenance actions.
- Analysed device power production differences between a standard theoretical spectrum and a real recorded spectrum using OWC devices in deep ocean basin test at MaREI facility.

Commented [AB15]: Put methods first, then Killard point work, then spectral shape – to better reflect actual flow of thesis.

The overarching goal of this thesis work has been to implement data-driven methods to improve the accuracy, dependability and reliability of metocean characterisation methods for Marine Renewable Energy. The research has brought together methods previously unused, or confined to the fields of computer science or statistics, to provide an enhanced understanding of the characteristics of the available wave energy resource. For commercial applications of MRE technologies to succeed, clarity and accuracy of this information will be paramount. In this context, this thesis constitutes a timely, relevant and valuable contribution to this field.

7.1 Machine Learning Applied to Wave Parameters

This work, conducted primarily in Chapter 3, has analysed the potential for the application of ML methods to Marine Renewable Energy analysis. The ML model created for the enhancement of wave parameter conversion has shown to provide improved accuracy in the determination of related wave parameters, and has additionally shown benefits in the estimation of wave parameters which are absent from limited datasets. This approach has been validated at both the Killard Point and Belmullet Berth B sites. The prediction accuracy has shown to be much improved in the ML model in comparison to the existing CWPR and Bretschneider models, even under relatively ideal conditions for each model. These findings were consistent across the two sites studied, as well as at different time scales and accounting for the effect of seasonal variability.

The improved estimates of wave parameters have resulted in an improvement in the ultimate prediction of energy production, with this being determined using the

theoretical WEC device at both sites. The implementation of the ML model resulted in approximately a 4% improvement over the constant Wave Period Ratio method, and approximately a 7-27% improvement over the Bretschneider method dependant on the site. This finding is significant, and suggests that current methods used are not optimal for the prediction of energy production using an estimated T_e parameter. This improvement in the prediction of energy production should offer a significant benefit for developers in improving the certainty of energy production.

The calibration of hindcast model data to better fit recorded site conditions for the Killard Point site, performed in Chapter 3, is achieved using this model and represents a significant step toward producing the best possible energy output estimate for the WestWave project.

The time required to train the ML model has been characterised, informing its use alongside future buoy deployments and in future projects. The short training time required makes this a useful addition to short term buoy deployments typical of MRE projects. It was demonstrated that the ML model can determine credible estimates of the relationship between wave period parameters with as little as 50 hours of recorded data, though this learning rate was found to particularly dependant on the variability and seasonality of the dataset under study. This learning time is far quicker than was anticipated, and will expand the potential utility of short buoy deployments when used in conjunction with this method of determining WPRs; offering large benefits in terms of time savings and easing the burden of an extended data capture campaign significantly. To guarantee a well-trained model that is effective at predicting conditions in all seasons, an extended deployment covering all seasons is still preferable as the accuracy of the model continues to improve as more training data is supplied.

Alongside the model created, a lookup table which defines the average Wave Period Ratio for each sea-state on a site-by-site basis has been created. This provides a more immediately applicable method, which will allow device developers to make easy design decisions relating to the WPR ratio when limited datasets are available. This work provides an easily implementable method to enhance the accuracy of wave parameter conversion.

7.2 Extreme Wave Assessment Techniques

Chapter 4 proposes a methodology for optimized prediction of extreme conditions. The work addresses methods of extreme wave prediction currently in use, and focusses on the determination of alterations to these methods which improve the accuracy, utility and reliability of extreme wave estimates produced. The work performed here has succeeded in providing greater accuracy through an improved understanding of the influence of selection thresholds on the resultant extreme wave prediction, through automated selection of the best-fitting distribution for wave conditions at the site, and via greater knowledge of the relationships between wave parameters at these extreme conditions.

Extreme analysis has been performed for the Belmullet Berth B site to demonstrate and validate these proposed techniques. Particular emphasis is placed upon the determination of extreme values using limited-in-time buoy datasets, including an analysis of the influence of threshold selection, and dependence of threshold selection on data availability. This has found that many challenges are presented by limited recorded data, which necessitate careful selection in the analysis of extreme waves; with the ultimate prediction being highly dependent on the choice of threshold used.

A new methodology for determining extreme wave periods, that is the wave periods occurring coincidentally with the most extreme wave heights, is established and analysed using a limiting-steepness based approach. This approach is seen to provide a limiting bound to inform the relationships between wave parameters during extreme conditions.

Regression analysis has been used to further determine Wave Parameter Relationships occurring coincidentally with the most extreme wave heights. Significantly, the relationship between H_s and H_{max} or T_z magnitudes can be determined for conditions defined as extreme wave events. With this relationship tailored to a particular site, an improved estimate of wave parameters coincident with future extreme H_s events can be determined. This will see additional benefit as further data is gathered in future. These relationships have been derived for Belmullet Berth B data, finding that the AI reaches a ratio of approximately 1.65

during extreme H_s conditions, which is consistent with the lower-end of many industry assumptions for this ratio. The impact being that the H_{max} likely to occur with the extreme H_s condition is significantly lower than those produced by the theorised 1.87 - 2.00 AI ratio which is often used in extreme analysis in the industry.

Using this regression methodology, H_{max} and T_z magnitudes can be calculated based on a method which is tailored to each site, rather than assuming values of the anomaly index and wave steepness that have been derived empirically elsewhere. Informed by QQ plots which examine the asymptotic or otherwise relationship of extreme conditions, and by statistical fitting; the best fitting extreme distribution for the data has been identified, allowing for increased confidence in the prediction of extreme results, rather than reliance on operator selection, as has been done in the past.

At both the Belmullet and Killard Point sites, the extreme values of H_s and H_{max} were identified using Generalised Extreme Value techniques and the corresponding extreme T_z and AI values were determined using the results of the regression analysis on these parameters. Extreme H_s values of 17.1m at Belmullet Berth B, 10.7m nearshore at Killard Point, and 14.84m offshore at Killard Point for 20-year return period have been determined.

The average conditional exceedance rate (ACER) method is applied to the prediction of extreme wave heights using a cross-validation method to obtain an insight into its behaviour. The analysis of ACER as a prediction method for H_s at the M3 buoy has shown that the method provides reasonable estimates of predicted extreme wave heights, and does so using sub-asymptotic data that does not require that extreme events occur in the recorded data to make a prediction. The use of a cross-validated approach allowed for additional insight into the influence of the selected data on the resulting prediction, while highlighting aspects of the prediction that were particularly affected by either the variation in conditions encountered in the dataset, or the length of return period for which extreme values were predicted. It was found, however, that even amongst 1-year segments of the dataset with similar maxima encountered, there was significant variation in the predicted value. Despite this, the

ACER method implemented with cross-validation approach shows promise for more consistent and informative prediction of extremes.

The motivation for this work comes primarily from the Offshore Renewable Energy sector, whose sustainability is dependent on reducing both cost and risk. Using the results produced by this work, which provide more accurate design information, and thus more certainty in terms of the survivability of a structure and represent a de-risking of the proposed project, the results provide technology developers with guidelines for the development of devices which can survive to the extreme conditions that will be experience at exposed Atlantic sites.

7.3 Metocean Analysis of Killard Point to IEC standards

The focus of this work was on performing a first-of-kind numerical modelling and wave resource characterization study to IEC 62600-101 standards for Wave Energy Resource Assessment and Characterization, using Ireland's first commercial wave energy farm project as a test case for exploring the validity, cost and the practicality of implementing the IEC-TS. The research in Chapter 5 represents an important development for the future of Marine Resource assessment, and will serve to inform future use of, and improvements to, the IEC-TS.

A comprehensive metocean assessment of the Killard Point site has been performed, which covers accessibility, extremes, directionality, monthly and annual variation of conditions, and power production. Hindcast Numerical Modelling has been conducted to IEC-TS standards. This analysis has been the first application of the IEC-TS to a commercial project. A Class 1 model assessment was performed for the Killard Point Site, using parametric wave data inputs (H_s, T_p, Peak Direction) and a 3rd generation spectral wave model, Mike 21 SW. 24 years of high quality hindcast data was produced, with output at multiple validation points indicative of likely locations for WEC deployment, and with results comparing favorably to state of the art hindcast models for Ireland. This gives a much greater understanding of the characteristics of energetic sites on the West Coast of Ireland.

The research further implemented a number of novel methods and improved tools for resource assessment developed in this thesis, and succeeded in improving energy production prediction via improved Wave Period Parameter estimations. This was

achieved through the development of both a Machine Learning based methodology which improved the accuracy of T_e energy period prediction, and a characterization of the WPR through binning of values of these ratios across the most commonly occurring conditions at the site.

The Extreme Wave determination methodology developed was used to obtain estimates of Extreme Wave conditions for wave height and period parameters at the Killard Point site, and to validate the utility of this approach in providing estimates which give increased information for the development of Marine Renewable Energy Projects.

A new methodology has been developed for assessing numerical model forecast performance for Irish Wave Energy sites. Section 5.4.7 analyses Marine Institute Forecast model data, identifying trends in model behaviour and performance. The impact of forecast model performance on power production accuracy has been analysed and quantified. This result indicates that the Marine Institute Forecast could prove valuable in informing future design decisions for MRE projects, informing them of both the magnitude and expected variability of the resource.

The variability of wave resource and potential energy production has been assessed in detail, providing stakeholders with important information for the provisioning of energy and grid resources, as well as affording the opportunity to formulate an operations and maintenance protocol which minimizes the disruption to operations and loss of energy production. Given the current reticence in lending for Marine Renewable Energy (MRE) projects, it is absolutely vital that these modelling results are as accurate and dependable as possible. The analysis performed in this work is a significant step towards quantification of resource that is appropriate for the advancing level of MRE development now being seen. These improvements and novel applications are an instrumental development for the future of Marine Resource assessment.

7.4 Impact of Spectral Shape on Device Energy Production

The work done in Chapter 6 has examined the impact of spectral shape on WEC energy production. The power production difference between recorded time-series

data and theoretical spectra has been verified, with this taking place in both a numerical analysis, and using a scaled wave energy device in tank tests.

The correlation between the conditions at the Killard Point site and the Bretschneider Spectrum has been determined across a large range of sea-states. The Bretschneider Spectrum has been shown to reasonably represent the conditions at Killard Point, however there is clear value to be found in modifying the parameters of the spectrum to achieve a better representation of the recorded data, with this achieving very accurate replication of the wave spectral energy profile. The resource at Killard Point has been accurately characterised and segregated according to sea-states at a division of 0.5m H_s and 1s T_p. The average WPR for each bin was produced. A clear variation between sea-states was determined from this, with significant deviation from the assumed average WPR based on the Bretschneider Spectrum. This WPR analysis can be used as a simple mask to apply to the T_{01} wave period parameter to produce the T_{02} and T_e periods in an accurate representation of the conditions at Killard Point.

Oscillating Water Column devices have been constructed with the aim of verifying these power production differences in a real-world scenario. This is done in a fashion which is simple and easily replicable, such that this design can easily be used to test these impacts elsewhere at low cost. The impact of spectral shape on device energy production has been demonstrated, both through a numerical model demonstrated in WAMIT for a cylinder-type device, and through tank testing of a 1:50 scale OWC device. Neglecting the bi-modal sea-states, which could not be accurately re-created in the tank within the testing timeframe, power production differences as large as 41% were found between the recorded data and a Bretschneider Spectrum generated with equivalent parameters. While the determination of variation in power production has been somewhat hampered by the inability of the wave tank to generate the requested wave conditions, particularly for more complex (multi-modal) sea-states, it has still proven useful in outlining the large variation in power production from that predicted using a theoretical approach.

Based on the work done in validating the variation in spectral shape and its resultant impact, as well as the effort to generate a standardised approach for metocean

characterisation in the newly-formed IEC-TS, a strategy has been outlined for the optimal determination of energy production for varying stages of proposed developments, which will prove a large benefit to developers in determining the optimal characterisation approach, appropriate to the project level.

Looking towards the commercial application of Marine Renewable Energy devices, this work has demonstrated the value of improved spectral fitting, novel methods of resource binning and characterisation, and displayed a testing framework that should be used for future device testing to enhance the accuracy of the energy estimates produced, greatly enhancing the accuracy of spectral shape characterisation and its impacts in MRE projects.

7.5 Further Work

The research conducted in this thesis has explored a broad range of analysis and assessment options in metocean resource assessment, and has provided suggestions for improving these which fall in line with what will be required for successful commercial deployments of WECs in the near future. An enhanced understanding of the characteristics of the Killard Point site has been developed, with this being assessed using the newly formed IEC-TS, representing the first commercial application of these standards.

The analysis of metocean conditions at Killard Point site will be used to drive the design, construction and operation of the WestWave project; informing the survivability, accessibility and reliability of WECs at the site, as well as providing detailed information on the level and variability of power production expected. This will enable detailed techno-economic assessment of the project.

The process of assessing the project to these rather onerous standards has highlighted a number of gaps and opportunities for further research which would aid in improving the energy production potential certainty of WEC deployments.

The analysis of extreme waves which takes place in this work has brought more certainty to the prediction of periods coincident with extreme waves, important information for device developers in determining the extreme energy associated with the event. The Extreme Wave assessment techniques used, including the

application of the ACER method to the prediction of extreme waves using a cross-validated method, would be well served by trials at further sites. This work could be expanded by studying H_{max}/H_s ratios and wave period relationships at a number of other sites to determine the level of repeatability of this analysis technique in locations with varying climates. A focus on determining a method of better integrating the cross-validation aspect of the ACER method to inform variability in predictions, as well as providing more concrete analysis of the influence of data length on the return period prediction possible would be of great value. Using this, alongside the overall methodology in Chapter 4, it will be possible to produce a model which fully characterises the extreme wave events likely at an increased number of locations around the Irish Coast, providing the basis for an atlas of the likely extreme events.

The forecasting prediction work conducted using the Marine Institute SWAN-derived forecast model will prove imminently useful in determining deployment and operations and maintenance strategy at the Killard Point site, and thus a more detailed assessment of this model which includes buoys placed further offshore, expanding the prediction window of the model, would be of great commercial interest. Additionally, implementing the ML model developed in Chapter 3, with the inclusion of a time-lag term to boost the predictive ability of the model for spatially separated but correlated buoy datasets, would provide a large benefit in the predictive ability of the model and extend its applicability. Coupling the Marine Institute forecast model with the Mike 21 SW model for Killard Point would enable highly accurate prediction of the local wave climate.

A major addition to the ML methodology developed is planned, and already underway as part of the author's Fulbright-Marine Institute award taking place at Oregon State University. This development seeks to extend the capability of the ML model by adding the ability to re-create the spectral shape at the site, using a weighted spectral-basis approach to determine the most likely spectral shape. This approach will involve training the model by providing H_s, T_e pairs alongside the recorded spectral shape. The aim is to be able to provide an accurate re-creation of spectral shape based solely on the trained model and limited information on the

summary wave parameters. This would have a multitude of benefits, but would chiefly enable more detailed analysis of energy production based on H_s, T_e. for the WestWave project. This would enable enhanced energy prediction production based on data provided by the Marine Institute forecast model; having far wider applicability as increasing WEC deployment projects are commissioned. This is a significant enhancement to current site assessment and characterisation that warrants investigation beyond the initial assessment of estimated device performance based on standard and non-standard (machine-learned) spectral shapes. Alongside the work done in Chapter 6, it should provide the needed push for device developers to characterise device energy production based on a fully frequency-based analysis, rather than relying on the use of the power matrix approach which lacks the precision to correctly determine expected energy production for a device in a given sea-state.

The variation in energy production between the use of an assumed spectral shape and utilising the real time-series information – highlighted in Chapter 6 has shown that the use of an empirical spectral shape has a very large impact on the determination of energy production, and has highlighted the need to provide alternative methods to improve the certainty of these estimates. The methods explored, including the use of a lookup-table generated which outlines an average WPR for each sea-state, and the modification of the standard Bretschneider spectrum to better fit the spectral shape of the recorded conditions, have both shown promise. This should be explored at other sites and with other empirical spectra to determine the impact that this can have over a larger set of locations and conditions. Given the issues with replication of bi-modal spectra in the tank testing environment, it would be beneficial to attempt to address the causes of this, and re-visit the impact of spectral shape on the energy production of scale model physical device performance, particularly given that the bi-modal spectra are likely to show the greatest deviation in energy production from the theoretical spectral shapes, and were additionally found to be a relatively common occurrence at the sites studied.

Steps should also be taken to implement these methods, and the suggested framework in Section 6.5 in commercial developments as a means of improving the

accuracy, certainty, and applicability of the energy production estimates generated. This author will be joining IEC panel for IEC TS 626-100 with the aim of advising the development of the updated IEC-TS standards, and will push to have the impact of these methods reflected and outlined within.

References

van ‘t Veer, R. and Tholen, H. J. (2008) ‘Added Resistance of Moonpools in Calm Water’, *Volume 6: Nick Newman Symposium on Marine Hydrodynamics; Yoshida and Maeda Special Symposium on Ocean Space Utilization; Special Symposium on Offshore Renewable Energy*, pp. 153–162. doi: 10.1115/OMAE2008-57246.

Agrawal, J. D. and Deo, M. C. (2004) ‘Wave parameter estimation using neural networks’, *Marine Structures*, 17(7), pp. 536–550. doi: 10.1016/j.marstruc.2005.01.001.

Alexandre, E. *et al.* (2015) ‘A hybrid genetic algorithm—extreme learning machine approach for accurate significant wave height reconstruction’, *Ocean Modelling*, 92, pp. 115–123. doi: 10.1016/j.ocemod.2015.06.010.

Ambühl, S., Kofoed, J. P. and Sørensen, J. D. (2014) ‘Stochastic modeling of long-term and extreme value estimation of wind and sea conditions for probabilistic reliability assessments of wave energy devices’, *Ocean Engineering*. Elsevier, 89, pp. 243–255. doi: 10.1016/j.oceaneng.2014.08.010.

Aqumarine Power Ltd. (2014) *Aquamarine Power announces plans to downsize business*. Available at: http://www.aquamarinepower.com/news/aquamarine-power-announces-plans-to-downsize-business.aspx (Accessed: 9 June 2015).

Arinaga, R. A. and Cheung, K. F. (2012) ‘Atlas of global wave energy from 10 years of reanalysis and hindcast data’, *Renewable Energy*. Elsevier Ltd, 39(1), pp. 49–64. doi: 10.1016/j.renene.2011.06.039.

Astariz, S. and Iglesias, G. (2015) ‘The economics of wave energy: A review’, *Renewable and Sustainable Energy Reviews*, 45, pp. 397–408. doi: 10.1016/j.rser.2015.01.061.

Babarit, a. *et al.* (2012) ‘Numerical benchmarking study of a selection of wave energy converters’, *Renewable Energy*. Elsevier Ltd, 41, pp. 44–63. doi: 10.1016/j.renene.2011.10.002.

Bahaj, A. S. (2011) ‘Generating electricity from the oceans’, *Renewable and Sustainable Energy Reviews*. Elsevier Ltd, 15(7), pp. 3399–3416. doi:

10.1016/j.rser.2011.04.032.

Barker, A. and Murphy, J. (2015) 'Reliability of Extreme Wave Prediction Methods', pp. 1–8.

Barker, A. and Murphy, J. (2016) 'Machine Learning approach for optimal determination of Wave Parameter Relationships', *IET Renewable Power Generation: OSES 2016 Special Issue*.

Barrett, S., Holmes, B. and Lewis, A. (2007) 'Scalability of a Benign Wave Energy Site', in *7th European Wave and Tidal Energy Conference (EWTEC)*.

Battjes, J. a and Groenendijk, H. W. (2000) 'Wave height distributions on shallow foreshores', *Coastal Engineering*, 40(3), pp. 161–182. doi: 10.1016/S0378-3839(00)00007-7.

Battjes, J. a and Janssen, P. A. E. M. (1978) 'Energy Loss and Set-Up due to breaking of random waves'.

Blavette, A. (2013) *Grid integration of wave energy & generic modelling of ocean devices for power system studies*.

Booij, N., Ris, R. C. and Holthuijsen, L. H. (1999) 'A third-generation wave model for coastal regions: 1. Model description and validation', *Journal of Geophysical Research*, 104(C4), pp. 7649–7666. doi: 10.1029/98JC02622.

Bretschneider, C. L. (1951) *The Generation and Decay of Wind Waves in Deep Water*. University of California, Institute of Engineering Research (IER series 29). Available at: https://books.google.ie/books?id=69hYHQAACAAJ.

Bretschneinder, C. L. (1964) 'Generation of Waves by Wind State of the Art', *International Summer Course Lunteren*, p. 160. doi: 10.1017/CBO9781107415324.004.

Cahill, B. (2014) 'WAVE PERIOD RATIOS AND THE CALCULATION OF WAVE POWER', *2nd Marine Energy Technology Symposium*, pp. 1–10.

Cahill, B. and Lewis, T. (2013) 'Characteristics of the Wave Energy Resource at the Atlantic Marine Energy Test Site'.

Chwastyk, P. and Kołosowski, M. (2014) 'Estimating the cost of the new product in development process', *Procedia Engineering*. Elsevier B.V., 69, pp. 351–360. doi: 10.1016/j.proeng.2014.02.243.

Cid, A. *et al.* (2016) 'Long-term changes in the frequency, intensity and duration of extreme storm surge events in southern Europe', *Climate Dynamics*. Springer Berlin Heidelberg, 46(5–6), pp. 1503–1516. doi: 10.1007/s00382-015-2659-1.

Clément, A. *et al.* (2002) 'Wave energy in Europe: Current status and perspectives', *Renewable and Sustainable Energy Reviews*, 6(5), pp. 405–431. doi: 10.1016/S1364-0321(02)00009-6.

Coles, S., Heffernan, J. and Tawn, J. (2000) 'Dependence Measures for Extreme Value Analyses', pp. 339–365.

Cooley, J. W. and Tukey, J. W. (1965) 'An Algorithm for the Machine Calculation of Complex Fourier Series', *Mathematics of Computation*, 19(90), p. 297. doi: 10.2307/2003354.

Cuadra, L. *et al.* (2016) 'Computational intelligence in wave energy: Comprehensive review and case study', *Renewable and Sustainable Energy Reviews*, 58(MAY), pp. 1223–1246. doi: http://dx.doi.org/10.1016/j.rser.2015.12.253.

Dalton, G. J., Alcorn, R. and Lewis, T. (2010) 'Case study feasibility analysis of the Pelamis wave energy convertor in Ireland, Portugal and North America', *Renewable Energy*. Elsevier Ltd, 35(2), pp. 443–455. doi: 10.1016/j.renene.2009.07.003.

Dalton, G. J., Alcorn, R. and Lewis, T. (2012) 'A 10 year installation program for wave energy in Ireland: A case study sensitivity analysis on financial returns', *Renewable Energy*. Elsevier Ltd, 40(1), pp. 80–89. doi: 10.1016/j.renene.2011.09.025.

Danish Hydraulic Institute (2015) 'Mike 21 Wave Modelling', pp. 1–18.

Datawell (2012) 'Datawell Waverider Installation Guide Datawell BV ocea nog raphic in s tru men ts', pp. 1–8.

St. Denis, M. and Pierson, J. W. (1953) 'On the Motions of Ships in Confused Seas'.

Department of Communications and Resources, E. & N. (2014) 'Offshore Renewable Energy Development Plan: A Framework for the Sustainable Development of

Ireland's Offshore Renewable Energy Resource', (February). Available at: http://www.dccae.gov.ie/energy/SiteCollectionDocuments/Renewable-Energy/20140204 DCENR - Offshore Renewable Energy Development Plan.pdf.

Draper, L. (1972) 'Extreme Wave Conditions In British And Adjacent Waters'.

Ecofys *et al.* (2011) 'Financing Renewable Energy in the European Energy Market', p. 264.

Engineers, U. A. C. of (1995) 'Field Wave Gaging Program, Wave Data Analysis Standard'.

EquiMar (2010a) *D2.3 Application of numerical models*, *Assessment*.

EquiMar (2010b) *Protocols for wave and tidal resource assessment*, *Equitable Testing and Evaluation of Marine Energy Extraction Devices in terms of Performance, Cost and Environmental Impact*.

ERC and UCD (2017) *MULTIWAVE Project*. Available at: http://www.ercmultiwave.eu/ (Accessed: 31 December 2017).

EU (2008) 'Reference Document on Renewable Energy Sources Policy and Potential'.

Evans, D. V. and Porter, R. (1995) 'Hydrodynamic characteristics of an oscillating water column device', *Applied Ocean Research*, 17(3), pp. 155–164. doi: 10.1016/0141-1187(95)00008-9.

Falcão, A. F. D. O. (2010) 'Wave energy utilization: A review of the technologies', *Renewable and Sustainable Energy Reviews*, 14(3), pp. 899–918. doi: 10.1016/j.rser.2009.11.003.

Falnes, J. (2007) 'A review of wave-energy extraction', *Marine Structures*, 20(4), pp. 185–201. doi: 10.1016/j.marstruc.2007.09.001.

Fernández, J. C. *et al.* (2015) 'Significant wave height and energy flux range forecast with machine learning classifiers', *Engineering Applications of Artificial Intelligence*, 43(AUGUST), pp. 44–53. doi: 10.1016/j.engappai.2015.03.012.

Folley, M. and Whittaker, T. J. T. (2009) 'Analysis of the nearshore wave energy resource', *Renewable Energy*. Elsevier Ltd, 34(7), pp. 1709–1715. doi:

10.1016/j.renene.2009.01.003.

Gallagher, S. *et al.* (2013) 'A 34-year nearshore wave hindcast for Ireland (Atlantic and Irish sea coasts): Wave climate and energy resource assessment', pp. 0–9.

Gallagher, S. *et al.* (2016) 'The nearshore wind and wave energy potential of Ireland: A high resolution assessment of availability and accessibility', *Renewable Energy*, 88, pp. 494–516. doi: 10.1016/j.renene.2015.11.010.

Garrad, A. (2012) 'The lessons learned from the development of the wind energy industry that might be applied to marine industry renewables', *Philosophical Transactions of the Royal Society A: Mathematical, Physical and Engineering Sciences*, 370(1959), pp. 451–471. doi: 10.1098/rsta.2011.0167.

Gelci, R. and Cazalé, H. (1953) 'Une théorie énergétique de la houle appliquée au Maroc', *Soc. Sci. Nat. Phys. Maroc, Comptes Rendus*, 4(64–65).

Globwave (2012) 'Deliverable D.18: Annual Quality Control Report, Phase 2'.

Gorman, R. M., Bryan, K. R. and Laing, A. K. (2003) 'Wave hindcast for the New Zealand region: Nearshore validation and coastal wave climate', *New Zealand Journal of Marine and Freshwater Research*, 37(3), pp. 567–588. doi: 10.1080/00288330.2003.9517190.

Greene, K. (2000) 'Technological innovation and economic progress in the ancient world: M. I. Finley re-considered', *The Economic History Review*. Blackwell Publishers Ltd, 53(1), pp. 29–59. doi: 10.1111/1468-0289.00151.

Greig, J., Jason, I. and Edinburgh Designs (2012) *Edinburgh Designs Wave Generation Software Manual*.

Guedes Soares, C. (1984) 'Representation of double-peaked sea wave spectra', *Ocean Engineering*, 11(2), pp. 185–207. doi: 10.1016/0029-8018(84)90019-2.

Guedes Soares, C. *et al.* (2014) 'Numerical evaluation of the wave energy resource along the Atlantic European coast', *Computers and Geosciences*. Elsevier, 71, pp. 37–49. doi: 10.1016/j.cageo.2014.03.008.

Gunn, K. and Stock-Williams, C. (2012) 'Quantifying the global wave power resource', *Renewable Energy*. Elsevier Ltd, 44, pp. 296–304. doi: 10.1016/j.renene.2012.01.101.

Hasselmann, K. (1974) 'On the spectral dissipation of ocean waves due to white capping', *Boundary-Layer Meteorology*, 6(1), pp. 107–127. doi: 10.1007/BF00232479.

Hasselmann, S. *et al.* (1985) 'Computations and Parameterizations of the Nonlinear Energy Transfer in a Gravity-Wave Specturm. Part II: Parameterizations of the Nonlinear Energy Transfer for Application in Wave Models', *Journal of Physical Oceanography*, pp. 1378–1391. doi: 10.1175/1520-0485(1985)015<1378:CAPOTN>2.0.CO;2.

Hastie, T., Tibshirani, R. and Jerome, F. (2009) 'The Elements of Statistical Learning', *The Mathematical Intelligencer*, 27(2), pp. 83–85. doi: 10.1007/b94608.

Hirsh, R. (1999) 'PURPA: The Spur to Competition and Utility Restructuring', *The Electricity Journal*, 12(7), pp. 60–72.

Holthuijsen, L. H. (2007) *Waves in Oceanic and Coastal Waters*.

Holthuijsen, L. H., Booij, N. and Herbers, T. H. C. (1989) 'A prediction model for stationary, short-crested waves in shallow water with ambient currents', *Coastal Engineering*, 13(1), pp. 23–54. doi: 10.1016/0378-3839(89)90031-8.

Hughes, M. G. and Heap, A. D. (2010) 'National-scale wave energy resource assessment for Australia', *Renewable Energy*. Elsevier Ltd, 35(8), pp. 1783–1791. doi: 10.1016/j.renene.2009.11.001.

Hydro International (2005) 'COMPARISON OF DIRECTIONAL WAVE Triaxys Wave Buoy and RD Instruments ADCP'.

IH Cantabria (2014) *AMEVA*. Available at: http://ihameva.ihcantabria.com/ (Accessed: 2 December 2015).

International Electrotechnical Comission (2014) *IEC 62600-101 TS Ed. 1: Marine Energy – Wave, tidal and other water current converters – Part 101: Wave energy resource assessment and characterization. Document 114/145/DTS.*

International Electrotechnical Comission (2015) 'IEC TS 62600-101 TECHNICAL', pp. 1–8.

Jager, D. De *et al.* (2011) 'Financing Renewable Energy in the European Energy

Market', p. 264.

Janssen, P. A. E. M. (1991) 'Quasi-linear Theory of Wind-Wave Generation Applied to Wave Forecasting', *Journal of Physical Oceanography*, pp. 1631–1642. doi: 10.1175/1520-0485(1991)021<1631:QLTOWW>2.0.CO;2.

Janssen, P. A. E. M. *et al.* (1997) 'Verification of the ECMWF wave forecasting system against buoy and altimeter data', *Weather and Forecasting*, 12(4), p. 763-784--. doi: 10.1175/1520-0434(1997)012<0763:VOTEWF>2.0.CO;2.

Johnson, H. K. and Kofoed-Hansen, H. (2000) 'Influence of Bottom Friction on Sea Surface Roughness and Its Impact on Shallow Water Wind Wave Modeling', *Journal of Physical Oceanography*, 30(7), pp. 1743–1756. doi: 10.1175/1520-0485(2000)030<1743:IOBFOS>2.0.CO;2.

Jonathan, P. and Ewans, K. (2013) 'Statistical modelling of extreme ocean environments for marine design: A review', *Ocean Engineering*. Elsevier, 62, pp. 91–109. doi: 10.1016/j.oceaneng.2013.01.004.

Jordan, M. I. and Mitchell, T. M. (2015) 'Machine learning: Trends, perspectives, and prospects', *Science*, 349(6245), pp. 255–260. doi: 10.1126/science.aaa8415.

Journée, J. M. J. and Pinkster, J. (2002) 'Introduction in Ship Hydromechanics', *TU Delft*, 1(April), p. 120. doi: 10.1111/ejh.12375.

Kerbiriou, M.-A. *et al.* (2007) 'Influence of an improved sea-state description on a wave energy converter production', p. 463e473. doi: 10.1115/OMAE2007-29254.

Komen, G. J. (1994) 'Dynamics and Modelling of Ocean Waves.', *Cambridge University Press,* p. 532 pp.

Longuet-Higgins, M. S. (1952) 'On the Statistical Distribution of the Heights of Sea Waves', *Journal of Marine Research*, pp. 245–266.

Lu, S. *et al.* (2015) 'Machine Learning Based Multi-Physical-Model Blending for Enhancing Renewable Energy Forecast – Improvement via Situation Dependent Error Correction .*', *2015 European Control Conference (ECC)*, pp. 1–8.

Mackay, E. B. L., Bahaj, A. S. and Challenor, P. G. (2010a) 'Uncertainty in wave energy resource assessment. Part 1: Historic data', *Renewable Energy*. Elsevier Ltd, 35(8),

pp. 1792–1808. doi: 10.1016/j.renene.2009.10.026.

Mackay, E. B. L., Bahaj, A. S. and Challenor, P. G. (2010b) 'Uncertainty in wave energy resource assessment. Part 2: Variability and predictability', *Renewable Energy*. Elsevier Ltd, 35(8), pp. 1809–1819. doi: 10.1016/j.renene.2009.10.027.

Manly Hydraulics Laboratory (2017) *Wave Data Analysis and Statistics*. Available at: http://new.mhl.nsw.gov.au/data/realtime/wave/AnalysisAndStatistics (Accessed: 3 January 2018).

Marine Institute (2015) *Marine Institute*. Available at: www.marine.ie (Accessed: 1 October 2015).

Marine Institute (2016) *Wave Forecasts*. Available at: http://www.marine.ie/Home/site-area/data-services/marine-forecasts/wave-forecasts.

Marine Institute (2018) *Galway Bay Test Site - Marine Institute*. Available at: https://www.marine.ie/Home/site-area/infrastructure-facilities/ocean-energy/galway-bay-test-site-0.

Marsland, S. (2015) *Machine learning: an algorithmic perspective*. CRC press.

Mathiesen, M. *et al.* (1994) 'Recommended practice for extreme wave analysis', *Journal of Hydraulic Research*. Taylor & Francis, 32(6), pp. 803–814. doi: 10.1080/00221689409498691.

Mazas, F., Garat, P. and Hamm, L. (2014) 'Questioning MLE for the estimation of environmental extreme distributions', *Ocean Engineering*. Elsevier, 92, pp. 44–54. doi: 10.1016/j.oceaneng.2014.09.034.

MET Eireann (2017) *Sea Area Forecast*. Available at: https://www.met.ie/forecasts/sea-area.asp (Accessed: 30 December 2017).

Michael E. McCormick (1981) 'Ocean wave energy conversion'.

Mitsuyasu, H. (2002) 'A Historical Note on the Study of Ocean Surface Waves', *Journal of Oceanography*, 58, pp. 109–120.

Naess, a., Gaidai, O. and Karpa, O. (2013) 'Estimation of extreme values by the

average conditional exceedance rate method', *Journal of Probability and Statistics*, 2013. doi: 10.1155/2013/797014.

National Instruments (2017) *National Instruments: Lab View*. Available at: http://www.ni.com/en-ie/shop/labview.html (Accessed: 27 July 2017).

Netherlands Enterprise Agency (2017) 'Wave & Tidal Energy`Ireland', pp. 1–26. Available at: http://www.renewableuk.com/en/renewable-energy/wave-and-tidal/.

NOAA (2017) *NCEP Central Operations*. Available at: http://mag.ncep.noaa.gov/ (Accessed: 28 November 2017).

NOAA, NESDIS and STAR (2017) *Altimetric Bathymetry*. Available at: https://www.star.nesdis.noaa.gov/sod/lsa/AltBathy/ (Accessed: 31 December 2017).

O'Reilly, W. C. *et al.* (1996) 'A Comparison of directional buoy and fixed platform measurements of pacific swell', *Journal of Atmospheric and Oceanic Technology*, pp. 231–238. doi: 10.1175/1520-0426(1996)013<0231:ACODBA>2.0.CO;2.

OES IA and IEA Energy Technology Network (2012) 'Implementing Agreement on Ocean Energy Systems - Annual Report', pp. 1–158.

opera (2017) *MARMOK-A-5 celebrates its first anniversary in the water connected to the grid*. Available at: http://opera-h2020.eu/?p=1002 (Accessed: 26 December 2017).

Padilla-Hernández, R. *et al.* (2007) 'Modeling of Two Northwest Atlantic Storms with Third-Generation Wave Models', *Weather and Forecasting*, 22(2000), pp. 1229–1242. doi: 10.1175/2007WAF2005104.1.

Policy Department A and ITRE committee (2014) 'Ocean Research in Horizon 2020: The Blue Growth Potential'.

Ramos, V. and Ringwood, J. V (2016) 'Assessing the utility and effectiveness of the IEC standards for wave energy resource characterisation', *Progress in Renewable Energies Offshore*, pp. 27–36.

Rascle, N. and Ardhuin, F. (2013) 'A global wave parameter database for geophysical applications. Part 2: Model validation with improved source term parameterization',

Ocean Modelling. Elsevier Ltd, 70, pp. 174–188. doi: 10.1016/j.ocemod.2012.12.001.

Reeve, D. E. *et al.* (2011) 'An investigation of the impacts of climate change on wave energy generation: The Wave Hub, Cornwall, UK', *Renewable Energy*. Elsevier Ltd, 36(9), pp. 2404–2413. doi: 10.1016/j.renene.2011.02.020.

Reikard, G. (2009) 'Forecasting ocean wave energy: Tests of time-series models', *Ocean Engineering*, 36(5), pp. 348–356. doi: 10.1016/j.oceaneng.2009.01.003.

reNEWS (2015) *Holyrood wraps up Pelamis deal*. Available at: http://renews.biz/82652/holyrood-grabs-pelamis-assets/ (Accessed: 9 June 2015).

Rice, S. O. (1944) 'Mathematical analysis of random noise', *The Bell System Technical Journal*, 23(3), pp. 282–332. doi: 10.1002/j.1538-7305.1944.tb00874.x.

Robertson, B. *et al.* (2016) 'Influence of wave resource assessment methodology on wave energy production estimates', *Renewable Energy*, 86(April), pp. 1145–1160. doi: 10.1016/j.renene.2015.09.020.

Sakhare, S. and Deo, M. C. (2009) 'Derivation of wave spectrum using data driven methods', *Marine Structures*. Elsevier Ltd, 22(3), pp. 594–609. doi: 10.1016/j.marstruc.2008.12.004.

Sarkar, D. and Dias, F. (2015) 'A Machine Learning Approach to the Analysis of Wave Energy Converters', in *ASME 2015 34th International Conference on Ocean, Offshore and Arctic Engineering Volume 9: Ocean Renewable Energy*, pp. 1–9.

Saulnier, J. B. *et al.* (2011) 'Wave groupiness and spectral bandwidth as relevant parameters for the performance assessment of wave energy converters', *Ocean Engineering*, 38(1), pp. 130–147. doi: 10.1016/j.oceaneng.2010.10.002.

Savitzky, A. and Golay, M. J. E. (1964) 'Smoothing and Differentiation of Data by Simplified Least Squares Procedures.', *Analytical Chemistry*. American Chemical Society, 36(8), pp. 1627–1639. doi: 10.1021/ac60214a047.

Schafer, R. W. (2011) 'a Savitzky-Golay Filter?', *IEEE Signal Processing Magazine*, (July), pp. 111–117.

SEAI (2016) 'Energy in Ireland 1990 – 2015', p. 86. doi: http://www.seai.ie/Publications/Statistics_Publications/Energy_in_Ireland/Energy-

in-Ireland-1990-2015.

SEAI (2017) *Atlantic Marine Energy Test Site (Full Scale)*. Available at: http://www.oceanenergyireland.ie/TestFacility/AMETS (Accessed: 28 December 2017).

Sharma, N. *et al.* (2011) 'Predicting solar generation from weather forecasts using machine learning', *2011 IEEE International Conference on Smart Grid Communications, SmartGridComm 2011*, pp. 528–533. doi: 10.1109/SmartGridComm.2011.6102379.

Sheng, W., Alcorn, R. and Lewis, A. (2014) 'Assessment of primary energy conversions of oscillating water columns. I. Hydrodynamic analysis', *Journal of Renewable and Sustainable Energy*, 6(5). doi: 10.1063/1.4896850.

Smith, G. H., Venugopal, V. and Wolfram, J. (2006) 'Wave period group statistics for real sea waves and wave energy extraction', *Proceedings of the Institution of Mechanical Engineers, Part M: Journal of Engineering for the Maritime Environment*. SAGE Publications, 220(3), pp. 99–115. doi: 10.1243/14750902JEME37.

Statistics for Innovation (2013) *The ACER method - a new approach to extreme value prediction*. Available at: http://sfi.nr.no/sfi/index.php/The_ACER_method_-_a_new_approach_to_extreme_value_prediction (Accessed: 25 December 2017).

Stopa, J. E. *et al.* (2016) 'Comparison and validation of physical wave parameterizations in spectral wave models', *Ocean Modelling*, 103(July), pp. 2–17. doi: 10.1016/j.ocemod.2015.09.003.

Sui, X. *et al.* (2017) 'Sea surface height measuring using InSAR altimeter', *Geodesy and Geodynamics*. Elsevier Ltd, 8(4), pp. 278–284. doi: 10.1016/j.geog.2017.03.005.

Sustainable Energy Authority Ireland, ESBI and Marine Institute (2005) 'Accessible Wave Energy Resource Atlas : Ireland : 2005', (December), p. viii.

Sverdrup, H. U. and Munk, W. H. (1947) 'Wind, Sea, and Swell. Theory of Relations For Forecasting', *United States Navy Department Hydrographic Office*, (601), p. 44.

Teillant, B. *et al.* (2012) 'Productivity and economic assessment of wave energy projects through operational simulations', *Renewable Energy*. Elsevier Ltd, 48, pp.

220–230. doi: 10.1016/j.renene.2012.05.001.

The Australian (2014) *Oceanlinx, wave energy developer, goes bankrupt*. Available at: http://www.theaustralian.com.au/business/latest/oceanlinx-wave-energy-developer-goes-bankrupt/story-e6frg90f-1226871245413 (Accessed: 9 June 2015).

The European Marine Energy Centre Ltd. (2009) *Assessment of Wave Energy Resource*, *Renewable Energy*. Available at: www.emec.org.uk/standards/assessment-of-wave-energy-resource/.

The Fleet Numerical and Oceanography Centre (2017) *Naval Oceanography Portal*. Available at: http://www.usno.navy.mil/FNMOC (Accessed: 28 November 2017).

The SWAMP Group (1985) 'The Sea Wave Modelling Project (SWAMP): Principal results and conclusions', *Ocean Wave Modelling*.

Tibshirani, R. (1996) 'Regression Shrinkage and Selection via the Lasso', *Journal of the Royal Statistical Society. Series B (Methodological)*. [Royal Statistical Society, Wiley], 58(1), pp. 267–288. Available at: http://www.jstor.org/stable/2346178.

Tidal Energy Today (2016) *Oregon's NNMREC bags $40M to build wave energy test site*. Available at: https://tidalenergytoday.com/2016/12/22/oregons-nnmrec-bags-40m-to-build-wave-energy-test-site/ (Accessed: 28 December 2017).

Tolman, H. (2002) 'The 2002 release of WAVEWATCH III', *7th International Workshop on Wave Hindcasting …*, 657575. Available at: http://nopp.ncep.noaa.gov/mmab/papers/tn220/mmab220.pdf.

Tolman, H. L. (2009) 'User manual and system documentation of WAVEWATCH-IIITM version 3.14', *Technical note*, (3.14), p. 220. doi: 10.3390/ijerph2006030011.

Tolman, H. L. (2014) 'User manual and system documentation of WAVEWATCH III', *User manual and system documentation of WAVEWATCH III version 4.18*. doi: 10.3390/ijerph2006030011.

Tolman, H. L. and Tolman, H. L. (1991) 'A Third-Generation Model for Wind Waves on Slowly Varying, Unsteady, and Inhomogeneous Depths and Currents', *Journal of Physical Oceanography*, pp. 782–797. doi: 10.1175/1520-0485(1991)021<0782:ATGMFW>2.0.CO;2.

Tucker, M. J. and Pitt, E. G. (2001) *Waves in Ocean Engineering*. Edited by Elsevier.

USGS (2007) 'Acoustic Doppler Current Profiler Applications Used in Rivers and Estuaries by the U . S . Geological', pp. 1–4.

Vissio, G. *et al.* (2017) 'ISWEC linear quadratic regulator oscillating control', *Renewable Energy*, 103, pp. 372–382. doi: 10.1016/j.renene.2016.11.046.

WAMDIG (1988) 'The WAM Model - a third gene-ration ocean wave prediction model , 1988: ', *Journal of Physical Oceanography, 18 (12), 1775 – 1810.*

Wamit (2012) *WAMIT 7.0 User manual OR - The Massachusets Institute of Technology*. Available at: citeulike-article-id:12810784.

You, Z.-J. and Callaghan, D. (2013) 'Discussion of "Modelling significant wave height distributions with quantile functions for estimation of extreme wave heights" [Ocean Eng. 54 (2012) 119–131]', *Ocean Engineering*. Elsevier, 70, pp. 208–210. doi: 10.1016/j.oceaneng.2013.05.024.

Young, I. R. (1999) 'Seasonal Variability of the Global Ocean Wind and Wave Climate', *Int. J. Climatol.*, 19(July 2015), pp. 931–950. doi: 10.1002/(SICI)1097-0088(199907)19.

Zheng, Z. *et al.* (2016) 'Dynamics of anchor last deployment of submersible buoy system', *Journal of Ocean University of China*, 15(1), pp. 69–77. doi: 10.1007/s11802-016-2627-3.

Appendix A – Bi-Modal Wave Reproduction in Deep Ocean Basin

Bi-Modal Sea-States

These sea-states were Bretschneider representations with the equivalent H_s and T_p to the selected bi-modal sea-states. NB: The "Bretschneider Representation" bimodal runs are not actually bi-modal sea states, merely the equivalent H_s and T_p to the selected time-series bi-modal sea states.

TABLE 100: RMSE REQUESTED VS. RECORDED – BRETSCHNEIDER REPRESENTATION OF BIMODAL SEA-STATES

Sea-State Number	***Metric: Root Mean Square Error (mm)***					
Wave Probe	1	2	3	4	5	6
1	8.23	9.2	6.85	7.26	9.14	8.01
2	7.9	6.29	7.65	6.19	8.16	6.21
3	6.9	7.1	6.96	7.45	6.95	7.19
4	9.08	9.47	9.46	9.27	9.72	9.56
5	10.9	12.2	12.5	12.4	13.5	13

The results are consistent with those of the Bretschneider waves examined in Table 90 and the error in the reproduction of H_s is seen to be quite minimal.

TABLE 101: RMSE REQUESTED VS RECORDED - REAL BIMODAL SEA-SEA STATES

Wave Probe	1	2	3	4	5	6
Sea-State Number	*Metric: Root Mean Square Error (mm)*					
1	23.1	23	22.9	22.6	22.7	22.7
2	22.5	22.5	22.4	22.1	22.3	22.1
3	25.1	25	24.8	24.7	24.9	24.7
4	29.1	28.8	28.7	28.7	28.7	28.7
5	31.6	31.7	31.4	31.3	31.4	31.4

The RMSE values of H_s for bi-modal sea-states are markedly higher than those of the uni-modal/Bretschneider sea-states. The error values are consistent across wave probes, but totally inconsistent with what is being requested. The RMSE value for each probe and sea state has been assessed. The reproduction of Bretschneider

waves in the tank proves the most accurate, while the tank is less well able to replicate the supplied real wave time-series conditions. For all categories of sea-state, the RMSE increases with increasing H_s.

TABLE 102: H_S SCATTER INDEX REQUESTED VS. RECORDED - BRETSCHNEIDER REPRESENTATION OF BI-MODAL SEA-STATES

Sea-State Number	***Metric: Scatter Index***					
Wave Probe	1	2	3	4	5	6
1	0.06	0.07	0.06	0.06	0.07	0.06
2	0.06	0.05	0.06	0.05	0.06	0.05
3	0.04	0.05	0.04	0.05	0.04	0.05
4	0.05	0.05	0.05	0.05	0.05	0.06
5	0.05	0.06	0.07	0.06	0.07	0.08

TABLE 103: H_S SCATTER INDEX REQUESTED VS. RECORDED - BI-MODAL SEA-STATES

Sea-State Number	***Metric: Scatter Index***					
Wave Probe	1	2	3	4	5	6
1	0.23	0.23	0.24	0.22	0.23	0.22
2	0.27	0.25	0.26	0.29	0.28	0.28
3	0.24	0.26	0.26	0.28	0.28	0.26
4	0.27	0.28	0.29	0.29	0.30	0.28
5	0.27	0.28	0.29	0.29	0.30	0.29

TABLE 104: R^2 CORRELATION COEFFICIENT FOR REQUESTED VS RECORDED TIME-SERIES - BRETSCHNEIDER BIMODAL EQUIVALENT REPRESENTATIONS

Sea-State Number	***Metric: Root Mean Square Error (mm)***					
Wave Probe	1	2	3	4	5	6
1	0.90	0.87	0.93	0.92	0.87	0.90
2	0.91	0.94	0.91	0.94	0.90	0.94
3	0.95	0.95	0.95	0.94	0.95	0.94
4	0.93	0.93	0.93	0.93	0.92	0.92
5	0.92	0.90	0.89	0.89	0.87	0.88

TABLE 105: R^2 CORRELATION COEFFICIENT FOR REQUESTED VS RECORDED TIME-SERIES - BRETSCHNEIDER BIMODAL EQUIVALENT REPRESENTATIONS

Sea-State Number	***Metric: Root Mean Square Error (mm)***					
Wave Probe	1	2	3	4	5	6
1	-0.04	-0.05	-0.06	-0.04	-0.04	-0.05
2	0.00	0.00	0.00	0.00	0.00	0.01
3	0.01	0.02	0.02	0.02	0.01	0.02
4	-0.01	0.00	-0.01	-0.01	-0.01	-0.01
5	0.02	0.01	0.01	0.01	0.01	0.00

There is almost no correlation between the requested and recorded time-series data when attempting to generate bi-modal time-series-derived waves in the tank. It remains to be seen if the spectral parameters will match between the requested and recorded time-series, but it is likely that the power production results for this portion of the test will need to be discounted given the inability of the tank to correctly produce the desired wave conditions.

TABLE 106: H_S BIAS REQUESTED VS. RECORDED - BRETSCHNEIDER REPRESENTATION OF BI-MODAL SEA-STATES

Sea-State Number	***Metric: Root Mean Square Error (mm)***					
Wave Probe	1	2	3	4	5	6
1	6.29	7.02	5.16	5.60	7.02	6.08
2	6.34	5.03	6.12	4.97	6.54	4.94
3	5.07	5.29	5.20	5.59	5.24	5.24
4	6.91	7.18	7.10	7.00	7.28	7.22
5	8.27	9.15	9.41	9.44	10.41	9.99

TABLE 107: H_S BIAS REQUESTED VS. RECORDED - BI-MODAL SEA-STATES

Sea-State Number	***Metric: Root Mean Square Error (mm)***					
Wave Probe	1	2	3	4	5	6
1	18.42	18.32	18.15	17.99	18.08	18.00
2	17.97	17.97	17.83	17.73	17.79	17.74
3	20.00	19.87	19.74	19.64	19.82	19.74
4	23.43	23.25	23.10	23.09	23.14	23.09
5	25.30	25.27	25.13	24.98	25.06	25.12

TABLE 108: REQUESTED H_S VS. RECORDED H_S – BRETSCHNEIDER REPRESENTATION OF BI-MODAL WAVES

Wave Probe		1	2	3	4	5	6
Sea-State Number	*H_s Requested (m)*	***H_s Recorded (m)***					
1	3.68	3.52	3.48	3.41	3.34	3.40	3.42
2	3.66	3.51	3.50	3.46	3.35	3.53	3.43
3	4.32	4.16	4.17	4.02	3.98	4.13	4.10
4	5.01	4.83	4.79	4.73	4.59	4.74	4.65
5	5.41	5.28	5.20	5.16	4.98	4.98	4.97

TABLE 109: PERCENTAGE DEVIATION FROM REQUESTED H_S – BRETSCHNEIDER REPRESENTATION OF BI-MODAL WAVES

Wave Probe		1	2	3	4	5	6
Sea-State Number	*H_s Requested (m)*	***% Deviation H_s Recorded from Requested***					
1	3.68	4.40%	5.63%	7.36%	9.41%	7.83%	7.16%
2	3.66	4.28%	4.46%	5.61%	8.58%	3.67%	6.43%
3	4.32	3.67%	3.32%	6.84%	7.84%	4.37%	5.07%
4	5.01	3.55%	4.40%	5.67%	8.41%	5.34%	7.25%
5	5.41	2.47%	4.01%	4.66%	8.12%	8.00%	8.24%

TABLE 110: REQUESTED H_S VS. RECORDED H_S – BIMODAL SEA-STATES

Wave Probe		1	2	3	4	5	6
Sea-State Number	*H_s Requested (m)*	***H_s Recorded (m)***					
1	3.70	2.59	2.54	2.46	2.43	2.46	2.43
2	3.68	2.49	2.49	2.43	2.38	2.41	2.37
3	4.33	2.69	2.66	2.59	2.56	2.61	2.56
4	5.03	2.78	2.72	2.65	2.63	2.65	2.62
5	5.44	3.26	3.25	3.15	3.11	3.12	3.10

TABLE 111: PERCENTAGE DEVIATION FROM REQUESTED H_S – BIMODAL SEA-STATES

Wave Probe		1	2	3	4	5	6
Sea-State Number	*H_s Requested (m)*	***% Deviation H_s Recorded from Requested***					
1	3.70	29.87%	31.16%	33.56%	34.14%	33.44%	34.36%
2	3.68	32.38%	32.40%	33.93%	35.46%	34.48%	35.47%
3	4.33	37.84%	38.57%	40.33%	41.02%	39.70%	40.91%
4	5.03	44.74%	45.90%	47.33%	47.66%	47.25%	47.87%
5	5.44	40.07%	40.23%	42.03%	42.84%	42.69%	43.04%

The deviation from the requested H_s is appreciably higher for bi-modal sea-states, reaching as high as 47.87% for bi-modal sea-state 4, which has an H_s of 5.03m (at full scale), yet the tank failed to produce a H_s value of greater than 2.78m – owing to the lack of custom transfer function for generating these waves. This removes the ability to provide an accurate comparison between the bi-modal sea-states and an equivalent Bretschneider Spectrum.

TABLE 112: REQUESTED T_P VS. RECORDED T_P – BRETSCHNEIDER REPRESENTATION OF BI-MODAL WAVES

Wave Probe		1	2	3	4	5	6
Sea-State Number	*T_p Requested (s)*	***T_p Recorded (s)***					
1	11.91	11.91	11.91	11.91	11.91	11.91	11.91
2	12.57	12.57	12.57	12.57	12.57	12.57	12.57
3	12.57	12.57	11.91	12.57	11.91	12.57	12.57
4	12.57	12.57	12.57	12.57	12.57	12.57	12.57
5	12.57	12.57	12.57	12.57	12.57	12.57	12.57

TABLE 113: PERCENTAGE DEVIATION FROM REQUESTED T_P – BRETSCHNEIDER REPRESENTATION OF BI-MODAL WAVES

Wave Probe		1	2	3	4	5	6
Sea-State Number	*T_p Requested (s)*	***% Deviation T_p Recorded from Requested***					
1	11.91	0.00%	0.00%	0.00%	0.00%	0.00%	0.00%
2	12.57	0.00%	0.00%	0.00%	0.00%	0.00%	0.00%
3	12.57	0.00%	5.26%	0.00%	5.26%	0.00%	0.00%
4	12.57	0.00%	0.00%	0.00%	0.00%	0.00%	0.00%
5	12.57	0.00%	0.00%	0.00%	0.00%	0.00%	0.00%

TABLE 114: REQUESTED H_S VS. RECORDED T_P – BIMODAL SEA-STATES

Wave Probe		1	2	3	4	5	6
Sea-State Number	*T_p Requested (s)*	***T_p Recorded (s)***					
1	12.50	10.77	10.77	10.77	10.77	11.31	10.77
2	13.11	10.77	10.77	10.77	10.77	10.77	10.77
3	12.70	11.31	11.31	11.31	11.31	11.91	11.31
4	12.90	11.91	11.91	11.91	11.91	11.91	11.91
5	13.33	10.77	10.77	11.31	11.31	11.31	11.31

TABLE 115: PERCENTAGE DEVIATION FROM REQUESTED T_P – BIMODAL SEA-STATES

Wave Probe		1	2	3	4	5	6
Sea-State Number	*T_p Requested (s)*	***% Deviation T_p Recorded from Requested***					
1	12.50	13.80%	13.80%	13.80%	13.80%	9.49%	13.80%
2	13.11	17.84%	17.84%	17.84%	17.84%	17.84%	17.84%
3	12.70	10.90%	10.90%	10.90%	10.90%	6.22%	10.90%
4	12.90	7.70%	7.70%	7.70%	7.70%	7.70%	7.70%
5	13.33	19.19%	19.19%	15.15%	15.15%	15.15%	15.15%

Overall, T_p values are reproduced accurately in the tank, with the exception of the bi-modal sea-states; in which the variation from the requested value can reach as much as 20%, which effectively invalidates the study for the purposes of characterising the variation in energy production for bi-modal sea-states. Despite this, the Bretschneider and time-series tests should provide ample data for comparison of the device power production.

7.5.1.1 Errors in reproduction of waves (Bi-Modal)

The level of error in the reproduction of Bi-Modal sea-states was worthy of further investigation.

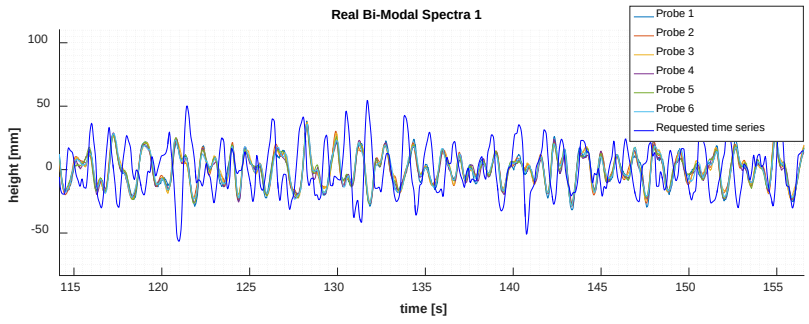


FIGURE 210: RECORDED AND REQUESTED DATA FOR GENERATION OF BI-MODAL SEA-STATE

There is a marked difference apparent when the results of the bi-modal sea-state generation are examined, as against the generation of uni-modal sea-states. There was a very large difference between the requested and recorded time-series, with

the waves produced failing to match either the amplitude or the phase of the requested time-series. It is unclear how much of this is attributable to the altered sampling frequency of the input time-series due to scaling and the removal of fine phase information required to accurately generate these bi-modal sea-states, and what effect is brought about by the transfer function calibration to generate these wave conditions.

In addition to examining the phase and amplitude of the bi-modal sea-state generation, the resultant H_s and T_p of the time-series were examined to see if the reproduction maintained the spectral characteristics to a greater degree than it did the finer wave characteristics.

The difference in H_s was in the region of 30-45% for each of the 5 bi-modal sea states examined. Below are tables which outline the requested and recorded H_s and T_p and the relative error in their reproduction.

TABLE 116: REQUESTED VS. RECORDED H_S FOR BIMODAL SEA-STATES

Real Bi-Modal waves												
Probe	1		2		3		4		5		6	
Requested H_s	H_s	% Diff.	H_s	% Diff.	H_s	% Diff.	H_s	% Diff.	H_s	% Diff.	H_s	% Diff.
3.70	2.59	29.87 %	2.54	31.16 %	2.46	33.56 %	2.43	34.14 %	2.46	33.44 %	2.43	34.36 %
3.68	2.49	32.38 %	2.49	32.40 %	2.43	33.93 %	2.38	35.46 %	2.41	34.48 %	2.37	35.47 %
4.33	2.69	37.84 %	2.66	38.57 %	2.59	40.33 %	2.56	41.02 %	2.61	39.70 %	2.56	40.91 %
5.03	2.78	44.74 %	2.72	45.90 %	2.65	47.33 %	2.63	47.66 %	2.65	47.25 %	2.62	47.87 %
5.44	3.26	40.07 %	3.25	40.23 %	3.15	42.03 %	3.11	42.84 %	3.12	42.69 %	3.10	43.04 %

TABLE 117: DEVICE POWER PRODUCTION (MEGAWATTHRS) FOR BI-MODAL REAL WAVE SEA-STATES AND BRETSCHNEIDER WAVES

	Bretschneider Waves					Bi-Modal Real Waves					Difference (%)				
	H_s (m)	T_p (s))	1m	.75 m	.5m	H_s (m)	T_p (s))	1m	.75 m	.5m	H_s (m)	T_p (s))	1m	.75m	.5m
1	3.54	11.91	2.32E+05	2.90E+05	4.35E+05	2.53	10.78	1.20E+05	1.91E+05	2.92E+05	40.06%	10.53%	93.02%	51.88%	48.89%
2	3.54	12.57	2.60E+05	2.98E+05	4.28E+05	2.48	10.78	1.32E+05	2.02E+05	2.72E+05	42.62%	16.67%	97.38%	47.53%	57.37%
3	4.22	11.91	3.83E+05	4.67E+05	6.58E+05	2.64	11.31	1.51E+05	2.22E+05	3.03E+05	59.89%	5.26%	152.57%	110.23%	117.48%
4	4.91	12.57	5.83E+05	6.95E+05	9.75E+05	2.68	11.91	1.97E+05	2.82E+05	3.90E+05	82.84%	5.56%	195.72%	146.58%	149.86%
5	5.31	12.57	7.26E+05	8.26E+05	1.13E+06	3.19	11.31	2.84E+05	3.95E+05	5.55E+05	66.51%	11.11%	155.56%	109.02%	102.70%